Synthesis and Characterization of Upconversion Nanoparticles for Applications in Life Sciences

Doctoral thesis

in fulfilment of the requirements for the degree

"doctor rerum naturalium"
(Dr. rer. nat.)

in the scientific discipline "Physical Chemistry"

submitted to the
Faculty of Science
of the University of Potsdam
by

Selma Nacak

Potsdam, March 2021

1. Gutachter: Prof. Dr. Michael Kumke
2. Gutachter: Prof. Dr. Ilko Bald
3. Gutachter: Prof. Dr. Niko Hildebrandt

Zusammenfassung

Aufgrund ihres hohen Potenzials für biologische Anwendungen haben aufkonvertierende Nanopartikel (UCNPs) in den letzten Jahren wachsende Aufmerksamkeit auf sich gezogen. Im Gegensatz zu herkömmlichen Fluorophoren, wie Farbstoffe und Quantenpunkte sind UCNPs in der Lage Photonen mit niedriger Energie zu Photonen mit höherer Energie zu konvertieren. Sie werden im Infrarot-Bereich (NIR) angeregt und emittieren Photonen in sichtbaren und NIR-Bereich. Zudem, besitzen UCNPs herausragende Eigenschaften wie reduzierte Autofluoreszenz, tiefe Gewebedurchdringung, geringe Zytotoxizität, lange Lebensdauern und die Möglichkeit zur Mehrfarben-Bildgebung. Die Untersuchung des Aufkonversion-Lumineszenz-Verhaltens von UCNPs in verschiedenen Wirtsgittern, die mit verschiedenen Ionen kodotiert sind, ist noch erforderlich, um den Einfluss der strukturellen Veränderungen auf Aufkonversion-Lumineszenz-Mechanismus besser zu begreifen. Für den Erhalt von schnell einsatzbereiten UCNPs ist die Untersuchung der Synthesemöglichkeiten von hydrophiler UCNPs in einem Schritt mit einer einfachen, umweltfreundlichen, kostengünstigen Methode von entscheidender Bedeutung.
Der Hauptfokus dieser Doktorarbeit liegt in der Erforschung der Wirkung der Kodotierung mit Gd^{3+} auf der Struktur von $NaYF_4$:Yb^{3+}:Er^{3+}:Eu^{3+} und Na_xScF_{3+x}:Yb^{3+}:Er^{3+}:Eu^{3+} UCNPs und deren Aufkonversion-Lumineszenz-Verhalten. Die erste Reihe von Proben wurde durch thermische Zersetzung synthetisiert. Die Oberfläche von UCNPs wurde mit Ölsäure bedeckt. Die Lumineszenz- sowie und die dynamische Lichtstreuungsmessungen der Proben wurden in Cyclohexan durchgeführt. Das Synthese-Verfahren der zweiten Probereihe war die Mikrowellen-unterstützte hydrothermale Synthese. Die Lumineszenzspektren der Essigsäure-bedeckten hydrophilen UCNPs wurden in Milli-Q-Wasser aufgenommen. Die Röntgenbeugung (XRD), Transmissionselektronenmikroskopie (TEM), Rasterelektronenmikroskopie (SEM), dynamische Licht-Streuung (DLS) und Lumineszenz Spektren von Eu^{3+} bei Raum- und ultraniedriger Temperatur wurden zur Sammlung der Strukturinformationen verwendet. Die Ergebnisse wurden im Zusammenhang mit den Aufkonversion-Lumineszenzspektren (UCL) der Proben in $NaYF_4$ und Na_xScF_{3+x}, vergleichend diskutiert. Die Ergebnisse der stationären und zeitaufgelösten Lumineszenz-Messungen der neuartigen spektroskopischen Sonde Eu^{3+} erlaubten Informationen über die kleinen strukturellen Unterschiede zu sammeln. Die Parallel-Faktoranalyse (PARAFAC) ergab, dass die Proben in $NaYF_4$ 2 verschiedene Eu^{3+} Spezies (in zwei verschiedenen Standortsymmetrien) beinhalten, während die Proben in Na_xScF_{3+x} drei verschiedene Eu^{3+} Spezies aufweisen. Die Änderungen der Aufkonversion-Lumineszenz-Eigenschaften der Proben wurden mit der Veränderung der Gitterstruktur durch Kodotierung mit Gd^{3+} bestimmt. Die Ergeb-

nisse der leistungsdichteabhängigen Aufkonversion-Lumineszenz-Messungen sorgen für das Verständnis des Aufkonversion-Lumineszenz-Mechanismus in den UCNPs, in Bezug auf die Gd^{3+}-Kodotierung. Das temperaturabhängige Aufkonversion-Lumineszenz-Verhalten der ersten Probereihe zeigte eine hohe relative Temperaturempfindlichkeit zwischen 288 K und 323 K.
Der zweite Schwerpunkt der Doktorarbeit liegt in der Untersuchung der Wirkung verschiedener Synthese-Parameter auf die Struktur beziehungsweise auf das Aufkonversion -Lumineszenz-Verhalten von Essigsäure (AA) bedeckten hydrophilen $NaGdF_4$:Yb^{3+} :Er^{3+} UCNPs, die durch Mikrowellen-unterstützte hydrothermale Synthesemethode hergestellt wurden. Nach der strukturellen Charakterisierung durch XRD, SEM und DLS wurden die stationären und zeitaufgelösten Aufkonversion-Lumineszenz-Eigenschaften der Proben untersucht. Die hexagonalen $NaGdF_4$:Yb^{3+}:Er^{3+} UCNPs wurden in einer Stunde unter milden Synthesebedingungen (bei 150 °C) produziert. Die Verwendung von Ethylenglykol als Teil des Mediums resultierte in Nanopartikel mit einer durchschnittlichen Größe unter 100 nm befanden.
Schließlich wurden die NIR-Anregung zu NIR-Lumineszenz - Eigenschaften der Na_xScF_{3+x}:Yb^{3+}:Tm^{3+}:Gd^{3+} UCNPs und Na_xScF_{3+x}:Nd^{3+}:Yb^{3+}, Na_xScF_{3+x}:Nd^{3+} :Yb^{3+}:Fe^{3+} Stokes-Shift Nanopartikel kurz untersucht, da die Entwicklung von Nanopartikeln mit hoheffizienter NIR-Lumineszenz entscheidend für die Verwendung von Lanthanoid dotierten Nanopartikeln in der Lebenswissenschaften ist. Die Polyethylenimin (PEI) bedeckten hydrophilen Na_xScF_{3+x}:Yb^{3+}:Tm^{3+}:Gd^{3+} UCNPs wurden durch hydrothermale Synthesemethode im Autoklaven erzeugt. Der Einfluss des niedrigen und hohen Molekulargewichts (M_W) von PEI sowie der Reaktionstemperatur auf die Gitterstruktur und das Aufkonversion-Lumineszenz-Verhalten wurden gemäßden Ergebnissen der XRD, TEM und der stationären und zeitaufgelösten Aufkonversion-Lumineszenz Aufnahmen diskutiert. Bei den UCNPs, die mit PEI (M_W = 25000 (10 Gew.%)) bei 250 °C synthetisiert wurden, haben sich sphärische Partikel mit einer durchschnittlichen Partikelgröße von 124±14 nm gebildet. Diese zeigten das höchste NIR-Blau-Intensitätsverhältnis und die längsten Lumineszenz-Abklingszeiten. Andererseits gibt es für die Na_xScF_{3+x}:Nd^{3+}:Yb^{3+} Stokes-Shift-Nanopartikel nur TEM-Bilder und stationäre Lumineszenz Spektren. Die Veränderung der spektralen Verteilung von Yb^{3+} und Nd^{3+} wurde mit zunehmender Konzentration an Yb^{3+} und Fe^{3+} beobachtet.

Abstract

In recent years, upconversion nanoparticles (UCNPs) have attracted more attention due to their high potential for biological applications. Unlike conventional fluorophores like dyes and quantum dots, UCNPs are able to convert multiple photons of lower energy to photons of higher energy. They are excited by long wavelength excitation in near infrared region (NIR) and emit photons in visible and NIR region. Furthermore, UCNPs possess outstanding properties such as reduced autofluorescence background, deep tissue penetration, low cytotoxicity, and long luminescence lifetimes, and the possibility for multicolour imaging. The investigation of upconversion luminescence (UCL) behaviours of UCNPs in different lattices codoped with various ions is still a need to understand the structural change on the UCL mechanism. Besides, the study of the synthesis possibility of hydrophilic UCNPs in one step using simple, environment friendly, inexpensive methods are vital to obtain ready for use UCNPs rapidly.
The primary work of this thesis is focused on the research of the effect of the Gd^{3+} codoping on the structure of $NaYF_4$:Yb^{3+}:Er^{3+}:Eu^{3+} and Na_xScF_{3+x}:Yb^{3+}:Er^{3+}:Eu^{3+} UCNPs and UCL behaviours. The first set of samples was synthesized by thermal decomposition method, capped with oleic acid (OA), and the luminescence measurements and dynamic light scattering measurements were carried out in cyclohexane. The synthesis method for the second set of samples was the microwave-assisted hydrothermal one step synthesis method. The luminescence spectra of acetic acid capped hydrophilic UCNPs were recorded as they were in Milli-Q water. The X-ray diffraction (XRD), transmission electron microscopy (TEM), scanning emission microscopy (SEM), dynamic light scattering (DLS), and luminescence spectra of Eu^{3+} at room and ultralow temperature were used for gathering the structural information. The results were discussed in connection with upconversion luminescence (UCL) spectra for samples in $NaYF_4$ and Na_xScF_{3+x}, comparatively. The results of steady state and time resolved luminescence measurements of the novel spectroscopic probe Eu^{3+} allowed us to have information about the small structural differences. The multiway decomposition method parallel factor (PARAFAC) analysis determined that the samples in $NaYF_4$ have 2 different Eu^{3+} species (in two different site symmetry) whereas the samples in Na_xScF_{3+x} include three different Eu^{3+} species. The changes of UCL properties of samples were determined with the alteration of the lattice structure by codoping with Gd^{3+}. The results of power density dependent UCL measurements provide an understanding of the UCL mechanism in UCNPs in relation to Gd^{3+} codoping. The temperature dependent UCL behaviours of the first set of samples showed a high relative sensitivity at between 288 and 323 K.
The second focus of the thesis is the investigation of the effect of various synthesis pa-

rameters on the structure of acetic acid (AA) capped hydrophilic $NaGdF_4$:Yb^{3+}:Er^{3+} UCNPs obtained by microwave-assisted hydrothermal synthesis method as well as their UCL behaviours. After structural characterization by XRD, SEM, and DLS, the steady state and time resolved UCL properties were investigated. The hexagonal $NaGdF_4$:Yb^{3+}:Er^{3+} UCNPs were produced in one hour under mild synthesis condition (at 150 °C). Using ethylene glycol as a part of the medium resulted in sub-100 nm nanoparticles.

Finally, the NIR excitation to NIR luminescence properties of Na_xScF_{3+x}:Yb^{3+}:Tm^{3+} :Gd^{3+} UCNPs and Na_xScF_{3+x}:Nd^{3+}:Yb^{3+} Na_xScF_{3+x}:Nd^{3+}:Yb^{3+}:Fe^{3+} Stokes-shift nanoparticles were shortly investigated, since the development of nanoparticles with high efficiency NIR luminescence is crucial to the use of lanthanide doped nanoparticles in life science. The polyethylene imine (PEI) capped hydrophilic Na_xScF_{3+x}:Yb^{3+}:Tm^{3+} :Gd^{3+} UCNPs were generated by a hydrothermal synthesis method in autoclave. The influence of the low and high molecular weight (M_W) of PEI and the reaction temperature on the lattice structure and UCL behaviours were discussed according to results of X-ray diffraction (XRD), transmission electron microscopy (TEM) and steady state, time resolved UCL records. The UCNPs synthesized with 25000 M_W (10 wt%) PEI at 250 °C were formed as spherical particles with an average particle size of 124±14 nm. They demonstrated the highest NIR to blue intensity ratio and the longest decay times. On the other hand, for the Na_xScF_{3+x}:Nd^{3+}:Yb^{3+} Stokes-shift nanoparticles there is only TEM images and steady state luminescence records. The alteration on the spectral distribution of Yb^{3+} and Nd^{3+} was observed with increasing of the concentration of Yb^{3+} and Fe^{3+}.

Dedication

To my lovely parents Sabiha, Fikret and my sweet siblings Aytekin, Semra, Gültekin

Declaration

Hiermit versichere ich, dass ich die hier vorgelegte Dissertation selbstständig verfasst und keine anderen als die angegebenen Quellen und Hilfsmittel verwendet habe.
Ich versichere, dass diese Arbeit noch nicht an anderer Stelle zur Erlangung des Doktorgrades eingereicht worden ist.

Potsdam, März 2021

(Selma Nacak)

Acknowledgements

It would not have been possible to finish this dissertation without the generous support and help of kind people around me, to only some of whom I can deliver my acknowledgements here.
First of all, I sincerely devote my gratitude to my supervisor, Prof. Dr. Michael U. Kumke. There are no words to express my thanks to him. His generous support, guidance, patience, and encouragement have been endless during my Ph.D. at the University of Potsdam. He has been given me lots of chances to learn from laboratory works, conferences, seminars and collaborating with other scientists. His invaluable suggestions made me find the right decisions for my work. Being able to study under his supervision was one of the most important experiences in my life.
I am grateful to Prof. Dr. Hans-Gerd Löhmannsröben for giving me the excellent opportunity to study in his group. Outstanding technical equipment, friendly and supportive colleagues with different scientific backgrounds, and unique working conditions have been offered me as well as a perfect working atmosphere.
I owe a big thank you to all my colleagues at the Department of Physical Chemistry for providing a stimulating and lovely environment. Thus, I could enjoy studying with them every day. My thanks go particularly to Philipp U. Bastian, Sean Mc Gee, Katja Burek, and Toni Haubitz for taking the time for me whenever I needed them and explaining everything in detail and with great patience. I could learn to set up the laser and spectroscopic system with the kind help of Philipp U. Bastian and Sean Mc Gee. I would like to thank Michael Kryzczmonik for the synthesis of nanoparticles and the spectroscopic measurements.
My great friends Emine Ertürk and Melissa Jane Monks made my study and my life in Germany enjoyable. I am incredibly happy to have had the chance to enjoy their office friendship as well. They have been supported me to overcome of all difficulties in my life and became like a family while I have been in Germany far away from my family.
I would also like to acknowledge Dr. C. Günter for helping with XRD measurements, Dr. Peter Werder for helping with SEM and DLS measurements, Dr. Fabiola Balderas-Valadez and Katlen Brennenstuhl for helping with SEM measurements, Petra Schrade, and Dr. rer. nat. Sara Timm for helping with TEM measurements, Simon Blake for helping me with the correction of my dissertation.
I would like to thank the Ministry of National Education, the Republic of Turkey, for the financial support throughout all those years.
I am eternally grateful to my dearest parents and siblings, who have been a constant source of love, peace, and encouragement for me. A special thanks to my lovely little

niece Dilşat Zeynep and nephews Kemal and Göktürk Yasin, whose presence is the source of happiness even living so far away.

Contents

Chapter 1

Introduction

1.1 Upconversion (general aspects)

Nowadays, multimodal bioimaging offers excellent opportunities in biology and medi cine. This technique combines two or more bioimaging techniques such as fluorescence imaging, magnetic resonance imaging (MRI), positron emission tomography (PET), and computed tomography (CT).[1][2] Besides providing the highest sensitivity and spatial resolution for in vitro experiments, optical imaging can also enable to give information on a cellular or molecular level. Furthermore, this technique is low-cost, robust, and compact compared to MRI, PET, and CT.[3] The fluorescence imaging is based on the naturally fluorescent species or samples made fluorescent by adding synthetic fluorescent probes, labels, or nanoparticles. Among those, the nanoparticles provide fluorescence imaging with other imaging techniques make and find a large field of application for in vivo bioimaging.[1][2]
Luminescence is the emission of electromagnetic radiation from excited states of atoms or molecules after some external stimulus such as light absorption, mechanical action, chemical reaction, cathode rays, ultrasound, etc. Fluorescence is one type of photoluminescence (PL) and occurs when an atom or molecule is excited by absorbing photons with a particular wavelength and then radiates photons with different wavelengths.[4][5] Most PL materials obey Stoke's law that refers to the fluorescence emission that should appear at a longer wavelength than the incident light.[4][6] However, some of the materials can emit light with higher energy than the incident light, according to the anti-Stokes law. As one type of anti-Stokes processes, upconversion (UC) represents a non-linear optical phenomenon, where the emission (e.g., UV, visible or NIR range) occurs after two or more low-energy near-infrared (NIR) or infrared (IR) photons via real long-lived intermediated electronic states.[4] [6] [7] [8] [9] [10] The initiation of using of UC process can be ascribed to Bloembergen with his work of the infrared quantum counter in 1959.[11] Afterwards, Auzel's experimental work in the 1960s has started active studies in the UC field.[12] Notably, the reports about the first efficient UCL in ion-doped systems in the mid-1970s and high brightness UC materials, which can be obtained more cheaply than thin films or crystals, have attracted increasing interest.[4] [8] [10] [13]
Anti-Stokes emission can also take place on two-photon fluorescence and second har-

monic generation. In two-photon fluorescence, two low-energy photons must be absorbed simultaneously via a "virtual" intermediate electronic state to excite the electron to a high excited electronic state. The other anti-Stokes process, second harmonic generation, called frequency doubling, also requires a "virtual" intermediate electronic state, coherent excitation wavelength, and non-linear medium for converting low-energy absorbing photons to high-energy emission photons. Unlike these phenomena, UC doesn't demand coherent radiation, generates higher-energy emission light by abundant ladder-like energy states, and a lower excitation power density of $\sim$0.1 W/cm^2, which means cheaper pulsed laser sources for excitation.[6] [8] [9] [14] Constantly, the two-photon fluorescence and second harmonic generation require 5–10 orders of magnitude higher excitation power. Their quantum efficiency is more than 5 orders of magnitude lower than those of UCL.[13] [15]
Current research on UCL is focused on lanthanide-doped materials because lanthanide ions promise to provide a unique upconversion and Stokes-shift properties in nanoscale materials for various bioimaging techniques.

1.2 Advantage of lanthanide ions in upconversion

The 14 metallic chemical elements from lanthanum (La, atomic number 58) to lutetium (Lu, atomic number 71) are named lanthanides (Ln), which located in the sixth period and IIIB group in the periodic table.[16] [17] Ln ions are luminescent except for La(III) and Lu(III) ions. The f-f emission lines of the luminescent Ln ions cover the entire spectrum from UV to visible and NIR ranges, with examples Nd(III), Eu(III), and Er(III), respectively.[16] [18] [19] The general electronic configuration of lanthanides is [Xe]4f^{n}5d^{1}6s^2 with n = 0 La and n = 14 Lu. They exhibit [Xe]4f^n configuration in their most stable oxidation state +3, mainly in water, and have similar physical and chemical properties. There are only a few stable Ln ions in other oxidation states like Eu(II), Yb(II), Sa(II) Ce(IV), Tb(IV).[10] [16] [20] Lanthanides are referred to as the rare earth elements with the inclusion of Scandium (Sc) and Yttrium (Y), which have similar chemical properties to lanthanide elements because of their outermost (n-1)d^{1}ns^2 electronic configuration.[10] [21]
In quantum systems with parity forbidden, the selection rules can be relaxed when the Ln ions are under the influence of a ligand-field. The non-centrosymmetric interactions lead to the mixing of electronic states of opposite parity into the 4f wavefunctions. Thus, f–f electric dipole transitions become partially allowed, and the luminescence lifetime of the electronic states is relatively long.[13] [18] The long lifetime of electronic states increases the probability of interaction with subsequent photons in the upconversion process.[13] Although the transition metals and actinides fulfill this task like Ln ions when embedded in a host material, Ln ions are used predominantly in UC systems. Because the materials doped Ln ions exhibit abundant metastable states (except Yb^{3+}) showing high potential for UCL and do not require low operating temperature like the material doped these transition metals and actinides.[9] [10] [22]
The conventional molecular probes in PL are organic dyes and quantum dots based on the Stokes-shift emission process after being excited by UV or visible light. Short-wavelength excitation causes low penetration depth in biological tissues, potential DNA

damage, and cell death by long term irradiation. Furthermore, the significant autofluorescence and strong light scattering from the biological samples (such as fur, skin and, tissues) because of the exciting at short wavelengths result in a low signal-to-background ratio (SBR). The "optical transparency window" for biological tissues is found in the NIR range of 700 - 1100 nm.[6] [7] [23] UC materials can be excited by NIR light, which allows deeper penetration depth and reduces photodamage effects. Besides these, the autofluorescence and the light scattering are minimized by NIR radiation leading to an increase in the SBR significantly. Nd^{3+} and Yb^{3+} ions can be excited at about 800 and 980 nm, respectively.[7] Organic dyes exhibit broad emission spectra due to the reason that the strong coupling with vibrations occurs.[18] This limits multiplexing experiments with different organic dyes. In contrast, UC materials show a narrow f-f emission bandwidth (10 – 20 nm full-width at half-maximum) due to completely shielding of 4f electrons by the filled $5s^2$ $5p^6$ sub-shell electrons. Therefore, f-f electronic transitions are hardly affected by the surrounding environment. Their sharp emission bands and anti-Stokes character allow optical multiplexing experiments.[6] [10] For example, $NaYF_4$:Yb^{3+}:Er^{3+} nanoparticles present well separated emissions in green (at about 550 nm) and in red (at about 660 nm) region.[7] f-f transitions of Ln^{3+} ions are Laporte (parity) forbidden, since the initial and final states display the same parities. The resultant parity prohibition leads the excited states of Ln^{3+} ions to a long lifetime typically in the μs to ms range, which makes them ideal for the time-resolved luminescence detection technique.[13] Long luminescence lifetime eliminates the unwanted short-lived background luminescence that comes from biological tissues or other short components. Because of improved SBR, this technique provides a higher detection sensitivity than a conventional steady-state luminescence detection technique.[10] [23] As one type of fluorophore, quantum dots (QD) also possess good properties for bioapplication such as large molar extinction coefficients, high quantum yields, narrow emission bandwidths, and high photostability. However, these heavy metal-based materials (e.g., cadmium, mercury, and lead) show potential toxicity for human health and the environment, which limits their use. Additionally, they suffer from intermittent emission, namely photoblinking and the change in the emission band due to particle size distribution. On the contrary, Ln^{3+} doped UC materials exhibit low toxicity and constant emission due to no impact of the external factors like solvent, particle size or shape, on the intra-f-f electronic transition. Thus, they are suitable for long-term repetitive imaging. Unlike QDs and molecular dyes, UC materials are stable against photochemical degradation. UC materials can also display linear Stokes-shift emission, like conventional fluorophores. Consequently, the outstanding advantages of Ln^{3+} UC materials make them admirable candidates in bioapplications, such as theranostics, drug delivery, and therapy.[4] [6] [7] [8] [10] [18] [23] Furthermore, they can be used excellently in fields like telecommunication, photovoltaics and magnetic refrigeration.[24]

1.3 Upconversion mechanisms

Upconversion nanoparticles normally require dopant ions and host materials, which determine mainly luminescence efficiency and colour tuning. Dopant ions are lumines-

cence centers and mostly consist of sensitizer and activator pairs. Host materials enable the energy transfer by supplying space for dopant ions with suitable distance. More importantly, the host lattice can provide a phonon assisted energy transfer between sensitizer and activator if there is a slight energy mismatch between these pairs.[10] Regarding composition, UNCPs allow several UC mechanisms. We present the UCL process in figure 1.1 generally under five different UC mechanisms, named excited states absorption (ESA), energy transfer upconversion (ETU), photon avalanche (PA), cooperative sensitization upconversion (CSU), energy migration upconversion (EMU).[10] [25]

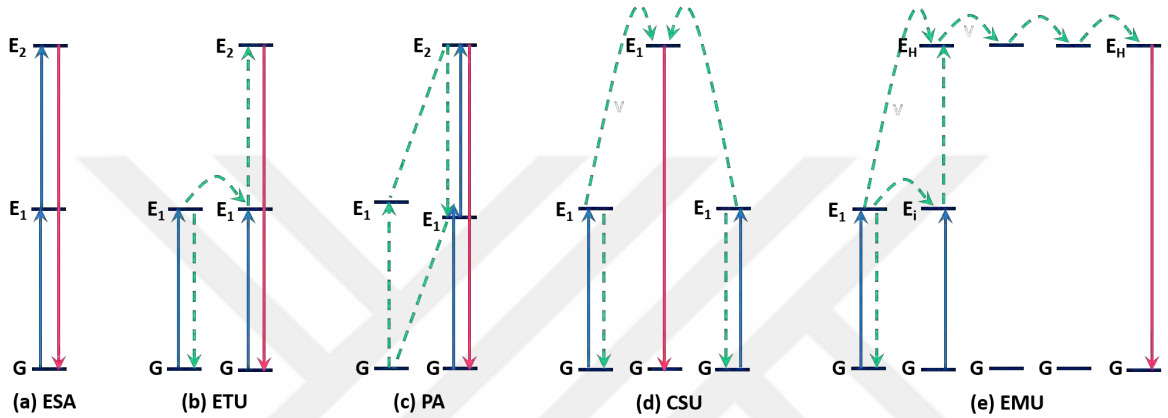

Figure 1.1: (Representative UC processes involved GSA, ESA and ET steps for lanthanide-doped UCNPs: (a) excited states absorption (ESA), (b) energy transfer upconversion (ETU), (c) photon avalanche (PA), (d) cooperative sensitization upconversion (CSU), (e) energy migration upconversion (EMU)(drawn based on the diagram in Chen‘s paper)[7]

The ESA process was proposed theoretically by N. Bloombergen in 1959, who first set up an IR quantum counter device by means of UC material.[10] [26] The single ion-based ESA process is characterized by the sequential absorption of two or more photons via a real intermediate electronic state. As shown in figure 1.1 (a), an electron is first promoted from the ground state (G) to the intermediate state (E1) of an ion by absorbing a photon with resonance energy with the energy between G and E1. This transition is termed as ground state absorption (GSA). After GSA, excited state absorption (ESA) process occurs, in which the transition of the excited electron in E1 to the higher electronic state (E2) occurs by sequential absorption of the second pump photon again under resonance conditions. The electron in E2 is relaxed to G emitting photon, which has higher energy than the absorbed photons. The lanthanide ions such as Er^{3+}, Tm^{3+}, Ho^{3+} are used commonly in systems in which ESA takes place.[10] [13] [25] [26] However, for avoiding the luminescence quenching in this process, the dopant ion concentration should be kept low (for instance, less than 3% for Er^{3+} and no more than 1% for Tm^{3+}).[25] In addition, the relatively low absorption cross section of used ions demands the excitation source with a high pump power density. Due to these

reasons, the ESA process is not effortlessly observed in UCNP systems.[10] [13] [25] [26]
In 1966, Auzel described another UC mechanism, which occurs via energy transfer between luminescent centers (sensitizer and activator ions).[10] [13] [26] This mechanism referred to the energy transfer upconversion is depicted in figure 1.1 (b). First, GSA takes place in both the sensitizer and the activator resulting in the promotion of the electron from G to E1. Secondly, the sensitizer transfers its energy to the adjacent activator non-radiatively, which causes the electron in E1 of the activator to go up to the E2. Afterward, the electron drops back to G resulting in emission with a higher energy photon than excitation photon. Since the non-radiative energy transfer can occur under resonance condition, the energy difference between G and E1 of the sensitizer should be resonant with that between E1 and E2 of the activator. If this condition is not fulfilled in the system and there is only a slight energy difference, the phonon energy of the crystal matrix, in which the dopant ions are embedded, can assist the energy transfer.[10] [13] [25] [26] One or two phonons can assist the energy transfer for small energy mismatches (100 cm^{-1}).[15] The distance of the ion pairs in the crystal matrix influences the efficiency of the ETU process, as well as the efficiency of UCL. This process can happen between two identical activator-activator ions or different sensitizer-activator ions. Yb^{3+} ion is the most employed sensitizer with its simple energy state structure and large absorption cross-section (compared with other lanthanides) at about 980 nm. The energy difference between its $^2F_{7/2} - {}^2F_{5/2}$ states exhibits a similar value with a large number of f-f transitions of Er^{3+}, Tm^{3+}, Ho^{3+} ions. As another sensitizer, Nd^{3+} ion can be excited upon about 800 nm. Since the water absorption lower at 800 nm than at 980 nm, using Nd^{3+} means the lower thermal effect for samples in water. This advantage makes Nd^{3+} more suitable than Yb^{3+} for biological applications. Since the UC efficiency in the ETU process is approximately two orders of magnitude larger than that in the ESA process, ETU is the most applied process in UC systems.[10][13] [25] [26]
The PA-based UC process involves cross-relaxation energy transfer between adjacent ions, shown in figure 1.1 (c). This complex mechanism required high pump intensity and long irradiation time. In the PA process, the population of the intermediate state, E1, is provided through a weak and non-resonant GSA step. Afterward, the cross-relaxation energy transfer occurs between the excited ion and the adjacent ion, which is in the ground state, G. The population of E2 increases exponentially after promiting electrons from E1 to E2 by resonant ESA step. Radiative relaxation from E2 to G produces emission light with higher energy than excitation light energy. PA process is much less efficient than the ETU process, and there are only a few applications in UC nanomaterials.[10] [26] [27] [28] [29]
CSU process in figure 1.1 (d) occurs between two sensitizers (generally the same type) and one activator. After the electrons in G of sensitizers are excited to E1 by absorption of resonance energy photons, the contained energy of sensitizer ions is transferred cooperatively to the activator ion. Thus, the electron in G of the activator is excited first to E1, next to E2. The radiative relaxation of an electron from the excited state, E2, to the ground state, G, results in UC emission. This UC process is less efficient than ESA and ETU processes and needs a high dopant concentration (approximately

75%) for taking place in UC nanoparticles. Its relatively low efficiency limits the use of the CSU process in materials for biological application.[7] [10] [28]
Recently the core-shell nanoparticles have been intensively studied. This structure allows another UC process, termed energy migration upconversion, EMU. The energy transfer in this process is achieved using four types of ions: (I) sensitizer, (II) accumulator, (III) migrator, (IV) activator. The sensitizer ion is excited to E1 via the GSA step. Due to the ETU process, the energy is transferred from the sensitizer to the accumulator to excite it to E2. Following this, the energy transfer proceeds from the accumulator to the migrator. After the activator is taken the energy from the migrator, the radiative relaxation occurs from E2 to G producing UC emission.[10] [13] [25] [26]

1.4 Design of upconversion nanoparticles

1.4.1 Sensitizer, activator

As mentioned in section 1.3, the ETU process demands a sensitizer and activator ions pair for energy transfer. Among the Ln^{3+} ions, Yb^{3+} is the most used sensitizer owing to its relatively large absorption cross-section upon about 980 nm excitation light, a simple energy diagram with only one excited state splitting into three Stark-states under the crystal field influence.[30] The energy difference between the ground state $^2F_{7/2}$ and the excited state $^2F_{5/2}$ of Yb^{3+} matches very well with some of the energy differences in ladder-like energy states of Er^{3+}, Tm^{3+}, Ho^{3+}. Er^{3+} ion enables the emission light in blue (410 nm, and 487 nm) after the sequential absorption of three photons. This ion emits the light in green (at 525 nm and 543 nm) and in red (at 655 nm) after absorption of at least two photons. On the other hand, Tm^{3+} can emit light in blue (at 450 nm and 475) and in NIR range (at 800 nm), after the subsequential absorption of four and two photons, respectively.[9] [10] [31] [32] [26] [33] For avoiding concentration quenching and obtaining high-efficiency UCL, the balancing of amounts of those ions in the host material is substantial. Therefore, the sensitizer concentration is kept usually around 20 mol% and activators below 2 mol% in rare-earth fluoride UC nanoparticles ($AREF_4$).[9] [25] [26] [33] [34]

1.4.2 Host material

The role of the host material in high-efficiency UCL is significant. These materials should supply some properties such as optical stability, transparency to the excitation light, and UC emission light, similar ionic size to that of the dopant ions, and low phonon energy. Besides these, an asymmetrical crystal field of host material provides the opposite parity mixing of f states. Thus, the parity forbidden f-f electric dipole transitions of Ln^{3+} ions can occur in the UC nanoparticles. The rare earth metal fluorides, oxides, sulfides, and sulfur oxides exhibit well that conditions. As one type of host material, Ln^{3+} doped β - $NaYF_4$ most efficient crystal matrix for UCL, so far.[9] [13] [25] [26]

1.4.3 Core-shell structure

One other way to produce high UC efficiency is the core-shell design of UCNPs. The shell on the core can be inactive or active, homogenous or heterogeneous. The aim use of the inactive shell is mostly to reduce the energy losses in the area close to the surface, blocking the non-radiative energy transfer pathways to the surface. As for the active shell, it can be applied as an adjustment of optical properties such as UCL intensity, the variation of emission colours, allowing or preventing some energy transfers. These advantages of core-shell UCNPs make them useful materials in biological application.[13] [25]

1.5 Synthesis of UCNPs

The composition, shape, size, phase, the grade of crystallinity of UCNPs affect extremely on the upconversion luminescence efficiency as well as their application. Due to the control of these features, various synthesis methods have been developed in the field of nanotechnology. The reproducibility of UCNPs and creating them monodisperse stand in front of us as the main challenges. Furthermore, uniform, monodisperse, small, and water-soluble particles with high UCL intensity are demanded for biological applications.[10] [25] [35]

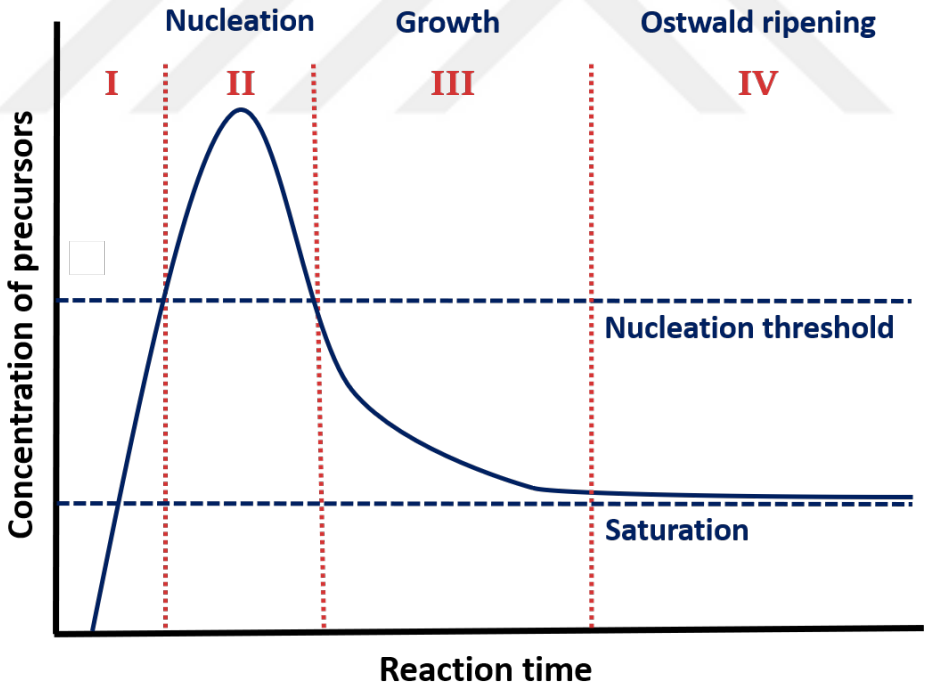

Figure 1.2: Schematic illustration of the LaMer theory for the nucleation and growth process of particles (drawn based on LaMer's paper)[36]

Victor LaMer has been studied the nucleation-growth mechanism(shown in figure 1.2)

intensively [36] and Mai et al. offered the distinct stages for the mechanism of particle formation: (i) delayed nucleation of nanocrystals, (ii) enlargement of the size by monomer supply, (iii) decrease of the size by the dissolution of the particle (iv) formation of final material by aggregation.[37]
On the other hand, Ostwald ripening strategy, in which the energetically favored larger particles are formed from energetically less stable smaller particles, are used widely for UCNP synthesis.[7]

1.5.1 Thermal decomposition method

In the thermal decomposition method, a solution from the noncoordinating solvent and coordination ligand included the organometallic precursors, is heated up to a little higher temperature than the decomposition temperature (<300 °C) of organometallic precursors.[10] [25] The noncoordinating solvent such as 1-octadecene (ODE) serves high-temperature reaction environment, while the coordinating ligand like oleic acid (OA) provides growth control of the UCNP coating their surface, stabilization of particles in solution by means of repulsive interactions. Lanthanide trifluoroacetate is used mostly as a precursor. Although the high quality, monodisperse, uniform UCNPs can be prepared using this method, the requirement of expensive air-sensitive precursors, the necessity of further surface modification process for using UCNPs in bioapplication, the emergence of hazardous byproducts, and the necessity of keeping the temperature in a narrow range (10 °C) in order to ensure the reproducibility restrict the use of this synthesis method.[10] [25] [35]

1.5.2 High temperature coprecipitation method

Another method for the synthesis of high-quality UCNPs is the high temperature coprecipitation method, which finds the widest usage area in UCNP synthesis. The reaction mixture consists of inorganic rare earth salts, coordinating ligand, noncoordinating solvent (like ODE and OA, respectively), and materials like NH_4F and NaF. The mixture is heated to a certain high temperature (such as 300 °C), and high crystallinity, uniform particles are obtained via Oswald ripening. This method is uncomplicated, low-cost, and user/environment friendly compared to the thermal decomposition method. Since the method allows the use of ligands such as polyethyleneimine (PEI [38] and polyvynilpyrrolidone (PVP [39]), the hydrophilic UCNPs can be synthesized in one step via high temperature coprecipitation method. Furthermore, the fabrication of sub-10 nm particles is possible by the application of this method.[10] [25]

1.5.3 Hydro(solvo)thermal method

Hydro(solvo)thermal method enables the direct synthesis of both hydrophilic and hydrophobic UCNPs by utilization the convenient noncoordinating solvent (such as water [40] , ethanol [41] , ODE [42]) coordinating ligand (such as acetic acid (AA) [43] , PEI [38] [41]). This method requires specialized reaction vessels resisting high temperature and pressure above the critical point of the solvent. Thus, the high solubility and

reactivity of the inorganic precursors in the solvent can be achieved. Autoclaves and microwaves are often used to provide a suitable environment for synthesis conditions. Compared to other synthesis methods, this method makes it possible to produce high crystallinity UCNPs at lower temperatures but does not allow the tracking of the particles as they grow.[7] [10] [25] [35]
The synthesis methods of UCNPs are not limited with previously mentioned three methods. Besides these, there are several other synthesis methods such as microemulsion [36] , wet chemical [44] , ionothermal [45] , and ion-exchange [46] methods.[10] [25]

1.6 Surface functionalization of UCNPs

The UCNPs produced by previously mentioned methods are generally hydrophobic because of the chemical properties of surfactant ligands used.[47] In order to use of UCNPs in a biological environment for imaging and therapy, they need to exhibit usually three main characteristics (i) water solubility, (ii) being stable in a biological buffer as well as no agglomeration by electrostatic and/or steric repulsions (iii) having reactive groups (like carboxyl, thiol, aldehyde, amino, and other groups) for further bioconjugation with a biomedical interest such as antibodies, DNA, proteins, folic acid, and drugs. In the next section, the common surface functionalization strategies developed for the stabilization of nanoparticles in water is explained.[7] [25] [33] [47] [48] [49] [50]

1.6.1 Ligand exchange method

One of the most used surface functionalization method is the ligand exchange method in which the original hydrophobic ligands on the UCNPs surface are replaced by hydrophilic ligands with reactive end groups (-COOH, -NH_2 or -SH) like poly(acrylic acid) (PAA) [51], poly(ethyleneglycol) (PEG) - phosphate [52], mercaptopropionic acid (MPA) [1], 2-aminoethyl dihydrogen phosphate (AEP) [53] [54], P(MEO2MA - co - AcSEMA) copolymers. [7] [25] [47] [48] [49] [50] [55] OA is the most used coordinating ligand on the UCNPs surface with a long chain hydrocarbon and carboxyl group (-COOH).[7] The hydrophilic ligand can exchange with that hydrophobic ligand due to stronger coordination ability with the lanthanide ions on the surface.[7] [25] For producing hydrophilic UCNPs using this method is easy and provides nanoparticles generally with smaller hydrodynamic diameters. On the other hand, the hydrophilic UCNPs present restricted colloidal stability, and their UCL intensity can be decreased due to the quenching of high-frequency vibrational groups, such as -OH and -NH_2.[7] [25] [47] [49] [50]

1.6.2 Ligand oxidation

In the ligand oxidation method, oxidizing agents such as Lemieux-von Rudloff reagents, ozone, or 3-chloroperoxy-benzoic acid are utilized to oxidize the carbon-carbon double bond of the hydrophobic coordinating ligand on the UCNP surface like OA and

oleylamine (OM). Thus, UCNPs are water-soluble. Li et al.[56] developed this method for the first time using Lemieux-von Rudloff reagent for oxidizing of unsaturated bonds of OA ligands. This resulted in the formation of azelaic acid with the free carboxylic acid group, allowing further conjugation with various biomolecules, such as streptavidin.[7] [25] [47] Despite the simplicity of the ligand oxidation method, the produced hydrophilic UCNPs show low water stability. Furthermore, this method requires a long reaction time and gives a low yield.[7] [25]

1.6.3 Ligand removal

As another surface functionalization method, the ligand-free removal method is carried out for removing OA from the particle surface. This simple method makes the UCNPs water dispersible. The removing of OA occurs either direct acid treatment or excess ethanol treatment under ultrasonication. The obtained ligand-free UCNPs have a strong coordination capability finally by Ln^{3+} ions on the surface. Thus, the particles can be conjugated with biomolecules containing electronegative groups such as -SH, -COOH, -NH_2, or -OH.[7] [25] [47] The long storage time in aqueous solution without aggregation formation of UCNPs makes this method important.[25]

1.6.4 Layer-by-layer assembly

Layer by layer approach provides the electrostatic deposition of oppositely charged polyelectrolytes on the particle surface.[7] [25] [47] [50] Li et al. [57] obtained water-dispersible UCNPs by depositing of PAH/PSS/PAH, (PAH = poly(allylamine hydrochloride), PSS = poly(styrene sulfonate)) on the surface of UCNPs.[7] [25] [47] The amino rich shell then could be attached to biotin for further conjugation to several proteins such as streptavidin and avidin.[47] The adjustment of NP, salt, and polyelectrolyte concentrations and the type of polyelectrolyte chains is significant for avoiding agglomeration of UCNPs.[49] This method provides the UCNPs high stable water solubility through the strong interaction between oppositely charges polyelectrolytes. Furthermore, the optical properties of UCNPs remain unchanged because of the no direct interaction of coating amphiphilic molecules with the particle surface.[7] [47] Nevertheless, the substantial increase in the hydrodynamic radius of UCNPs after coating the particles with several layers is mostly unsuited for bioapplications.[47]

1.6.5 Amphiphilic polymer coating

Another method used to convert the hydrophobic UCNPs to hydrophilic ones is the amphiphilic polymer coating. Polymers such as poly(maleic anhydride-alt-1-octadecene) (PMAO) [58] , poly((ethylene glycol)-block-lactic acid) (PEG-b-PLA) [59] , 6 - aminohexanoic acid (6AA) [60] and N-dodecyl-polyisobutylene-alt-maleamic acid (PMA) [61] overcoat the hydrophobic coordinating ligand on the particle surface.[7] The hydrophobic part of amphiphilic polymer intercalates with the hydrophobic ligand via hydrophobic interactions, and the hydrophilic part stretches into the water. The obtained hydrophilic UCNPs are very stable in water but exhibit mostly a relatively large

hydrodynamic radius, which is not favorable for use in biological medium.[7] [49] [50]

1.6.6 Silica encapsulation

This method can be applied for the encapsulation of both hydrophobic and hydrophilic UCNPs. In most cases, a layer of amorphous silica functionalized with reactive groups such as -COOH, -NH_2, -SH is coated onto the particle surface, allowing further bioconjugations. The strategies followed for encapsulation depend on the type of particle surface (hydrophilic or hydrophobic). The well known Stöber process based on the hydrolysis of Si alkoxide is utilized to coat a SiO_2 layer on the hydrophilic UCNPs.[7] [48] [49] [50] The hydrophobic UCNPs are coated commonly by the reverse microemulsion strategy, in which the water droplets act as nanoreactors dispersed in a bulk oil phase.[49] Additionally, the mesoporous silica coating provides space for the storage of drugs and other biomolecules. This method enables the control of the silica shell thickness by adjusting the reagent concentration and reaction time.[7] The UCNPs obtained by silica encapsulation show some advantages like high colloidal stability and biocompatibility.[49]

1.6.7 Direct synthesis of hydrophilic UCNPs

The functionalization techniques mentioned above utilized for manufacture hydrophilic UCNPs from hydrophobic UCNPs are applied after the synthesis of UCNPs. However, these show some disadvantages such as complicated synthesis process, time-consuming, low yielding, and less UCL efficiency after functionalization.[47] [62] Consequently, these lead researchers to develop a one-step synthesis method to directly produce water-soluble UNCPs for biological applications.[47] For this purpose, hydrothermal microemulsion synthesis, ligand assisted methods, ionothermal synthesis, or polyol process are mostly used one step synthesis methods.[47] [63] [64] Up to now, poly(ethylene glycol) (PEG), poly(vinyl pyrrolidone) (PVP), poly(ethylene imine) (PEI), polyacrylic acid (PAA) [65], ethylenediaminetetraacetic acid (EDTA) [66] and acetic acid (AA) [64] have been employed as hydrophilic coordinating ligand on the particle surface in this method.[62] [67] Thus, the particle surface has -COOH, -NH2, and other hydrophilic functional groups, which increase the solubility of UCNPs in water and enable further bioconjugation with biological molecules.[25] [63] Han et al. carried out a one step synthesis strategy using amino acids as coordinating hydrophilic ligand and functional component. The surface modification of UCNPs with different biological molecules was then possible since amino acids have both reactive groups, carboxyl and amino. The group could use the amino acid-functionalized $NaLuF_4$:Gd^{3+}:Yb^{3+}:Tm^{3+} UCNPs in UCL/MRI in vivo bimodal imaging.[63] MRI as a non-invasive visualization technique utilize signals governed by several parameters such as proton density, relaxation times, proton exchange rates, and water diffusion under the influence of an external magnetic field.[68] Using more than one imaging method integrate the advantages of different techniques and provide high accuracy in clinical diagnosis and medical treatment.[63] Nevertheless, one step synthesis methods require improvement still to obtain monodisperse, uniform, and small NPs.[47]

1.7 Eu^{3+} as structural probe

Eu^{3+} ion can be used as an excellent structural probe in materials for site symmetry determination due to the fine structure and relative intensities of transitions in absorption and luminescence spectra. The crystal field created by ligands effects the 4f electrons of Eu^{3+} and causes mixing of electronic states. The crystal field perturbation by the crystalline host matrix is reflected by the change of the spectral distribution and decay time. Its nondegenerate starting levels $^7F_0$ and $^5D_0$ in luminescence and absorption spectra make Eu^{3+} more attractive and useful than other lanthanide ions for determining the ion's site symmetry.[69]
The electronic configuration of Eu^{3+} with 60 electrons can be shown as [Xe]$4f^6$ or in short $4f^6$. There are 3003 ways to arrange these six electrons into the seven 4f orbitals. The 3003 total degeneracy of the [Xe]$4f^6$ electronic configuration is given by the following combinatorial formula:

$$\binom{14}{n} = \frac{14!}{n!(14-n)!} \tag{1.1}$$

Here n represents the number of electrons, which is 6 for trivalent Eu^{3+} ion.[69] There are three particular effects, which lift totally or partly the degeneracy of the $4f^6$ configuration: (I) Colombic interaction, (II) spin-orbit coupling, and (III) the crystal field perturbation. The Colombic interaction, the electron repulsions between different electrons in 4f shell, causes the splitting to the order of 10^4 cm^{-1}. The interaction between the spin magnetic moment of the electron and the magnetic field induces the spin-orbit coupling, which splits terms into J-levels with the order of 10^3 cm^{-1}.[13] [69] [70] The interactions between the 4f electrons and the electrons of ligands surrounding of Ln^{3+} ions induce the crystal (ligand, Stark) field effect.[69] This effect is responsible for the lifting of 2J+1 (J = total angular quantum number) degenaracy of the energy levels in the free ion. The splitting of the degenerate energy levels is to the order of 10^2 cm^{-1} or less.[13] [18] [69] The multiplicity of a term is given (2S+1)(2L+1). S and L represent here the spectroscopic terms, the total spin quantum number, and the total orbital angular momentum quantum number, respectively. Due to the spin-orbit coupling, a further splitting occurs into a number of spectroscopic levels $^{(2S+1)}\Gamma_J$ with a (2J+1) multiplicity. Γ is the letter (S,P,D,F,G...) depends on L values (0,1,2,3,4...). J is the quantum number related to the total angular momentum J, which can have the values between (L+S) and (L - S). According to these calculations, the multiplicity of Eu^{3+} ion is 49, with the splitting of ground terms into $^7F_0$, $^7F_1$, $^7F_2$, $^7F_3$, $^7F_4$, $^7F_5$, $^7F_6$. Because the $4f^6$ shell of Eu^{3+} is less than half filled its ground state starts with $^7F_0$ according to Hund's third rule (the lowest possible J value).[18] [69]
The Judd Ofelt theory simplified the calculation of the radiative rates of Ln^{3+} ions in solids or solutions by using experimental parameters of optical absorption and emission spectra. To utilize this theory for calculations, usually, two main approximations are made: (I) all the Stark sublevels are equally populated, (II) the host matrix elements are optically isotropic.[13] [18] [71]

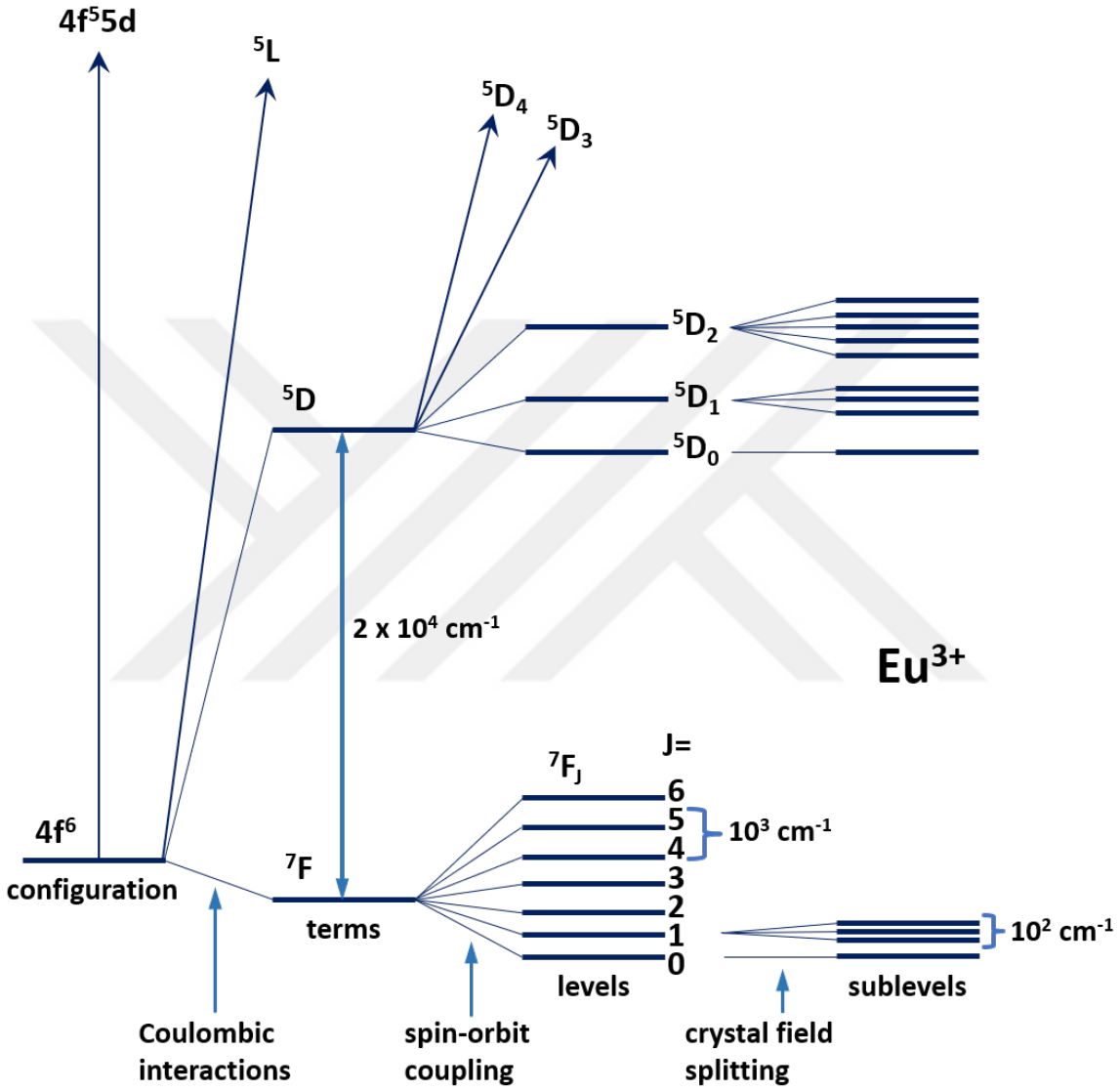

Figure 1.3: Partial Jablonski energy level diagram of Eu^{3+} ion (drawn based on the diagram in Werts' paper)[70]

The odd parity electric dipole (ED) transition is not allowed because of Laporte's parity selection rule. Nevertheless, the asymmetrical crystal field effect can make possible the ED transition allowing the mixing of electronic levels and relaxing the selection rules so that the transition can take place in absorption and luminescence spectra of Eu^{3+} ion. It is often called induced (or forced) ED transition. The Judd Ofelt theory can be utilized for calculation of the intensities of the ED transitions.[13] [18] [69] On the other hand, the $^7F_1 \rightarrow {}^5D_0$ transition of Eu^{3+} ion has a magnetic dipole (MD) character. This transition is allowed between states with the same parity (Laporte selection rule) but exhibits a weak intensity. For the reason of the less effect of the crystal field on the MD transition of Eu^{3+} ion, the MD transition is considered to be constant.[13] [18] [69] The $^7F_2 \rightarrow {}^5D_0$ transition of Eu^{3+} is highly sensitive to minute changes in the ion environment and called hypersensitive transition. Its intensity is used for getting information about the crystal field symmetry of the Eu^{3+} ion site and polarizability of the ligands.[18] [69]
As mentioned above, Eu^{3+} ion is a unique spectroscopic probe owing to its particular electronic configuration. The combination of the structural analysis techniques like XRD and RAMAN with spectroscopic studies of Eu^{3+}, such as the position of emission wavelength, asymmetry ratio of $^5D_0 \rightarrow {}^7F_2$, and $^5D_0 \rightarrow {}^7F_1$ transitions (R_A) and lifetime allow in-depth structural analysis.[2] [69] [72] The asymmetry ratio R_A represents the integrated intensity ratio between the hypersensitive ED transition $^5D_0 \rightarrow {}^7F_2$ and the MD transition $^5D_0 \rightarrow {}^7F_1$ ($R_A = I(^5D_0 \rightarrow {}^7F_2) \ / \ I(^5D_0 \rightarrow {}^7F_1)$) and is used to identify the high symmetry data .[73] [74] Observation of the $^5D_0 \rightarrow {}^7F_J$ transitions make it possible to determine the point group symmetry of the Eu^{3+} site. Furthermore, lifetime analysis provides to indicate the presence of different Eu^{3+} sites in the host material.[72] Recording the emission and excitation spectra at ultralow temperatures (T<10 K) provide the minimizing of the spectral broadening of electronic transitions (inhomogeneous broadening, electron-phonon effects) and resolving the small changes in the electronic spectra of chemical species in different environments. Using a narrow-bandwidth laser source at ultralow temperature allow to probe the number of isosymmetric Eu^{3+} species and to study the splitting pattern on the luminescence spectra.[73][74] [75]

1.8 Scope of the thesis

Thus far, we have explained the unique optical properties of UCNPs, the current state of progress and research on the topic, and the promising advantages of UCNPs for the potential applications in the biomedical field. Despite all developments, there is still a need to research the UCL mechanism thoroughly, the synthesis conditions to control the size and the crystalline phase. Furthermore, there is a requirement to improve the synthesis protocols for generating hydrophilic UCNPs with simple, green, low cost and effective one step synthesis protocols. In this thesis, we focused on the specific objectives listed as follows:

1 The investigation of morphological and photophysical properties of oleic acid capped UCNPs $NaYF_4$:Yb^{3+}:Er^{3+}:Eu^{3+} and Na_xScF_{3+x}:Yb^{3+}:Er^{3+}:Eu^{3+} by stepwise

doping of Gd^{3+} synthesized by thermal decomposition methods. (chapter 3)

2 The microwave-assisted, hydrothermal, one step synthesis of hydrophilic, dual functional UCNPs $NaGdF_4$:Yb^{3+}:Er^{3+} under various conditions such as reaction time, solvent ratio, the composition of medium to establish a synthesis protocol that would allow to precisely control the size and the crystalline phase of UCNPs and studying morphological and photophysical properties of synthesized UCNPs (chapter 4)

3 The microwave-assisted, hydrothermal, one step synthesis of hydrophilic UCNPs $NaYF_4$:Yb^{3+}:Er^{3+}:Eu^{3+} and Na_xScF_{3+x}:Yb^{3+}:Er^{3+}:Eu^{3+} by stepwise doping of Gd^{3+} and investigation of their morphological and photophysical properties (chapter 5)

4 Preliminary investigations of morphological and photophysical properties of hydrophilic UCNPs Na_xScF_{3+x}:Yb^{3+}:Tm^{3+}:Gd^{3+} and Stokes-shift photoluminescence of Na_xScF_{3+x}:Nd^{3+}:Yb^{3+} and Na_xScF_{3+x}:Nd^{3+}:Yb^{3+}:Fe^{3+} nanoparticles. (chapter 6)

Chapter 2

Experiments, materials, measurements

2.1 Chemicals and materials

The chemicals and materials used for syntheses are listed in the appendix.

2.2 Synthesis

2.2.1 Synthesis of $NaYF_4(Na_xScF_{3+x})$:18%Yb^{3+}:2%Er^{3+} :0.5%Eu^{3+}:yGd^{3+} UCNPs[76]

(Percent signs remark concentration in mol%, unless otherwise stated.)
Synthesis of NaY:$Gd_{0,7.5,15,30}$ and NaSc:$Gd_{0,7.5,15,30}$ samples were carried out according to the thermal decomposition method under Ar atmosphere. ODE served as a high boiling solvent, OA as a capping agent. The Y^{3+} ions (Sc^{3+} for NaSc:$Gd_{0,7.5,15,30}$ samples) were replaced by Gd^{3+} ions to investigate the effect of Gd^{3+} on the properties of UCNPs. The concentration of the lanthanide ions (Ln^{3+}) Er^{3+} and Yb^{3+} was maintained constant. The synthesis of sample NaSc:Gd_{15} is given as example. $ScCl_3{\cdot}6H_2O$ (0.645 mmol), $YbCl_3{\cdot}6H_2O$ (0.18 mmol), $GdCl_3{\cdot}6H_2O$ (0.15 mmol), $ErCl_3$ (0.02 mmol) and $EuCl_3{\cdot}6H_2O$ (0.005 mmol) were dispersed in a mixture of ODE (17.5 mL) and OA (7.5 mL). In order to remove all gas, a vacuum at 1 mbar was applied for 45 minutes. After that, the mixture was heated up to 150 °C under Argon atmosphere and stirred until a clear and light yellow-green solution was formed. After the cooling down of the clear solution to 45 °C, NH_4F (150 mg) and NaOH (75 mg) were added to the reaction flask. The temperature of the solution was then raised up to 290 °C. The solution was stirred at this temperature for 90 minutes. The product was cooled down to room temperature naturally; afterwards, it was filled into centrifuge tubes. The particles were collected by centrifugation at 8000 rpm for 20 min, washed with ethanol three times, and re-dispersed in cyclohexane.

Table 2.1: The nomenclature for samples OA@$NaYF_4$(Na_xScF_{3+x}):18%Yb^{3+}:2%Er^{3+}: 0.5%Eu^{3+}:y%Gd^{3+}

Sample: OA@$NaYF_4$($Na_xScF_{(3+x)}$): 18%Yb^{3+}: 2%Er^{3+}: 0.5%Eu^{3+}: y%Gd^{3+}	Nomenclature
OA@$NaYF_4$:Yb^{3+}:Er^{3+}:0%Gd^{3+}	NaY:Gd_0
OA@$NaYF_4$:Yb^{3+}:Er^{3+}:7.5%Gd^{3+}	NaY:$Gd_{7.5}$
OA@$NaYF_4$:Yb^{3+}:Er^{3+}:15%Gd^{3+}	NaY:Gd_{15}
OA@$NaYF_4$:Yb^{3+}:Er^{3+}:30%Gd^{3+}	NaY:Gd_{30}
OA@$Na_xScF_{(3+x)}$:Yb^{3+}:Er^{3+}:0%Gd^{3+}	NaSc:Gd_0
OA@ $Na_xScF_{(3+x)}$:Yb^{3+}:Er^{3+}:7.5%Gd^{3+}	NaSc:$Gd_{7.5}$
OA@ $Na_xScF_{(3+x)}$:Yb^{3+}:Er^{3+}:15%Gd^{3+}	NaSc:Gd_{15}
OA@ $Na_xScF_{(3+x)}$:Yb^{3+}:Er^{3+}:30%Gd^{3+}	NaSc:Gd_{30}

*Gd^{3+} concentration and lattices were changed, Yb^{3+} and Er^{3+} concentrations are kept constant. OA= oleic acid, % as mol percentage

2.2.2 Synthesis of AcOH@$NaGdF_4$:18%Yb^{3+}:2%Er^{3+} UCNPs - microwave protocol 1 [64]

AcOH@$NaGdF_4$: 18%Yb^{3+}: 2%Er^{3+} UCNPs were prepared by solvothermale method using microwave-assisted synthesis process in ethanol (EtOH) - acetic acid mixture. In a typical synthesis procedure, NaOH (7.5 mmol) was dissolved in 2 mL Milli-Q water under stirring at 1000 rpm. AcOH (2mL) and EtOH (8 mL) were then mixed with a NaOH solution. Further, $GdCl_3{\cdot}6H_2O$ (0.8 mmol), $YbCl_3{\cdot}6H_2O$ (0.18 mmol), $ErCl_3$ (0.02 mmol) and NH_4F (4 mmol) were added into the solution. The mixture was stirred at RT for 30 min. Then, the whole reaction mixture was filled in a microwave reaction vessel, tightly sealed, and heated to 150 °C. The mixture was stirred at this temperature for 4 h with a speed of 600 rpm. After cooling down to 40°C the entire arrangement naturally, the nanoparticles were collected by centrifugation at 9000 rpm for 8 min, washed with water and ethanol (3:7 v/v) mixture three times. One part of particles was dissolved in Milli-Q water and kept in fridge at 4 °C. The remained part was dried at room temperature (RT).
*For samples AcOH@$NaYF_4$(Na_xScF_{3+x}):18%Yb^{3+}:2%Er^{3+}:1%Eu^{3+}:y%Gd^{3+}, the Y^{3+} ions (Sc^{3+} for samples in Na_xScF_{3+x} lattice) were replaced by Gd^{3+} ions to investigate the effect of Gd^{3+} on the properties of UCNPs. Besides, $EuCl_3{\cdot}6H_2O$ (0.01mmol) added into these samples while using the concentration of $Y(Sc)Cl_3{\cdot}6H_2O$ of 0.79 mmol.

Table 2.2: The nomenclature for samples AcOH@$NaGdF_4$:18%Yb^{3+}:2%Er^{3+} synthesized under various synthesis conditions

Sample: AcOH@$NaGdF_4$: 18%Yb^{3+}: 2%Er^{3+}	Nomenclature
AcOH@$NaGdF_4$:Yb^{3+}:Er^{3+}_1h (H_2O:EtOH:AcOH = 1:4:1), 600 rpm, 150 °C	NaGd:Er_1h
AcOH@$NaGdF_4$:Yb^{3+}:Er^{3+}_2h (H_2O:EtOH:AcOH = 1:4:1), 600 rpm, 150 °C	NaGd:Er_2h
AcOH@$NaGdF_4$:Yb^{3+}:Er^{3+}_3h (H_2O:EtOH:AcOH = 1:4:1), 600 rpm, 150 °C	NaGd:Er_3h
AcOH@$NaGdF_4$:Yb^{3+}:Er^{3+}_4h (H_2O:EtOH:AcOH = 1:4:1), 600 rpm, 150 °C	NaGd:Er_4h
AcOH@$NaGdF_4$:Yb^{3+}:Er^{3+}_4h (H_2O:EtOH:AcOH = 1:3:2), 600 rpm, 150 °C	NaGd:Er_4h_(1:3:2)
AcOH@$NaGdF_4$:Yb^{3+}:Er^{3+}_4h (H_2O:EtOH:AcOH = 1.5:5:3), 600 rpm, 150 °C	NaGd:Er_4h_(1.5:5:3)
AcOH@$NaGdF_4$:Yb^{3+}:Er^{3+}_4h (H_2O:EtOH:AcOH = 1:4:3), 600 rpm, 150 °C	NaGd:Er_4h_(1:4:3)
AcOH@$NaGdF_4$:Yb^{3+}:Er^{3+}_20min (H_2O:EG:AcOH = 1:4:1), 600 rpm, 150 °C	NaGd:Er_20min_EG
AcOH@$NaGdF_4$:Yb^{3+}:Er^{3+}_1h (H_2O:EG:AcOH = 1:4:1), 600 rpm, 150 °C	NaGd:Er_1h_EG
AcOH@$NaGdF_4$:Yb^{3+}:Er^{3+}_2h (H_2O:EG:AcOH = 1:4:1), 600 rpm, 150 °C	NaGd:Er_2h_EG
AcOH@$NaGdF_4$:Yb^{3+}:Er^{3+}_4h (H_2O:EG:AcOH = 1:4:1), 600 rpm, 150 °C	NaGd:Er_4h_EG
AcOH@$NaGdF_4$:Yb^{3+}:Er^{3+}_4h (H_2O:EG:AcOH = 1:4:1), 1000 rpm, 150 °C	NaGd:Er_4h_1000rpm
AcOH@$NaGdF_4$:Yb^{3+}:Er^{3+}_4h (H_2O:EG:AcOH = 1:4:1), 600 rpm, 200 °C	NaGd:Er_4h_200°C
AC@$NaGdF_4$:Yb^{3+}:Er^{3+}_4h (H_2O:EtOH:AC = 1:4:1), 600 rpm, 150 °C	NaGd:Er_4h_AC
AcOH@$NaGdF_4$:Yb^{3+}:Er^{3+}_20min (H_2O:EG:AcOH = 1:4:1), 600 rpm, 150 °C	NaGd:Er_20min_EG_1/3V
AcOH@$NaGdF_4$:Yb^{3+}:Er^{3+}_20min (H_2O:G:AcOH = 1:4:1), 600 rpm, 150 °C	NaGd:Er_20min_G_1/3V

*The synthesis conditions are given in nomenclature as follow: NaGd:Er_x_R_S_L _s_T_V (x for the reaction time, R for the ratio of solvents (H2O:EtOH:AcOH), S for the solvent changed in the mixture, L for surface ligand, s for stirring speed, T for reaction temperature, V for the volume of the reaction mixture, respectively). If not stated otherwise, the reaction temperature is 150 °C, the stirring speed is 600 rpm, the capping agent is acetic acid, the ratio of solvents (water:ethanol:acetic acid) is 1:4:1, and the volume of the mixture prepared for the reaction is 12 mL. Ethylene glycol and glycol were used instead of ethanol, amino cellulose was used instead of acetic acid for

one sample, and it is donated. The volume of two samples is 4 mL and denoted with 1/3V in nomenclature. AcOH = Acetic acid, EtOH = Ethanol, EG = Ethylene glycol, G=Glyserol, AC = Aminocellulose, h = reaction time in hours, min = reaction time in minutes, rpm for stirring speed during reaction, 1/3V = 1/3 volume of the others, (x:y:z) = ratio of solvents.

Table 2.3: The nomenclature for samples AcOH@$NaYF_4$(Na_xScF_{3+x}):18%Yb^{3+}:2%Er^{3+} :0.5%Eu^{3+}:y%Gd^{3+}

Sample: AcOH@$NaYF_4$($Na_xScF_{(3+x)}$): 18%Yb^{3+}: 2%Er^{3+}: 1%Eu^{3+}: y%Gd^{3+}	Nomenclature
AcOH@$NaYF_4$:Yb^{3+}:Er^{3+}:0%Gd^{3+}	A@NaY:Gd_0
AcOH@$NaYF_4$:Yb^{3+}:Er^{3+}:7.5%Gd^{3+}	A@NaY:$Gd_{7.5}$
AcOH@$NaYF_4$:Yb^{3+}:Er^{3+}:15%Gd^{3+}	A@NaY:Gd_{15}
AcOH@$NaYF_4$:Yb^{3+}:Er^{3+}:30%Gd^{3+}	A@NaY:Gd_{30}
AcOH@ $Na_xScF_{(3+x)}$:Yb^{3+}:Er^{3+}:0%Gd^{3+}	A@NaSc:Gd_0
AcOH@ $Na_xScF_{(3+x)}$:Yb^{3+}:Er^{3+}:7.5%Gd^{3+}	A@NaSc:$Gd_{7.5}$
AcOH@ $Na_xScF_{(3+x)}$:Yb^{3+}:Er^{3+}:15%Gd^{3+}	A@NaSc:Gd_{15}
AcOH@ $Na_xScF_{(3+x)}$:Yb^{3+}:Er^{3+}:30%Gd^{3+}	A@NaSc:Gd_{30}

*Gd^{3+} concentration and lattice were changed, Yb^{3+} and Er^{3+} concentrations were kept constant. AcOH= acetic acid, % as mol percentage

2.2.3 Synthesis of PEI@Na_xScF_{3+x}:18%Yb^{3+}:2%Tm^{3+} UCNPs - autoclave protocol [77]

The synthesis of sample $PEI800_5$_200°C is given as example. PEI with average molecular weight (M_W) 800 was dissolved in Milli-Q water for preparing PEI stock solution (5 wt%). $ScCl_3$, $YbCl_3$, $TmCl_3$, $GdCl_3$ and NaCl stock solutions (0.2 M) were prepared by dissolving $SCl_3{\cdot}6H_2O$, $YbCl_3{\cdot}6H_2O$, $TmCl_3{\cdot}6H_2O$, $GdCl_3{\cdot}6H_2O$ and NaCl in Milli-Q water, respectively. In a typical synthesis procedure, NaCl (5 mL), $ScCl_3$ (3.6 mL), $YbCl_3$ (0.9 mL), $TmCl_3$ (0.1 mL), $GdCl_3$ (0.4 mL) stock solutions were added to EtOH (30 mL) with 10 mL PEI stock solution. After stirring for 10 min, 5 mmol NH_4F was added. The mixture was poured into a glass reaction vessel for autoclave. After putting the glass reaction vessel in the autoclave, the mixture was heated subsequently to 200 °C for 24 h with stirring. The nanoparticles obtained were collected by centrifugation at 8000 rpm for 15 min, washed with ethanol two times and with water two times. One part of particles were dissolved in Milli-Q water and kept in fridge at 4 °C. The remaining part was dried at room temperature (RT).

Table 2.4: The nomenclature for samples PEI@Na_xScF_{3+x}:18%Yb^{3+}:2%Tm^{3+} under various synthesis conditions

Sample PEI@$Na_xScF_{(3+x)}$:18%Yb^{3+}:2%Tm^{3+}:7.5%Gd^{3+}	Nomenclature
5%PEI800@ $Na_xScF_{(3+x)}$:Yb^{3+}:Tm^{3+}:Gd^{3+}_200°C_24h	$PEI800_5$_200°C
5%PEI25000@ $Na_xScF_{(3+x)}$:Yb^{3+}:Tm^{3+}:Gd^{3+}_200°C_24h	$PEI25000_5$_200°C
10%PEI25000@ $Na_xScF_{(3+x)}$:Yb^{3+}:Tm^{3+}:Gd^{3+}_200°C_24h	$PEI25000_{10}$_200°C
10%PEI25000@ $Na_xScF_{(3+x)}$:Yb^{3+}:Tm^{3+}:Gd^{3+}_250°C_24h	$PEI25000_{10}$_250°C
10%PEI25000@ $Na_xScF_{(3+x)}$:Yb^{3+}:Tm^{3+}:Gd^{3+}_300°C_24h	$PEI25000_{10}$_300°C

*The M_W of polymer, the PEI concentration and temperature were changed, lattice, lanthanide ions concentration, and reaction time were kept constant. h= reaction time in hours, % as weight percentage

2.2.4 Synthesis of PEI@Na_xScF_{3+x}: 2%Nd^{3+}:y%Yb^{3+} NPs and PEI@Na_xScF_{3+x}:2%Nd^{3+}:2%Yb^{3+}:z%Fe^{3+} NPs – microwave protocol 2

PEI was dissolved in Milli-Q water for preparing PEI stock solution (5 wt%). $ScCl_3$, $NdCl_3$, $YbCl_3$, $FeCl_3$ and NaCl stock solutions (0.2 M) were prepared by dissolving $SCl_3{\cdot}6H_2O$, $NdCl_3{\cdot}6H_2O$, $YbCl_3{\cdot}6H_2O$, $FeCl_3{\cdot}6H_2O$ and NaCl in Milli-Q water, respectively. The parts of Sc^{3+} were replaced by Yb^{3+} ions (Fe^{3+} for NaSc:Nd_2:Yb_2:Fe_x NPs), whereas the concentration of Nd^{3+} ion (as well as Yb^{3+} ion for NaSc:Nd_2:Yb_2:Fe_x NPs) was kept constant. In a typical synthesis procedure, NaCl (2mL), $ScCl_3$ (1.6 mL), $YbCl_3$ (0.36 mL), $NdCl_3$ (0.04 mL) stock solutions were added to EtOH (12 mL) with 4 mL PEI stock solution. After stirring for 10 min, NH_4F (2.5 mmol) was added. The mixture was poured into a rection vessel for microwave. After putting the reaction vessel in the microwave, the mixture was heated subsequently to 200 °C for 4 h with stirring. The nanoparticles obtained were collected by centrifugation at 8000 rpm for 15 min, washed with ethanol two times and with water two times. One part of particles were dissolved in Milli-Q water and kept in fridge at 4 °C. The remaining part was dried at room temperature (RT).

Table 2.5: The nomenclature for samples PEI@Na_xScF_{3+x}:2%Nd^{3+}:y%Yb^{3+} NPs and PEI@Na_xScF_{3+x}:2%Nd^{3+}:2%Yb^{3+}:z%Fe^{3+}

Sample: PEI@$Na_xScF_{(3+x)}$:2%Nd^{3+}:y%Yb^{3+}:z%Fe^{3+}	Nomenclature
PEI@ $Na_xScF_{(3+x)}$: 2%Nd^{3+}:2%Yb^{3+}	NaSc:Nd_2:Yb_2
PEI@ $Na_xScF_{(3+x)}$: 2%Nd^{3+}:4.5%Yb^{3+}	NaSc:Nd_2:$Yb_{4.5}$
PEI@ $Na_xScF_{(3+x)}$: 2%Nd^{3+}:9%Yb^{3+}	NaSc:Nd_2:Yb_9
PEI@ $Na_xScF_{(3+x)}$: 2%Nd^{3+}:18%Yb^{3+}	NaSc:Nd_2:Yb_{18}
PEI@ $Na_xScF_{(3+x)}$: 2%Nd^{3+}:2%Yb^{3+}:5%Fe^{3+}	NaSc:Nd_2:Yb_2:Fe_5
PEI@ $Na_xScF_{(3+x)}$: 2%Nd^{3+}:2%Yb^{3+}:10%Fe^{3+}	NaSc:Nd_2:Yb_2:Fe_{10}
PEI@ $Na_xScF_{(3+x)}$: 2%Nd^{3+}:2%Yb^{3+}:20%Fe^{3+}	NaSc:Nd_2:Yb_2:Fe_{20}
PEI@ $Na_xScF_{(3+x)}$: 2%Nd^{3+}:2%Yb^{3+}:30%Fe^{3+}	NaSc:Nd_2:Yb_2:Fe_{30}
PEI@ $Na_xScF_{(3+x)}$: 2%Nd^{3+}:2%Yb^{3+}:40%Fe^{3+}	NaSc:Nd_2:Yb_2:Fe_{40}

*First, the Yb^{3+} concentration after that Fe^{3+} concentrations were changed. Capping agent, lattice, Nd^{3+} concentration was kept constant. PEI = Polyethyleneimine

2.3 Instrumentation

2.3.1 Structural characterization

XRD(1): The X-ray diffraction patterns of NaY:$Gd_{0,7.5,15,30}$ and NaSc:$Gd_{0,7.5,15,30}$ samples were recorded using a D5005 (Siemens AG, Munich, Germany) in a range of 3-70°/2θ with a divergence aperture, scattering ray aperture and graphite monochromatized Cu Kα radiation (λ = 0.15406 nm). The scanning step was 0.02°/2θ with a 4 s accumulation time per step.
XRD(2): For all remaining samples, X-ray powder diffraction data were collected on a PANalytical Empyrean powder X-ray diffractometer in a Bragg-Brentano geometry. The diffractometer was equipped with a PIXcel1D detector utilizing Cu Kα radiation (with Kα wavelength λ = 1.5419 Å) operating at 40 kV and 40 mA. θ/θ scans were operated in a 2θ range of 4 - 70° with a step size of 0.0131° and a sample rotation time of 1 s within 190 min. For fluorescence reduction, the pulse height distribution (PHD) level of the detector was set to 45 - 80 with an active length of 3.0061°.
TEM(1): JEM 1011 transmission electron microscope (Jeol Ltd, Tokyo, Japan) was operated using a wolfram hairpin cathode, an accelerating voltage of 80 kV, and a molybdenum panel to study of size and morphology of the samples. The TEM images were recorded utilizing a side-mounted Olympus Mega View G2 (Olympus Germany GmbH, Hamburg, Germany).
TEM(2): The TEM images of some samples (denoted in discussion) were recorded

with a transmission electron microscope (Tecnai G2 F20 XTwin, from FEI/Thermo Fisher Scientific) operating at 200 kV acceleration voltage.
SEM(1): The SEM images were recorded by scanning emission microscope (Quanta 250, FEI, Eindhoven, Netherlands) using a wolfram hairpin cathode, an accelerating voltage of 20 kV with a pressure of about 10^{-2} Pa.
SEM(2): For the recording of SEM images of some samples, Zeiss, Gemini ultra plus was used equipped with Tungsten-zircon field-emission filament (Schottky type). The operation was made at an acceleration voltage of between 10 and 20 kV and a pressure of 10^{-6} Pa. All samples were put on the 300 - mesh copper grids (Plano GmbH, Wetzlar, Germany) and left to dry for measurements.
For the determination of NP diameter, the software Image Sys Prog (version 1.2.5.16 $\times$64) was used.
DLS: The Brownian motion of the particles in the sample is first measured by dynamic light scattering. Afterward, the size can be determined using the relationship between diffusion speed and size. DLS measurements were carried out by utilizing a ZETASIZER Nano ZS (Malvern Instruments Ltd, Herrenberg, Germany) at 25°C with a detection angle of 173° to study the particle size and distribution of UCNPs. He-Ne laser at $\lambda = 633$ nm was operated as a light source. The measurements were carried out in cyclohexane for hydrophobic samples and in Milli-Q water for hydrophilic samples. The mobility and charge (Zeta potential) were analyzed with the same device using the technique of Electrophoretic Light Scattering (ELS).

2.3.2 Steady state and time resolved luminescence measurements of Er^{3+} at RT

Room temperature steady state and time resolved UCL spectra were obtained by means of a wavelength tunable pulsed Nd:YAG laser (Quanta Ray, Spectra-Physics, Mountain View, CA) and OPO system (GWU-Lasertechnik Vertriebsges.mbH, Erftstadt, Germany) functioning at 10 Hz as excitation light source. All UCL spectra were recorded using an intensified CCD-camera (iStar DH720-18V-73. Andor Technology, Belfast, Great Britain) connected a spectrograph (Shamrock SR 303i, Andor Technology, Belfast, Great Britain) equipped with a 600 lines/mm grating.
The variable gate-step size was used for increasing the detection window step-wise during time resolved luminescence measurements of all samples. This makes it possible to acquire more data points at shorter times after laser excitation. Thus, investigating the components with faster decay time is easier and more reliable. The "boxcar"technique was applied for recording the time resolved luminescence spectra. This technique provides to convert the amplitude A_i to "true amplitude"F_i by reason of the dependence of A_i on the detection gate width t_{gate}. [78] Equation 2.1 shows this relation:

$$F_{\mathrm{i}} = \frac{A_{\mathrm{i}}}{\tau_{\mathrm{i}}(1 - e^{\frac{t_{\mathrm{gate}}}{\tau_{\mathrm{i}}}})} \tag{2.1}$$

F_i describes the coefficient evaluated by gate width $\mathrm{t_{gate}}$ correction. A_i is the experimental coefficient (amplitude of the fit function). t_{gate} corresponds to the detection

gate width (recording time of the luminescence). τ_i is the luminescence decay time of the i species. Luminescence decay curves were fitted according to equation 2.2:

$$I(t) = y_0 + A_1 e^{-k_1 t} + A_2 e^{-k_2 t} \tag{2.2}$$

$k_i = 1/\tau_i$ is the rate constant, *I(t)* describes the luminescence intensity in dependence on time *t*, y_0 is the offset of the fitting function and accounts for background signal contribution, and t_i is the luminescence decay time of the i component. From coefficients A_1 and A_2 the relative fractions f_i were calculated according to equation 2.3:

$$f_{\mathrm{i}} = \frac{F_{\mathrm{i}}\tau_{\mathrm{i}}}{\Sigma_{\mathrm{k}} F_{\mathrm{k}}\tau_{\mathrm{k}}} \tag{2.3}$$

*Room temperature steady state measurements for Stokes-shift luminescence (for Nd^{3+} and Yb^{3+}) in NIR region were carried out using the same Nd:YAG laser - OPO system operating at 10 Hz as excitation light source. All spectra was recorded using an intensified CCD-camera (iDus InGaAs 1.7) coupled a spectrograph (Shamrock SR-303i, Andor Technology, Belfast, Great Britain)) equipped with a 600 lines/mm grating. The NaSc:Nd_2:Yb_y samples (as well as NaSc:Nd_2:Yb_2:Fe_z) were measured in a solid phase. All other samples were measured as a colloidal solution in quartz cuvettes sealed with Parafilm®.

2.3.3 Upconversion luminescence measurements at various temperatures

The UCL properties of UCNPs were investigated at various temperatures. Their spectra were recorded by using the same experimental set up as for the UCL measurements at room temperature. In order to control the temperature of samples, a water-cooled Peltier element-based temperature adjustable sample holder (temperature controller GR2012 itron32, JUMO GmbH & Co, Fulda, Germany) and a conventional temperature sensor (Testo 945, Testo AG, Lenzkirch, Germany) were utilized. The samples were kept for 15 minutes at a certain temperature to ensure temperature stability. All samples were in quartz cuvettes sailed with Parafilm® during the measurements.
The population of two energy states of Er^{3+} ($^2H_{11/2}$ and $^4S_{3/2}$) are influenced by the temperature. The ratio of UCL intensities of the $^2H_{11/2} \rightarrow {}^4I_{15/2}$ (G1) and $^4S_{3/2} \rightarrow {}^4I_{15/2}$ (G2) transitions ($R_{G1/G2}$) followed the Boltzmann type distribution. This can be expressed as the following equation:

$$R = \frac{I_{\mathrm{G1}}}{I_{\mathrm{G2}}} = A exp\left(-\frac{\Delta E_{\mathrm{G1/G2}}}{k_{\mathrm{B}} T}\right) \tag{2.4}$$

Where I_{G1} and I_{G2} are the integrated UCL intensities corresponding to the $^2H_{11/2} \rightarrow {}^4I_{15/2}$ and $^4S_{3/2} \rightarrow {}^4I_{15/2}$ transitions, respectively, A is the pre-exponential factor, ΔE is the energy gap between two emitting states (G1 and G2), k_B is the Boltzmann constant and T is the absolute temperature.[79]
The calculated energy gaps were used to determine the absolute (S_A) and relative (S_R)

sensor sensitivity. These important parameters for sensing applications can be express in equation 2.5 and 2.6:[79]

$$S_{\mathrm{A}} = \frac{\partial(FIR)}{\partial T} = FIR\left(\frac{\Delta E}{k_{\mathrm{B}}T^2}\right) \tag{2.5}$$

$$S_{\mathrm{R}} = 100\%\frac{1}{FIR}\frac{\partial(FIR)}{\partial T} = 100\%\left(\frac{\Delta E}{k_{\mathrm{B}}T^2}\right) \tag{2.6}$$

2.3.4 Power dependence of upconversion luminescence measurements at room temperature

Power dependency of UCL at room temperature was studied by exciting with a power range between 0.4 - 17.3 W/cm^2. The spectra was recorded upon 976 nm excitation light with experimental set up for UCL measurements mentioned above. The excitation light was attenuated using the neutral density filters (optical density 0.1-1.0). The dependence of the UCL intensity I on the excitation power P is indicated with equation 2.7:[80]

$$I \propto P^{\mathrm{n}} \tag{2.7}$$

here n represents the number of photons that are required to populate the emitting state of the lanthanides under unsaturated conditions, which means the filling of high-lying excited states less possible due to the strong radiative emission from the lower lying intermediate states under low power density of excitation.[81]
The energy of OPO pulses during the spectroscopic measurements was monitored with a pyroelectric detector (PEM 45K USB by Sensor und Lasertechnik GmbH) capable of handling up to 1 J/cm^2.

2.3.5 Steady state and time resolved luminescence measurements of Eu^{3+} at RT

For the set of samples NaY:$Gd_{0,7.5,15,30}$ and NaSc:$Gd_{0,7.5,15,30}$, steady state and time resolved luminescence measurements of Eu^{3+} were carried out using a wavelength tunable pulsed Nd:YAG/OPO laser system (pump laser: Quantaray, Spectra–Physics, Mountain View, CA, USA; OPO: GWU, GWU-Lasertechnik Vertriebsges. mbH, Erftstadt, Germany) operating at 20 Hz as an excitation light source. The intensified CCD camera (iStar DH720-18H-13, Andor Technology, Belfast, Great Britain) was integrated to a spectrograph (MS257 Modell 77700A, Oriel Instruments) equipped with a 300 lines/mm grating. “boxcar”technique was used for the recording of time resolved luminescence spectra.
*Steady state and time resolved luminescence spectra of Eu^{3+} for the set of samples A@NaY:$Gd_{0,7.5,15,30}$ and A@NaSc:$Gd_{0,7.5,15,30}$ were recorded using the same setup for UCL measurements at RT.

2.3.6 Steady state and time resolved luminescence measurements of Eu^{3+} at ultralow temperature (∼4K)

The total luminescence spectra (TLS) or excitation-emission-matrix spectra (EEMS)) of Eu^{3+} ion ($^7F_0 \rightarrow {}^5D_0$ transition) for the set of samples NaY:$Gd_{0,7.5,15,30}$ and NaSc:$Gd_{0,7.5,15,30}$ were recorded using the same set up for UCL measurements at room temperature. The only difference was the coupling with an optical multicore Y-shaped fiber for sending the excitation light and for collecting the emission light at the same time. The colloidal samples (in cyclohexane) in NMR tubes placed inside of a copper sample holder were set in a vacuum chamber attached to the cold plate of a closed cycle liquid helium cryostat. The sample chamber was cooled to ∼4 K using the cryostat system, which consists of a helium compressor unit (Sumitomo Heavy Industries Ltd., Markt Indersdorf, Germany), a vacuum pump (Leybold vacuum Turbolab 80, Oerlikon, Köln, Germany) and a temperature controller (331 temperature controller, Lake Shore, Westerville, OH). To excite the $^7F_0 \rightarrow {}^5D_0$ transition of Eu^{3+}, the excitation light was sent to the samples with a scan speed of 0.05 nm/min between 575 - 582 nm.

2.3.7 Time-resolved area normalized emission spectra (TRANES)

Time-resolved emission spectra were evaluated to investigate the influence of the altering of lattice on the luminescence spectra. TRANES give information about small time-dependent differences in the spectral intensity distribution of a luminescence spectrum. As mentioned, the time-resolved emission spectra were recorded at different delay times after the laser pulse for the determination of the luminescence decay kinetic. The TRANES were calculated by normalizing the area of the emission spectrum recorded for decay kinetic determination.

2.3.8 Characterization using PARAFAC

The parallel factor analysis (PARAFAC) is known as one of several decomposition methods for multi-way data. It can deconvolute emission data into several species, predicated on the assumption that the total measured emission spectrum result from the superposition of the weighed spectra of single species. Thus, PARAFAC deconvolutes the data into pure excitation spectrum and emission spectrum of each pure Eu^{3+} species. PARAFAC merges the distributions of similar but only slightly different spectra (species) into a single species with an average emission spectrum or excitation spectrum. A three-dimensional analysis of doping concentration-excitation-emission tensor (from TLS data at 4 K) was done and found the single excitation spectrum, emission spectrum for each present Eu^{3+} species. Additionally, it has extracted the relative emission intensities of each Eu^{3+} species for each doping concentration of Gd^{3+}.[74]

2.3.9 Crystal field strength parameter

$^7F_1$ state of Eu^{3+} split into maximal three Stark-levels due to the crystal field effect. Crystal field strength parameter ($N_V(B_{2q})$) is an important value to define the effective crystal field around the Eu^{3+} ion. The number of negative charges, the distance of the neighbouring ions of Eu^{3+} (in our case Y^{3+}, Sc^{3+}, Gd^{3+}, Eu^{3+}, Na^+, F^-, vacant lattice places) in combination with the bond angles change the charge density in the surrounding of Eu^{3+} ion, as well as the value $N_V(B_{2q})$. For weak crystal fields $N_V(B_{2q})$ can be calculated according to equation 2.8:

$$N_{\mathrm{v}}(B_{2\mathrm{q}}) = \sqrt{\frac{\pi(2+\alpha^2)}{0.3}}\Delta E \tag{2.8}$$

$$\alpha = \frac{E_{\mathrm{b}} - E_{\mathrm{c}}}{\Delta E/2} \tag{2.9}$$

where the ΔE value is the energy difference between $^7F_{1\text{-}1}$ and $^7F_{1\text{-}3}$ Stark-levels (in cm^{-1}), E_b is the barycentre (mean energy) of the $^7F_1$ multiplet, E_c is the peak position of $^7F_{1\text{-}2}$ (in cm^{-1}). The corresponding peak positions of $^7F_1$ multiplet are determined using a Gauss regression.[82][83]

Chapter 3

Comparison of OA capped UCNPs using different host lattices: Yttrium vs Scandium lattice

3.1 Introduction

As known, the UCL properties of UCNPs are significantly affected by the host lattice. [84] So far, the effects of synthesis method, reaction time, temperature, the ratio of precursors, dopant concentration etc. on the UCL properties have been investigated. [4] [85] [86] Hexagonal $NaYF_4$:Yb^{3+}:Er^{3+} is known as the most efficient UCNP reported up to date, which offers about one order of magnitude enhancement of UCL efficiency relative to cubic $NaYF_4$:Yb^{3+}:Er^{3+}.[87][88] The reason for this is, the lower site symmetry of hexagonal $NaYF_4$ host lattice for lanthanide ions compared to cubic $NaYF_4$ host lattice.[89] The sufficiently raise of reaction temperature and time can lead cubic $NaYF_4$ to hexagonal $NaYF_4$, but at the same time, result in undesirable aggregation and larger crystal size of UCNPs. As the most studied UCNPs, $NaYF_4$:Yb^{3+}:Er^{3+} UCNPs are used often as reference material for comparing the properties of UCNPs in other host lattices. However, many research groups have codoped the host lattice with various lanthanide ions (Gd^{3+} [90], Lu^{3+} [91]) or non-lanthanide ions (Mn^{2+} [92], Li^{+} [93], Fe^{3+} [94], Ca^{2+} [95]) in order to tailor the local symmetry environments of the rare earth ions in the host lattice by this means to enhance the UCL intensity. The high tendency of light lanthanides towards electron cloud distortion is in favour of the formation of hexagonal $NaYF_4$.[88] Thus, Wang et. al [88] codoped $NaYF_4$:Yb^{3+}:Er^{3+} UCNPs with Gd^{3+} and observed cubic to hexagonal phase conversion of $NaYF_4$ crystal with increasing amount of Gd^{3+} ion from 0 to 30 mol% after heating at 200 °C for only 2 h. UCNPs in Na_xScF_{3+x} have not been yet investigated widely despite of its high potential application as a host lattice. In our knowledge Pei et al. [96], Teng et al. [97] and Ai et al. [98], Cao et al. [86] studied systematically the controlled synthesis of Na_xScF_{3+x} UCNPs under various conditions. These UCNPs are characterized by their strong red emission. However, further studies are still required to understand the properties of Na_xScF_{3+x} crystal lattice. Gd^{3+} codoping causes the local symmetry change in the host lattice as well as the change of UCL properties; furthermore, to pro-

vide the application of UCNPs in magnetic resonance imaging (MRI) and computed tomography (CT).[99]
Among the various measurement techniques, the fluorescence intensity ratio of thermally coupled energy levels (TCL) in rare earth ions is widely used to determine temperature. [100] The energy gap between TCL must be larger than 200 cm^{-1} to avoid strong overlapping of two emission bands. Besides, it must be shorter than 2000 cm^{-1} to make it possible that the Ln^{3+} owns the minimum population in the temperature region measured. In UCNPs Er^{3+} is the most used rare earth ion due to its thermally coupled intense green emission bands ($^2H_{11/2} \rightarrow {}^4I_{15/2}$ and $^4S_{3/2} \rightarrow {}^4I_{15/2}$). [101] UCNPs attract great attention for use in non-contact temperature determination technique, which is the most promising method at sub-micrometer and nanometer scale due to its precious properties like high spatial, thermal, and temporal resolutions, large measurement ranges and reasonable price.[101]
In this chapter we demonstrate the effect of various concentrations of Gd^{3+} ion on the crystal structure, morphology and photophysical properties of the oleic acid capped $NaYF_4$:Yb^{3+}:Er^{3+}:Eu^{3+} and Na_xScF_{3+x}:Yb^{3+}:Er^{3+}:Eu^{3+} UCNPs synthesized via thermal decomposition method. Since the UCNPs in $NaYF_4$ lattice are studied intensively, it can be regarded as reference lattice. Therefore, the results from measurements of UCNPs in $NaYF_4$ and Na_xScF_{3+x} lattices are evaluated comparatively.
Four samples in $NaYF_4$ and four samples in Na_xScF_{3+x} host lattices were synthesized with an amount of 0, 7.5, 15 and 30 mol% Gd^{3+}, respectively. Gd^{3+} ions replace by Y^{3+} (Sc^{3+}) with respect to desired Gd^{3+} content. The concentration of Yb^{3+} and Er^{3+} was kept stable at 18 mol% and 2 mol%, respectively. The samples were codoped additionally with 0.5 mol% of Eu^{3+} to analyze the structural change and speciation deeper. After structural characterization, the ratio of the intensity of green to red UCL (G_T/R), decay kinetics, power dependent and temperature dependent behaviors of UCL were intensely studied. We gained a detailed perspective about the change of the local symmetry environment by means of decay kinetic, R_A and TLS results of Eu^{3+} ion. Furthermore, PARAFAC analysis of TLS data used for obtaining deeper insight into local symmetry.

3.2 Structural characterization

3.2.1 XRD

The evolution of the XRD patterns of the UCNPs in $NaYF_4$ and Na_xScF_{3+x} lattices prepared with 0, 7.5, 15 and 30 mol% of Gd^{3+} concentrations are shown in figure 3.1 (a) and (b). The $NaYF_4$ forms a thermodynamically stable host lattice in cubic or hexagonal phases.[80] Their unit cell structures are shown in figure 3.2 (a) and (b), respectively. The normalized XRD patterns of all NaY:$Gd_{0,7.5,15,30}$ samples agreed well with the standard pattern of α - $NaYF_4$ (ICSD card 77099). When no Gd^{3+} was doped in $NaYF_4$, the strong diffraction peaks of the cubic phase at 28.2°, 46.8°, 55.3° and the weak diffraction peaks of the hexagonal phase at 30.8°, 43.4°, and 62.8° can be observed. These show that the sample consists of cubic and hexagonal mixed phases. After the addition of Gd^{3+}, the diffraction peaks of the hexagonal phase are

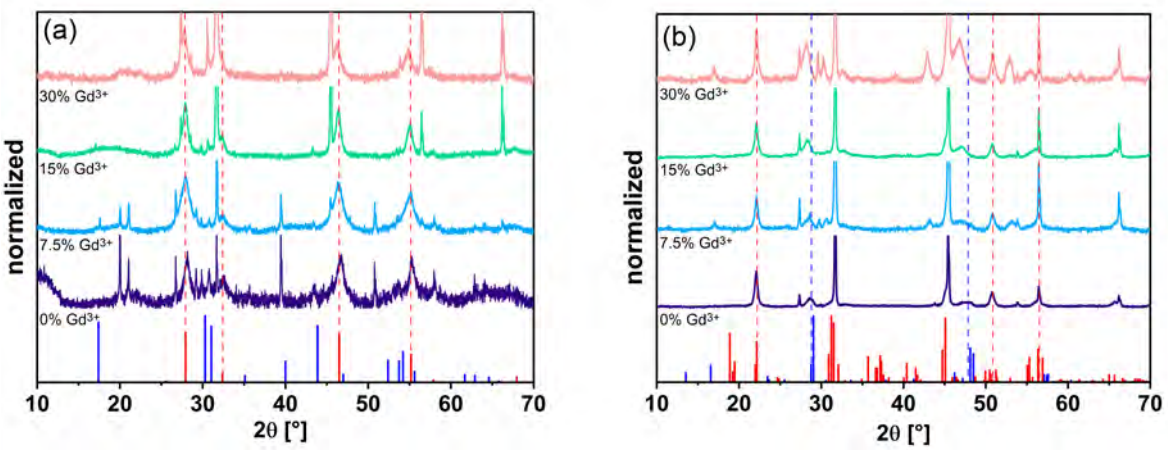

Figure 3.1: (a) X-ray diffraction patterns of NaY:$Gd_{0,7.5,15,30}$ (red lines belong to the standard XRD patterns of the cubic phase $NaYF_4$ (ICSD card 77099) and blue lines to the hexagonal phase $NaYF_4$ (ICSD card 51916)) (b) X-ray diffraction patterns of NaSc:$Gd_{0,7.5,15,30}$ (red lines belong to the standard XRD patterns of the monoclinic phase $NaScF_4$ (ICSD card 400723) and blue lines to the hexagonal phase of Na_3ScF_6 (COD ID: 1515376)).

gradually disappeared. The peak positions corresponding to the reflection planes at 28.2° and 55.3° are shifted each time about 0.2° gradually to the lower angle with the increasing of Gd^{3+} concentration, indicating successful doping of Gd^{3+} ions into the host lattice. This proves that the cell volume of the sample becomes larger when the Gd^{3+} concentration increases because of the larger ionic radius of Gd^{3+} ion (0.938 Å). The Gd^{3+} ions occupy Y^{3+} (0.90 Å) sites to expand the lattice volume. [102] Although the increasing of Gd^{3+} ion concentration caused the alteration on the lattice unit cell parameter of $NaYF_4$, the phase transformation to the pure hexagonal phase was not observed conversely in Wang et. al. research.[88] No peak of hexagonal phase $NaGdF_4$ is observed for samples in NaY:$Gd_{0,7.5,15,30}$.

Na_xScF_{3+x} host lattice is found in monoclinic or hexagonal phases thermodynamically stable. [96] Their unit cell structures are shown in figure 3.3 (a) and (b), respectively. NaSc:Gd_0 shows the diffraction peaks at 22.1°, 50.8°, 56.4° of the monoclinic phase (ICSD card 400723) and the diffraction peak at 28.7° of the hexagonal phase (COD ID: 1515376) (see figure 3.1 (b)). The sample without Gd^{3+} ion is a mixed monoclinic and hexagonal phase. The diffraction peaks of hexagonal Na_xScF_{x+3} become stronger with an increasing amount of Gd^{3+}. In samples with Gd^{3+}, some additionally peaks at 39.0°, 43.0°, and 52.9° appeared, which belong to hexagonal phase $NaGdF_4$ crystal. These peaks are much stronger for samples NaSc:$Gd_{7.5}$ and NaSc:Gd_{30}. It must be considered that some peaks could belong to other lanthanide crystals and silica crystals resulting from corrosion. The increasing of Gd^{3+} concentration leads to a shift of diffraction peaks to the lower angle, gradually. Gd^{3+} ion has a larger ionic radius than that of Sc^{3+} ion (0.75 Å) [102], which means the unit cell volume of Na_xScF_{3+x} is increasing when the Gd^{3+} concentration increases. Consequently, it can be said, the Gd^{3+} addition leads to the unit cell parameter change, expansion of unit cell volume

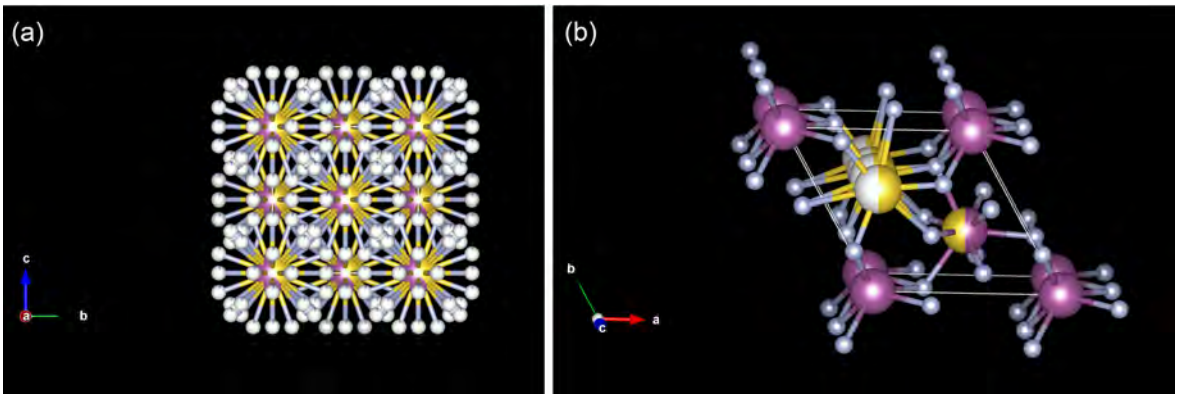

Figure 3.2: Unit cell structure of (a) cubic $NaYF_4$ (ICSD card 77099, space group Fm3m) (b) hexagonal $NaYF_4$ (ICSD card 51916, space group P6). Colour key: yellow equal to Na^+, violet equal to Y^{3+}, grey equal to F^- ions. Images created by using open-source software package VESTA. [103] [104]

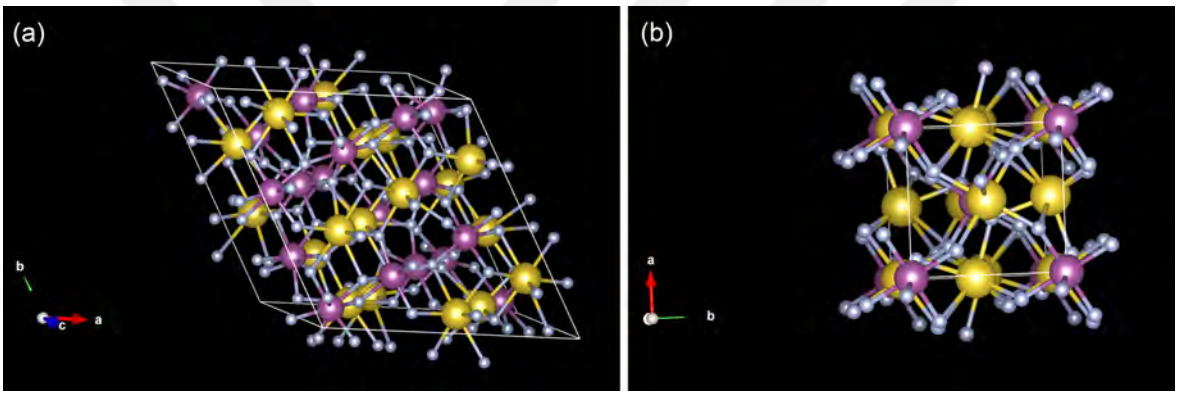

Figure 3.3: Unit cell structure of (a) monoclinic Na_xScF_{3+x} (ICSD card 400723, space group P21/c) and (b) hexagonal Na_xScF_{3+x} (COD ID: 1515376, space group P31). Colour key: yellow equal to Na^+, violet equal to Sc^{3+}, grey equal to F^- ions. Images created by using open-source software package VESTA. [105] [98]

and lattice distortion in both $NaYF_4$ and Na_xScF_{3+x}lattices.

3.2.2 TEM

Figure 3.4 (a) and (b) shows low and high magnification TEM images (TEM1) of $NaY:Gd_{7.5}$ UCNPs and figure 3.4 (c) the particle size distribution histogram of the same sample. The UCNPs are nearly monodispersed with an average size of 6±1 nm. The set of samples in $NaYF_4$ lattice exhibit similar particle sizes between 6 and 9 nm, as shown in table 3.1. While the sample was polydisperse without Gd^{3+}, the addition of 7.5 mol% of Gd^{3+} leads the particles to be monodisperse. The sample with 15 mol% of Gd^{3+} consists of nanoparticles in different sizes and shapes like triangles, hexagons, and squares. Further addition of Gd^{3+} made UCNPs monodisperse again (figure A.1). Gd^{3+} did not affect the average size of particles, but a certain amount of Gd^{3+} leads

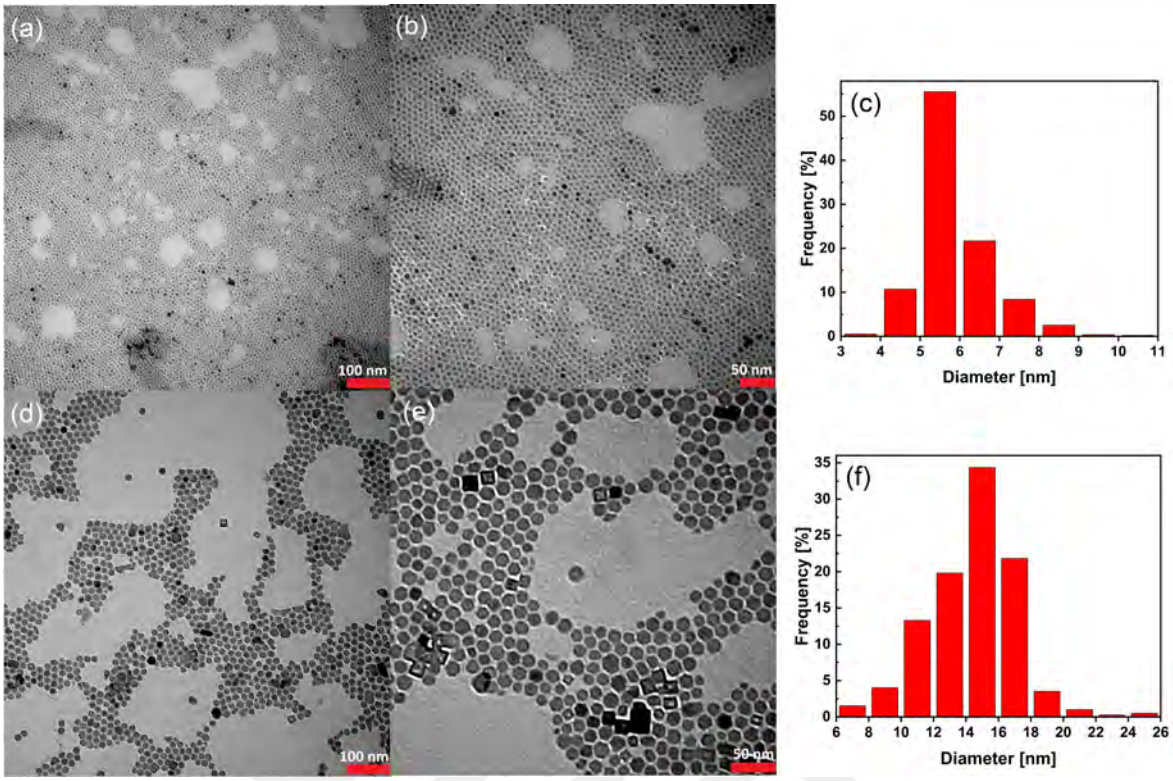

Figure 3.4: (a),(b) TEM images of NaY:$Gd_{7.5}$ UCNPs with a scale bar = 100 and 50 nm, respectively (c) Particle size distribution histogram of NaY:$Gd_{7.5}$ according to TEM (d),(e) TEM images of NaSc:$Gd_{7.5}$ UCNPs with a scale bar = 100 and 50 nm, respectively (f) Particle size distribution histogram of NaSc:$Gd_{7.5}$ according to TEM.

UCNPs to crystallize in different shapes.
Figure 3.4 (d) and (e) show low and high magnification TEM images of NaSc:$Gd_{7.5}$ UCNPs and figure 3.4 (f) the particle size distribution histogram of the same sample. As seen, the UCNPs are monodisperse and in a hexagonal shape with an average size of 16±6 nm. All samples in Na_xScF_{3+x} lattice were formed with a very similar average particle size between 11 and 15 nm (table 3.1). Here the particles without Gd^{3+} are formed in different shapes like triangles, hexagons, squares, and rods (figure A.2). Its average particle size has a large standard deviation. After the addition of 7.5 mol% Gd^{3+} UCNPs convert to monodisperse and uniform particles in a hexagonal shape. The only difference of UCNPs with 15 mol% Gd^{3+} is that they are formed in a square shape. The sample with 30 mol% Gd^{3+} in Na_xScF_{3+x} lattice show similar tendency like NaSc:$Gd_{7.5}$ UCNPs. They appear in different shapes, and their average size has a large standard deviation.

3.2.3 DLS

The UCNPs in cyclohexane were analyzed by DLS to complement the TEM results. The value of hydrodynamic diameters is normally larger than the particle size due to

the layer of surface ligands and solvent molecules on UCNPs.[106] On the contrary, the organic surface ligands are hardly seen on the TEM image because of the low contrast of their carbon atoms on the copper grids filmed with carbon. As shown in table 3.1, the hydrodynamic diameter of the most UCNPs in $NaYF_4$ lattice are slightly larger than their size obtained by TEM. The UCNPs NaY:Gd_{15} and NaY:Gd_{30} show a smaller hydrodynamic diameter than their size. If we consider the errors, the values are in aggreement. The hydrodynamic diameters of the UCNPs in Na_xScF_{3+x} lattice are larger than their particle size, as expected. The DLS results corroborate well the particle sizes calculated using TEM images.
As TEM and DLS results reveal, the samples in Na_xScF_{3+x} lattice (mainly monoclinic) are obviously larger (approximately 2 times) than the samples in $NaYF_4$ lattice (mainly cubic) with and without Gd^{3+} ion. A certain amount of Gd^{3+} leads UCNPs in both lattices to be monodisperse and uniform particles.

Table 3.1: Obtained hydrodynamic diameters and particle sizes of UCNPs in $NaYF_4$ and Na_xScF_{3+x} calculated from DLS and TEM analysis.

	Y^{3+} host lattice				Sc^{3+} host lattice			
Gd^{3+} [mol%]	0	7.5	15	30	0	7.5	15	30
R_H (DLS) [nm]	7±2	8±2	7±3	6±1	12±4	16±6	29±11	28±10
R (TEM) [nm]	6±2	6±1	9±5	7±1	12±6	15±2	14±1	11±5

3.3 Upconversion luminescence properties of Er^{3+}

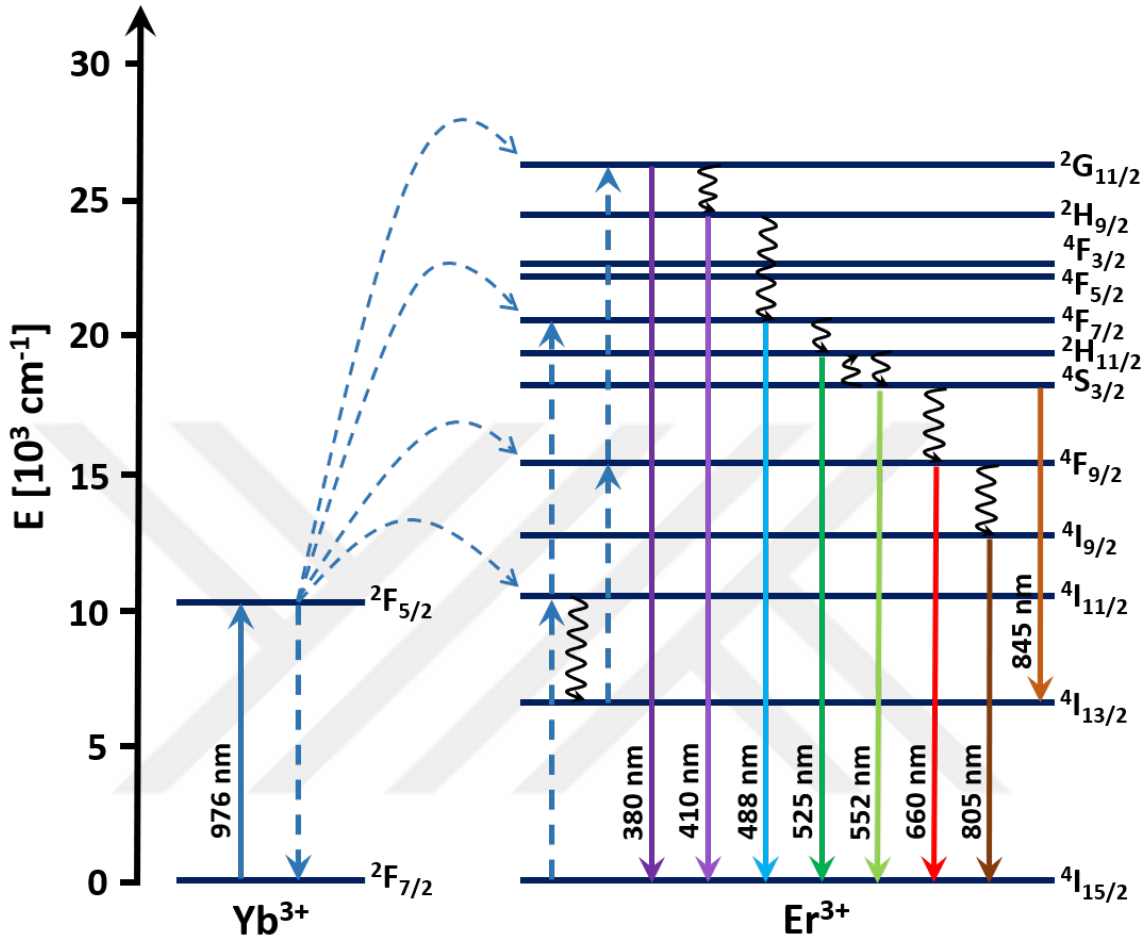

Figure 3.5: Schematic energy level diagram of Yb^{3+} and Er^{3+} showing energy transfer from Yb^{3+} to Er^{3+}. Diagram is drawn based on Gainers paper.[107]

3.3.1 UCL bands and decay kinetics of UCL

All the synthesized NaY:$Gd_{0,7.5,15,30}$ and NaSc:$Gd_{0,7.5,15,30}$ UCNPs dispersions in cyclohexane exhibit three characteristic UCL bands of Er^{3+} in the range of 500 and 700 nm upon excitation at 976 nm. As displayed figure 3.6 (a) and (d) the UCL bands located at 521 and 539 nm belong to green emissions (both together G_T) and the UCL band located at 653 nm to red emission. The green emissions centered at 521 nm corresponds to $^2H_{11/2} \rightarrow {}^4I_{15/2}$ transition (G1) and centered at 539 nm to $^4S_{3/2} \rightarrow {}^4I_{15/2}$ transition (G2) of Er^{3+} ion. The red emission centered at 653 nm involved with $^4F_{9/2} \rightarrow {}^4I_{15/2}$ transition (R) of Er^{3+} ion.[84] The shape of UCL spectra of NaY:Gd_0 UCNPs is only slightly different than that of NaY:$Gd_{7.5,15,30}$ UCNPs. The G_T to R integrated UCL

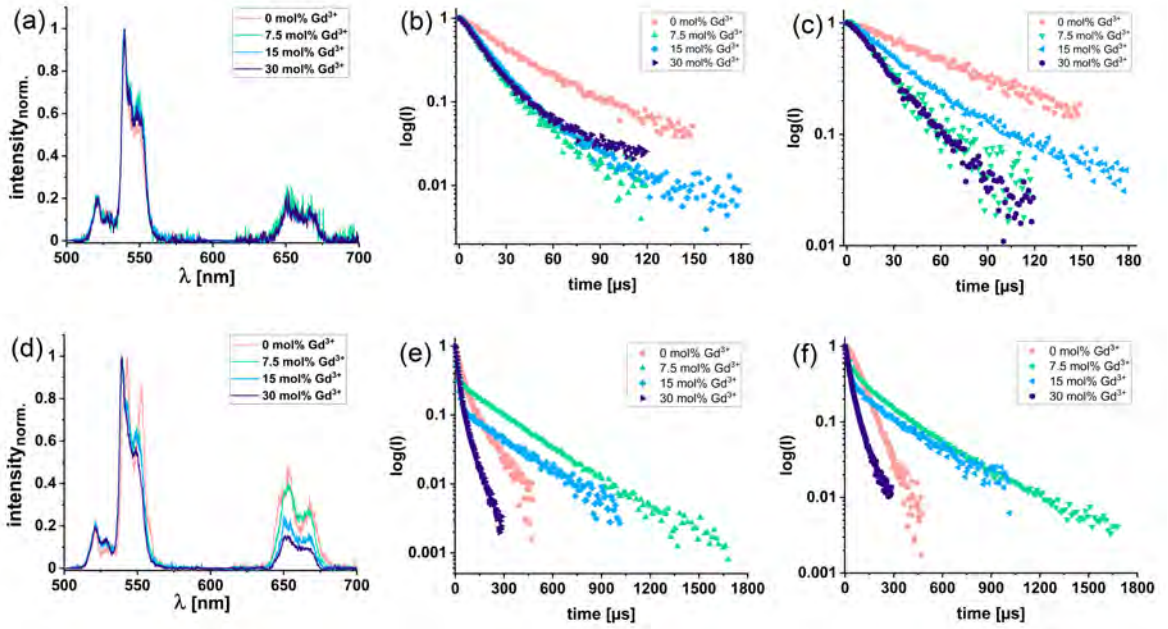

Figure 3.6: (a) Normalized UCL spectra of NaY:$Gd_{0,7.5,15,30}$ UCNPs. Normalized UCL decay kinetics of (b) the G_T (c) the R emissions of Er^{3+} for NaY:$Gd_{0,7.5,15,30}$ (d) Normalized UCL spectra of NaSc:$Gd_{0,7.5,15,30}$ UCNPs. Normalized UCL decay kinetics of (e) the G_T (f) the R emissions of Er^{3+} for NaSc:$Gd_{0,7.5,15,30}$ All measurements carried out in cyclohexane with experimental parameters: λ_{ex} = 976 nm, exposure time = 0.017 secs, delay time after the laser pulse = 500 ns (steady state) 60 ns (time resolved), gate width = 90 μs (steady state), 1 ms (time resolved), number of accumulations = 150 (steady state) 200 (time resolved).

intensity ratios stay almost constant at all Gd^{3+} amounts.
On the other hand the NaSc:Gd_0 UCNPs show a spectral shift and change of spectral shape after adding Gd^{3+} ion (figure 3.6 (d)). The relative UCL intensity of the R band to the G_T band showed a significant concentration dependence. It is decreasing gradually with increasing of Gd^{3+} amount in the UCNPs. It reached its minimum value at 30 mol% Gd^{3+} doping ratio. It is not possible that these ions are quenched by an energy transfer to the Gd^{3+} ions. Since its lowest excited state (in UV region) is located much higher than most excitation states of Yb^{3+} and Er^{3+}.[84] So, the G_T to R ratio increase with increasing of content of Gd^{3+}.
The reason for that different behaviours in different lattices can be explained via ionic radius of the exchanged ions. The ionic radius of Gd^{3+} is remarkably similar to the ionic radius of Y^{3+}. Therefore, it only slightly affected the distances between Yb^{3+} and Er^{3+} and caused only a slight change on the site symmetry of Yb^{3+} and Er^{3+} ions. On the other hand, the difference between ionic radii of Gd^{3+} and Sc^{3+} ions is much larger. For this reason, further Gd^{3+} addition could make the distance between Yb^{3+} and Er^{3+} ions larger, which reduce the cross relaxation ($^4F_{7/2} + {}^4I_{11/2} \rightarrow {}^4F_{9/2} + {}^4F_{9/2}$) and depopulation of $^2H_{11/2} + {}^4S_{3/2}$ states of Er^{3+}.[86] The population of $^4F_{9/2}$ state

through cross relaxation is decreasing with increasing of Gd^{3+} content. This explains the gradually decrease of red UCL intensity.[108] The G_T emission band is dominant in both $NaYF_4$ and Na_xScF_{3+x} lattice.
Decay kinetics of the G_T and R emission bands for all UCNPs were also studied. These show a complex time dependence. The data for G_T and R emission bands of Er^{3+} were evaluated by fitting with monoexponential (all $NaY:Gd_{0,7.5,15,30}$ UCNPs) and biexponential decay law (see equation 2.1 in the section 2.3.2). Biexponential decay fitting results from the two different Er^{3+} species. Since the non-radiative deactivation of excited state occurs by surface defects and high vibrational states of surface-bound ligands and solvent molecules because of matching their states with phonon states of lattice, it is expected the Er^{3+} ions on and near the surface show a short UCL decay time (τ_1) and the relative sheltered Er^{3+} ions in the bulk phase (inside UCNPs) exhibit long UCL decay time (τ_2). [40] [99]
Figure 3.6 (b) and (c) show the UCL decay kinetics of G_T and R emission bands, respectively, for $NaY:Gd_{0,7.5,15,30}$ UCNPs. As it is seen, $NaY:Gd_0$ exhibits a slow decay rate, while UCNPs doped with Gd^{3+} display a fast decay rate.

Table 3.2: The UCL decay parameters and fractions of G_T emission of Er^{3+} for UCNPs codoped with Gd^{3+} in cyclohexane under pulsed wave excitation of 976 nm.

mol% Gd^{3+}	Y^{3+} host lattice	Sc^{3+} host lattice			
	τ_1[µs]	τ_1[µs]	χ_1 [%]	τ_2[µs]	χ_2 [%]
0	33	33±1	43	142±11	57
7.5	16	11	8	258±2	92
15	20	12	22	275±6	78
30	17	15	50	57±1	50

Table 3.3: The UCL decay parameters and fractions of R emission of Er^{3+} for UCNPs codoped with Gd^{3+} in cyclohexane under pulsed wave excitation of 976 nm.

mol% Gd^{3+}	Y^{3+} host lattice	Sc^{3+} host lattice			
	τ_1[µs]	τ_1[µs]	χ_1 [%]	τ_2[µs]	χ_2 [%]
0	73±2	88±1	-	-	-
7.5	26	36±1	13	282±2	87
15	37	23	16	259±7	84
30	25	20±1	60	107±30	40

The decay times of G_T and R emission bands (table 3.2 and 3.3, respectively) show that $NaY:Gd_{0,7.5,15,30}$ UCNPs have only one type of Er^{3+} species. As seen, $NaY:Gd_0$

has the highest values for both emission bands (τ_1 = 33 μs for G_T, τ_1 = 73 µs for R). The addition of Gd^{3+} ion reduces the values between 16 and 20 μs for G_T and between 25 and 37 μs for R. The reason for the significant decrease of decay times from no Gd^{3+} to Gd^{3+} can be a large amount of crystal defect and surface defect due to replacing Y^{3+} ions with Gd^{3+} ions, which leads to the increase of non-radiative decay rates.
Decay curves of NaSc:$Gd_{0,7.5,15,30}$ UCNPs can be classified into two groups looking at the decay curves (figure 3.5 (e) and (f)) and the decay times of long-lived Er^{3+} species of G_T band (table 3.2). NaSc:Gd_0 and NaSc:Gd_{30} display fast decay rate and has relatively shorter decay times in comparison of NaSc:$Gd_{7.5}$ and NaSc:Gd_{15} UCNPs. The decay times of short-lived species for G_T and R bands are 34 and 88 μs, respectively. After addition of Gd^{3+} the decay times of short-lived Er^{3+} species decrease drastically. The τ_1 value of R band decrease only slightly with the increasing of Gd^{3+} amount. In contrast short-lived species, the decay time of G_T band of long-lived species increase with enhancement of Gd^{3+} content up to 15 mol%. At 30 mol% of Gd^{3+}, the τ_2 value of G_T decrease drastically to 57 μs. The sample NaSc:$Gd_{7.5}$ exhibits the highest τ_2 value and highest contribution of long-lived Er^{3+} species. The alteration of Sc^{3+} host lattice after adding 7.5 and 15 mol% of Gd^{3+} may corroborate the stabilization of excited states of Er^{3+} and decrease of interaction with lattice and surface group vibration. Since the decay curve of R band of NaSc:Gd_0 was fitted single-exponential function, it is not possible to compare the change of τ_2 value from no Gd^{3+} to with Gd^{3+}. The τ_2 values are 282 and 259 μs for NaSc:$Gd_{7.5}$ and NaSc:Gd_{15}, respectively. At 30 mol% of Gd^{3+} τ_2 value of R decrease drastically to 107 μs similarly for G_T band. The reason of the enhancement of decay time of long-lived species for G_T and R bands after introducing of 7.5 and 15 mol% of Gd^{3+} could be the slower energy transfer from Yb^{3+} to Er^{3+} because of the increased distance between them. The high amount of long-lived Er^{3+} species for NaSc:$Gd_{7.5}$ and NaSc:Gd_{15} (92% and 78% for G_T, 87% and 84% for R) indicate more homogenous site of Er^{3+} ions with smaller number of defects. The high amount of deactivation centers with further addition of 30 mol% of Gd^{3+} could quench G_T and R emissions. Since the short-lived species are on and near the surface and addition of Gd^{3+} can lead more defect of crystal on the surface and present of other deactivation centers it can be expected that the addition of Gd^{3+} ion reduce the decay time of short species.
As seen the τ_1 values of G_T and R bands of NaSc:Gd_0 are higher than those of NaY:Gd_0. After addition Gd^{3+} these values decrease more in Na_xScF_{3+x} lattice than in $NaYF_4$ lattice. This can be attributed to a larger defect in bulk and on the surface of NaSc:$Gd_{7.5,15,30}$ UCNPs due to enhancement of Gd^{3+} content. The decay times of R bands are longer than those of G_T bands for both set of samples, since R emission requires more relaxation processes and could have contribution of three photon process.

3.4 Power dependent UCL properties

For a better understanding of the upconversion mechanism, investigation of the excitation -power-density-dependent behaviour of UCL is important.[109] As exemplarily shown in figure 3.7 (a) and (b),the G1, G2, and R UCL intensities of NaY:Gd_{30} and NaSc:Gd_{30} UCNPs increases with increasing of excitation power density from 2.9

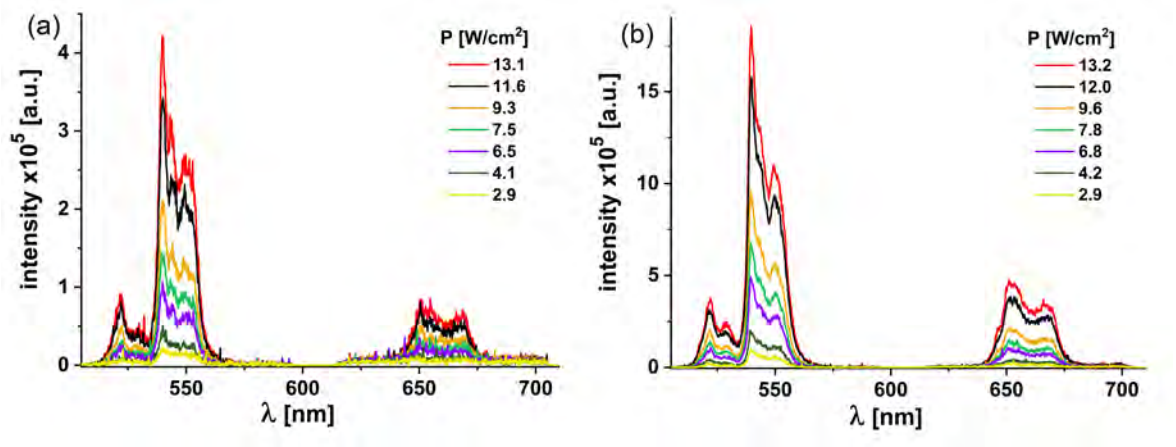

Figure 3.7: (a) UCL spectra of NaY:Gd_{30} (b) UCL spectra of NaSc:Gd_{30} dependent on the pump power density between 2.9 and 13.2 W/cm^2. All measurements carried out in cyclohexane with experimental parameters: λ_{ex} = 976 nm, exposure time = 0.017 secs, delay time after the laser pulse = 500 ns, gate width = 500 μs, number of accumulations = 100.

W/cm^2 up to 13.2 W/cm^2.The green and red logarithmic UCL intensities are proportional to the logarithmic excitation power density (equation 2.7).The calculated slopes (n) at relatively lower pump powers is approximately equal to the number of pump photons involved in the excitation process.[110] [111] Therefore, the double logarithmic plots of G1, G2, and R UCL intensities versus excitation power density and linear fitting curves for NaY:Gd_{30} and for NaSc:Gd_{30} are depicted in figure 3.8 (a) and (b), respectively. The slopes of the plots give the number of photons used for G1, G2, and R UCL. The plots show linearity as expected at the low excitation power density range.[111] [112]

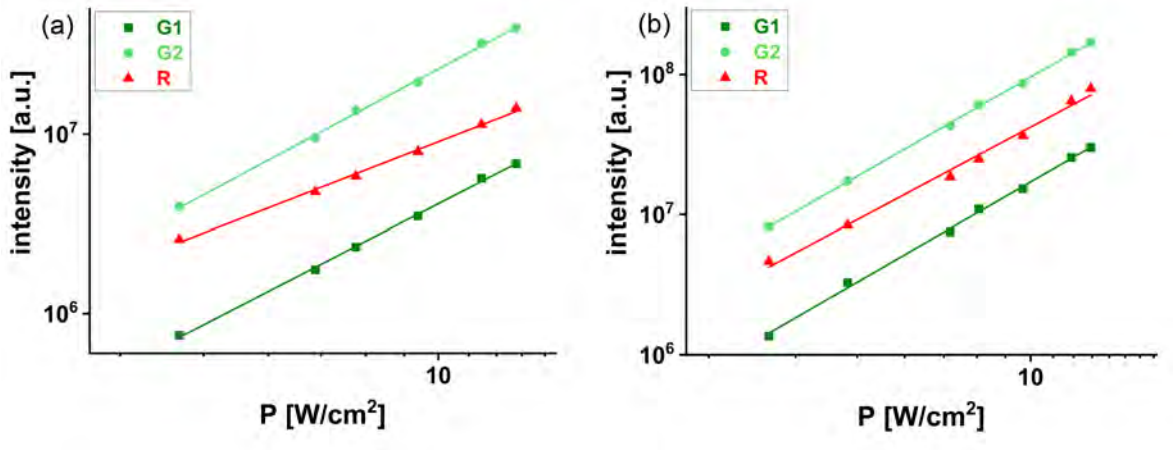

Figure 3.8: The double logarithmic plots of G1, G2 and R emission intensities of Er^{3+} versus pump power density for the samples (a)NaY:Gd_{30} (b)NaSc:Gd_{30}.

The population of the energy states involved green and red UCL exhibit a quasi-quadratic relationship with excitation power density at low Er^{3+} and Yb^{3+} concentrations. [113] Since we doped the UCNPs with a low amount of Er^{3+} and Yb^{3+} it is expected that the n values obtained from slopes should be about 2.[80]

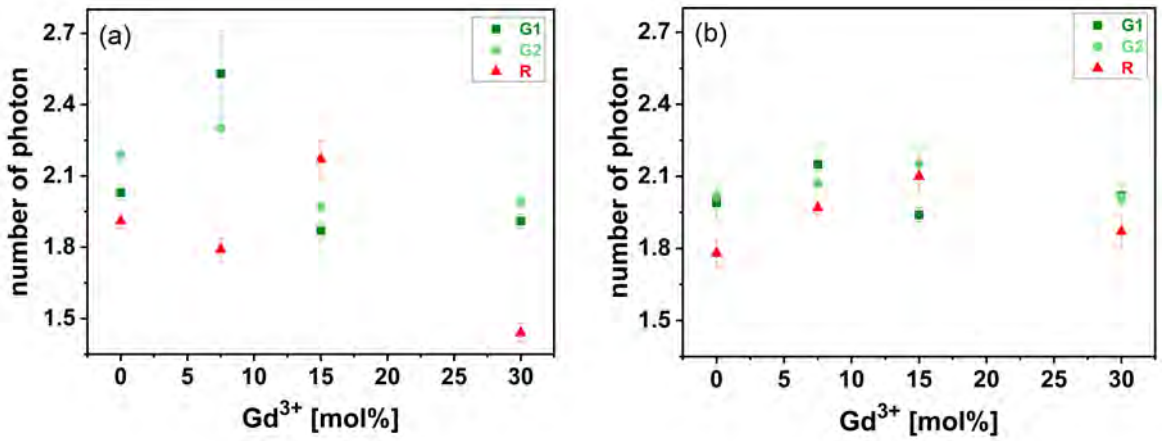

Figure 3.9: Number of photons for G1, G2, and R emission bads of Er^{3+} for UCNPs in (a) $NaYF_4$ and (b) Na_xScF_{3+x} lattices.

Figure 3.9 (a) and (b) show the number of photons for G1, G2, and R emission bands of Er^{3+} for NaY:$Gd_{0,7.5,15,30}$ and NaSc:$Gd_{0,7.5,15,30}$ UCNPs, respectively. For the G1, G2 and R emissions that occur with a 2 photon process for all UCNPs. The n-values slightly under 2 can be attributed to the occurrence of the saturated UC emission process.[114] Further, the reason for this could be the disturbance of the crystal structure especially after addition of 30 mol% of Gd^{3+} yielded deactivation centers. The relative smaller values of NaSc:Gd_0 and NaSc:Gd_{30} agree with the relative shorter decay times of that samples than that of NaSc:$Gd_{7.5}$ and NaSc:Gd_{15}.
Because of the relatively small particle size of NaY:$Gd_{0,7.5,15,30}$ UCNPs, the effect of other factors such as surface/crystal defects, impurities, and high-energy vibrational modes of surface ligands on the UCL process are enormous. This makes it difficult to interpret the random change of n-values for G1, G2, and R bands for this set of samples.

3.5 Temperature dependent UCL properties

Under 976 nm pulsed excitation, temperature-dependent UCL spectra of all UCNPs ranging from 288 to 323 K were recorded. The G1 and G2 UCL show a remarkable dependence on the temperature due to the thermal coupling between $^2H_{11/2}$ and $^4S_{3/2}$ states of Er^{3+}. Since the energy difference between $^2H_{11/2}$ and $^4S_{3/2}$ states is very small to be between 200 and 2000 cm^{-1}, the $^2H_{11/2}$ state of Er^{3+} is repopulated from $^4S_{3/2}$ states utilizing thermal agitation.[101][115]
According to equation 2.4 the $\ln(I_{G1}/I_{G2})$ was plotted as a function of inverse absolute temperature (1/T). As shown in figure 3.10 (b) the experimental data was

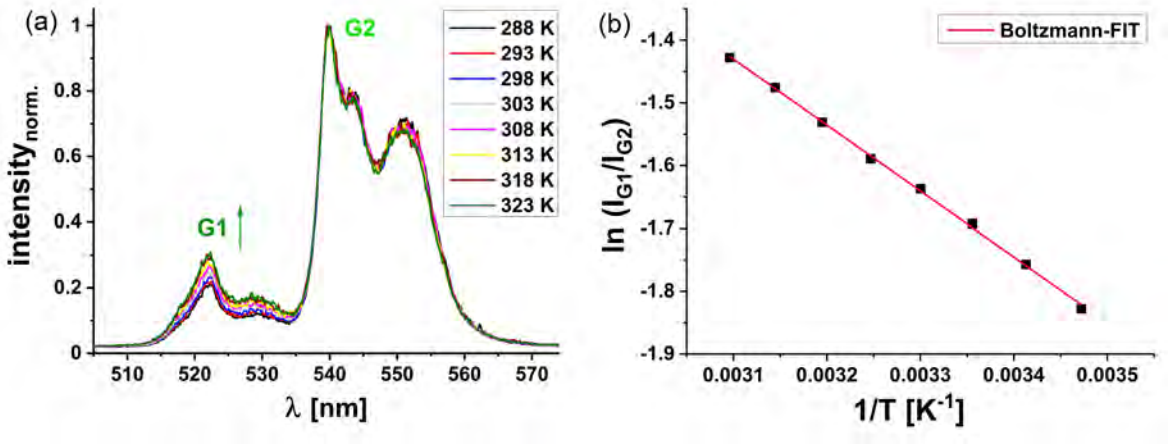

Figure 3.10: (a) Normalized UCL spectra of NaSc:$Gd_{7.5}$ in cyclohexane at different temperatures between 288 K and 323 K at 976 nm excitation wavelength (b) The plot of ln (I_{G1}/I_{G2})) versus 1/T of NaSc:$Gd_{7.5}$. All measurements carried out in cyclohexane with experimental parameters: exposure time = 0.017 secs, delay time after the laser pulse = 500 ns, gate width = 250 μs, number of accumulations = 200.

well fitted according to equation 2.4. The energy gap values (ΔE) calculated are displayed in figure A.8. The values decrease slightly after addition of 7.5 and 15 mol% of Gd^{3+} from 835 cm^{-1} to 807 cm^{-1} and 786 cm^{-1} for UCNPs in $NaYF_4$ lattice, respectively. The value is drastically low (482 cm^{-1}) at the 30 mol% Gd^{3+} doping level in this lattice. The energy gap value of TCL for UCNPs in Na_xScF_{3+x} lattice is first 739 cm^{-1} without Gd^{3+}, it decreases to 730 cm^{-1} with 7,5 Gd^{3+}. After increasing to 804 cm^{-1} it decreases drastically to 693 cm^{-1}. The low energy gap leads to the increase non-radiative relaxation rate, while the relatively high energy gap (around 800 cm^{-1}) leads to decrease that rate and the higher temperature sensitivity.[116][117] Thus, the sensitivity of samples NaY:$Gd_{0,7.5,15}$ and NaSc:$Gd_{0,7.5,15}$ is expected to be high.

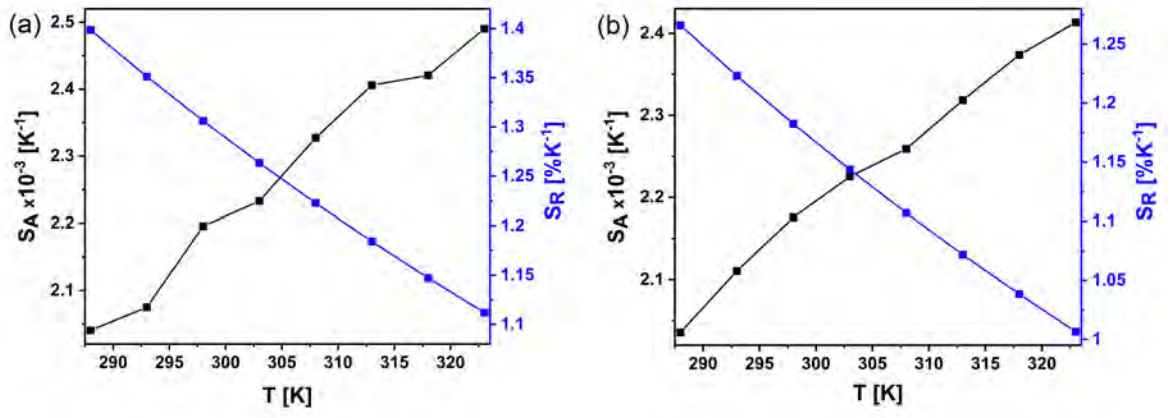

Figure 3.11: Absolute and relative sensitivity of the samples (a) NaY:$Gd_{7.5}$ (b) NaSc:$Gd_{7.5}$ for the temperature range of 288 K - 323 K based on the intensity ratio G1/G2.

Figure 3.11 (a) and (b) show exemplary the graphs of the S_A and S_R values (equation 2.5 and 2.6) against the temperature for samples NaY:$Gd_{7.5}$ and NaSc:$Gd_{7.5}$, respectively. The values of S_R are calculated to be between 1.11 and 1.40% K^{-1} (S_A = 0.0020 – 0.0025 K^{-1}) for NaY:$Gd_{7.5}$ at temperature between 288 and 323 K. Zhang et al. studied the temperature sensitivity of hexagonal $NaYF_4$:Yb^{3+}:Er^{3+} core UCNPs with an average particle size of 23 nm. The sensitivity of these core UCNPs increases from 0.0030 to 0.0035 K^{-1} as temperature increases from 301 to 337 K. However the agreement between high thermal response and relative thermal sensitivity (S_R > 1% K^{-1}) of the small NaY:$Gd_{7.5}$ UCNPs (6 nm) make them still a promising material in the physiological temperature range.[118] The same argument is valid for NaSc:$Gd_{7.5}$ UCNPs since they exhibit the S_R values between 1.00 and 1.27 % K^{-1} (S_A = 0.0020 – 0.0024 K^{-1}) at temperature between 288 and 323 K.
As seen in figures A.9 and A.10 the linear relation between sensitivities and temperature continues after adding 7.5 and 15 mol% of Gd^{3+} ion for samples in $NaYF_4$ and Na_xScF_{3+x}. The values of sensitivities at some points differ drastically from others for samples NaY:Gd_{30} and NaSc:Gd_{30}. This result corroborates with the small ΔE values of these samples. The small energy gap between $^2H_{11/2}$ - $^4S_{3/2}$ states, possible crystal defect with high amount of Gd^{3+}, as well as a large non-radiative transition rate between $^2H_{11/2}$ - $^4S_{3/2}$ states lead to nonlinear correlation between temperature and sensitivity. The most suitable energy gap to provide an agreement between high thermal response and relative thermal sensitivity is 835 cm^{-1} (NaY:Gd_0) for the set of sample in $NaYF_4$ and 804 cm^{-1} (NaSc:Gd_{15}) for the set of sample in Na_xScF_{3+x}.

3.6 Luminescence properties of Eu^{3+}

3.6.1 Luminescence properties at RT

The luminescence spectra of Eu^{3+} ions in NaY:$Gd_{0,7.5,15,30}$ and NaSc:$Gd_{0,7.5,15,30}$ UCNPs were recorded at RT upon excitation at 395 nm. The spectra were then normalized to integrated intensity of the $^5D_0 \rightarrow {}^7F_1$ transition. As shown in figure 3.12 (a) and (b) three characteristic emission bands are observed at 579 nm, 590 nm and 614 nm for all samples, corresponding to transitions $^5D_0 \rightarrow {}^7F_0$, $^5D_0 \rightarrow {}^7F_1$, $^5D_0 \rightarrow {}^7F_2$, respectively. The spectral intensity distribution changes after adding Gd^{3+} ion into the sample in $NaYF_4$ lattice. No more drastically change is observed with increasing of Gd^{3+} concentration. There is an obvious blue-shift of the maximum (anti- nephelauxetic behaviour) of $^5D_0 \rightarrow {}^7F_0$ transition after adding Gd^{3+} indicating occurrence of a weak crystal field strength.[69] The emission of the $^5D_0 \rightarrow {}^7F_2$ transition dominate other transitions in the spectra for all NaY:$Gd_{0,7.5,15,30}$ samples. This indicates that the Eu^{3+} ions are partly located in a low symmetry site without inversion centre.[72] The relative intensity of the $^5D_0 \rightarrow {}^7F_0$ and $^5D_0 \rightarrow {}^7F_2$ transitions to the $^5D_0 \rightarrow {}^7F_1$ transition is lower for the sample without Gd^{3+} than that for samples doped with Gd^{3+} indicating higher symmetry site of an amount of Eu^{3+} ions in NaY:Gd_0.[69] The relative intensities of these transitions are similar for all samples containing Gd^{3+}.
The spectral distribution of NaSc:Gd_0 UCNPs alters strongly with addition of 7.5 mol% of Gd^{3+}, while this remains similar with increase of Gd^{3+} content. The dominating

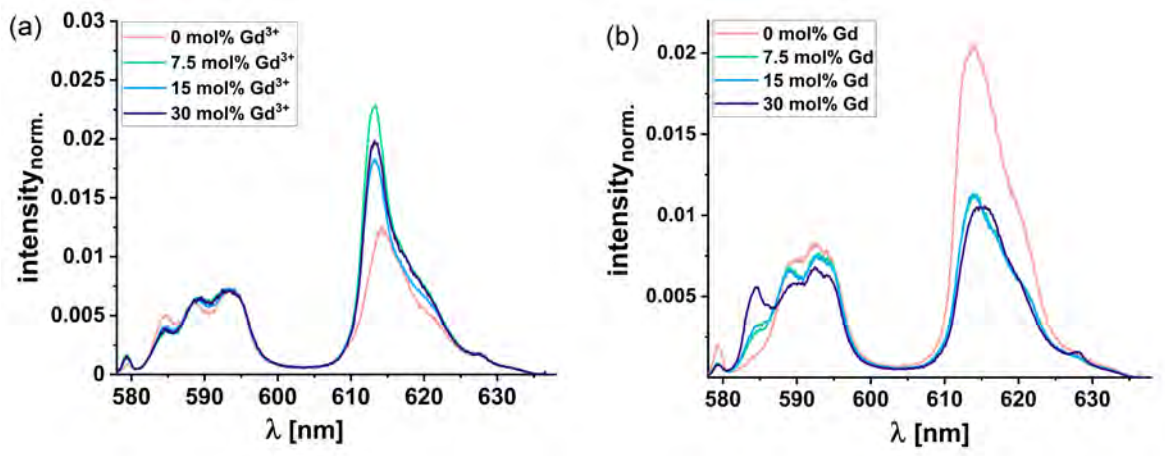

Figure 3.12: The luminescence emission spectra of Eu^{3+} (normalized to the MD transition) upon 395 nm excitation for the samples (a) NaY:$Gd_{0,7.5,15,30}$ (b) NaSc:$Gd_{0,7.5,15,30}$. All measurements carried out in cyclohexane with experimental parameters: exposure time = 0.021 secs, delay time after the laser pulse = 10 μs, gate width = 500 μs, number of accumulations = 100.

emission of the $^5D_0 \rightarrow {}^7F_2$ transition in the spectra indicates the low symmetry site (without inversion center) of Eu^{3+} in samples NaSc:$Gd_{0,7.5,15,30}$. The relative intensity of the $^5D_0 \rightarrow {}^7F_0$ and $^5D_0 \rightarrow {}^7F_2$ transitions to the $^5D_0 \rightarrow {}^7F_1$ transition is higher for the sample without Gd^{3+} than that for samples doped with Gd^{3+} indicating lower symmetry site of Eu^{3+} in NaSc:Gd_0. The presence of Gd^{3+} causes broadening (gradually emerging of a shoulder) on the $^5D_0 \rightarrow {}^7F_1$ transition band of NaSc:Gd_0. This shoulder at 584 nm appeared after adding Gd^{3+} can be attributed to the $^5D_1 \rightarrow {}^7F_3$ transition, which means high distortion around the Eu^{3+} ions (new symmetry site). As aforementioned this is expected since Gd^{3+} doping deteriorates the crystallinity of the Na_xScF_{x+3} lattice due to the large ionic radius compared to Sc^{3+}.
The presence of the emission band of $^5D_0 \rightarrow {}^7F_0$ transition in each emission spectra is an evident that the Eu^{3+} ions in all samples occupy C_{nv}, C_n or C_s symmetry, which are part of the monoclinic and hexagonal crystal systems.[119] However, some Eu^{3+} ions can be still found in other symmetry sites. For instance, the observed small splitting of $^7F_1$ state suggests that the system has a a cubic or approximately cubic symmetry. The observed shifts indicate that another site or species of Eu^{3+} emerge with introduce of Gd^{3+} in the host lattice. The red-shift of $^5D_0 \rightarrow {}^7F_0$ could imply the smallest number of defects in the close vicinity of the Eu^{3+} ions, while the blue-shift means exactly opposite.[69] There are three Stark-splitting on the $^5D_0 \rightarrow {}^7F_1$ transition band for all samples, while the environmentally hypersensitive $^5D_0 \rightarrow {}^7F_2$ transition bands show no splitting aside from a further shoulder at about 621 and 628 nm.
The luminescence decay kinetics of Eu^{3+} ion were analysed using a global fit model for the $^5D_0 \rightarrow {}^7F_1$ and $^5D_0 \rightarrow {}^7F_2$ transitions due to the same decay kinetic rates of these transitions (excluding transition $^5D_1 \rightarrow {}^7F_3$). As shown in figure 3.13 (a) the decay behaviours of all samples are similar for samples in $NaYF_4$ lattice. Still the NaY:Gd_0 exhibit a little slower behaviour. A biexponential law was chosen for the calculation

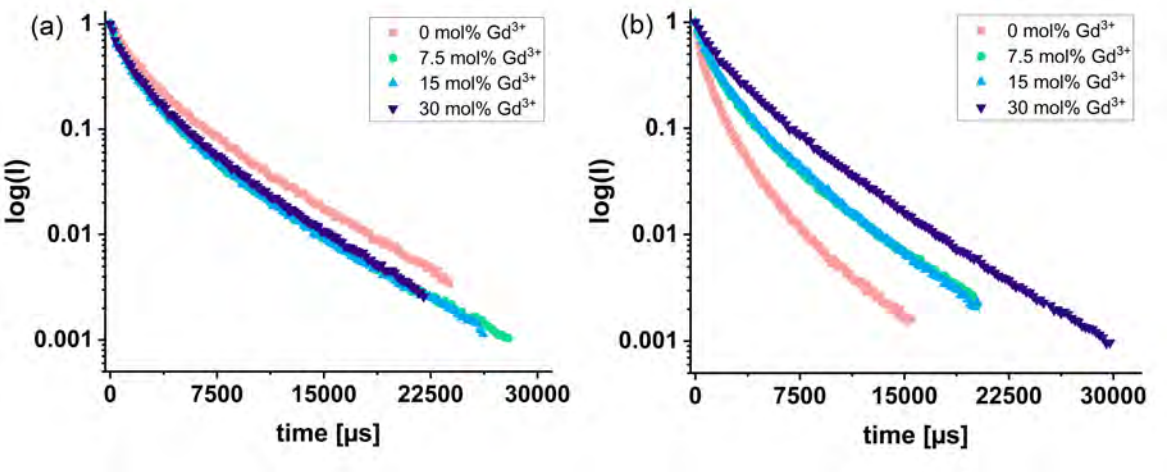

Figure 3.13: Luminescence decay curves of $^5D_0 \rightarrow {}^7F_2$ transitions of Eu^{3+} for the samples (a) $NaY:Gd_{0,7.5,15,30}$ (b) $NaSc:Gd_{0,7.5,15,30}$. All measurements carried out in cyclohexane with experimental parameters: λ_{ex} = 395 nm, exposure time = 0.017 - 0.034 secs, delay time after the laser pulse = 10 μs, gate width = 500 μs, number of accumulations = 100.

of decay times of MD ($^5D_0 \rightarrow {}^7F_1$) and ED ($^5D_0 \rightarrow {}^7F_1$) emissions. As shown in table 3.4, $NaY:Gd_{0,7.5,15,30}$ samples have 2 different species. The decay time value is 1369 μs for the short-lived species of $NaY:Gd_0$, while the value is 4853 μs for long-lived species of that sample. The τ_1 values of short-lived Eu^{3+} species for $NaY:Gd_{7.5,15,30}$ samples are 1213, 1065 and 1072 μs, respectively. There is a decreasing of values with increasing of Gd^{3+} concentration. The same trend is observed for long-lived species. Their values are 4626, 4285 and 4256 μs, respectively. As can be seen, the short and long decay time values for the samples $NaY:Gd_{15}$ and $NaY:Gd_{30}$ are almost the same, which means that the environment at this level of Gd^{3+} is very similar. The decrease of the values shows that the increasing the Gd^{3+} content causes environmental change such as alteration of interatomic distances, structural defects and the introduction of charges. This agreed well in the occurrence of blue-shift of the maximum of the $^5D_0 \rightarrow {}^7F_0$ transition after adding Gd^{3+} in $NaYF_4$ lattice and the results of decay times of Er^{3+}. The fractions of short- (between 32% and 44%) and long-lived (between 56% and 68%) Eu^{3+} species are remarkably similar for all samples.
The decay behaviours of $NaSc:Gd_{0,7.5,15,30}$ samples are again different than that of $NaY:Gd_{0,7.5,15,30}$ samples. The curves of $NaSc:Gd_{7.5}$ and $NaSc:Gd_{15}$ are very similar, while the curves of $NaSc:Gd_0$ and $NaSc:Gd_{30}$ distinguish significantly from others with their relatively fast and slow decay rates, respectively. The decay times of short-lived Eu^{3+} species of $NaSc:Gd_{0,7.5,15,30}$ samples are 481, 981, 989 and 1474 μs, respectively. There is an increase in decay time with the increasing of Gd^{3+} amount in the lattice. Furthermore, the decay times of long-lived species increase with increasing of Gd^{3+} concentration. The values are 2232, 3554, 3544, 4475 μs, respectively. These results show that the alteration in the crystal lattice by Gd^{3+} addition support the radiative emission from $^5D_0$ state. The fractions of τ_1 (between 28% and 34%) and τ_2 (between

66% and 72%) remain almost same for samples NaSc:$Gd_{0,7.5,15,30}$.

Table 3.4: Luminescence decay parameters of Eu^{3+} for UCNPs under pulsed wave excitation of ∼579 nm at RT.

mol% Gd^{3+}	Y^{3+} host lattice				Sc^{3+} host lattice			
	τ_1[µs]	χ_1[%]	τ_2[µs]	χ_2[%]	τ_1[µs]	χ_1[%]	τ_2[µs]	χ_2[%]
0	1369±25	32	4853±52	68	481±11	34	2232±31	66
7.5	1213±19	44	4626±50	56	981±16	35	3554±34	65
15	1065±24	36	4285±53	64	989±15	33	3544±31	67
30	1072±26	32	4256±57	68	1474±33	28	4475±36	72

The luminescence decay times of the short- and long-lived Eu^{3+} species in Na_xScF_{x+3} lattice are significantly lower than those in $NaYF_4$ lattice up to 15 mol% of Gd^{3+} even their larger particle size. Interestingly after adding 30 mol% Gd^{3+} these reached even higher values than those of sample NaY:Gd_{30}. Although the addition of Gd^{3+} cause more alteration in crystal structure of Na_xScF_{x+3} lattice and leads to more expansion the lattice, it supports the radiative relaxation of Eu^{3+} and Er^{3+} with exception of 30 mol% of Gd^{3+}. This can be attributed strong crystal field by the smallest number of defects around Eu^{3+} ions as red-shift of the maximum of the $^5D_0 \rightarrow {}^7F_0$ transition with addition of Gd^{3+} indicates.

3.6.2 Luminescence properties at ultralow temperature (∼4K)

For a better speciation analysis by luminescence spectroscopy, the inhomogeneous spectral broadening of the electronic transitions must be eliminated, and site-selective excitation must be achieved for the speciation analysis using the luminescence spectroscopy. For this reason, the luminescence kinetic and total luminescence spectra (TLS) of Eu^{3+} were recorded for all samples at ultralow temperature (∼4 K). The luminescence kinetic measurements were carried out at two excitation wavelengths, which are determined for each sample using the corresponding excitation wavelength of each totally different emission spectra, in other says, of the species. The luminescence decay curves of $^5D_0 \rightarrow {}^7F_1$ and $^5D_0 \rightarrow {}^7F_2$ transitions emerging from excitation at two different wavelengths for each sample were analysed with a double exponential global regression model. The decay curves of all samples, measured at higher excitation wavelengths, are shown in figure 3.14 (a) and (b).

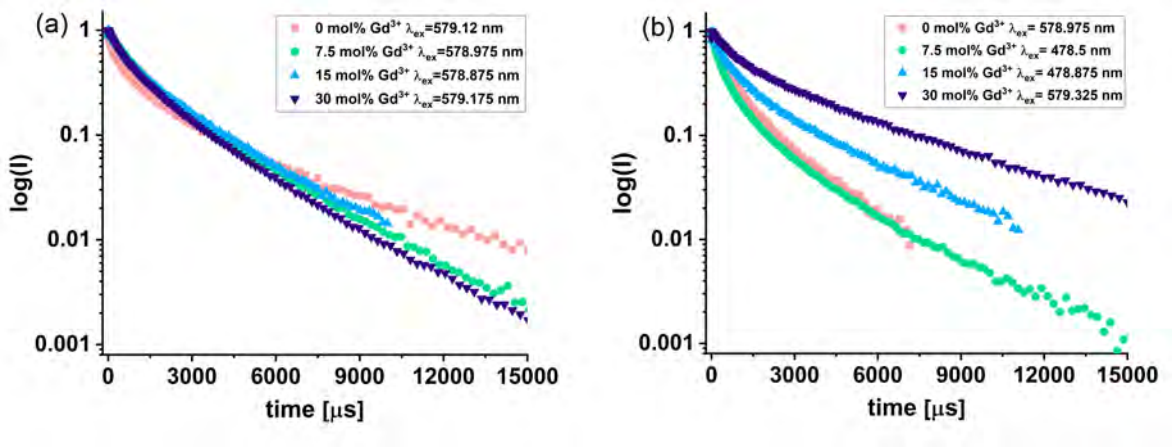

Figure 3.14: Luminescence decay curves of $^5D_0 \rightarrow {}^7F_2$ transitions of Eu^{3+} for the samples (a) $NaY:Gd_{0,7.5,15,30}$ (b) $NaSc:Gd_{0,7.5,15,30}$ under pulsed wave excitation at higher excitation wavelengths (∼579 nm). All measurements carried out in cyclohexane with experimental parameters: exposure time = 0.017 secs, delay time after the laser pulse = 500 ns, gate width = 200 μs, number of accumulations = 100.

Table 3.5: Luminescence decay parameters of Eu^{3+} for UCNPs under pulsed wave excitation at higher excitation wavelengths (∼579 nm) at ∼4 K.

mol% Gd^{3+}	Y^{3+} host lattice				Sc^{3+} host lattice			
	τ_1[μs]	χ_1[%]	τ_2[μs]	χ_2[%]	τ_1[μs]	χ_1[%]	τ_2[μs]	χ_2[%]
0	480±17	20	3655±76	80	356±11	23	1769±47	77
7.5	639±10	21	2583±26	79	396±6	35	2505±42	65
15	503±15	15	2510±44	85	473±12	19	2781±61	81
30	640±13	26	2743±27	74	751±15	13	4359±49	87

As seen, the behaviours of luminescence decay kinetic rates are similar to that obtained at RT for $NaY:Gd_{0,7.5,15,30}$. $NaY:Gd_0$ is different from others, while $NaY:Gd_{7.5,15,30}$ samples show similar behaviour. Finding two different species despite site selective excitation proof that the small amount of the other species was excited unintentionally during measurements. The short species for $NaY:Gd_{0,7.5,15,30}$ samples are 480, 639, 503 and 640 μs, respectively. It can be seen that the values for $NaY:Gd_0$ and $NaY:Gd_{15}$ are similar and shorter than the values for $NaY:Gd_{7.5}$ and $NaY:Gd_{30}$. Since the long-lived Eu^{3+} species are found in bulk and shielded from the environment, these values can give more information about the alteration in the crystal lattice. This shows that the sample without Gd^{3+} in the $NaYF_4$ lattice exhibit the longest luminescence decay time.

After adding Gd^{3+} there is a drastic decrease in decay time, and the values are similar for all samples codoped with Gd^{3+}. The decay time values of long-lived species for all samples in the $NaYF_4$ lattice are 3655, 2583, 2510, and 2543 μs. These decreasing trends of decay times with enhancement of the content of Gd^{3+} agree well with decay times determined after RT measurements.
If we look at the luminescence decay rates of NaSc:$Gd_{0,7.5,15,30}$ samples, we can see that the samples with Gd^{3+} emit much longer than the sample without Gd^{3+}. Both short- and long-lived species show a systematically increase with increasing the Gd^{3+} concentration. The values are 356, 396, 473 and 751 μs for short-lived species and 1769, 2505, 2781 and 4359 μs for long-lived species, respectively. As seen, these increasing trend of luminescence decay time values agreed well with other decay time values obtained from the records at RT. The decay times of short- and long-lived species in Na_xScF_{3+x} lattice are again significantly lower than those in $NaYF_4$ lattice up to 15 mol% of Gd^{3+}. Short- and long-lived Eu^{3+} species of NaSc:Gd_{30} have the highest values in NaSc:$Gd_{0,7.5,15,30}$ set and even in NaY:$Gd_{0,7.5,15,30}$ set. The fractions of τ_1 and τ_2 are similar for both set of samples.
The metal-ligand bonding and the crystal environment strongly influence on the electric dipole (ED) transition. In contrast, these parameters show no effect on the magnetic dipole (MD) transition. Thus, the asymmetric ratio (R_A) of the intensity of the hypersensitive ED transition to the intensity of the MD transition can help to characterize the environment of the Eu^{3+} ion in the crystal lattice.[120] The asymmetric ratios over delay times obtained from kinetic records upon site selective excitation at ~579 nm wavelength for all samples are shown in figure 3.15 (a) and (b). The R_A values for all samples change with increasing delay time. From 100 μs up to a certain point, there is more than one species contribution. After that point, we expect that the R_A values form a horizontal line in the graph, as only the long-lived species (in a two species system) is left, and its peak ratios do not change anymore.
The samples NaY:$Gd_{7.5}$ and NaY:Gd_{15} show the trend as described. After 400 μs they show almost the same ratio for all time points. NaY:Gd_0 show a slight increase even after 1 ms, while NaY:Gd_{30} exhibit a decrease. This indicates a contribution of a third species in both samples.

But for samples in Na_xScF_{x+3}, the number of species can be at least 3 since they exhibit a decreasing trend after an increasing ratio. All 3 species contribute to the emission up to 350 μs. After that, 2 long-lived species of decay times remain.
If Eu^{3+} ions in a site with center of symmetry (inversion center), the $^5D_0 \rightarrow {}^7F_2$ transition is strictly forbidden according to Judd-Ofelt theory. Therefore, the stronger distortion of the site from a high symmetry leads to more intense $^5D_0 \rightarrow {}^7F_2$ transition. So that, the R_A values can be used as a measure of the asymmetry of the Eu^{3+} site.[69] Although this statement is not always correct, it can broaden our perspective during the interpretation of all results complementarily. The R_A values are below 1, the site symmetry of Eu^{3+} is highly symmetric, and if the value is higher than 1 there will be a low symmetry environment around Eu^{3+}.[121] As seen in figure 3.15 (a), the environment of NaY:$Gd_{0,7.5,15,30}$ samples is lower in symmetry with increasing of content of Gd^{3+}. If one compares all samples, the NaY:Gd_{30} will have the lowest symmetry. The R_A values for NaY:Gd_0 start from under 1 increase gradually up to

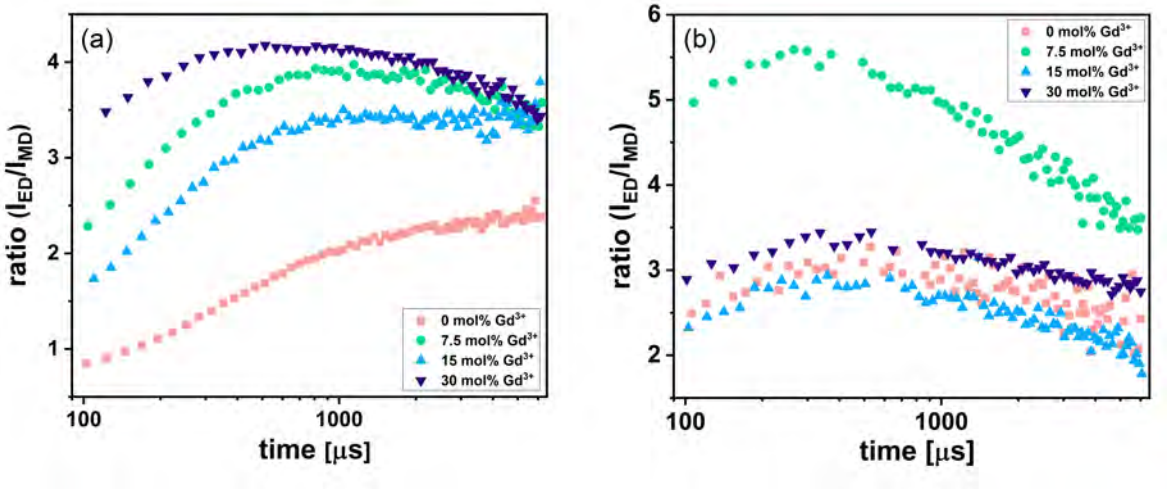

Figure 3.15: Asymmetric ratio R_A of the intensities of ED emission to MD emission of Eu^{3+} against decay time for the samples (a) NaY:$Gd_{0,7.5,15,30}$ (b) NaSc:$Gd_{0,7.5,15,30}$.

over 2 with increasing decay time. This means that the short-lived species resides in a high symmetry environment, while the long-lived species have relatively low symmetry site. The short-lived species of NaY:$Gd_{7.5}$ and NaY:Gd_{15} also have a highly symmetric environment, while the long-lived species have lower symmetry. In NaY:Gd_{30}, it seems that the species with the shortest- and the longest lifetime have relatively high symmetry environment, while the middle one a little high symmetry.
All NaSc:$Gd_{0,7.5,15,30}$ samples have a R_A value over 2 (figure 3.15 (b)). The environment of Eu^{3+} in NaSc:$Gd_{7.5}$ shows the lowest symmetry, while the others exhibit relatively high symmetry and similar environment.
Total luminescence spectra (TLS) were recorded to get a clear overview of the amount, distribution, and homogeneity of the Eu^{3+} species in the samples. For obtaining TLS spectra, samples were excited in an absorption range of 575 - 582 nm with a speed of 0.05 nm/s, and the corresponding emission spectra were recorded between 577.5 – 643.5 nm. In order to plot TLS, the emission intensities were translated to a colour scale from the lowest intensities (dark blue < white) to the highest (white < red). The emission wavelengths are shown on the x axis, while the excitation wavelengths are shown on the y axis. As shown in figure 3.16 (a) (samples NaY:$Gd_{0,7.5,15,30}$) , the spectral width of the emission band of $^5D_0 \rightarrow {}^7F_2$ transition decreases after adding Gd^{3+} indicating more homogeneous symmetry site of Eu^{3+} ions. Further addition of Gd^{3+} caused just a slight narrowness at the aforementioned band. The spectral intensity distribution of the band of $^5D_0 \rightarrow {}^7F_1$ transition change drastically with presenting of Gd^{3+}, while further addition makes just slightly difference. The two distinct bright spots of that transition for sample NaY:Gd_0 show two Eu^{3+} species. The one species excited at 578.9 nm is the red-shifted and indicates that this Eu^{3+} species is undergoing a strong crystal field because of the smallest number of defects close to these Eu^{3+} ions. The other species excited at 578.0 nm is located in a low symmetry site.
Figure 3.16 (b) show a drastic broadening of emission band ($^5D_0 \rightarrow {}^7F_2$ transition) and the excitation band after adding 7.5 mol% Gd into the sample in Na_xScF_{3+x} lattice.

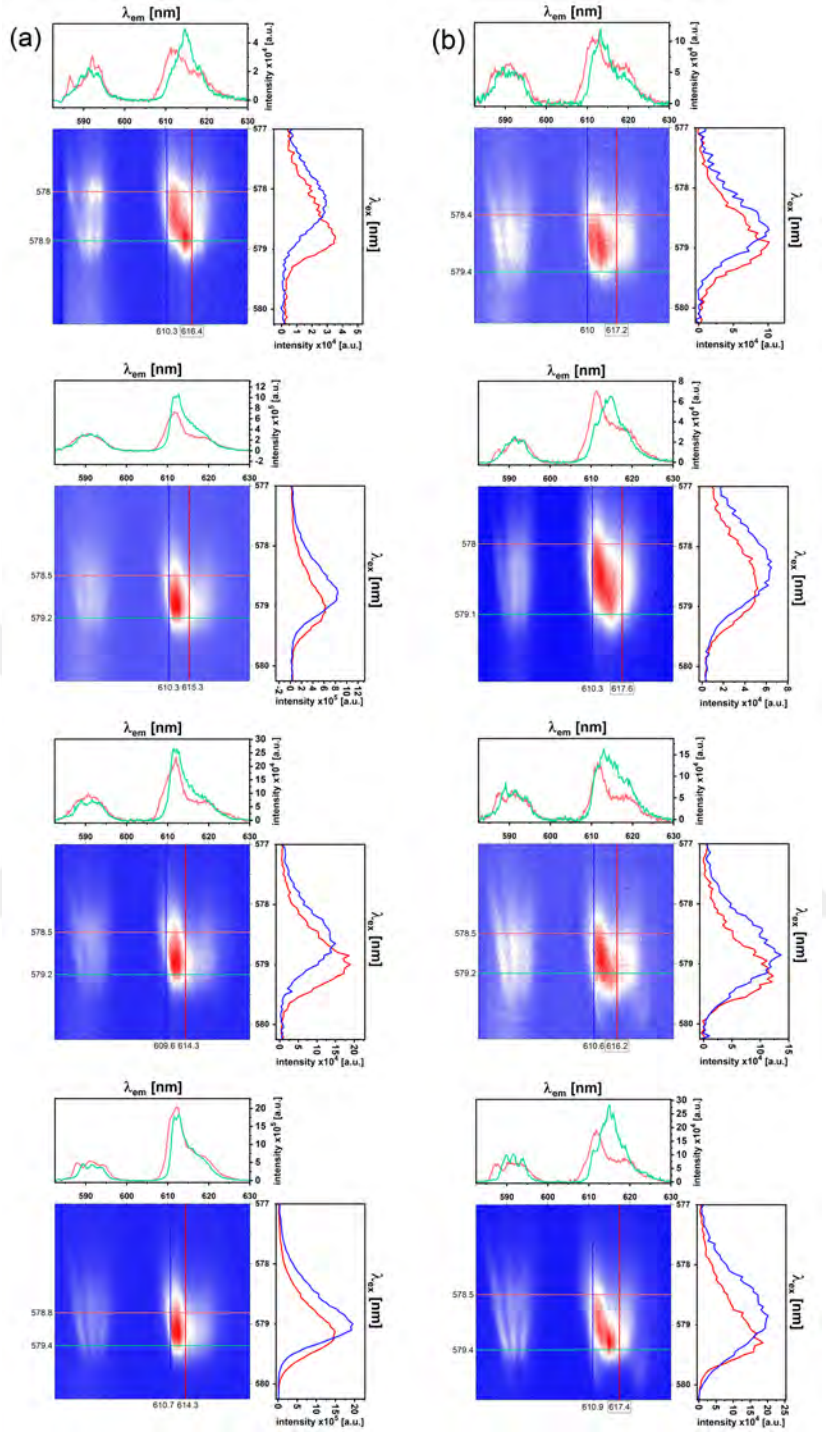

Figure 3.16: TLS of $^5D_0 \rightarrow {}^7F_1$ and $^5D_0 \rightarrow {}^7F_2$ transitions of Eu^{3+} at excitation wavelengts between 577 nm and 580.5 nm for the samples (a) NaY:$Gd_{0,7.5,15,30}$ (from top to the bottom) (b) NaSc:$Gd_{0,7.5,15,30}$ (from top to the bottom). All measurements carried out in cyclohexane with experimental parameters: exposure time = 0.017 secs, delay time after the laser pulse = 500 ns, gate width = 200 μs, number of accumulations = 100.

Further addition of Gd^{3+} leads the corresponding emission and excitation bands to narrower band width, which means that Eu^{3+} ions are located in more homogenous environment for NaSc:$Gd_{15,30}$. Looking at TLS images it can be determined two major species at ∼578 nm and ∼579 nm. The Eu^{3+} species at around 578 nm relatively low symmetry site since a red-shift appears upon excitation at around 579 nm due to formation high symmetry.
Samples in Na_xScF_{3+x} lattice show always broader emission and excitation band widths compared with samples in $NaYF_4$ lattice, which imply the broadening in the distribution of the angles and the distances between Eu^{3+} ions in the first coordination sphere of Eu^{3+} in Na_xScF_{3+x} lattice more than that in $NaYF_4$ lattice.[73] The intensity of $^5D_0 \rightarrow {}^7F_2$ transition is dominant relatively to that of $^5D_0 \rightarrow {}^7F_1$ transition in all samples. This fact with existence of excitation of $^5D_0 \rightarrow {}^7F_0$ transition indicate that excited Eu^{3+} ions are not located in the site with inversion symmetry.[122] The narrower band width of MD emission band at high excitation wavelength indicates the high symmetry Eu^{3+} species. It is observed that the most significant change takes place when going from no Gd^{3+} to Gd^{3+} for both set of samples.
All TLS spectra are processed in a PARAFAC analysis. Figure 3.17 shows the emission (a) and excitation (b) spectra of Eu^{3+} species in $NaYF_4$ lattice. As seen, the samples have 2 different Eu^{3+} species. One of them shows a narrow emission and excitation band with a longer excitation wavelength, and the other one displays broad emission and excitation due to a less homogenous environment and possible crystal defects. The relative intensity of species over Gd^{3+} concentration for NaY:$Gd_{0,7.5,15,30}$ in figure 3.17 (c) show that the relative intensities of the second species are dominant until 15 mol% of Gd^{3+}. The relative intensities of species are almost the same when adding 30 mol% Gd^{3+}. Although it was clear that the sample NaY:Gd_0 has 2 different Eu^{3+} species according to TLS, PARAFAC analysis results in only one species. Because PARAFAC is limited to distinguish the similar spectral forms, it only splits up the species distribution with the highest intensity into several components instead of trying to find a new minor species. Therefore, future work is needed to improve the PARAFAC analysis concerning this case.

The samples in Na_xScF_{3+x} lattice have 3 different emission and excitation bands (figure 3.17 (d) and (e) due to finding of Eu^{3+} in 3 different sites. The emission and excitation bands broaden from species 1 to species 3, indicating the existence of 3 different sites from homogenous to less homogeneous for Eu^{3+} ions. The intensities of first species is dominant for samples NaSc:$Gd_{0,15,30}$ while the third ones is dominant in sample NaSc:$Gd_{7.5}$. This corresponds to the TLS (broadening in TLS), and R_A (low symmetry site) results well, which give more detailed information about the crystal field effect as well as the site of Eu^{3+} by getting the spectra at low temperature (∼4K). The relative intensity contribution of the third one for the samples NaSc:$Gd_{0,15,30}$ and the second one for the sample NaSc:$Gd_{7.5}$ is extremely low. For this reason maybe its decay time could not be determined even using the evaluation low temperature decay kinetics.
From the PARAFAC analysis, the crystal field strength parameters of the Eu^{3+} species were calculated (according to equation 2.8). As seen in table 3.6, first species in $NaYF_4$ lattice have a strength parameter of 645 cm^{-1} and the second one 739 cm^{-1} indicating 1. Eu^{3+} species in strong crystal field, while the 2. Eu^{3+} species in relatively weak crystal

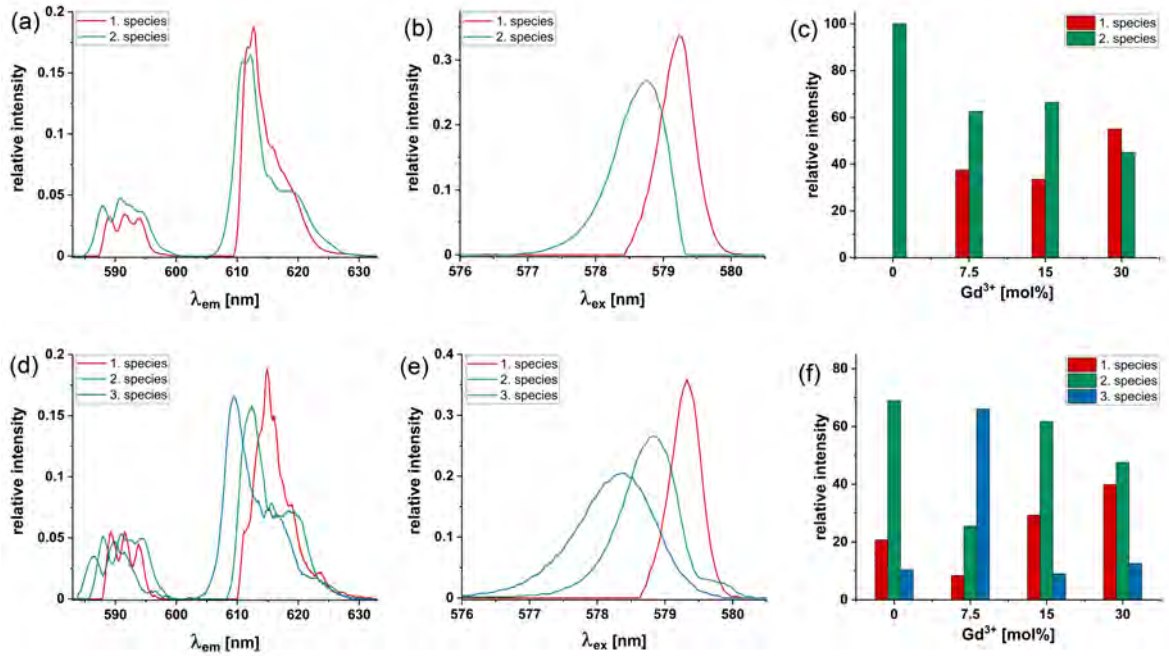

Figure 3.17: The emission, excitation spectra and relative intensity of Eu^{3+} species depending Gd^{3+} concentration calculated by using Parafac analysis based on the TLS (a), (b), (c) for $NaY:Gd_{0,7.5,15,30}$, respectively, (d), (e), (f) for $NaSc:Gd_{0,7.5,15,30}$, respectively.

field. Besides this, crystal field strength parameter of three species in Sc^{3+} lattice are 594 cm^{-1}, 809 cm^{-1}, 1368 cm^{-1}, respectively. The crystal field is strong for 1. Eu^{3+} species, medium for 2. Eu^{3+} species and weak for 3. Eu^{3+} species.

Table 3.6: Crystal field strength parameters of samples in $NaYF_4$ and Na_xScF_{3+x} lattices calculated for excitation maxima of each species.

	Y^{3+} lattice		Sc^{3+} lattice		
Species	1	2	1	2	3
N [cm^{-1}]	645	739	594	809	1368

3.7 Conclusion

The UCL properties of UCNPs based on $NaYF_4$ and Na_xScF_{3+x} doped with Yb^{3+}, Er^{3+} and Eu^{3+} were studied comparatively with regard to Gd^{3+} codoping. The UCNPs in $NaYF_4$ without Gd^{3+} are formed in a mixed phase of cubic and hexagonal phases. Gd^{3+} codoping caused a gradual expansion in the cubic unit cell, whereas the intensity of the reflexes of hexagonal phase decrease with increasing of the Gd^{3+} concentration

in $NaYF_4$. The UCNPs with no Gd^{3+} codoping in Na_xScF_{3+x} lattice are formed in a mixed phase of monoclinic and hexagonal phases. The increase of Gd^{3+} leads to the gradually expanding in monoclinic and hexagonal phase of Na_xScF_{3+x} and to stronger reflexes of hexagonal Na_xScF_{3+x} and $NaGdF_4$. The TEM records show that codoping UCNPs with different amounts of Gd^{3+} result in the change of the particle shape, while the particle size remains unaffected by the change of Gd^{3+} concentration. The particle sizes calculated using TEM images and hydrodynamic diameters of particles determined by DLS analyze corroborate well with each other.
The structural change by Gd^{3+} codoping is reflected by the alteration of the UCL spectra of Er^{3+}. The slightly change of the red to green emission intensity ratio in $NaYF_4$ lattice is observed after adding Gd^{3+}. The reason for this the slightly change of environment of Er^{3+} ions due to similar ionic radius of Y^{3+} and Gd^{3+}. On the other hand, the spectral distribution of UCL for samples in Na_xScF_{3+x} altered remarkably from no Gd^{3+} to Gd^{3+} in samples and the red to green emission intensity ratio changed gradually with increase of the Gd^{3+} concentration from 0 to 30 mol%, indicating the extrem change of site symmetry of Er^{3+} due to increasing of Gd^{3+}, which has larger ionic radius than Sc^{3+}. The results of time resolved and temperature dependent UCL measurements of Er^{3+} also show the significant effect of Gd^{3+} amount on the UCL properties. Gd^{3+} supported the longer decay time of long-lived Er^{3+} species and higher temperature sensitivity for UCNPs in Na_xScF_{3+x} lattice. The highest range of S_R value is 1.39 - 1.11 $\%K^{-1}$ (S_A = 0.0022 – 0.0027 K^{-1}) between 288 and 323 K belonged to sample containing 15 mol% of Gd^{3+}. On the other hand, the UCNPs in $NaYF_4$ lattice has the highest decay time and temperature sensitivity values in absent of Gd^{3+}. The range of S_R value of that sample is 1.45 – 1.15 $\%K^{-1}$ (S_A = 0.0028 – 0.0035 K^{-1}) between 288 and 323 K. However, all UCNPs show a high temperature sensitivity in aforementioned range, which make it possible to use them in biological field. The number of photons used for G1, G2 and R emissions of Er^{3+} lie at 2 for all samples.
Eu^{3+} exhibited its great potential as an optical probe even at RT for deeper investigating the structural change with the amount of Gd^{3+} from 0 to 30 mol%. First the blue-shift of the maximum of the $^5D_0 \rightarrow {}^7F_0$ transition in emission spectra of Eu^{3+} after addition of Gd^{3+} for samples in $NaYF_4$ show that the Gd^{3+} lead to low site symmetry. This also explains the decrease of decay times of Eu^{3+} with the increasing amount of Gd^{3+}. The time resolved luminescence analysis of Eu^{3+} at RT and ultralow temperature indicated that there are two Eu^{3+} species (two different site symmetry) of samples in $NaYF_4$. The cubic $NaYF_4$ crystal offer only one site (4a) to Y^{3+}, while the hexagonal $NaYF_4$ provides 2 different sites (1a and 1f) to Y^{3+}. Since Eu^{3+} ions occupy the 4a site in cubic $NaYF_4$ lattice. The main part of UCNPs are in the cubic phase. Therefore we can assume that the Eu^{3+} ions are located in cubic $NaYF_4$. The short-lived Eu^{3+} species can be attributed to the Eu^{3+} ions placed on/near particle surface or in bulk with high defects in the first coordination sphere of Eu^{3+} (low symmetry site). The long-lived Eu^{3+} species should be then in the well crystalline bulk phase (high symmetry site). The plot of R_A ratio against the decay time indicated that the site symmetry of Eu^{3+} ions become lower with increasing of the Gd^{3+} concentration and give an idea that each sample in $NaYF_4$ lattice have two Eu^{3+} species. The transition

to lower symmetry gradually implies the reduction of the decay times of the UCL of Er^{3+} and Eu^{3+} luminescence of these samples. The TLS spectra recorded at ultralow temperature present the small differences in the electronic spectra of Eu^{3+} species in different environments. The significant resolving of two Eu^{3+} species is provided by two distinct spots of $^5D_0 \rightarrow {}^7F_1$ transition, observed especially in sample with no Gd^{3+} content. PARAFAC analysis revealed that there are two different Eu^{3+} species for samples in $NaYF_4$ except the sample without Gd^{3+}, although it was determined that there are obviously two different Eu^{3+} species in this sample. These results show the power of the use TLS and PARAFAC analysis together. However, PARAFAC needs to be improved in regard to the distinguish of similar spectral forms. PARAFAC separated the emission and excitation bands of each species and showed that the species in high symmetry sites have narrower and more structured emission and excitation bands.
On the other hand, the $^5D_0 \rightarrow {}^7F_0$ transition of Eu^{3+} for samples in Na_xScF_{3+x} show a red-shift after addition of Gd^{3+}, which indicates an alteration of Eu^{3+} site to higher symmetry as well as supporting longer decay time of Eu^{3+}. According to the time resolved luminescence analysis, two different Eu^{3+} species exist in each sample in Na_xScF_{3+x} lattice. Sc^{3+} has one site (2a) in the monoclinic Na_xScF_{3+x}. In that lattice, Eu^{3+} ions can occupy this site. The hexagonal Na_xScF_{3+x} offer one site (3a) to Sc^{3+} and hexagonal $NaGdF_4$ two sites (1a, 1f). The long-lived Eu^{3+} ions are located in bulk phase (high symmetry site) and short-lived species in on/near particles surface and in defect sites of bulk (low symmetry site). The plot of R_A against the decay time suggested that the site symmetry of Eu^{3+} converted to lower symmetry for only one sample codoped with 7.5 mol% of Gd^{3+}, while the other samples exhibit relatively high symmetry. Furthermore, it is determined that there are three Eu^{3+} species in each sample in Na_xScF_{3+x} using the plot of R_A against the decay time. The resolution of the small differences of the environment of Eu^{3+} species is achieved by TLS recorded at ultralow temperature. The separation of the emission and excitation spectra of each Eu^{3+} species performed by PARAFAC analysis showed that three different Eu^{3+} species present for samples in Na_xScF_{3+x}, indicating the existence of the weak, medium, and strong crystal field. The typical sharp and structured emission bands of Eu^{3+} with distinct splitting in high symmetry environment are determined. R_A results pointed also to the presence of three Eu^{3+} species in that lattice. As seen, carrying out complementary measurements illuminate the optical and structural properties more.
The high variation of the lattice parameter with addition of Gd^{3+} caused much higher effect on the crystal structure, UCL properties as well as the Eu^{3+} luminescence in Na_xScF_{3+x} than in $NaYF_4$.

Chapter 4

One step synthesized AcOH@$NaGdF_4$:Yb^{3+}:Er^{3+} UCNPs

4.1 Introduction

For biological application, UCNPs should be hydrophilic. As known, the commonly used methods (as mentioned in section 1.5) for the synthesis of UCNPs result in hydrophobic particles. This causes the requirement of further steps to make UCNPs water-soluble. Microwave-assisted hydrothermal synthesis method offers great chances to obtain hydrophilic UCNPs in one step. This method provides many valued advantages such as the transfer of the energy directly to the sample and uniformly to the whole reaction system, fast heat, reduction in reaction time, no toxic waste products, allowing the formation of hydrophilic uniform nanoparticles, cost-effective, user-friendly, green method.[77][123][43] The multifunctional UCNPs are particularly useful for many biological and medical applications. $NaGdF_4$:Yb^{3+}:Er^{3+} UCNPs can provide MRI/optical dual-mode imaging. The hexagonal phase $NaGdF_4$ is thermodynamically more stable compared with its cubic phase counterpart and displays approximately one to two orders of magnitude higher UCL efficiency.[124] It has a low phonon energy (350 cm^{-1}) and high chemical stability, which make it an efficient host lattice.[91] UCNPs in $NaGdF_4$ host lattice can offer a comparable UCL intensity in comparison with $NaYF_4$. Wang et al. [124] could obtain hexagonal $NaGdF_4$ UCNPs in an extremely short reaction time (1 min) and a relatively low reaction temperature (160 °C) using a microwave-assisted hydrothermal synthesis method. However, these oleic acid capped UCNPs are not water-soluble and need further steps to be hydrophilic. There is still the requirement of further investigations to produce hydrophilic hexagonal $NaGdF_4$ UCNPs in one step. The solvent composition, the volume ratio of solvents and capping agent, the viscosity of medium, the capping agent influence the particle size and morphology significantly.[125][40][126] Zeng et. al. obtained nanorods with a diameter of 70 nm and length of 150-175 nm, as a composition consisted of acetic acid, water, and cetyltrimethylammonium bromide (CTAB) was used. When the medium was composed of EtOH, water, and EDTA, the spherical nanoparticles were synthesized with an average particle size of 50 nm.[40]
In this chapter, we investigated the effects of the synthetic parameters (reaction time,

the volumetric ratio of solvents and capping agent, type of surface ligand, stirring speed, reaction temperature, the volume of the reaction mixture) on the crystal structure, morphology, and photophysical properties of acetic acid capped hydrophilic $NaGdF_4$:Yb^{3+}:Er^{3+} UCNPs synthesized via microwave-assisted hydrothermal method. 7 samples in a solution H_2O:EtOH:AcOH, 7 samples in a medium H_2O:EG:AcOH, 1 sample in H_2O:G:AcOH and 1 sample in H_2O:EtOH:AC were synthesized under various synthesis conditions. First the UCNPs were structurally characterized. Afterward, the relative R to G_T UCL intensities, decay kinetics, and power dependent behaviours of UCL were intensely studied.

4.2 Structural characterization

4.2.1 XRD

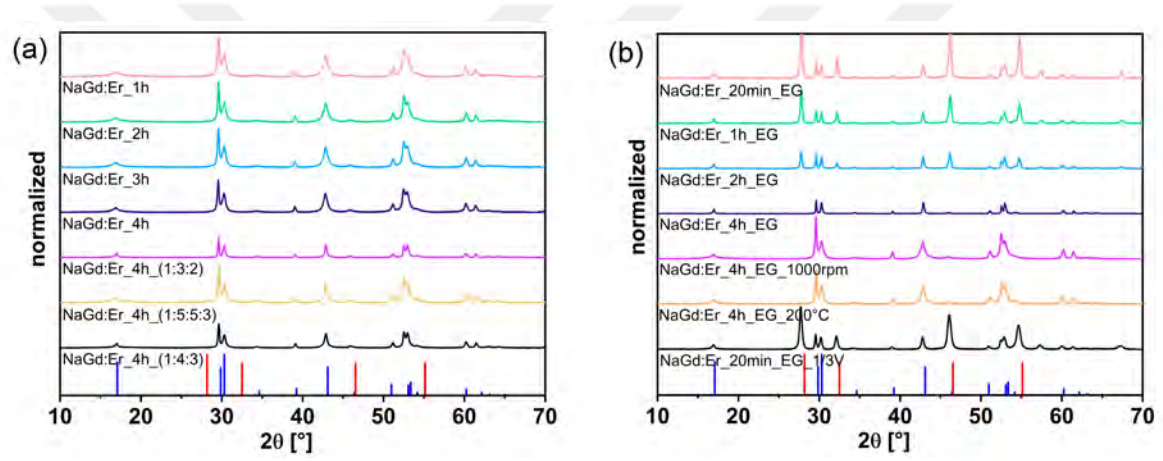

Figure 4.1: X-ray diffraction patterns of samples (a) NaGd:Er_1h, NaGd:Er_2h, NaGd:Er_3h, NaGd:Er_4h, NaGd:Er_4h_(1:3:2), NaGd:Er_4h_(1.5:5:3), NaGd:Er_4h_(1:4:3) (b) NaGd:Er_20min_EG, NaGd:Er_1h_EG, NaGd:Er_2h_EG, NaGd:Er_4h_EG, NaGd:Er_4h_EG_1000rpm, NaGd:Er_4h_EG_250°C, NaGd:Er_20min_EG_1/3V (red columns belong to the standard XRD patterns of the cubic phase $NaGdF_4$ (drawn based on Chen´s paper [128] and blue columns to the hexagonal phase $NaGdF_4$ (ICSD card 424381)).

The evolution of the XRD patterns of microwave synthesized NaGd:Er UCNPs shown in figure 4.1 (a) and (b), produced in a solution containing EtOH and EG, respectively. The temperature for all synthesis was set to 150 °C expect for the sample NaGd:Er_4h_EG_200°C. $NaGdF_4$ host lattice is found in hexagonal or cubic phase thermodynamically stable.[127] The unit cell structure of the hexagonal phase $NaGdF_4$ is shown in figure 4.2. As seen, the normalized XRD patterns of all samples synthesized in solution containing EtOH display a pure hexagonal $NaGdF_4$ (standard pattern from ICSD card 77099) with strong reflexes at 29.6°, 30.3°, 42.8°, 52.5°. No other impurity reflexes were detected, indicating the high purity of the obtained samples. To

our knowledge, it is reported to be the first time for generating hydrophilic UCNPs in hexagonal $NaGdF_4$ in one step under mild conditions like with a reaction time of 1 h and at a reaction temperature of 150 °C.
The samples (NaGd:Er_20min_EG, NaGd:Er_1h_EG, NaGd:Er_2h_EG and NaGd:Er_20min_EG_1/3V) synthesized in solution containing EG have reflexes of cubic $NaGdF_4$ on the normalized XRD patterns at 27.8°, 32.21°, 46.21°, 54.78°, 57.43° in addition to the reflexes of hexagonal $NaGdF_4$. As seen the longer heat treatment lead UCNPs (NaGd:Er_4h_EG, NaGd:Er_4h_EG_200°C and NaGd:Er_4h_1000rpm) to the pure hexagonal phase.
UCNPs synthesized with another capping agent (amino cellulose) exhibit reflexes of pure hexagonal $NaGdF_4$. The sample synthesized at 20 min in a solution containing glycerol has a mixed phase of cubic and hexagonal $NaGdF_4$ (figure A.11).
Obtaining pure hexagonal phase $NaGdF_4$ UCNPs (in EtOH) in contrast to the production of mixed phase UCNPs (in EG and G) below 4 h reaction time can be explained with high viscosity of EG, and G. Using high viscose solvents slow down the Ostwald ripening process as well as retarded emerging the hexagonal phase UCNPs.
It can be mentioned the slight shift from the standard pattern for all samples as expected since UCNPs doped with Yb^{3+} and Er^{3+}. However, there is no shift appeared in reflexes under different synthetic conditions, which shows that these conditions are not determinant in the lattice parameter of the $NaGdF_4$. The obvious alteration of the width of the reflection peaks determines the alteration of the crystal size of UCNPs. Comparing the width of the reflection peaks belonged different crystal phases, it can be seen that UCNPs in the cubic phase have smaller crystal size.

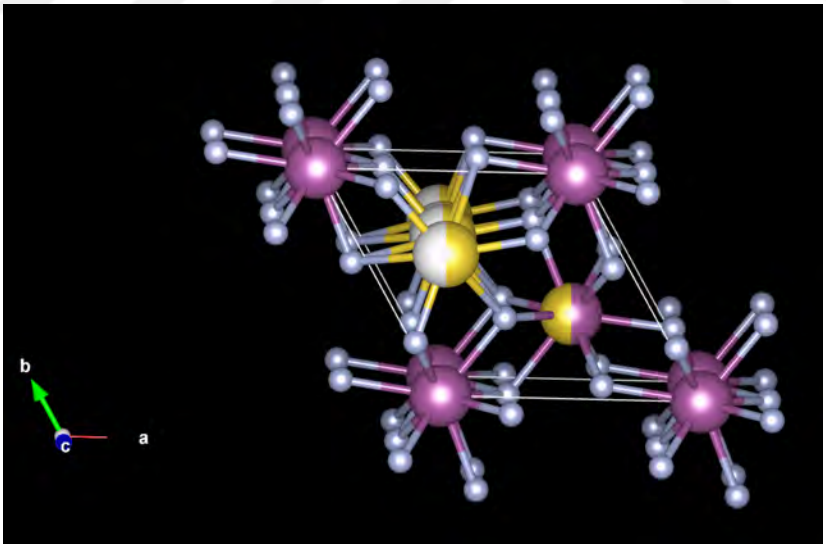

Figure 4.2: Unit cell structure of hexagonal $NaGdF_4$ (ICSD card 424381, space group P-6) Colour key: yellow = Na^+, violet = Gd^{3+}, grey = F^- ions. The balls marked with white in unit cell demonstrate that the positions are available either for vacancies or Na^+ ions. Images created by using open-source software package VESTA. (093)

4.2.2 SEM

The SEM images (SEM1) of NaGd:Er_4h_(1:3:2), NaGd:Er_4h_EG, NaGd:Er_20min_EG_1/3V and their particle size distribution histograms are shown in figure 4.3 (a-f), exemplarily. NaGd:Er_4h_(1:3:2) and NaGd:Er_4h_EG UCNPs are large hexagonal particles with average particle sizes of 141±21 and 286±31 nm, respectively. However, the NaGd:Er_20min_EG_1/3V UCNPs consist of small spherical particles associating with broad reflection peaks of cubic phase and large plate-like particles associating with narrow reflection peaks of hexagonal phase on the XRD pattern of the sample. These UCNPs have an average particle size of 38±12 nm.
AcOH capped UCNPs are first synthesized with a volumetric ratio of solvents and capping agent of 1:4:1 (H_2O:EtOH:AcOH) at different reaction times from 1 to 4 h. As seen in figure A.12 (a-i), the samples synthesized at 1, 2, and 3 h reaction times show similar form and particle size (99±34, 91±21, 99±32 nm, respectively). They exhibit small elliptical and large spherical cloud-like forms. 4 h reaction times result in slightly smaller average particle size (84±24 nm) and a distinct hexagon shape.

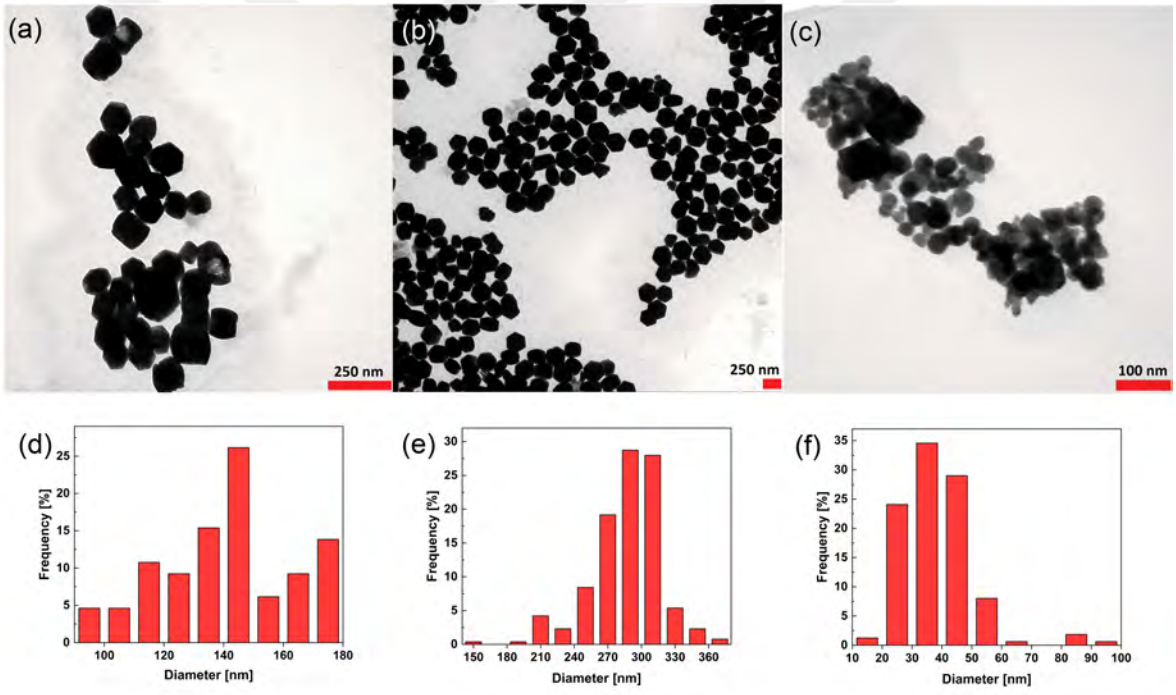

Figure 4.3: SEM images of (a) NaGd:Er_4h_(1:3:2) UCNPs with a scale bar = 250 nm (b) NaGd:Er_4h_EG UCNPs with a scale bar = 250 nm (c) NaGd:Er_20min_EG_1/3V UCNPs with a scale bar = 100 nm, Particle size distribution histogram of (d) NaGd:Er_4h_(1:3:2) (e) NaGd:Er_4h_EG (f) NaGd:Er_20min_EG_1/3V according to SEM.

Besides the effects of reaction time, the volumetric ratio of solvent and capping agent (H2O:EtOH:AcOH) may have considerable influence on the crystallization and shape evaluation of UCNPs. UCNPs with H_2O:EtOH:AcOH ratios 1:4:1, 1:3:2, 1:4:3 and 1.5:5:3 were synthesized at 4 h reaction time. Changing the ratio from 1:4:1 to 1:3:2

causes the formation of larger particles with well-shaped hexagons. Further increase of the concentration of AcOH leads to the formation of highly polydisperse UCNPs in an irregular shape, which indicates the significant effect of the concentration of the capping agent on the particle shape and size distribution. Besides the concentration of the capping agent, the polarity of the medium should be considered since the polarity of the medium change with alteration of the H_2O:EtOH:AcOH ratio. According to researches of Hussein et al. [129], and Chen et al. [130] it has been determined that the high volumetric ratio of EtOH (less polar solution) in a H_2O:EtOH solution caused larger, aggregated, and shapeless nanoparticles due to low value of the polarity index of the reaction medium. This can explain the formation of polydisperse UCNPs in an irregular shape with a high concentration of EtOH and AcOH.
The effects of the type of solvent on the size and morphology of the UCNPs were also investigated. The remarkably high amount of UCNPs synthesized using EG are small and round particles with an average particle size of 57±11, 47±9, 64±12 nm, respectively, up to 3 h reaction time. Small particles are spherical cubic $NaGdF_4$, which can be identified with larger reflection peaks of cubic $NaGdF_4$. The appearing large formation on the SEM image can be attributed to hexagonal $NaGdF_4$ nanorods/plates, which should be associated with narrow reflection peaks of hexagonal $NaGdF_4$ on the XRD pattern. The anisotropic growth of particles along the c-axis direction is typical for hexagonal $NaGF_4$ UCNPs in the form of the nanorods/plates.[124] The extending of the reaction time to 4 h caused the consumption of the small particles completely after Ostwald ripening, and pure hexagonal $NaGdF_4$ UCNPs were obtained in large sizes. As known, the excess of F^- facilitates the formation of the hexagonal $NaGdF_4$. Since the propagation of F^- ions slow in a viscose medium, the formation of cubic phase $NaGdF_4$ in a short time should be preferential.[131] The smaller size of these UCNPs compared with their counterparts synthesized using EtOH up to 3 h reaction time can also be attributed to the slow propagation of F^- ions since the excess of F^- leads to the enhancement of the aggregate size.[131]
Increasing the stirring speed (1000 rpm) and reaction temperature (200 °C) result in average particle size of about 100 nm. They are irregular shaped hexagonal UCNPs. The UCNPs capped AC are hexagon particles with an average particle size of 96±26 nm. The sample synthesized using glycerol (NaGd:Er_20min_G_1/3V) are formed as ill-shape UCNPs with an average particle size of 27±9 nm.

4.2.3 DLS

Except NaGd:Er_4h_(1:3:2) all UCNPs are stable in water by means of high Zeta potential (between 34 and 46 mV), as seen in table 4.1. NaGd:Er_3h is stable in water even after 1 month with a Zeta potential of about 35 mV. NaGd:Er_4h_(1:3:2) has an extremely low Zeta potential of -2.3±3.2 mV, which means that these UCNPs are not stable particles in water. If we consider the margin of errors, the values of the hydrodynamic diameters are associated well with average particle size for all samples.

Table 4.1: Obtained hydrodynamic diameters, particle sizes, and Zeta potential values of water soluble UCNPs in $NaGdF_4$ lattice calculated from DLS and TEM analysis.

Sample	R_H (DLS) [nm]	Zeta potential [mV]	R (SEM) [nm]
NaGd:Er_1h	99±29	39±5	99±34
NaGd:Er_2h	102±33 110±33 (20 days later)	34±5 39±7 (20 days later)	91±21
NaGd:Er_3h	94±25 92±26 (1 week later) 95±29 (1 month later)	34±7 34±6 (1 week later) 37±7 (1 month later)	99±32
NaGd:Er_4h	89±26	38±8	84±24
NaGd:Er_4h_(1:3:2)	234±96	-2.3±3.2	141±21
NaGd:Er_4h_(1.5:5:3)	116±38	36±6	109±34
NaGd:Er_4h_(1:4:3)	127±45	41±4	101±24
NaGd:Er_20min_EG	117±41	39±6	57±11
NaGd:Er_1h_EG	117±46	35±5	47±9
NaGd:Er_2h_EG	134±55	40±5	64±12
NaGd:Er_4h_EG	236±74	46±6	286±31
NaGd:Er_4h_AC	104±32	38±7	96±26
NaGd:Er_4h_1000rpm	102±35	40±5	105±28
NaGd:Er_4h_200°C	131±51	39±4	95±24
NaGd:Er_20min_EG_1/3V	-	-	38±12
NaGd:Er_20min_G_1/3V	-	-	27±9

4.3 Upconversion luminescence properties

4.3.1 UCL bands and decay kinetics of UCL of Er^{3+}

UCL spectra of all synthesized water-soluble samples were recorded in Milli-Q water upon 976 nm excitation wavelength. The spectral distribution of Er^{3+} emission bands appear with typical sharp Stark-splitting for hexagonal lattice, as Klier et. al. showed the spectral shape of Er^{3+} in $NaYF_4$ lattice after phase transition from cubic to hexagonal.[80] All samples exhibit three characteristic emission bands of Er^{3+} in at 527 nm (G1), 543 nm (G2) and 657 nm (R). Their corresponding transitions

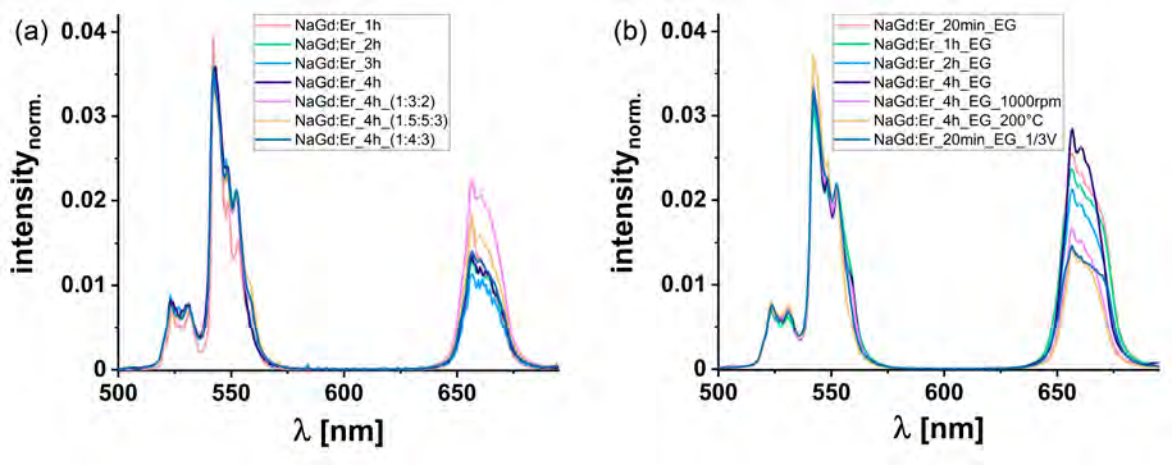

Figure 4.4: Normalized UCL spectra (to integrated intensity of G_T emission band) of UCNPs (a)NaGd:Er_1h, NaGd:Er_2h, NaGd:Er_3h, NaGd:Er_4h, NaGd:Er_4h_(1:3:2), NaGd:Er_4h_(1.5:5:3), NaGd:Er_4h_(1:4:3) (b) NaGd:Er_20min_EG, NaGd:Er_1h_EG, NaGd:Er_2h_EG, NaGd:Er_4h_EG, NaGd:Er_4h_EG_1000rpm, NaGd:Er_4h_EG_250°C, NaGd:Er_20min_EG_1/3V. All measurements carried out in Milli-Q water with experimental parameters: λ_{ex} = 976 nm, delay time after the laser pulse = 500 ns, gate width = 500 μs number of accumulations = 150 - 800.

are $^2H_{11/2} \rightarrow {}^4I_{15/2}$, $^4S_{3/2} \rightarrow {}^4I_{15/2}$ and $^4F_{9/2} \rightarrow {}^4I_{15/2}$, respectively.[84] As seen on the normalized UCL spectra (figure 4.4 (a)) relative R to G_T emission intensity remains almost constant for samples synthesized using EtOH with reaction times from 1 to 4 h. The highest relative intensity of R band belong to the sample NaGd:Er_4h_(1:3:2). For the samples synthesized using EG, the relative R to G_T emission intensity decreases with the increase of reaction time from 20 min to 3 h. It reaches the highest value at a reaction time of 4 h for sample NaGd:Er_4h_EG. Changing of stirring speed, reaction temperature, and the volume of reaction mixture cause a decrease in relative intensity of R emission band.

As seen in figure A.17, the highest relative intensity of R emission band in all samples was obtained using EG and 4 h reaction time. The spectral shapes of all samples are similar except samples synthesized with a reaction time of 4 h exhibiting a slightly shoulder at 559 nm. Looking at the XRD pattern, it can be argued that the pure hexagonal phase $NaGF_4$ crystal support red emission. As known, cross relaxation ($^4F_{7/2} + {}^4I_{11/2} \rightarrow {}^4F_{9/2} + {}^4F_{9/2}$) and depopulation of $^2H_{11/2} + {}^4S_{3/2}$ states of Er^{3+} lead to more intense red emission. The samples synthesized with a reaction time of 4 h can be more crystalline allowing cross relaxation for the benefit of the population of $^4F_{9/2}$ state.[86][108] The highest relative intensity of R band belong to the largest particles NaGd:Er_4h_(1:3:2) and NaGd:Er_4h_EG.

The emission spectra of samples NaGd:Er_1h, NaGd:Er_2h, NaGd:Er_3h, NaGd:Er_4h were recorded in a broader range between 320 and 890 nm. As seen in figure A.16, additionally the G1, G2 and R emission bands, the other emission bands of Er^{3+} centred at 380 nm ($^4I_{15/2} \rightarrow {}^4G_{11/2,\,9/2}$), 408 nm ($^4I_{15/2} \rightarrow {}^2H_{9/2}$) and

840 nm ($^4I_{15/2} \rightarrow {}^4I_{9/2}$) nm are apparent upon excitation at 976 nm.[70] The intensities of the $^4I_{15/2} \rightarrow {}^4G_{11/2,\,9/2}$ and $^4I_{15/2} \rightarrow {}^4I_{9/2}$ transitions are remarkably high for sample NaGd:Er_2h, which can be useful for bio-application, especially the transition $^4I_{15/2} \rightarrow {}^4I_{9/2}$ since this coincides with first biological window (650 – 950 nm).[132]

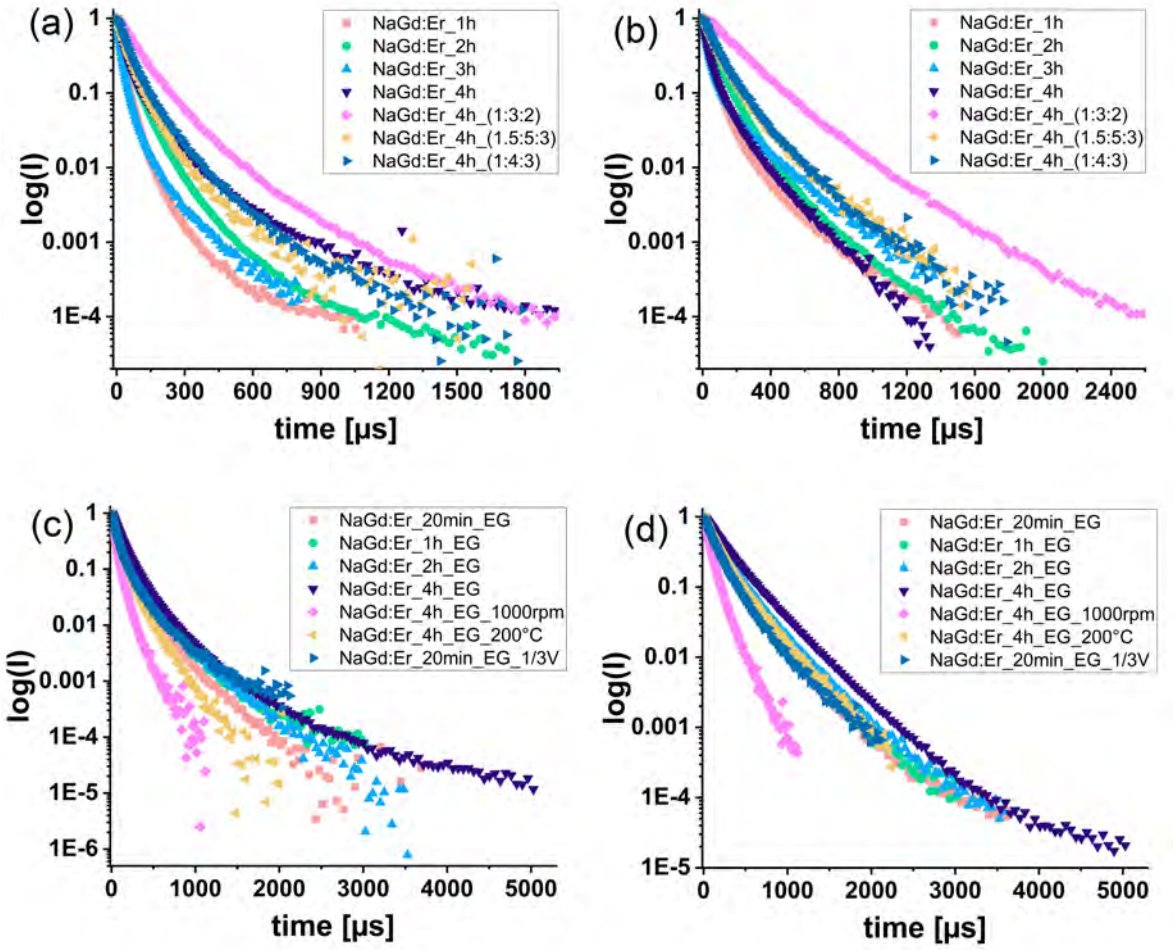

Figure 4.5: Normalized UCL decay kinetics of (a) the G_T (b) the R emissions of Er^{3+} for samples synthesized using EtOH. Normalized UCL decay kinetics of (c) the G_T (d) the R emissions of Er^{3+} for samples synthesized using EG. All measurements carried out in Milli-Q water with experimental parameters: $\lambda_{ex} = 976$ nm, delay time after the laser pulse = 500 ns, gate width = 500 μs number of accumulations = 120 - 200.

In figure 4.5 (a-d), normalized decay curves of G_T and R emission bands of samples synthesized using EtOH and EG are shown, respectively. The data for G_T and R emission bands of Er^{3+} were evaluated by fitting with biexponential decay kinetics for these samples. It is assumed that the short UCL decay time (τ_1) belongs to superficial Er^{3+} ions. Because surface defects and high vibrational surface-bound ligands lead these Er^{3+} ions to a non-radiative deactivation of excited state. Furthermore, the water as a solvent quenches strongly the luminescence of dopant ions due to its high energy (ca. 3500 cm^{-1}) of stretching vibration.[133] On the other hand, Er^{3+} ions in the bulk phase

have longer UCL decay time (τ_2) due to the shielding from quenchers.
As seen all samples synthesized below a reaction time of 4 h show a fast decay rate for G_T in samples synthesized in a medium containing EtOH. For R emission band, the decay rates are similar except for significantly slow decay rate of NaGd:Er_4h_(1:3:2). The decay rate of this sample is the slowest one for G_T and R emission bands, indicating the most crystalline UCNPs obtained with a long reaction time (4h) and with a higher concentration of capping agent (AcOH) compared with other samples synthesized using EtOH. The fraction of long-lived species of G_T and R bands increases with the increase of reaction time from 1 to 4 h (table 4.1). The decay time of long-lived species of Er^{3+} for the R band increases with increasing of the reaction time from 1 to 4 h, while that for the long-lived species of G_T band changes randomly. Because of the imperfect surface conditions, the random change of short decay species of Er^{3+} for both emission bands was expected. The alteration of the solvent ratio leads the particles to almost two times longer decay times. NaGd:Er_4h_(1:3:2) has the longest decay time for G_T (τ_1 = 91 μs and τ_2 = 239 μs) and for R (τ_1 = 210 μs and τ_2 = 552 μs) bands since it is the largest UCNPs in this set of samples. Interestingly this sample has drastically less amount of long-lived species (19% for G_T, 4% for R).
The fastest decay rate belongs to NaGd:Er_4h_EG_1000rpm (polydisperse, in irregular shape) and the slowest to NaGd:Er_4h_EG (large, in distinct shape) for G_T and R emission bands (figure 4 (c) and (d)) in the set of samples synthesized in a medium containing EG. The decay time of short- and long-lived Er^{3+} species of G_T and R emissions change according to their particle size (table 4.2) for reaction times between 20 min and 4 h. The larger the particles the longer the decay times. Interestingly the larger the particles the less the fraction of long-lived Er^{3+} species. The longest decay times of short- and long-lived species for G_T band belongs to the sample NaGd:Er_4h_EG (τ_1 = 112 μs and τ_2 = 315 μs). This sample have the decay time values of τ_1 = 225 μs and τ_2 = 403 μs for R band. The sample NaGd:Er_4h_200°C show a shorter decay time (τ_1 = 67 μs and τ_2 = 177 μs for G_T and τ_1 = 151 μs and τ_2 = 357 μs for R) than NaGd:Er_4h_EG. It could be expected that NaGd:Er_4h_200°C has longer decay times due to the high probability of formation of more crystalline particles and less defect in crystal lattice due to increased rection temperature to 200 °C. But here the particle sizes should be considered. Since average particle size of NaGd:Er_4h_EG almost 3 times larger than that of NaGd:Er_4h_200°C, its longer decay time for G_T and R emissions are reasonable.
Samples synthesized using EG show longer decay times compared with the samples synthesized using EtOH up to 3 h even average particle sizes of these UCNPs are smaller. Since surface to volume ratio is low for large UCNPs, it is expected the reduce surface-related quenching effects. Herein, we have to consider the particle shape. The UCNPs synthesized using EtOH exhibit a cloud-like shape (serrate surface), which have a much higher surface to volume ratio than that of smaller UCNPs. Decay times of R emission band are longer compared G_T emission for all samples. Besides, the fractions of long-lived species are less than that of short-lived species for all samples.

Table 4.2: UCL decay parameters of G_T and R emissions of Er^{3+} for all synthesized UCNPs.

Sample	G_T				R			
	τ_1[μs]	χ_1[%]	τ_2[μs]	χ_2[%]	τ_1[μs]	χ_1[%]	τ_2[μs]	χ_2[%]
NaGd:Er_1h	19	64	60±1	36	35	68	141±3	32
NaGd:Er_2h	34	61	94±1	39	62	69	165±3	31
NaGd:Er_3h	16	60	69±1	40	26	45	170±2	55
NaGd:Er_4h	21	54	94±1	46	37	44	181±2	56
NaGd:Er_4h_ (1:3:2)	91±1	81	239±13	19	210±3	96	552±141	4
NaGd:Er_4h_ (1.5:5:3)	39	61	110±3	39	75±1	63	211±5	37
NaGd:Er_4h_ (1:4:3)	47	63	135±4	37	77±1	58	197±7	42
NaGd:Er_20 min_EG	82±1	69	228±7	31	181±3	82	403±32	18
NaGd:Er_1h_ EG	72±1	47	209±3	53	166±4	62	335±13	38
NaGd:Er_2h_ EG	93±1	64	251±5	36	199±3	75	430±20	25
NaGd:Er_4h_ EG	112	74	315±6	26	225±5	54	403±11	46
NaGd:Er_4h_ AC	38	67	107±2	33	63±1	66	153±3	34
NaGd:Er_4h_ 1000rpm	39	66	107±3	34	71±1	58	174±10	42
NaGd:Er_4h_ 200°C	67±1	63	177±6	37	151±3	57	357±10	43
NaGd:Er_20 min_EG_1/3 V	46	40	186±3	60	124±3	52	301±9	48
NaGd:Er_20 min_G_1/3V	71±2	42	200±4	58	196±9	53	406±30	47

4.3.2 Power dependent UCL properties of Er^{3+}

Excitation-power-density-dependent measurements for four samples (NaGd:Er_1h, NaGd:Er_2h, NaGd:Er_3h, NaGd:Er_4h) were carried out to understand upconversion mechanism in water soluble UCNPs detailed. The power density dependent change of the UCL intensity of G_T, R, and NIR bands for sample NaGd:Er_4h are shown as in the example. The UCL intensity of these emission bands enhances with

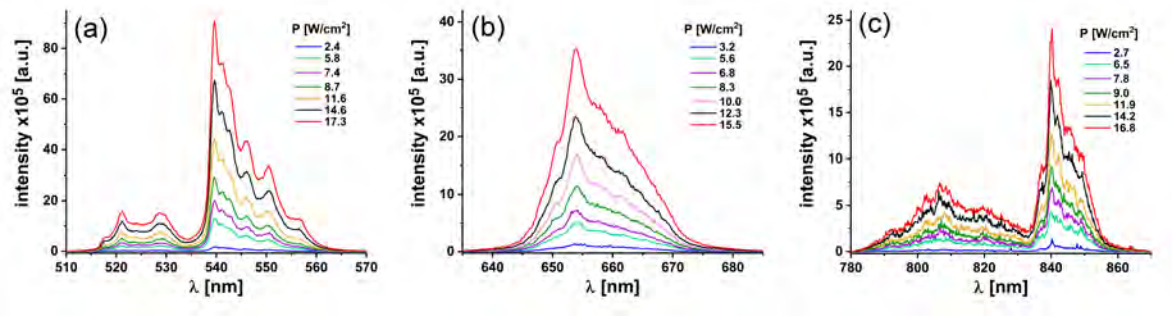

Figure 4.6: (a-c) UCL spectra of NaGd:Er_4h for G_T, R, and NIR emission bands dependent on the pump power density between 2.4 and 17.3 W/cm^2. All measurements carried out in Milli-Q water with experimental parameters: λ_{ex} = 976 nm, delay time after the laser pulse = 500 ns, gate width = 500 μs, number of accumulations = 150 - 200.

increasing of power density from 2.4 up to 17.3 W/cm^2 (figure 4.6 (a-c)). The double logarithmic plots of G1, G2, R, and NIR UCL intensities versus power density and the linear fits for the four samples mentioned above are presented in figure 4.7 (a). According to equation 2.7, the slopes of the plots give the number of photons used for G1, G2, R, and NIR UCL. In the relatively low power density range, the plots appeared linear as expected. Further, the n values obtained from slopes should lie about 2 since the UCNPs doped with a low amount of Er^{3+} (2 mol%) and Yb^{3+} (18 mol%).[80]

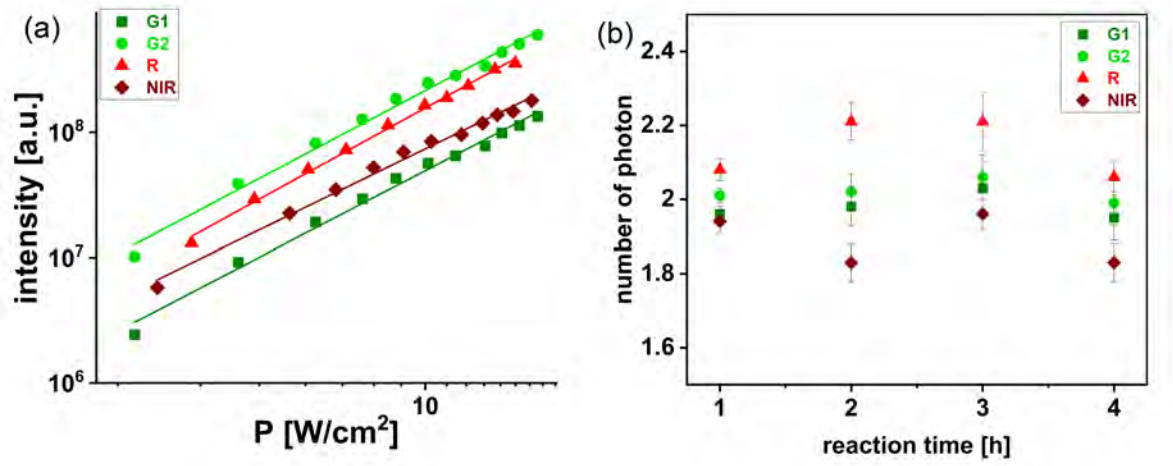

Figure 4.7: (a) The double logarithmic plots of G1, G2, R and NIR emission intensities of Er^{3+} versus pump power density for the sample NaGd:Er_4h (b)Number of photons for G1, G2, R and NIR emission bands of Er^{3+} for NaGd:Er_4h UCNPs.

As seen, G1, G2, R, and NIR emissions are involved with a 2 photon process (figure 4.7 (b)). The n values for G1, G2, R emission bands increase with the increase of reaction time up to 3 h. Further extending of reaction time leads to decrease n val-

ues of these bands. The particle sizes of NaGd:Er_1h, NaGd:Er_2h, NaGd:Er_3h similar; therefore, we can compare their properties considering the reaction time. The longer reaction time can lead UCNPs to a crystal structure with less defect. Thus, 3 photon process can also more often occur. However, the sample NaGd:Er_4h has a smaller n value for G1, G2, and R compared to other samples. The higher reaction time could bring a crystal structure with less defect, but smaller particle size means exposing to more quenching, especially by -OH stretching of water. For this reason, n values of G1, G2, and R could decrease. Energy back transfer from Er^{3+} to Yb^{3+} and cross relaxation between Er^{3+} ions or cooperative upconversion can also cause decreasing of n-values. Besides, n values of the NIR emission band change randomly with reaction time.

4.4 Conclusion

The morphologic and UCL properties of water-soluble, acetic acid capped UCNPs (additionally one sample capped with amino cellulose) were studied under various synthesis conditions. XRD, SEM, and DLS results clearly show the influences of the synthesis parameters on the particle morphology. All samples synthesized using EtOH resulted in a pure hexagonal phase $NaGF_4$:Yb^{3+}:Er^{3+} under each condition. In contrast, the samples synthesized using EG needed the increased reaction time from 20 min to 4 h for the phase transition from cubic to hexagonal. SEM results show that the average particle sizes of UCNPs synthesized using EG are smaller than the UCNPs synthesized using EtOH up to 3 h reaction time. The largest UCNPs were obtained using EG at 4 h reaction time and using EtOH at the same reaction time with H_2O:EtOH:AcOH ratio of 1:3:2, while the smallest UCNPs were produced using EG and G with a mixture volume of 1/3 and 20 min reaction time. The H_2O:EtOH:AcOH ratio can change particle size, shape, and colloidal stability drastically. Using viscose solvent EG, results in bimodal particle sizes, except samples synthesized for 4 h reaction time. The width of the reflection peaks of the samples, depending on the crystal type, are consistent with their average particle size. It was deduced that the high viscosity might be preferable for the formation of small cubic UCNPs at a short reaction time (1 - 3 h), whereas the low viscosity can result in pure hexagonal phase UCNPs with large particle size in a short reaction time (1 h). The relative R to G_T emission intensity of UCNPs alters depending on the reaction time, solvent, and capping agent ratio, type of solvent and capping agent. The highest τ_1 and τ_2 values for G_T band and the highest τ_1 for the R band belongs to sample synthesized with EG and at a reaction time of 4 h. The sample synthesized with a solvent capping agent ratio 1:3:2 has the highest τ_2 value for R band at a reaction time of 4 h. The longer reaction time supports the long decay time due to the emerging of crystals with less deactivation centers. The number of absorbing photons for the UCL mechanism of G1, G2, R and NIR emission bands are 2 for measured samples.

Chapter 5

Comparison of AA capped UCNPs using different host lattices: Yttrium vs Scandium lattice

5.1 Introduction

UCNPs synthesized by conventional methods are hydrophobic. Synthesis of hydrophilic UCNPs in one step is a new field and requires a lot of studies. The type and phase of host lattice of UCNPs is critical parameter, which effect on the UCL properties significantly. Hexagonal $NaYF_4$:Yb^{3+}:Er^{3+} offers about one order of magnitude enhancement of UCL efficiency relative to cubic $NaYF_4$:Yb^{3+}:Er^{3+}.[87] [88] The transition of cubic $NaYF_4$ to hexagonal $NaYF_4$ is possible raising the reaction temperature and time, sufficiently. Nevertheless, this induces obtaining undesirable aggregation and larger crystal size of UCNPs. As an alternative, many research groups have codoped the host lattice with various lanthanides (Gd^{3+}[90], Lu^{3+}[91]) or non-lanthanide ions (Mn^{2+}[92], Li^{+}[93], Fe^{3+}[94], Ca^{2+}[95]) in order to tailor the local symmetry environments of the rare earth ions in the host lattice. The high potential application of Na_xScF_{3+x} as a host lattice makes them noteworthy to study. The few studies about that lattice are related only to hydrophobic as-synthesized UCNPs.[96] [97] [98] [86] New studies are required to understand the properties of hydrophilic UCNPs in $NaYF_4$ and Na_xScF_{3+x} and the effect of the Gd^{3+} codoping on the host lattice as well as on the UCL properties. Codoping UCNPs with Gd^{3+} brings valuable advantages such as application of UCNPs in magnetic resonance imaging (MRI) and computed tomography (CT).[99]
In this chapter we demonstrate the effect of various concentration of Gd^{3+} ion on the crystal structure, morphology and photophysical properties of the acetic acid capped hydrophilic $NaYF_4$:Yb^{3+}:Er^{3+}:Eu^{3+} and Na_xScF_{3+x}:Yb^{3+}:Er^{3+}:Eu^{3+} UCNPs synthesized via microwave-assisted hydrothermal synthesis method, comparatively.
Four samples in $NaYF_4$ and four samples in Na_xScF_{3+x} host lattices were synthesized with an amount of 0, 7.5, 15 and 30 mol% Gd^{3+}, respectively. Gd^{3+} ions replace Y^{3+} (Sc^{3+}) with respect to desired Gd^{3+} content. The concentration of Yb^{3+} and Er^{3+} were kept stable at 18 mol% and 2 mol%, respectively. The samples were codoped additionally with 1 mol% of Eu^{3+} to analyze the structural change and speciation deeper.

After structural characterization, the intensity of green and red UCL, decay kinetics, and power dependent behaviours of UCL were intensely studied. We gained a detailed perspective about the change of the local symmetry environment by means of decay kinetic and TRANES results of Eu^{3+} ion.

5.2 Structural characterization

5.2.1 XRD

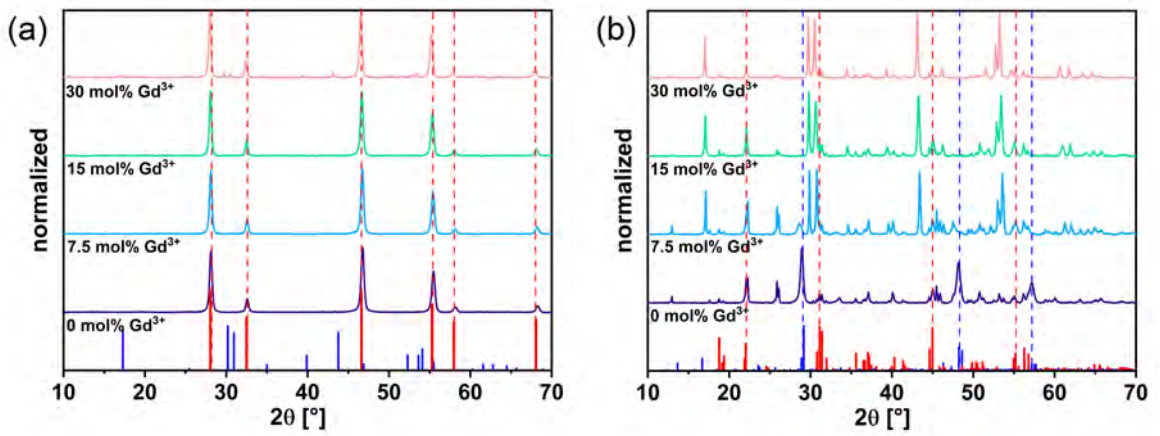

Figure 5.1: (a) X-ray diffraction patterns of A@NaY:$Gd_{0,7.5,15,30}$ (red columns belong to the standard XRD patterns of the cubic phase $NaYF_4$ (ICSD 77099) and blue columns to the hexagonal phase $NaYF_4$ (ICSD 51916)) (b) X-ray diffraction patterns of A@NaSc:$Gd_{0,7.5,15,30}$ (red columns belong to the standard XRD patterns of the monoclinic phase $NaScF_4$ (ICSD 400723) and blue columns to the hexagonal phase of Na_3ScF_6 (COD ID 1515376)).

The XRD patterns of UCNPs in $NaYF_4$ and Na_xScF_{3+x} lattices are shown in figure 5.1 (a) and (b), respectively. $NaYF_4$ lattice is found in cubic or hexagonal phase thermodynamically stable.[80] The normalized XRD patterns of UCNPs A@NaY:$Gd_{0,7.5,15,30}$ agreed well with the standard pattern of α - $NaYF_4$ (ICSD 77099). All samples in $NaYF_4$ without Gd^{3+} and with Gd^{3+} show strong diffraction peaks at 28.1°, 32.6°, 46.7°, 55.4°, 58.1°, 68.3° of the cubic phase. Only A@NaY:Gd_{30} has additional peaks on XRD pattern, which can be attributed to the β - $NaYF_4$ or hexagonal $NaGdF_4$. Since the Gd^{3+} concentration is high, some particles may be built up completely separated in hexagonal $NaGdF_4$ lattice or partially as a cluster of hexagonal $NaGdF_4$ in $NaYF_4$ lattice. The addition of Gd^{3+} leads the peak position at 46.7° ad 55.4° to the slightly shift to the lower angle. The value of the shift increases (0.05°, 0.07°, 0.1°) with increase of Gd^{3+} from 7.5 mol% to 30 mol%. This slightly shift proves that the increasing amount of Gd^{3+} lead the larger cell volume the sample due to the lager ionic radius of Gd^{3+} (0.938 Å) than that of Y^{3+} (0.90 Å). Besides, this result supports the interpretation, which suggests that the particles were formed from a mixed phase

of cubic $NaYF_4$ and hexagonal $NaGdF_4$. As expected, occupying the Y^{3+} sites from Gd^{3+} ions causes expand in lattice volume.[102] The alteration on the lattice unit cell parameter of $NaYF_4$ is slight and no phase transfer occurs due to the addition of Gd^{3+}. Na_xScF_{3+x} host lattice is stable in monoclinic or hexagonal phases thermodynamically. [96] As shown in figure 5.1 (b) the sample without Gd^{3+} exhibit strong diffraction peaks at 28.9°, 48.2° and 57.2° corresponding with hexagonal phase and at 22.1°, 22.3°, 31.1°, 45.1° and 55.1° corresponding with monoclinic phase. The intensity peaks at 28.9°, 48.2° and 57.2° decrease from 0 mol% to 7.5 mol% Gd^{3+} and disappear with further increasing of Gd^{3+} content. The peaks at 17.1, 29.9°, 30.8°, 43.4° and 53.6° belong to $NaGdF_4$ lattice, which appear on the diffraction pattern of samples doped Gd^{3+}. In sample A@NaSc:Gd_{30} it is observed only weak peaks of monoclinic Na_xScF_{3+x}, while diffraction peaks of $NaGdF_4$ are dominant for this sample. These results show that some UCNPs in samples doped Gd^{3+} are found completely in $NaGdF_4$ lattice or as a cluster of hexagonal $NaGdF_4$ in Na_xScF_{3+x} crystal. 0.2° shift of peaks of hexagonal Na_xScF_{3+x} are observed when changing the Gd^{3+} amount from 0 mol% to 7,5 mol%. No further shift was observed with addition of more Gd^{3+}. Normally, it is expected strong shift to the lower angle due to the large ionic radius of Gd^{3+} (0.938 Å). Its larger ionic radius compared to Sc^{3+} (0.75 Å) could lead to an expansion of the unit cell parameters of Na_xScF_{3+x}.[102] Maybe small amount of Gd^{3+} locate in Na_xScF_{3+x} lattice and the high amount of Gd^{3+} is used to build up UCNPs in only $NaGdF_4$ lattice. The other reason could be the heterogenous distribution of Gd^{3+} in Na_xScF_{3+x} causing like two different crystal in one UCNP.
Gd^{3+} caused an alteration and expand in unit cell parameter of cubic $NaYF_4$, while it leads to a mixed phase of Na_xScF_{3+x} to another mixed phase of monoclinic Na_xScF_{3+x} and hexagonal $NaGdF_4$. The reason of this could be the relative homogenous distribution of Gd^{3+} in UCNPs A@NaY:$Gd_{0,7.5,15,30}$ due to the similar ionic radius, while a relative distribution of Gd^{3+} is heterogenous in Na_xScF_{3+x}.

5.2.2 SEM

The sizes and crystal structures of the synthesized nanoparticles A@NaY:$Gd_{0,7.5,15,30}$ and A@NaSc:$Gd_{0,7.5,15,30}$ were characterized by SEM. Figure 5.2 (a) and (b) show the SEM image (SEM2) of A@NaY:Gd_{30} and its corresponding particle size distribution histogram, respectively. The particles are spherical with a high particle size distribution. The huge structure on the image could have remained organic structures since there is no additional narrow peaks of other crystal structures on the XRD pattern. As known, the electron density of the carbon atom is low for SEM measurements and the high accelerating voltages cause beam damage on the organic material. For these reasons, the record of SEM images of organic structures is difficult. Nevertheless, dense or accumulated organic structures can still be seen by SEM even with damages. The average particle size of that sample is 63±24 nm(table 5.1). The other UCNPs in set of A@NaY:$Gd_{0,7.5,15,30}$ have also spherical shape (figure A.20). The average particle sizes of A@NaY:$Gd_{0,7.5,15}$ are 76±26 nm, 47±18 nm, 51±9 nm, respectively. The addition of 7.5 mol% Gd^{3+} leads particle to a smaller average particle size, while this value slightly increases with further addition of Gd^{3+} (15 mol% and 30 mol%). It is seen

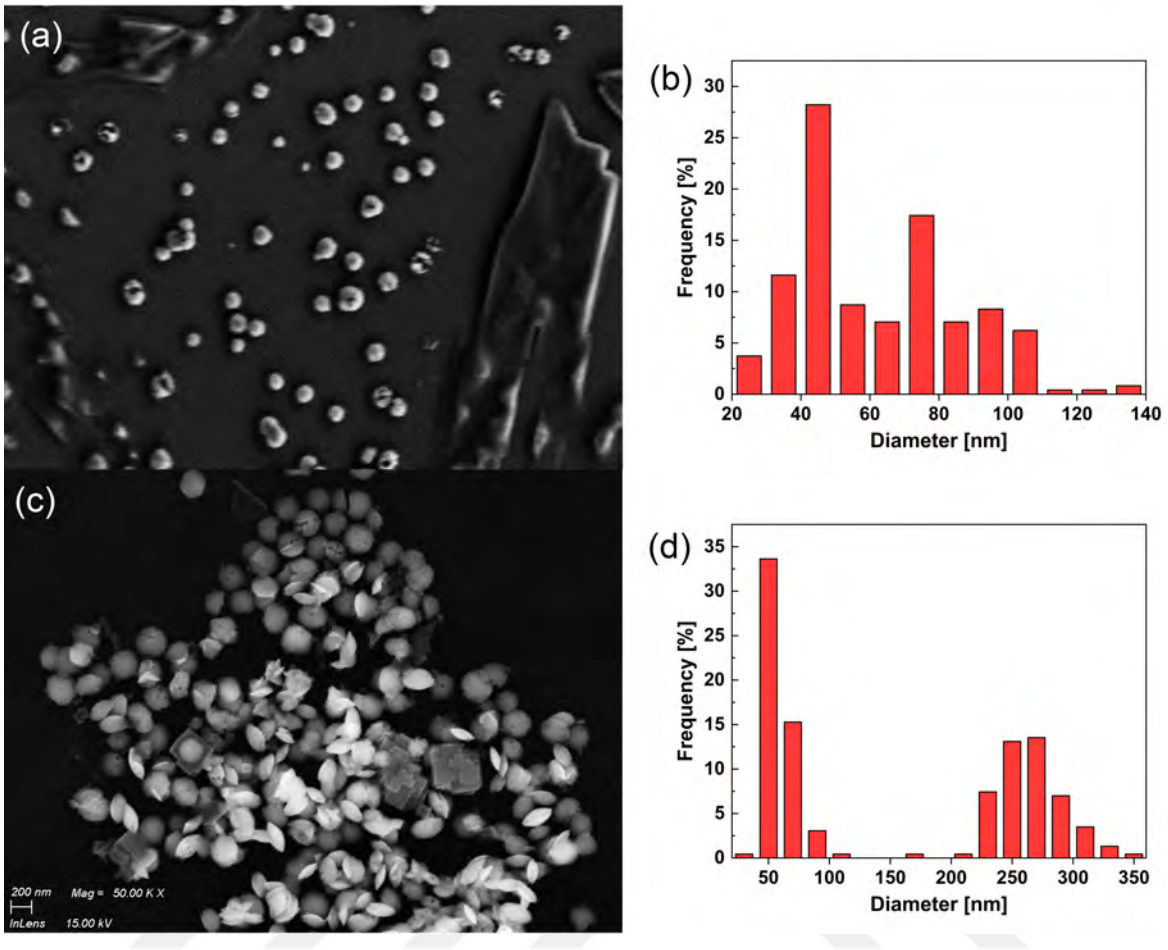

Figure 5.2: (a) SEM images of A@NaY:Gd_{30} UCNPs with a scale bar = 200 nm (b) Particle size distribution histogram of A@NaY:Gd_{30} according to SEM (c) SEM images of A@NaSc:Gd_{30} UCNPs with a scale bar = 200 nm (d) Particle size distribution histogram of A@NaSc:Gd_{30} according to SEM.

that the particle size distribution narrows with the increase of Gd^{3+} from 7.5 mol% to 30 mol%.

The lentil like and cubic crystals in sample A@NaSc:Gd_{30} are seen on the SEM image (figure 5.2 (c)). Its particle size distribution histogram (figure 5.2 (d)) shows that UCNPs growth in two different range of particle size. The average particle size of smaller UCNPs is 60±11 nm, while it is 266±27 nm for larger UCNPs of that sample. The shape of UCNPs for samples A@NaSc:Gd_0 and A@NaSc:Gd_{15} is spherical, while the sample A@NaSc:$Gd_{7.5}$ show again lentil like and cubic crystals (figure A.21). A@NaSc:$Gd_{7.5}$ show a bimodal particle size distribution with average particle size of 65±15 nm for small UCNPs and of 353±20 nm for large UCNPs. UCNPs without Gd^{3+} has an average particle size of 56±19 nm, while UCNPs with 15 mol% Gd^{3+} has 75±18 nm average particle size. SEM records show that the average particle sizes of UCNPs in $NaYF_4$ and average particle sizes of small UCNPs in Na_xScF_{3+x} are similar. Large UCNPs in Na_xScF_{3+x} with 7.5 mol% Gd^{3+} and 30 mol% Gd^{3+} could be UCNPs

in $NaGdF_4$, since their strong and sharp reflexion peaks indicate large crystal size.

Table 5.1: Obtained average particle sizes of AcOH capped hydrophilic UCNPs in $NaYF_4$ and Na_xScF_{3+x} using SEM results.

	Y^{3+} host lattice				Sc^{3+} host lattice			
Gd^{3+} [mol%]	0	7.5	15	30	0	7.5	15	30
R (SEM) [nm]	76±26	47±18	51±9	63±24	56±19	353±20 65±15	75±18	266±27 60±11

5.3 Upconversion luminescence properties

5.3.1 UCL bands and decay kinetics of UCL of Er^{3+}

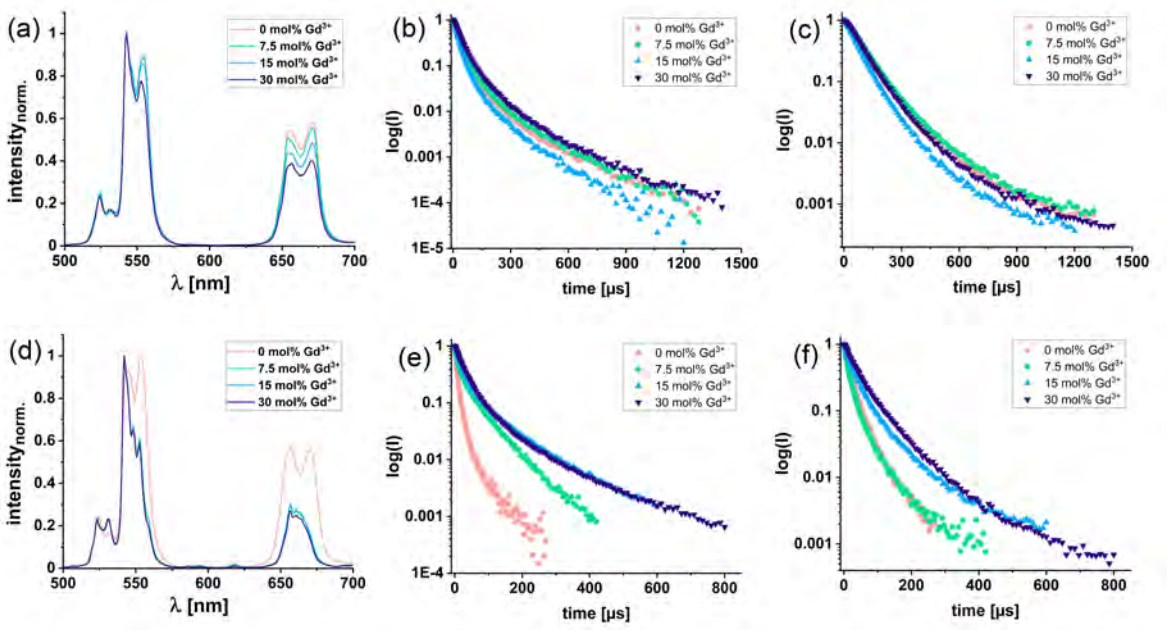

Figure 5.3: (a) Normalized UCL spectra of the A@NaY:$Gd_{0,7.5,15,30}$ UCNPs. Normalized UCL decay kinetics of (b) the G_T (c) the R emissions of Er^{3+} for A@NaY:$Gd_{0,7.5,15,30}$ (d) Normalized UCL spectra of the A@NaSc:$Gd_{0,7.5,15,30}$ UCNPs. Normalized UCL decay kinetics of (e) the G_T (f) the R emissions of Er^{3+} for A@NaY:$Gd_{0,7.5,15,30}$. All measurements carried out in Milli-Q water with experimental parameters: $\lambda_{ex} = 976$ nm, exposure time = 0.017 secs, delay time after the laser pulse = 500 ns, gate width = 500 μs, number of accumulations = 1000 (steady state) and 100-200 (time resolved).

The normalized emission spectra of A@NaY:$Gd_{0,7.5,15,30}$ and A@NaSc:$Gd_{0,7.5,15,30}$ UCNPs are shown in figure 5.3 (a) and (d), respectively. The emission band centered

at 528 nm, 550 and nm 663 belong to G1, G2, and R, respectively. G1 depicts $^2H_{11/2} \rightarrow {}^4I_{15/2}$ transition, G2 $^4S_{3/2} \rightarrow {}^4I_{15/2}$ transition (both = G_T) and R $^4F_{9/2} \rightarrow {}^4I_{15/2}$ transition of Er^{3+} ion.[84] The shape of emission bands are similar for A@NaY:$G_{d0,7.5,15,30}$ samples, indicating the similar site symmetry around Er^{3+}. The shape of G_T and R emission bands are typical for Er^{3+} ions in a cubic crystal lattice.[80] The R to G_T UCL intensity ratios decrease slightly with the increasing of Gd^{3+} concentration from 0 mol% to 30 mol%, indicating a small alteration of the local symmetry of Er^{3+}.
The spectral shape of NaSc:Gd_0 change totally after adding 7.5 mol% of Gd^{3+}. Furthermore, the width of G2 and R emission bands of NaSc:Gd_0 decrease with 7.5 mol% of Gd^{3+}. There is no further change on the spectral shape and width with increasing of Gd^{3+}. The significant change of the spectral shape from no Gd^{3+} to with Gd^{3+} show a considerable change of the site symmetry of Er^{3+}. These results agreed well with XRD patterns, on which appears the strong reflection peaks of hexagonal $NaGdF_4$ lattice. The R to G_T UCL intensity ratio decreases drastically from no Gd^{3+} to with 7.5 mol% Gd^{3+}. It stays stable with further adding of Gd^{3+}.
It is seen clearly that the green emission is dominant for both set of samples. At the same time, it should be considered that the ionic radius of Gd^{3+} is larger than that of Y^{3+} and Sc^{3+}, which lead the increase the distance between ions. The reason of decrease of relative intensity of R emission can be the increase of the distance between ions, since the larger distance reduce the cross relaxation ($^4F_{7/2} + {}^4I_{11/2} \rightarrow {}^4F_{9/2} + {}^4F_{9/2}$) and depopulation of $^2H_{11/2} + {}^4S_{3/2}$ states of Er^{3+}.[86] The decrease of probability of the population of $^4F_{9/2}$ state through cross relaxation with increasing of Gd^{3+} lead to decrease of relative intensity of R emission.
For analysis of the decay kinetics of G_T and R emission bands, all decay curves were fitted according to biexponential decay kinetics. The Er^{3+} ions near or on the surface lost their energy due to non-radiative deactivation by surface defects, high vibrational states of surface bound ligands and solvent molecules, in our case, strong -OH vibration of water. Thus, superficial Er^{3+} ions show a short UCL decay time (τ_1). On the contrary, it is expected from the relative sheltered Er^{3+} ions in the bulk phase that they have a longer UCL decay time (τ_2).[106] [99] The UCL decay curves of G_T and R emission bands of Er^{3+} for A@NaY:$Gd_{0,7.5,15,30}$ are shown in figure 5.3 (b) and (c), respectively. Both emission bands of all samples with and without Gd^{3+} show similar decay behaviour.
On the other hand the UCL decay curves of G_T and R emission bands of A@NaSc:$Gd_{0,7.5,15,30}$ UCNPs (in figure 5.3 (e) and (f) respectively) exhibit differences. The fast UCL decay of G_T and R emission slow down from 0 mol% Gd^{3+} to 30 mol% of Gd^{3+}, gradually.

Table 5.2: UCL decay parameters of G_T emissions of Er^{3+} in UCNPs codoped with Gd^{3+}.

mol% Gd^{3+}	Y^{3+} host lattice				Sc^{3+} host lattice			
	τ_1[µs]	χ_1[%]	τ_2[µs]	χ_2[%]	τ_1[µs]	χ_1[%]	τ_2[µs]	χ_2[%]
0	33	75	130±3	25	6	69	27±0.9	31
7.5	36	76	150±4	24	9	24	56	76
15	27	77	115±3	23	19	42	90±1	58
30	40	71	146±3	29	25	55	100±2	45

Table 5.3: UCL decay parameters of R emissions of Er^{3+} in UCNPs codoped with Gd^{3+}.

mol% Gd^{3+}	Y^{3+} host lattice				Sc^{3+} host lattice			
	τ_1[µs]	χ_1[%]	τ_2[µs]	χ_2[%]	τ_1[µs]	χ_1[%]	τ_2[µs]	χ_2[%]
0	80±1	84	210±17	16	13	38	38±1	62
7.5	88±1	88	262±40	12	12	49	46±1	51
15	66	83	160±10	17	26	51	81±2	49
30	82±1	89	230±26	11	33	46	88±2	54

The short and long decay times of G_T and R emission for A@NaY:$Gd_{0,7.5,15,30}$ UCNPs (table 5.2 and 5.3) increase first with changing the concentration of Gd^{3+} from 0 mol% to 7.5 mol%. After decreasing with addition of 15mol% Gd^{3+}, the τ_1 and τ_2 values increase again with enhancement of Gd^{3+} content up to 30 mol%. The decay times of long-lived Er^{3+} species for A@NaY:Gd7.5 and A@NaY:Gd_{30} could be enhanced due to the slower energy transfer from Yb^{3+} to Er^{3+} because of the increased distance between them with addition of Gd^{3+}. However, the reason of the decreased decay time of G_T and R emissions for A@NaY:Gd_{15} could be the relative inhomogeneous site of Er^{3+} ions and more deactivation centres in that sample compared to other samples in $NaYF_4$ lattice. The fractions of short-lived species of G_T and R emissions are much less than that of long-lived species for all samples in $NaYF_4$ lattice, indicating the high amount of Er^{3+} in a high symmetry site.
The gradually increase of decay times of short- and long-lived species for G_T and R bands with the increasing amount of Gd^{3+} is observed for samples A@NaSc:$Gd_{0,7.5,15,30}$ (table 5.2 and 5.3). The fraction values of samples in Na_xScF_{3+x} lattice alters randomly due to the bimodal character of samples A@NaSc:$Gd_{7.5}$ and A@NaSc:Gd_{30}.

The τ_1 and τ_2 values of R emission are higher than those of G_T emission for all samples in $NaYF_4$ and in Na_xScF_{3+x} lattice due to the requirement of more relaxation processes of R band and the contribution of three photon process to this band. The samples A@NaSc:$Gd_{0,7.5,15,30}$, despite their relative large average particle sizes show lower decay times τ_1 and τ_2 for G_T and R emission bands than the samples A@NaY:$Gd_{0,7.5,15,30}$.

5.3.2 Power dependent UCL properties of Er^{3+}

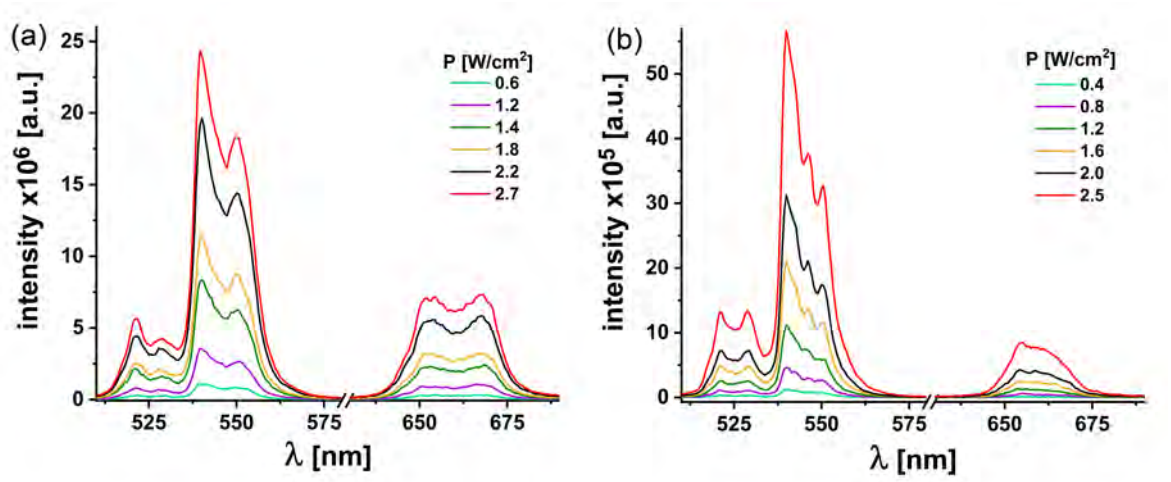

Figure 5.4: (a) UCL spectra of A@NaY:Gd_{30} (b) UCL spectra of A@NaSc:Gd_{30} dependent on the pump power density between 0.4 and 2.7 W/cm^2. All measurements carried out in Milli-Q water with experimental parameters: λ_{ex} = 976 nm, exposure time = 0.017 secs, delay time after the laser pulse = 500 ns, gate width = 500 μs, number of accumulations = 1000 (A@NaY:Gd_{30}) and 600 (A@NaSc:Gd_{30}).

In order to reveal the UC mechanism, the excitation power density dependence of G1, G2, and R emissions were investigated. The increase of the intensity of G_T and R emissions with increasing of power density from 0.4 to 2.7 W/cm^2 is shown for UCNPs A@NaY:Gd_{30} and A@NaSc:Gd_{30} exemplarily in figure 5.4 (a) and (b), respectively. Since the pump power is relatively low, it is expected that the number of pump photons involved in the excitation process is approximately equal to the n-values (equation 2.7).[110] [111] The linear curve fittings in the double logarithmic plot of G1, G2 and R UCL intensity against excitation power density of samples A@NaY:Gd_{30} and A@NaSc:Gd_{30} are shown in figure 5.5 (a) and (b) respectively. The slopes show linearity in a low range of excitation power density. The number of photons needed for G1, G2 and R emissions for the samples A@NaY:$Gd_{0,7.5,15,30}$ and A@NaSc:$Gd_{0,30}$ lie 2, since the concentration of Er^{3+} and Yb^{3+} is low in our samples (figure 5.6 (a) and (b)).
As seen in figure 5.6 (a), the n values for G1, G2, and R bands of A@NaY:Gd_0 are slightly over 2. After adding 7.5 mol% of Gd^{3+}, these values decrease below 2 and increase again with further adding of Gd^{3+}.
The slope factors of G1, G2 and R are below 2 for A@NaSc:Gd_0, while they lie over 2

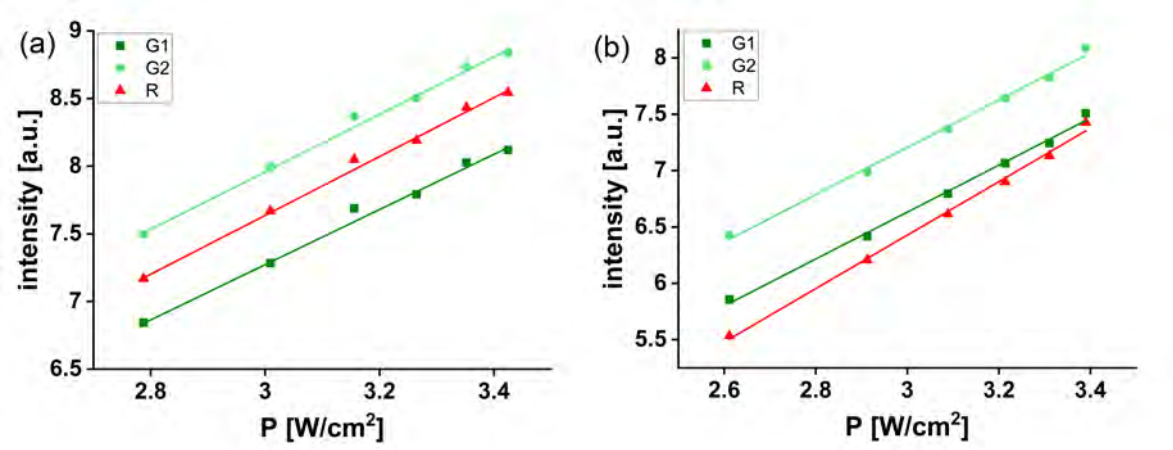

Figure 5.5: The double logarithmic plots of G1, G2 and R emission intensities of Er^{3+} versus pump power density for the samples (a)A@NaY:Gd_{30} (b)A@NaSc:Gd_{30}.

for A@NaSc:Gd_{30} (figure 5.10 (b)). No power density dependent measurements were carried out for samples A@NaSc:$Gd_{7.5}$ and A@NaSc:Gd_{15}.
The values below 2 obviously show the high non-radiative relaxation due to deactivation centres in the crystal. The other reason could be energy back transfer from Er^{3+} to Yb^{3+} or cooperative upconversion.

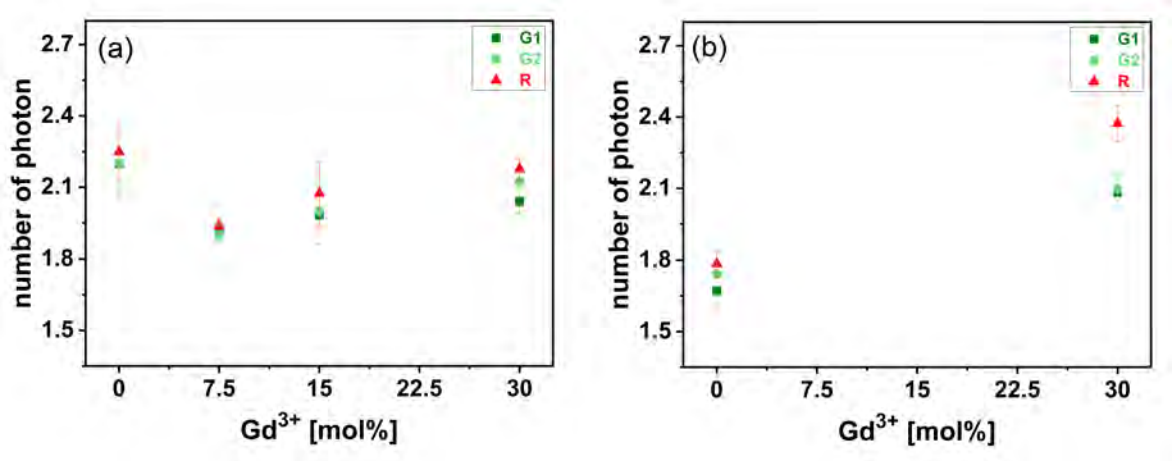

Figure 5.6: Number of photons for G1, G2, and R emission bads of Er^{3+} for UCNPs in (a) $NaYF_4$ and (b) Na_xScF_{3+x} lattices.

5.4 Luminescence properties of Eu^{3+} at RT

The steady state spectra of Eu^{3+} for the A@NaY:$Gd_{0,7.5,15,30}$ and A@NaSc:$Gd_{0,7.5,15,30}$ samples was investigated from a solution of the UCNPs dispersed in water. The luminescence spectra are recorded at RT upon excitation at 464.1 nm. The normalized

emission spectra to the integrated intensity of $^5D_0 \rightarrow {}^7F_1$ transition are shown in figure 5.7. The emission bands centred at 579 nm, 590 nm and 614 nm belong to the transitions $^5D_0 \rightarrow {}^7F_0$, $^5D_0 \rightarrow {}^7F_1$, $^5D_0 \rightarrow {}^7F_2$, respectively. The spectral intensity dis-

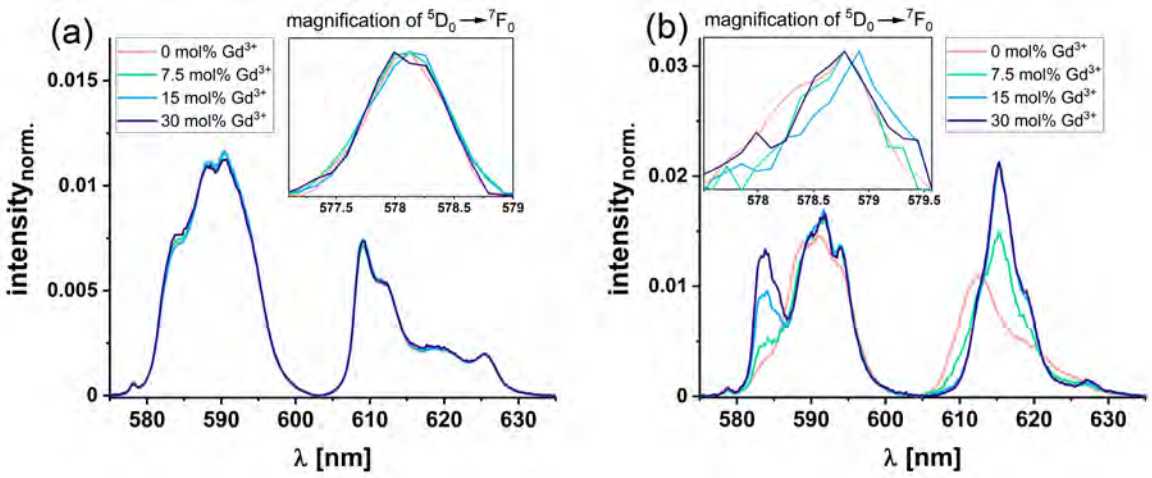

Figure 5.7: To MD transition normalized luminescence spectra of Eu^{3+} upon 464.1 nm excitation for the samples (a) A@NaY:$Gd_{0,7.5,15,30}$ (b) A@NaSc:$Gd_{0,7.5,15,30}$. All measurements carried out in Milli-Q water with experimental parameters: exposure time = 0.036 – 0.05 secs, delay time after the laser pulse = 50 μs, gate width = 500 μs, number of accumulations = 100 – 200.

tribution of samples in $NaYF_4$ lattice stays almost constant with and without Gd^{3+}. There is no obvious shift of maximum of $^5D_0 \rightarrow {}^7F_0$ transition, indicating that the increasing amount of Gd^{3+} show no observable effect on the crystal field strength in $NaYF_4$ crystal. The dominant emission band of the $^5D_0 \rightarrow {}^7F_1$ transition often indicates that the Eu^{3+} ions lie in centrosymmetrical sites.[69] [72] On the other hand, the observation of the emission band of $^5D_0 \rightarrow {}^7F_0$ transition is an indication that the symmetry at the location of Eu^{3+} ions is low and to be among the point groups C_{nv}, C_n or C_s.[69] This meant that at least one Eu^{3+} species is in a cubic or approximately cubic symmetry site. The XRD reflexes revealed that the samples A@NaY:$Gd_{0,7.5,15,30}$ are in pure cubic phase agree well with this result. There are two Stark-splitting on the $^5D_0 \rightarrow {}^7F_1$ transition band and four on the hypersensitive $^5D_0 \rightarrow {}^7F_2$ transition for all samples A@NaY:$Gd_{0,7.5,15,30}$. Samples in $NaYF_4$ lattice show also the band of $^5D_1 \rightarrow {}^7F_3$ transition at 584 nm indicated by disappearing of that band at a delay time of 1.28 ms.

The spectral distribution of NaSc:Gd_0 UCNPs alters strongly with addition of 7.5 mol% of Gd^{3+} and it continuous to alter with further addition of Gd^{3+} for samples synthesized in Na_xScF_{3+x} lattice. The blue-shift of the maximum of $^5D_0 \rightarrow {}^7F_0$ transition occurs with addition of 15 mol% Gd^{3+}, while a nephelauxetic behaviour takes place at 30 mol% of Gd^{3+}. The blue-shift show a weak crystal field in site of Eu^{3+} in A@NaSc:Gd_{15} UCNPs. The enhancement of the emission intensity of $^5D_0 \rightarrow {}^7F_2$ transition relatively to the $^5D_0 \rightarrow {}^7F_1$ transition with the increasing of Gd^{3+} content results from a transition of the site of Eu^{3+} to the lower symmetry. The intensity of

the emission band located at 583 nm attributed the $^5D_1 \rightarrow {}^7F_3$ transition increases with increasing of Gd^{3+} concentration for samples in Na_xScF_{3+x} lattice. The emission band of this transition disappeared at a delay time of 138 μs. This transition has a short luminescence. This change signifies that the more amount of Gd^{3+} leads to more deterioration of the Na_xScF_{x+3} crystal lattice as well as higher distortion around the Eu^{3+} ions (new symmetry site). Since the $^5D_0 \rightarrow {}^7F_0$ transition is observable for samples A@NaSc:$Gd_{0,7.5,15,30}$, these have Eu^{3+} ions in low symmetry site.

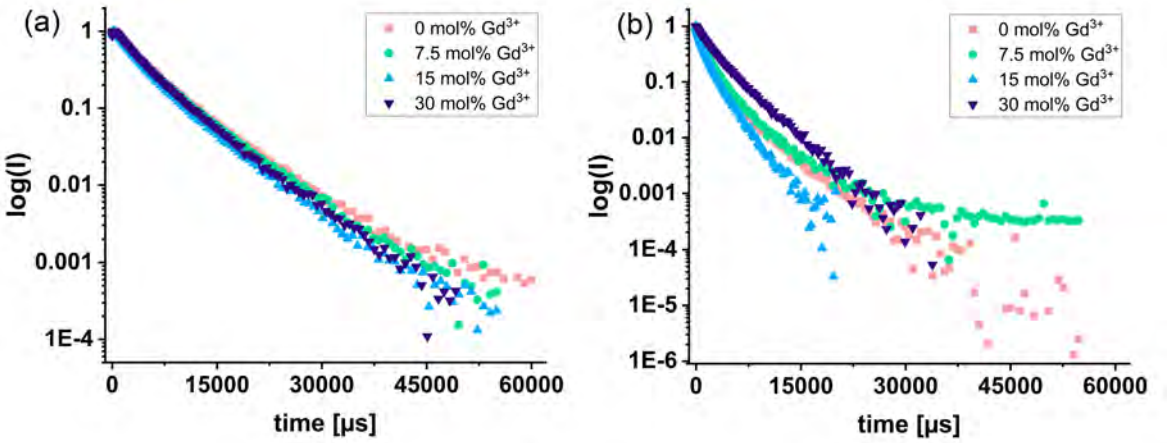

Figure 5.8: Luminescence decay curves of $^5D_0 \rightarrow {}^7F_1$ and $^5D_0 \rightarrow {}^7F_2$ transitions of Eu^{3+} for tha samples (a) A@NaY:$Gd_{0,7.5,15,30}$ (b) A@NaSc:$Gd_{0,7.5,15,30}$. All measurements carried out in Milli-Q water with experimental parameters: λ_{ex} = 464.1 nm, exposure time = 0.036 – 0.061 secs, delay time after the laser pulse = 500 ns, gate width = 500 μs, number of accumulations = 100 – 200

Figure 5.8 (a) and (b) show the decay curves of the ED and MD emission bands for samples A@NaY:$Gd_{0,7.5,15,30}$ and A@NaSc:$Gd_{0,7.5,15,30}$, respectively. The luminescence decay kinetics of Eu^{3+} in all samples were inversigated using biexponential global fit model for the $^5D_0 \rightarrow {}^7F_1$ and $^5D_0 \rightarrow {}^7F_2$ transitions.
The decay behaviours of Eu^{3+} for samples in $NaYF_4$ are similar in all concentrations of Gd^{3+} as observed for Er^{3+} in these samples. The shortest decay time of short- and long-lived species of Eu^{3+} (2178 and 6120 μs, respectively) belong to the A@NaY:Gd_{15}, which also has the shortest short- and long-lived Er^{3+} species for G_T and R bands. The τ_1 and τ_2 values of other samples decrease slightly from 2596 μs to 2178 μs and from 6890 μs to 6120 μs, respectively, with increasing of Gd^{3+} concentration up to 15 mol%. The decrease of the decay times shows that the increasing the Gd^{3+} content causes environmental change such as alteration of interatomic distances, structural defects and the introduction of charges. The values increase with addition of 30 mol% Gd^{3+} indicating higher symmetry in the site of Eu^{3+} ions. The short-lived Eu^{3+} species are about 28% while the long-lived species are about 72% in all samples A@NaY:$Gd_{0,7.5,15,30}$.
In the set A@NaSc:$Gd_{0,7.5,15,30}$ the decay bahaviours are similar. The shortest decay time of short- and long-lived species of Eu^{3+} (401 and 2035 μs, respectively) belong to the A@NaSc:Gd_{15}. This result agreed well with the appeared blue-shift of maximum

of $^5D_0 \rightarrow {}^7F_0$ transition. The τ_2 value decrease first from 3373 μs to 2035 μs with increasing of Gd^{3+} concentration from 0 to 15 mol%, while it increases to 3479 μs with addition of 30 mol% of Gd^{3+}. The fraction of short-lived species decreases obviously, while this increases for long-lived species with enhancement of Gd^{3+} content. This implies that the Gd^{3+} addition provide more crystalline environment for Eu^{3+} ions. The long decay times of Eu^{3+} ions for A@NaSc:Gd_{30} show that the alteration to the high symmetry site of Eu^{3+} in the crystal lattice occurs by addition 30 mol% of Gd^{3+}, so that the radiative emission from $^5D_0$ state is supported.
The luminescence decay times of the short- and long-lived Eu^{3+} species in Na_xScF_{3+x} lattice are significantly lower than these in $NaYF_4$ lattice. This can be attributed the relatively strong crystal field in site of Eu^{3+} (high symmetry site) in $NaYF_4$ lattice than in Na_xScF_{3+x} lattice providing longer decay time. The maximum of the $^5D_0 \rightarrow {}^7F_0$ transition in $NaYF_4$ lie at a shorter wavelength indicating the higher symmetry of $NaYF_4$ than Na_xScF_{3+x}. Because of the low emission intensity of $^5D_0 \rightarrow {}^7F_0$ transition, it is difficult to argue about the emerging of narrowness and asymmetry of that emission band relating to the amount of Gd^{3+}in UCNPs.

Table 5.4: Luminescence decay parameters of Eu^{3+} for UCNPs under pulsed wave excitation of 464.1 nm at RT

mol% Gd^{3+}	Y^{3+} host lattice				Sc^{3+} host lattice			
	τ_1[µs]	χ_1[%]	τ_2[µs]	χ_2[%]	τ_1[µs]	χ_1[%]	τ_2[µs]	χ_2[%]
0	2596±56	28	6890±69	72	751±11	39	3373±40	61
7.5	2553±56	27	6667±68	73	836±21	36	3224±56	64
15	2178±35	28	6120±44	72	401±15	16	2035±27	84
30	2445±53	28	6414±61	72	796±30	9	3479±30	91

In order to have a deep understanding of the influence of different dopping levels of Gd^{3+} on the crystal structure, the change of the spectral signature of the emission spectrum of Eu^{3+} with increasing delay time (TRANES) was analyzed. In figure 5.9 (a) and (b), the TRANES of samples A@NaY:$Gd_{0,7.5}$ and A@NaSc:$Gd_{0,7.5}$ are shown exemplarily. Two small Stark-splitting of $^7F_1$ state and four small Stark-splitting of $^7F_2$ state are observable for samples A@NaY:$Gd_{0,7.5,15,30}$ (A.26) . The emission band at about 583 nm disappeared with increasing of the delay time, signifying that this band belong to short lived $^5D_1 \rightarrow {}^7F_3$ transition. Except the change of the emission band of $^5D_1 \rightarrow {}^7F_3$ transition, there is no change on the spectral shape of Eu^{3+} in $NaYF_4$ lattice with different Gd^{3+} concentrations. Considering the low amount of the short-lived Eu^{3+} species, it can be said that the contribution of this species is not distinguished on the TRANES.

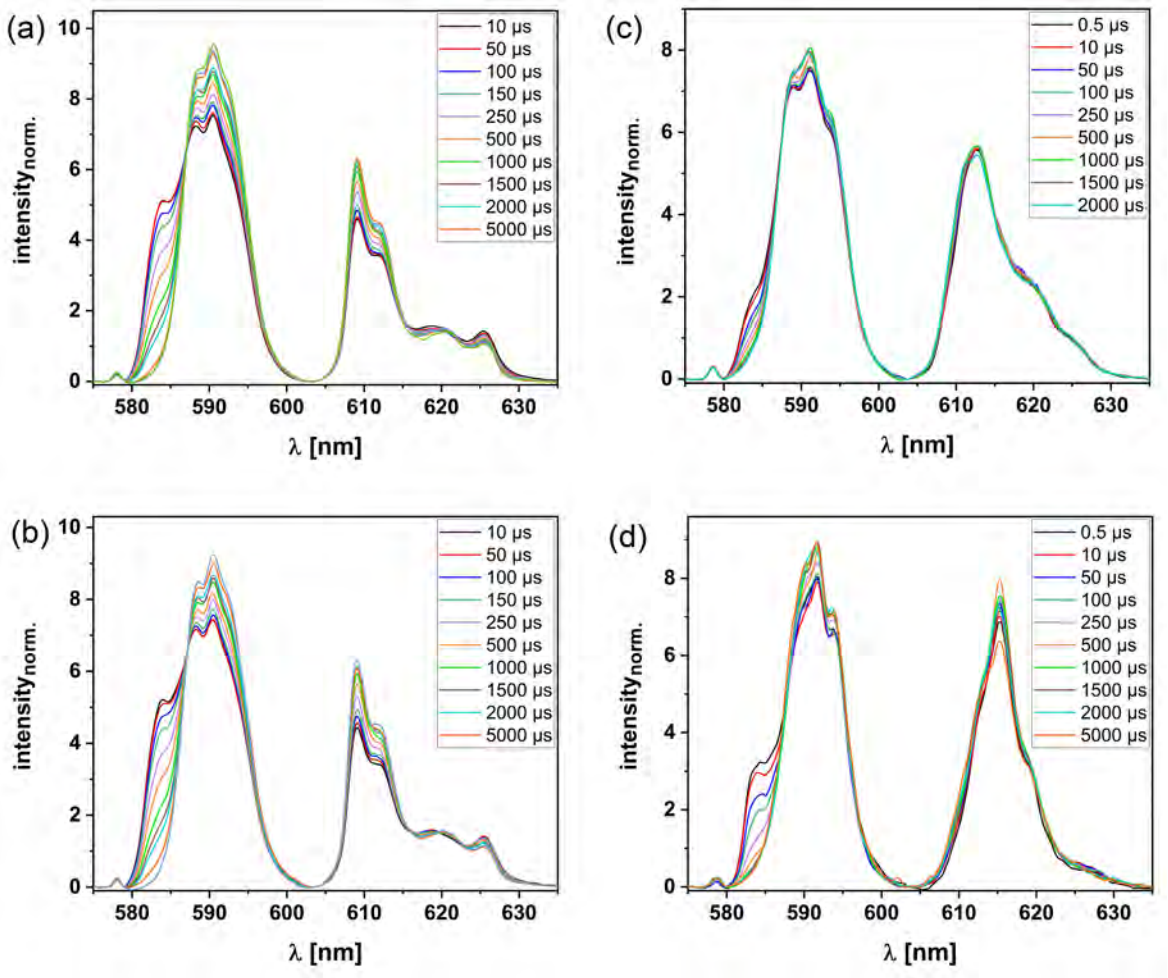

Figure 5.9: TRANES of (a) NaY:$Gd_{0,7.5}$ (b) NaSc:$Gd_{0,7.5}$. All measurements carried out in Milli-Q water with experimental parameters: λ_{ex} = 464.1 nm, exposure time = 0.05 secs, gate width = 500 μs, number of accumulations = 200 – 2000.

For the sample A@NaSc:Gd_0, three small Stark-splitting of $^7F_1$ state and three small Stark-splitting of $^7F_2$ state are observed. The addition of Gd^{3+} change the spectral shape drastically. There are still three small Stark-splitting of $^7F_1$ state, while the $^7F_2$ state exhibit four small Stark-splitting and a narrowing for samples A@NaSc:$Gd_{7.5,15,30}$. The narrowness of the ED and MD band and the increase of the relative intensity of ED band compared to MD band indicates the higher symmetry after adding of Gd^{3+}. Nevertheless the obviously increase of intensity of the emission band of $^5D_1 \rightarrow {}^7F_3$ transition prove the deterioration the Na_xScF_{3+x} crystal lattice as well as higher distortion around the Eu^{3+} ions (new symmetry site). Since the fraction of the short lived Eu^{3+} species is low for samples A@NaSc:$Gd_{0,7.5,15,30}$, its contribution cannot be extracted from TRANES.

5.5 Conclusion

In this chapter we have presented complementary data of different analytical methods to describe the effect of different amount of Gd^{3+} ions in samples A@NaY:$Gd_{0,7.5,15,30}$ and A@NaSc:$Gd_{0,7.5,15,30}$ on the morphological and photophysical properties of UCNPs. XRD results indicate that the 30 mol% Gd^{3+} leads pure cubic phase $NaYF_4$ to a mixed cubic and hexagonal phase. On the other hand, Gd^{3+} addition induces the alteration from mixed monoclinic and hexagonal Na_xScF_{3+x} to a mixed monoclinic Na_xScF_{3+x} and hexagonal $NaGdF_4$. The SEM images corroborate well the XRD results showing large particles corresponded with narrow XRD reflexions and small particles corresponded with broaden.
The UCL emission spectra of Er^{3+} show that the existence of Gd^{3+} in UCNPs can change the red to green emission intensity ratio in a small scale for samples in $NaYF_4$ and Na_xScF_{3+x} host lattices. The addition of Gd^{3+} caused a remarkably change of the spectral shape of UCL spectra in Na_xScF_{3+x}. The time resolved emission spectra of Er^{3+} recorded at 976 nm excitation wavelength reveal that the decay times of G_T and R emission cannot be altered efficiently with addition of Gd^{3+} for samples in $NaYF_4$, whereas the mixing with Gd^{3+} provide longer decay times in Na_xScF_{3+x}. Thus, the relative short decay time of Er^{3+} in Na_xScF_{3+x} compared to that in $NaYF_4$ can be raised remarkably doping with Gd^{3+}. The number of photons needed for G1, G2, and R emission are 2 for all samples, whose power density dependent measurements were carried out.
The use of Eu^{3+} as an optical probe made it possible to obtain additional information about the effect of Gd^{3+} on the crystal structure. According to XRD data, there is one site for Y^{3+} (4a) in cubic $NaYF_4$. Thus, there is one occupancy site for Eu^{3+} ions since they are placed in the site of Y^{3+} due to their same charge and similar ionic radius. However, the decay times prove that there are two Eu^{3+} species, one in high symmetry site (long-lived) and the other one in low symmetry site (short-lived species). The low symmetry site displays the surface related field in the particles because of the surface defects, high vibrational states of surface bound ligands, and strong -OH vibrations of water. Furthermore, the short lived Eu^{3+} species can be located in bulk with oxygen and -OH or vacancies in its first coordination sphere. The fraction of both species stayed constant for samples in $NaYF_4$ crystal lattice. Besides, the decay times of short-lived species (between 2178 – 2596 μs) close to each other, the same trend is recognized for long-lived species (between 6120 – 6890 μs). As seen, Gd^{3+} as a similar ion with Y^{3+} influences only slightly the crystal structure as well as the photophysical properties in $NaYF_4$.
In the monoclinic Na_xScF_{3+x}, Sc^{3+} can have one site (2a), which means that the doped Eu^{3+} ions can be found in one symmetry sites. The possible number of symmetry sites of Eu^{3+} is one in hexagonal Na_xScF_{3+x} (3a) and two for hexagonal $NaGdF_4$ (1a, 1f). The analysis of the time resolved measurements show that there are two different Eu^{3+} species for samples synthesized in Na_xScF_{3+x} lattice. One Eu^{3+} species is occupied a low symmetry site (short-lived) and one a high symmetry site (long-lived). The increasing of the Gd^{3+} ions in Na_xScF_{3+x} crystal lattice caused the gradual decrease of the fraction of the short-lived Eu^{3+} species (in the low site symmetry/on the surface),

indicating the less defect on the surface and in bulk. The decrease of the fraction of the short-lived Eu^{3+} species can also result from the formation of the large particle with the addition of Gd^{3+} since the surface to volume ratio is small in large particles. The alteration of the decay times in the various amount of Gd^{3+} is significant. The values τ_1 for short-lived Eu^{3+} species lie between 401 and 836 μs, while these are between 2035 and 3479 μs for long-lived Eu^{3+} species.
The maximum of the $^5D_0 \rightarrow {}^7F_0$ transition in $NaYF_4$ lying in a shorter wavelength indicates the higher symmetry of $NaYF_4$ than Na_xScF_{3+x}. Thus, the decay times of Er^{3+} and Eu^{3+} are longer for samples in $NaYF_4$ host lattice. The effect of Gd^{3+} on the crystal structure, UCL properties as well as the Eu^{3+} luminescence is much higher in Na_xScF_{3+x} than in $NaYF_4$ due to the high variation of the lattice parameter with addition of Gd^{3+}.

Chapter 6

Autoclave-based one step synthesized PEI@Na_xScF_{3+x}:18%Yb^{3+}:2%Tm^{3+} :7.5%Gd^{3+} UCNPs

6.1 Introduction

The electrostatic attraction between the net positive charge of PEI and the negative charge of cells can facilitate cell binding affinity, which makes PEI valuable to biological applications. PEI on the surface of UCNPs provides amino groups for conjugation to targeting ligands such as antibodies.[134] Wang et. al. studied [77] $NaYF_4$:Yb^{3+}:Er^{3+} UCNPs using 1 and 2 wt% high weight PEI. They synthesized 50 nm water soluble UCNPs biocompatible with human cells. However, there is only a few research about PEI capped UCNPs, and this topic needs further investigation. On the other hand, NIR to NIR upconversion using Yb^{3+}/Tm^{3+} sensitizer/activator couple has attracted investigations for use in biological applications since the light absorption coefficient of biological tissues is minimum in the region between 750 and 1000 nm.[135] [136] Gd^{3+} can provide magnetic property to UCNPs, which is crucial not only for MRI but also for magnetic bio-separation.[136]
In this chapter we studied first the effects of synthesis conditions (the type of PEI, ligand concentration and reaction temperature) on the crystal structure, morphology and photophysical properties of PEI capped hydrophilic $NaScF_4$:Yb^{3+}:Tm^{3+}:Gd^{3+} UCNPs synthesized using hydrothermal method in autoclave.
5 samples in Na_xScF_{3+x} host lattice were synthesized with 18 mol% Yb^{3+} and 2 mol% Tm^{3+} and 7.5 mol% Gd^{3+}. 2 types of PEI (800 M_W and 25000 M_W) are used as a capping agent with various concentrations. After structural characterization, the blue and NIR UCL intensity and decay kinetics were studied.

6.2 Structural characterization

6.2.1 XRD

The PEI coated Na_xScF_{3+x}:Yb^{3+}:Tm^{3+}:Gd^{3+} UCNPs were characterized through X-ray diffraction method to confirm the phase purity and structural analysis.

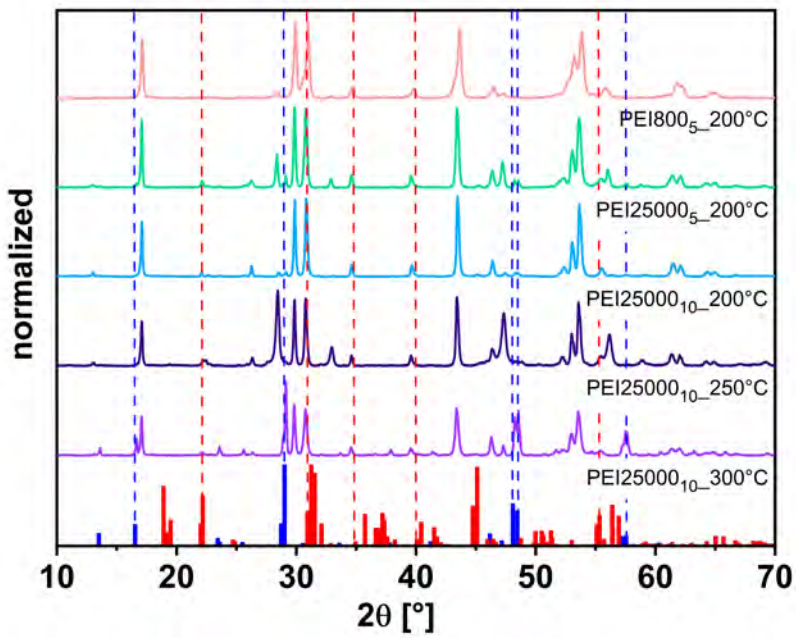

Figure 6.1: X-ray diffraction patterns of PEI800$_5$_200°C, PEI25000$_5$_200°C, PEI25000$_{10}$_200°C, PEI25000$_{10}$_250°C and PEI25000$_{10}$_300°C UCNPs (red lines belong to the standard XRD patterns of the monoclinic phase $NaScF_4$ (ICSD card 400723) and blue lines to the hexagonal phase of Na_3ScF_6 (COD ID: 1515376)).

Interestingly, the diffraction peaks of $NaGdF_4$ are dominant on the diffraction pattern of samples. The strongest peaks of that crystal are located at 17.0°, 29.9°, 30.8°, 43.4°, 53.0°, 53.6°. Other strong peaks belong to the hexagonal Na_xScF_{3+x} and located at 13.6°, 29.1°, 48.2°, 48.5°. The sample PEI25000$_{10}$_300°C has the strongest peaks of hexagonal Na_xScF_{3+x}. The weak peaks of monoclinic Na_xScF_{3+x} at 34.6°, 39.6°, 64.3° are observed on XRD patterns of all sample. The peak widths narrow if the used PEI change from 800 M_W to 25000 M_W. As known, the reaction temperature has a particular role in controlling the particle growth as well as the particle size and shape. The intensity of peaks of $NaGdF_4$ decrease and the intensity of peaks of hexagonal Na_xScF_{3+x} increases with increasing of reaction temperature from 200 °C to 250° and finally to 300°C. The asymmetric peaks in XRD pattern of PEI800$_5$_200°C turned to be symmetric for other samples. There is no shift of the peaks that belonged to $NaGdF_4$. On the other hand, the peak of hexagonal Na_xScF_{3+x} at 29.1° shows a shift 0.5° to higher degree from PEI25000$_{10}$_250°C to PEI25000$_{10}$_300°C, indicating a shrink in unit cell of hexagonal Na_xScF_{3+x} with increasing of reaction temperature.

6.2.2 SEM

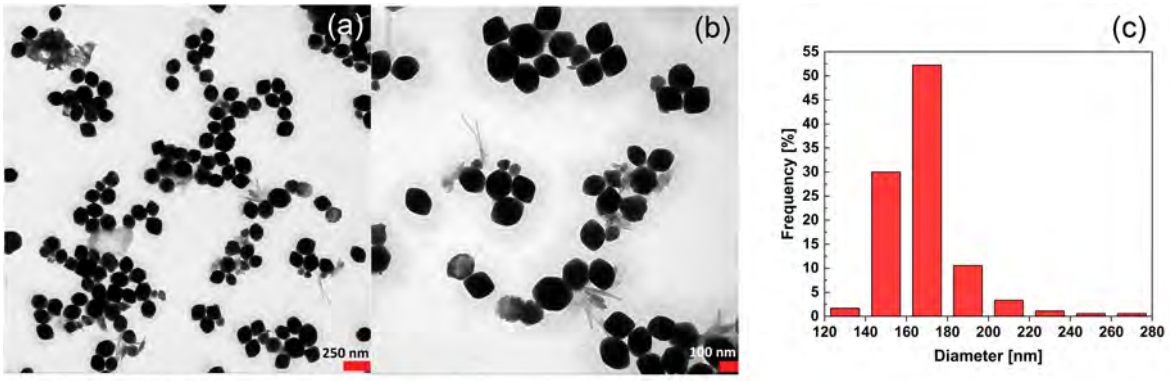

Figure 6.2: (a,b) SEM1 images of PEI25000$_{10}$_200°C UCNPs (c) Particle size distribution plots of PEI25000$_{10}$_200°C according to SEM1.

Figure 6.2 (a) and (b) show low and high magnification SEM images (SEM1) of PEI25000$_{10}$_200°C UCNPs, respectively and figure 6.2 (c) the particle size distribution histogram of the same sample. The UCNPs are nearly monodispersed with an average particle size of 168±18 nm (table 6.1). UCNPs synthesized with PEI 800 M_W formed in different undefined shapes, and their average particle size is 239±59 nm (figure A.25 for other SEM1 images). These are the largest particles in the set of PEI UCNPs. Using 5 w% PEI 25000 M_W bring more structured UCNPs with a large particle size distribution. Their average particle size is 114±55 nm. The heigh M_W PEI has more coordination sites per molecule and can bind on the surface of UCNPs strongly. As a result, it is possible to control the particle growth and stabilize the UCNPs against aggregation. Small UCNPs in the sample PEI25000$_5$_200°C are less-structured, round, and plate in shape, while large UCNPs well-structured round, rhombic, or hexagon particles. 250 °C reaction temperature (PEI25000$_5$_250°C) leads to a narrower particle size distribution and smaller average particle size UCNPs compared to the sample PEI25000$_5$_200°C, corresponding with XRD result. These particles are spherical. Further increase of reaction temperature to 300 °C (PEI25000$_5$_300°C) result in relatively monodisperse particles. They are spherical particles slightly larger than PEI25000$_5$_250°C UCNPs with an average particle size of 154±17 nm.

Table 6.1: Obtained particle sizes of PEI capped hydrophilic UCNPs in Na_xScF_{x+3} using SEM1 results.

Sample	PEI800$_5$_200°C	PEI25000$_5$_200°C	PEI25000$_{10}$_200°C	PEI25000$_{10}$_250°C	PEI25000$_{10}$_300°C
R (SEM) [nm]	239±59	114±55	168±18	124±14	154±17
I_{NIR}/I_B	33	52	34	98	46

6.3 Upconversion luminescence properties

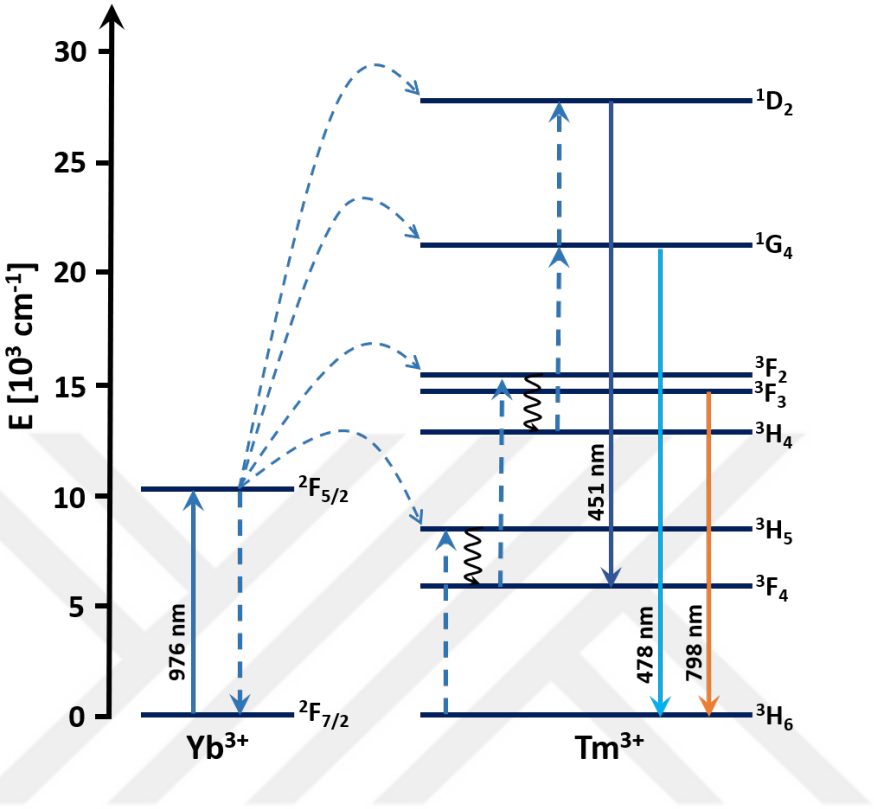

Figure 6.3: Schematic energy level diagram of Yb^{3+} and Tm^{3+} showing energy transfer from Yb^{3+} to Tm^{3+}. Diagram is drawn based on Arppes paper.[137]

6.3.1 UCL bands and decay kinetics of UCL of Tm^{3+}

The UCL spectra of PEI coated UCNPs in Na_xScF_{3+x} lattice were investigated by recording steady state and time resolved emission spectra in Milli-Q water at 976 nm excitation wavelength. The normalized UCL spectra of samples are shown in figure 6.4.

As seen, the UCL emission band centred at 798 nm exhibit relatively high intensity compared to the emission bands centred at 451 nm and 477 nm. The strong emission band at 798 belong to $^3H_4 \rightarrow {}^3H_6$ transition (NIR), the weak emission bands at 451 nm belong to the $^3F_4 \rightarrow {}^1D_2$ (B1) and at 477 nm to $^1G_4 \rightarrow {}^3H_6$ (B2) transitions (both B).[138] [139] The ratio of the intensity of NIR to B emission bands is 23 for $PEI25000_{10}$_200°C, while this value increases to 97 for $PEI25000_{10}$_250°C (table 6.1), making the NIR to NIR UCL efficiency more useful for bioimaging. The spectral shape of samples is similar. The NIR band of all samples show two small Stark-splitting. The light shoulder at 787 nm is observed for all samples. Another shoulder appeared at 819 nm on spectra of sample $PEI25000_5$_250°C.

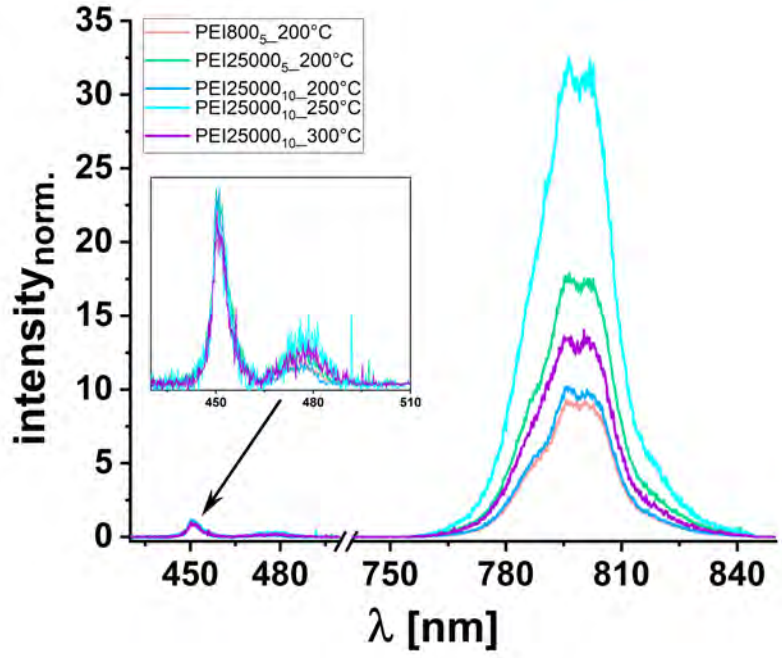

Figure 6.4: Normalized UCL spectra of PEI800$_5$_200°C, PEI25000$_5$_200°C, PEI25000$_{10}$_200°C, PEI25000$_{10}$_250°C and PEI25000$_{10}$_300°C UCNPs. All measurements carried out in Milli-Q water with experimental parameters: λ_{ex} = 976 nm, exposure time = 0.03 secs, delay time after the laser pulse = 500 ns, gate width = 500 μs, number of accumulations = 2000.

There is still no full explanation of the upconversion process of Yb^{3+}-Tm^{3+} sensitizer-activator system. Basically, two different scenarios have been considered after excitation of Yb^{3+} ions. Either a subsequential energy transfer to Tm^{3+} or a cooperatively energy transfer from several Yb^{3+} ions to Tm^{3+} occur. According to first scenario, Tm^{3+} is excited to $^3H_5$ energy state by energy transfer from Yb^{3+}. After a non-radiative relaxation to the $^3F_4$ energy state, the subsequential energy transfer from Yb^{3+} to Tm^{3+} excites it to $^3F_2$ state. The non-radiative relaxation to the $^3F_3$ state result in the emission at 798 nm. It can happen that new energy transfers to the $^3F_2$ state and the light is emitted from $^1G_4$ state at 478 nm, from $^1D_2$ state at 451 nm. In cooperative sensitization, Tm^{3+} ion is promoted directly to the $^1G_4$ state by energy transfer from excited Yb^{3+} ions, which are sufficiently close to Tm^{3+} ion.[140]

Decay kinetics of B and NIR emission bands were investigated. At low pulse power densities, the luminescence intensity of UCNPs was low and strongly quenched by water, which negatively affected the accuracy of the decay time measurements. The decay curves of B and NIR emission bands of PEI25000$_5$_200°C and PEI25000$_{10}$_200°C are shown exemplary in figure 6.3 (a) and (b), respectively. The data for B and NIR emission bands of Tm^{3+} were evaluated by fitting with monoexponential and biexponential decay kinetic excluding rise times, which are observed for some samples.

The τ_1 values of B emission for PEI800$_5$_200°C, PEI25000$_5$_200°C, PEI25000$_{10}$_200°C and PEI25000$_{10}$_250°C are similar and lie between 14 and 20 µs. The highest value for

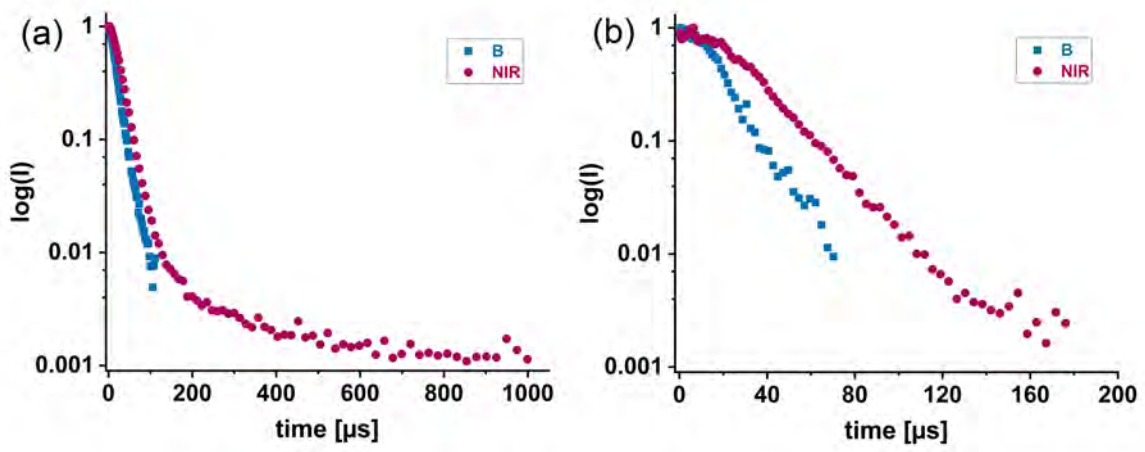

Figure 6.5: Normalized UCL decay kinetics of B and NIR_E emissions of Tm^{3+} of (a)$PEI25000_5$_200°C, (b)$PEI25000_{10}$_200°C UCNPs. All measurements carried out in Milli-Q water with experimental parameters: λ_{ex} = 976 nm, exposure time = 0.05 secs, delay time after the laser pulse = 500 ns, gate width = 500 μs, number of accumulations = 150-300.

that emission band is 576 µs, which belongs to the long-lived Tm^{3+} species of sample $PEI25000_{10}$_250°C despite of its relatively small particle size. The τ_1 values for NIR emission are between 21 and 34 µs for samples without $PEI25000_{10}$_250°C. Its short-lived species has the shortest decay time value (3 μs). The samples $PEI25000_5$_200°C, $PEI25000_{10}$_250°C and $PEI25000_{10}$_300°C have long-lived species, which indicate that these formed well crystalline UCNPs. The highest τ_2 value of NIR band belong to $PEI25000_5$_200°C, while the samples synthesized at higher temperature show smaller τ_2 values.

Table 6.2: UCL decay parameters of UCNPs in water under pulsed wave excitation of 976 nm.

Sample	$PEI800_5$ _200°C	$PEI25000_5$ _200°C	$PEI25000_{10}$ _200°C	$PEI25000_{10}$ _250°C	$PEI25000_{10}$ _300°C
τ_1 (B)	14	19	14	20	-
τ_2 (B)	-	-	-	576±36	-
τ_1 (NIR)	21	23	24	3	34±1
τ_2 (NIR)	-	468±71	-	89±4	150±52
I_{NIR}/I_B	32	50	33	97	46

6.4 Microwave based one step synthesized PEI@Na_xScF_{3+x}: 2%Nd^{3+}:y%Yb^{3+} and PEI@Na_xScF_{3+x}:2%Nd^{3+}:2%Yb^{3+}:z%Fe^{3+} NPs

6.4.1 Introduction

The interest of the NIR emission after energy transfer from Nd^{3+} to Yb^{3+} for photonic applications has been raised recently. The increased absorption of water within the tissue at 976 nm is a disadvantage of Yb^{3+} as a synthesizer. Using Nd^{3+} as a synthesizer significantly reduces water absorption at the excitation wavelength of about 800 nm.[141] Moreover, NIR emission of Yb^{3+} make this couple a promising concept in the using biological area since the wavelength range between 795 and 976 nm is nearly transparent for many biological matrices.[76] Rakov et. al. studied the down-shifting emission of Yb^{3+} in SrF2:Nd^{3+}:Yb^{3+}:Al^{3+} crystallin powders.[142] However, the energy transfer still needs to be improved. Fe^{3+} can be a promising codoping ion since it has abundant energy levels to enable energy exchange with Ln^{3+} ions. Further, doping the lattice with Fe^{3+} ion can tailor the local crystal field of the lanthanide ions and improve the down-conversion luminescence of particles. Fe^{3+} codoping provides to nanoparticles the application in magnetic-based therapies due to its paramagnetic properties.
We investigated briefly the effects different amount of Yb^{3+} and Fe^{3+} on the morphology and photophysical properties of PEI capped Na_xScF_{3+x}:Nd^{3+}:Yb^{3+} and Na_xScF_{3+x} :Nd^{3+}:Yb^{3+}:Fe^{3+} UCNPs synthesized microwave-assisted hydrothermal method.
5 samples with various Yb^{3+} concentration and 5 samples with constant Yb^{3+} concentration (2 mol%) and with various Fe^{3+} concentration were synthesized. Afterwards, the change of luminescence intensity of Yb^{3+} and Nd^{3+} in NIR range was studied.

6.4.2 Structural characterization

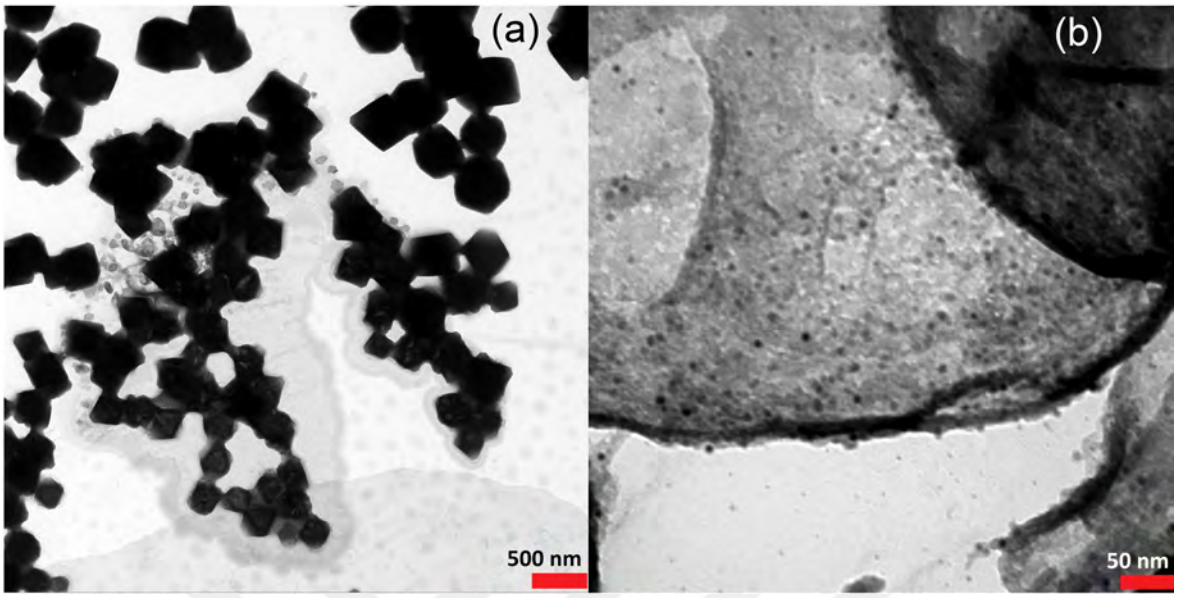

Figure 6.6: TEM2 images of (a) NaSc:Nd_2:Yb_9, (b) NaSc:Nd_2:Yb_2:Fe_{10} (Film-like structures can be attributed to the remaining organics after washing process).

Figure 6.1 (a) and (b) show the TEM2 images of samples NaScF_Nd_2_Yb_9 and NaScF_Nd_2_Yb_2_Fe_{10}. The average particle size of samples NaScF_Nd_2_Yb_9, NaScF_Nd_2_Yb_2_Fe_{10} and NaScF_Nd_2_Yb_2_Fe_{40} were determined using TEM2 images. Their average particle sizes are 123±80, 7±1 and 8±2 nm, respectively. As seen the particles without Fe^{3+} are large cubic and hexagon in shape. However, some small particles exist as well in that sample. Addition of Fe^{3+} lead to the formation of significantly smaller, spherical particles. The observable film-like structures can be the remaining organics after washing process.

6.4.3 Stokes-shift luminescence of Yb^{3+}

The steady state emission spectra of Yb^{3+} and Nd^{3+} ions of powder samples were recorded upon 800 nm pulsed excitation. The normalized emission spectra of samples with different amounts of Yb^{3+} and Fe^{3+} are shown in figure 6.5 (a) and (b), respectively.

The emission band at 974 nm can be attributed to $^2F_{5/2} \rightarrow {}^2F_{7/2}$ transition of Yb^{3+} and that at 1054 nm to $^4F_{3/2} \rightarrow {}^4I_{11/2}$ transition of Nd^{3+} ion. Since the energy transfer from Nd^{3+} to Yb^{3+} is possible, the disappearing of the Nd^{3+} emission band with increasing of Yb^{3+} concentration from 2 mol% to 18 mol% can be explained by a highly efficient energy transfer due to the existence of more Yb^{3+} ions close to Nd^{3+}. The spectral shape changes with increasing amount of Yb^{3+}. The emission band of Yb^{3+} broadens and its maximum exhibit a red-shift at the concentration level of 9 and 18 mol% Yb^{3+}. There is a decrease of relative emission intensity of $^4F_{3/2} \rightarrow {}^4I_{11/2}$ transition of Nd^{3+}, when the sample NaSc:Nd_2:Yb_2 codoped with increasing amount

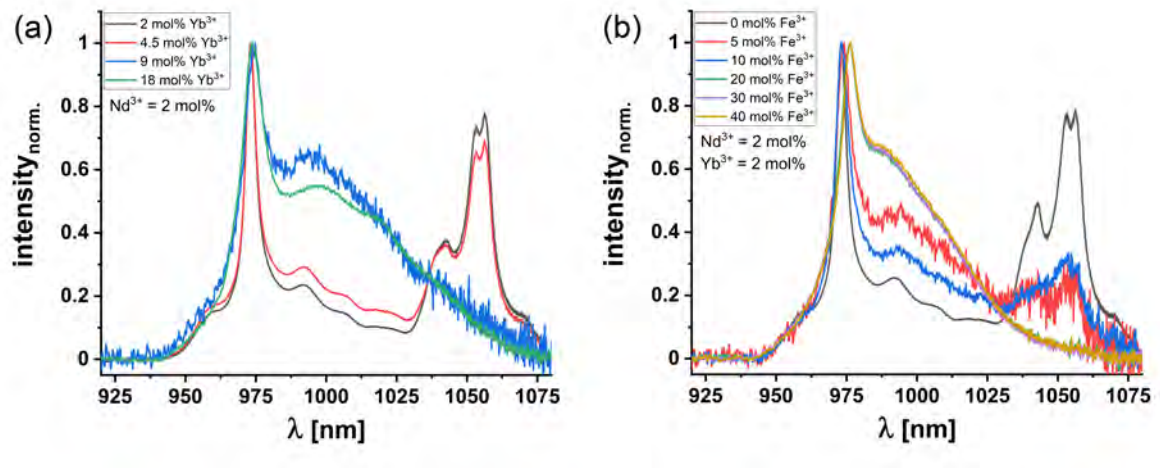

Figure 6.7: Normalized luminescence spectra of (a) NaSc:Nd_2:Yb_x (b) of NaSc:Nd_2:Yb_2:Fe_x. All measurements carried out using powder samples with experimental parameters: λ_{ex} = 800 nm, exposure time = 0.034 secs, delay time after the laser pulse = 500 ns, gate width = 500 μs, number of accumulations = 250.

of Fe^{3+} (5 - 40 mol%). The red-shift of maximum of Yb^{3+} emission band and the broadening of that band indicate that the effect of Fe^{3+} codoping is similar with Yb^{3+} codoping. The broadening of the emission band of Yb^{3+} arising at lower energies can be attributed to crystal field splitting.[143]

6.5 Conclusion

The results of preliminary studies about NIR to NIR upconversion and down-conversion particles in Na_xScF_{x+3} host lattice were presented in this chapter. XRD results show that the PEI coated UCNPs synthesized in autoclave were formed in a mixed phase of monoclinic/hexagonal Na_xScF_{x+3} and hexagonal $NaGdF_4$. The average particle sizes of hydrophilic UCNPs are between 114 and 239 nm with a large error. The highest NIR to B intensity ratio and the longest decay times belong to the UCNPs synthesized with a high molecular weight PEI (10 wt%) at 250 °C, which is valuable for biological imaging. However, further experiments are necessary to reduce the large particle sizes. The down-conversion nanoparticles doped only with Nd^{3+} and Yb^{3+} (9 mol%) exhibit large particle size (123±80 nm), while the particles additionally doped with Fe^{3+} (10 mol% and 40 mol%) have a remarkably small size (7 and 8 nm). It is seen that the energy transfer between Nd^{3+} and Yb^{3+} can be tailored by changing the Yb^{3+} concentration and codoping with various amount of Fe^{3+} ions. Despite the high potential of the down-conversion particles for application in the biological field, there is a need to carry out the basic measurements such as XRD, Zeta potential, decay times, and further experiments.

Chapter 7

Conclusion and future directions

7.1 Conclusion

Despite many kinds of research on the UCNPs, it is still a necessity to study their photophysical and structural properties in alternative host lattices for understanding the relationship of parameters with each other and for improving new synthesis protocols for obtaining hydrophilic UCNPs in a short time environment friendly.
The main conclusions based on the chapters are:
1 Oleic acid capped hydrophobic UCNPs in $NaYF_4$ and Na_xScF_{x+3} lattice doped with Yb^{3+}, Er^{3+} and Eu^{3+} were synthesized with various Gd^{3+} concentration (0-30 mol%) using thermal decomposition method successfully. The effect of the Gd^{3+} on the lattice structure was determined by gradually shifting the position of the reflexes to the lower angle on the XRD pattern of samples. There is no relation between particle sizes and Gd^{3+} content according to TEM results. The average particle sizes of UCNPs in $NaYF_4$ lattice lie between 6 and 9 nm, whereas this value for UCNPs in Na_xScF_{x+3} lattice is between 11 and 15 nm. The DLS results agree well with the average particle sizes calculated by using TEM images.
There is no difference of the UCL spectral distribution of Er^{3+} for samples in $NaYF_4$ lattice after adding Gd^{3+}. On the other hand, the UCL spectral distribution of Er^{3+} altered remarkably after adding Gd^{3+} for the samples in Na_xScF_{x+3} lattice. Since the difference of the ionic radius of Gd^{3+} and Sc^{3+} is larger than that between Gd^{3+} and Y^{3+}, it was expected that the introducion of Gd^{3+} into the Na_xScF_{x+3} lattice resulting in a more significant influence on the site symmetry of Er^{3+} compared to that in $NaYF_4$ lattice. It was possible to tune the longer UCL decay times of Er^{3+} with the addition of a certain amount of Gd^{3+} into the Na_xScF_{x+3} lattice. Furthermore, the temperature dependent measurements (between 288 and 323 K) of G1 and G2 emission bands of Er^{3+} showed that Gd^{3+} codoping can offer samples in Na_xScF_{x+3} lattice higher absolute and relative temperature sensitivity compared to sample without Gd^{3+}. The number of absorbing photons required for G1, G2 and R emissions is 2 for all samples. On the Eu^{3+} spectra, a gradually blue-shift of the maximum of $^5D_0 \rightarrow {}^7F_0$ transition for samples in $NaYF_4$ lattice and red-shift of the maximum of $^5D_0 \rightarrow {}^7F_0$ transition for samples in Na_xScF_{x+3} lattice were observed with increasing of Gd^{3+} concentration, which indicate that the increasing amount of Gd^{3+} lead the Eu^{3+} site to lower sym-

metry in $NaYF_4$ lattice and to higher symmetry in Na_xScF_{x+3} lattice. The generally decreasing of decay time values of Eu^{3+} in $NaYF_4$ and increasing of decay time values of Eu^{3+} in Na_xScF_{x+3} with increasing of the Gd^{3+} content agreed well with these results. The TLS spectra of Eu^{3+} allowed us to see the small differences of the environment of Eu^{3+} species. When the TLS spectra, R_A values, luminescence decay time values, and the result of PARAFAC analysis were interpreted together, it has been seen that there are two Eu^{3+} species for samples in $NaYF_4$ lattice and three Eu^{3+} species for samples in Na_xScF_{x+3} lattice. The main part of the samples was formed in cubic $NaYF_4$, which offers to Eu^{3+} one symmetry site (4a). However, two Eu^{3+} species were determined for the samples in this lattice. One can be located on/near the particle surface and in an environment with high crystal defects as well as high deactivation centres in bulk and another one is centred in a sheltered site in bulk. Monoclinic Na_xScF_{x+3} lattice provides one symmetry site (2a) to Eu^{3+} and hexagonal Na_xScF_{x+3} one site (3a). If we can consider that the predominantly amount of UCNPs is formed in these lattices, the three existing Eu^{3+} species can be placed in an environment with high defects like on the surface, in 2a site, and 3a site.

2 Acetic acid capped hydrophilic UCNPs in $NaGdF_4$ lattice doped with Yb^{3+} and Er^{3+} were synthesized under different synthesis parameter using hydrothermal synthesis method in a microwave, successfully. XRD patterns showed that the UCNPs in hexagonal $NaGdF_4$ could be synthesized even in one hour using EtOH. In EG, it was possible to obtain pure hexagonal $NaGdF_4$ first in a reaction time of 4 hours. DLS measurement showed that the UCNPs are for a long time stable in Milli-Q water. On the other hand, the synthesis of UCNPs in a relatively more viscose medium with EG and G instead of EtOH resulted in small UCNPs with an average particle size of sub-50 nm only in 20 min. Since small particle size is required from UCNPs to use them in life science, obtaining sub-50 nm hydrophilic UCNPs in one step and short reaction time is a very promising stage in synthesis. The UCNPs capped successively with AC can support bioconjugation like nanoparticle-biotin coupling, but the large average particle size of these UCNPs still needs to be reduced. The G emission intensity is dominant for all samples. Generally, the longer reaction time supported the longer decay time at 150 °C and 600 rpm, indicating the formation of crystal lattices with less deactivation centers. G1, G2, R, and NIR bands of Er^{3+} required 2 absorbing photons for UCL emission for samples synthesized in a medium containing EtOH at reaction times between 1 and 4 h.

3 Acetic acid capped hydrophilic UCNPs in $NaYF_4$ and Na_xScF_{x+3} lattice doped with Yb^{3+}, Er^{3+} and Eu^{3+} were synthesized with various Gd^{3+} concentration (0-30 mol%) using hydrothermal synthesis method in microwave, successfully. The alteration of the lattices with the increasing amount of Gd^{3+} was determined with the new reflexes and shift of the positions of some reflexes on the XRD pattern. The XRD and SEM results agreed well together.

The UCL emission spectra and decay times of Er^{3+} displayed that the effect of Gd^{3+} content is much higher in Na_xScF_{x+3}. The decay time values are higher for samples in $NaYF_4$ than these for the samples in Na_xScF_{x+3}. However, addition of Gd^{3+} support more efficiently the longer decay times in Na_xScF_{x+3}. The number of absorbing photons for G1, G2 and R emissions of Er^{3+} determined to be 2 for samples recorded their

power density dependent UCL spectra.
Eu^{3+} an optical probe enabled us to gain more information about the slight changes of the crystal structure, which mostly cannot be determined with XRD or TEM. The Eu^{3+} ions occupied the 4a site in the cubic $NaYF_4$. Two Eu^{3+} species determined by decay time measurements show that the short-lived species (in low symmetry site) related to the Eu^{3+} ions located on/near surface and in bulk with oxygen and -OH or vacancies in its first coordination sphere. The long-lived species (in high symmetry site) are located in the bulk phase. The effect of Gd^{3+} on the decay times of Eu^{3+} in $NaYF_4$ is slight.
The possible symmetry sites of Eu^{3+} are 2a in monoclinic Na_xScF_{x+3}, 3a in hexagonal Na_xScF_{x+3} and 1a, 1f in hexagonal $NaGdF_4$. The analyse of decay time measurements of Eu^{3+} indicated that there are only two Eu^{3+} species in the samples. The short-lived species is placed in the low symmetry site and the long-lived species in high symmetry site. The influence of Gd^{3+} on the decay times of Eu^{3+} in Na_xScF_{x+3} relatively strong compared to $NaYF_4$.
The maximum of the $^5D_0 \rightarrow {}^7F_0$ transition of Eu^{3+} lay in a shorter wavelength for samples in NaYF4 in comparison to the samples in Na_xScF_{x+3}. The analysis of Eu^{3+} luminescence spectra succeeded to explain the longer decay times of Er^{3+} and Eu^{3+} for samples in $NaYF_4$. This lattice has higher symmetry than Na_xScF_{x+3} lattice.
4 PEI capped hydrophilic UCNPs in Na_xScF_{x+3} lattice doped with Yb^{3+}, Er^{3+} and Gd^{3+} were synthesized by hydrothermal synthesis method in autoclave, successfully. According to XRD results, the UCNPs consist of mixed phase of monoclinic/hexagonal Na_xScF_{x+3} and hexagonal $NaGdF_4$. The average particle size of UCNPs lay between 114 and 239 nm. Using 10 wt% PEI and reaction time of 250 °C resulted in the highest NIR to B intensity ratio (98) and the longest decay times (89 µs). These values calculated after UCL measurements in water are favourable for bioimaging.
PEI capped Stokes-shift UCNPs in Na_xScF_{x+3} lattice doped with Nd^{3+} and Yb^{3+} were synthesized in microwave. The remarkable reduction of the average particle size of UCNPs occurred after doping with Fe^{3+} from 123 to 7 nm. The intensity ratio of the Yb^{3+} luminescence to Nd^{3+} were controlled by changing of concentration of Yb^{3+} afterwards Fe^{3+}.

7.2 Perspectives

The precious advantages of features of UCNPs such as Anti-Stokes type nonlinear UCL, emission, narrow emission bands, high resistance to photobleaching, low autofluorescence of NIR excitation, and emission in tissue make them excellent materials for use in biological applications. Understanding the UCL mechanism to tailor the UCL spectral distribution and to enhance the UCL intensity and of environment friendly, fast, inexpensive synthesis to produce the hydrophilic UCNPs with a good size control are still essential requirements for commercial production. Furthermore, NIR to NIR emission is expected to be very useful for high penetration tissue bioimaging.
The size of hydrophobic UCNPs synthesized by the thermal decomposition method in this work is suitable for biological application. Although this synthesis method pro-

vides a precise size and phase control with a well crystalline formation and high UCL intensity, it involved main challenges such as the generation of toxic by-products, extra steps to make UCNPs hydrophilic, which makes the process time-consuming and complicated. Furthermore, it mostly happened that these UCNPs are not stable in water and lost their UCL intensities extremely due to the strong -OH vibration after the functionalization process with hydrophilic ligands. For this reason, creating new synthesis protocols is essential.

In our work, we have generated hydrophilic UCNPs stable in Milli-Q water with a simple, fast, and low-cost method. However, their average particle sizes are very large, which prevents the use of them in vivo. The good control of the particle size can be achieved with mew experiments by changing some synthesis parameters such as the reaction medium, the capping agent, the reaction time and temperature, the ratio of precursors. Since the -COOH end-group of AcOH bind on the surface of the UCNPs, and it has no other end-group to offer bioconjugation, the surface of UCNPs should be capped with another surface ligands by ligand exchange or other surface functionalization methods. To overcome that kind of further steps, it can be used with some capping agents such as PEI and PAA, which have abundant free amine and carboxylic acid groups, respectively, and a high binding affinity to the surface of UCNPs.

There are only a few kinds of research about the NIR to NIR UCL and Stokes-shift luminescence using Ln ions. We synthesized hydrophilic UCNPs doped with Yb^{3+} and Tm^{3+} with a high NIR emission intensity upon 976 nm excitation. Although these properties and a high number of amino groups on the PEI offer valuable application potential in life science, these UCNPs need to be generated with a short reaction time and in smaller particle size to make it possible for a fast preparation of small UCNPs for use in vivo. Besides many benefits of these UCNPs, the excitation at 976 nm is at a disadvantage due to the high absorption of water at this wavelength, which causes fast heating in the sample as well as in the tissue. Against this, using the 800 nm excitation wavelength (Nd^{3+}) offers a slow and light rise of temperature of samples in water. For this, the efficient energy transfer between Nd^{3+} and Yb^{3+} is a necessity. The concentration of Nd^{3+} and Yb^{3+}, as well as intentional impurities, should be regulated for optimum energy transfer, and the complementary measurements like XRD, TEM, steady state, and time resolved luminescence should be carried out.

Eu^{3+} as an excellent optical probe can be used more to gain more and detailed information about the crystal structure of UCNPs. Thus, the results of Eu^{3+} luminescence measurements at RT and ultralow temperature help to explain the site symmetry of Ln^{3+} ions as well as the UCL behaviour.

Appendix

Table A.1: List of used chemicals.

Chemical name	Purity	Company
1-Octadecene ($CH_{18}H_{36}$)	90%	sigma Aldrich
Acetic acid ($C_2H_4O_2$)	100%	carl roth
Ammonium floride (NH_4F)	≥99.99%	sigma Aldrich
Cyclohexane (C_6H_{12})	≥99.9%	carl roth
Erbium(III)chloride ($ErCl_3$)	≥99.9%	sigma Aldrich
Ethanol absolute (C_2H_6O)	100%	VWR chemicals
Ethylene glycol ($(CH_2OH)_2$)	≥99.8%	sigma Aldrich
Europium(III)chloride hexahydrate ($EuCl_3{\cdot}6H_2O$)	≥99.99%	sigma Aldrich
Gadolinium(III)chloride hexahydrate ($GdCl_3{\cdot}6H_2O$)	≥99%	sigma Aldrich
Glycerol ($C_3H_8O_3$)	≥99.5% (water free)	carl roth
Iron(III) chloride hexahydrate ($FeCl_3{\cdot}6H_2O$)	≥99.0%	carl roth
Neodymium(III)chloride hexahydrate ($NdCl_3{\cdot}6H_2O$)	≥99.9%	sigma Aldrich
Oleic Acid ($C_{18}H_{34}O_2$)	90%	Alfa Aesar
Polyethylenimine, branched (average M_W ~800 by LS)		sigma Aldrich
Polyethylenimine, branched (average M_W ~25000 by LS)		sigma Aldrich
Scandium(III)chloride hexahydrate ($ScCl_3{\cdot}6H_2O$)	≥99.9%	Alfa Aesar
Sodium hydroxide (NaOH)	≥99%	carl roth
Thulium(III)chloride hexahydrate ($TmCl_3{\cdot}6H_2O$)	≥99.99%	sigma Aldrich
Ytterbium(III)chloride hydrate ($YbCl_3{\cdot}xH_2O$ (x≈6))	≥99.9%	Alfa Aesar
Yttrium(III)chloride hexahydrate ($YCl_3{\cdot}6H_2O$)	≥99.999%	sigma Aldrich

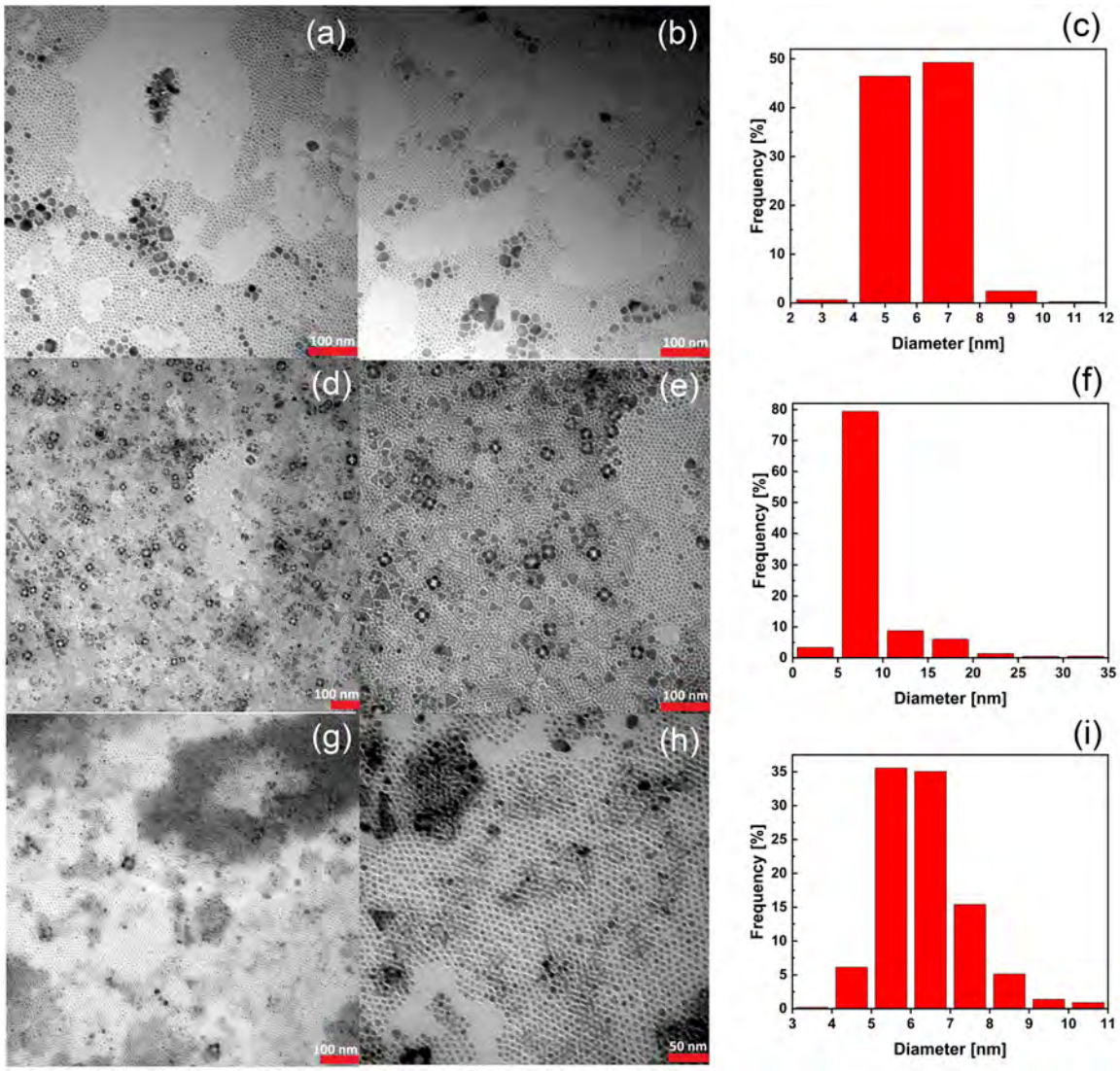

Figure A.1: (a,b) TEM images of NaY:Gd_0 UCNPs with a scale bar = 100 nm (c) Particle size distribution histogram of NaY:Gd_0 according to TEM (d,e) TEM images of NaY:Gd_{15} UCNPs with a scale bar = 100 nm (f) Particle size distribution histogram of NaY:Gd_{15} according to TEM (g,h) TEM images of NaY:Gd_{30} UCNPs with a scale bar = 100 nm and 50 nm, respectively (i) Particle size distribution histogram of NaY:Gd_{30} according to TEM.

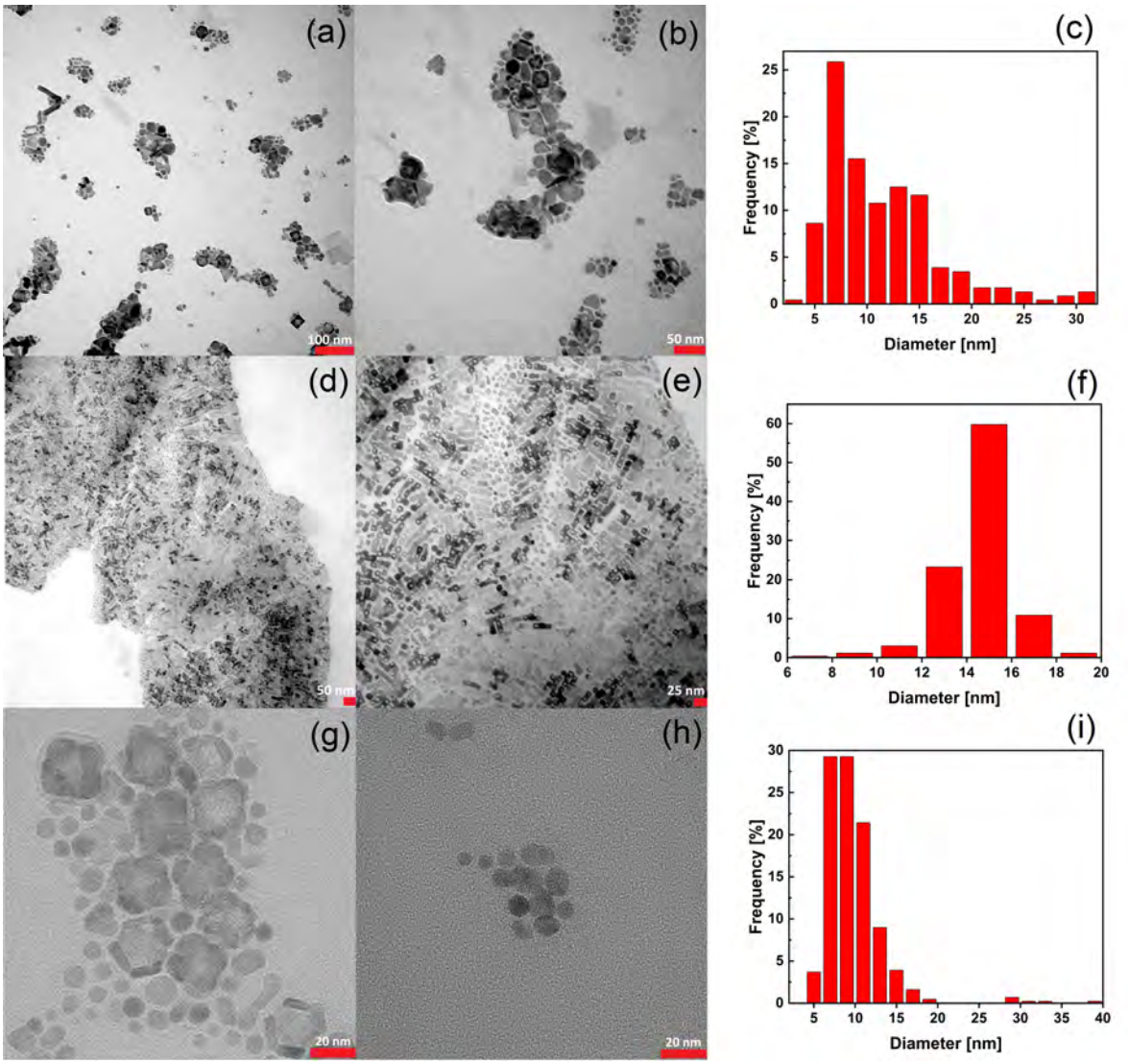

Figure A.2: TEM images of NaSc:Gd_0 UCNPs with a scale bar = 100 and 50 nm, respectively (c) Particle size distribution histogram of NaSc:Gd_0 according to TEM (d,e) TEM images of NaSc:Gd_{15} UCNPs with a scale bar = 50 and 25 nm, respectively (f) Particle size distribution histogram of NaSc:Gd_{15} according to TEM (g,h) TEM images of NaSc:Gd_{30} UCNPs with a scale bar = 20 nm (i) Particle size distribution histogram of NaSc:Gd_{30} according to TEM.

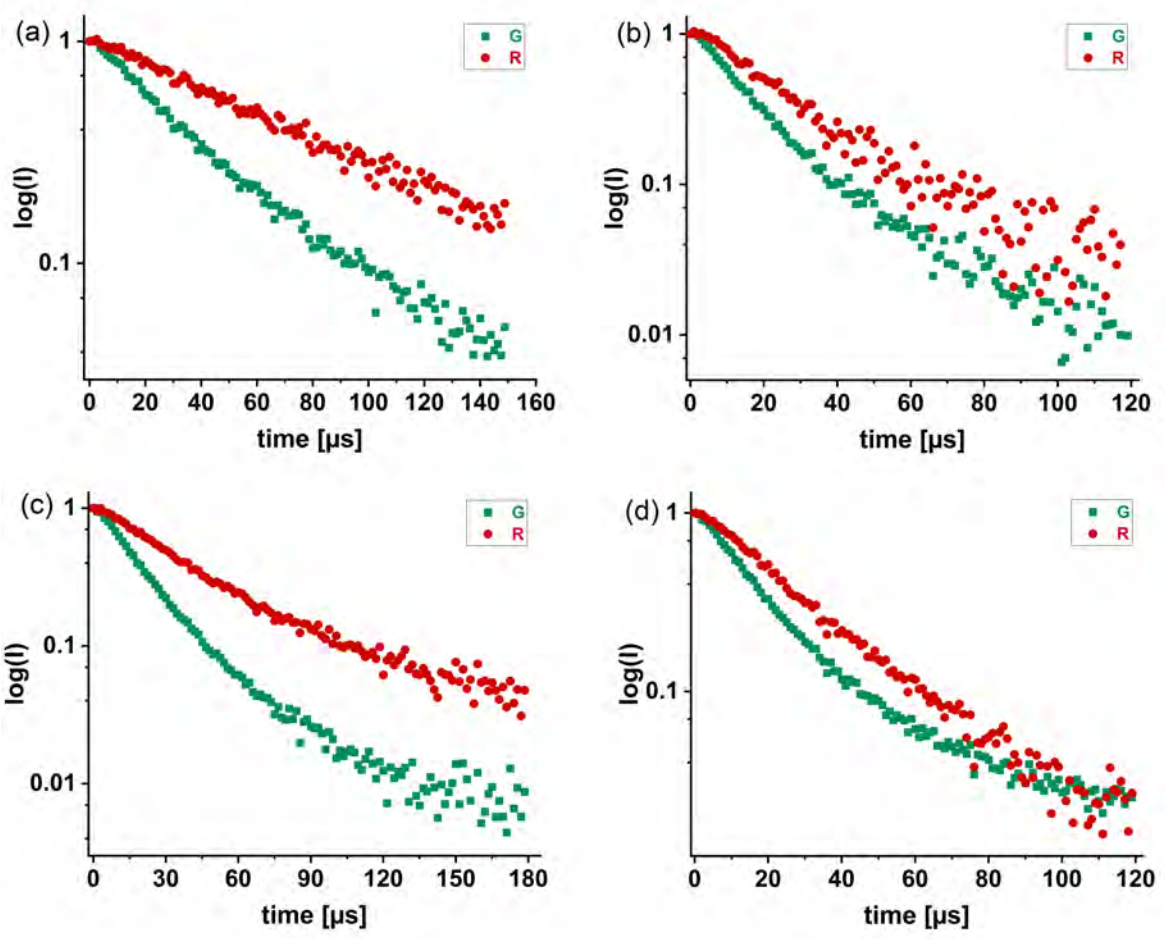

Figure A.3: Normalized UCL decay kinetics of the G_T and R emissions of Er^{3+} for (a) $NaY:Gd_0$ (b) $NaY:Gd_{7.5}$ (c) $NaY:Gd_{15}$ (d) $NaY:Gd_{30}$.

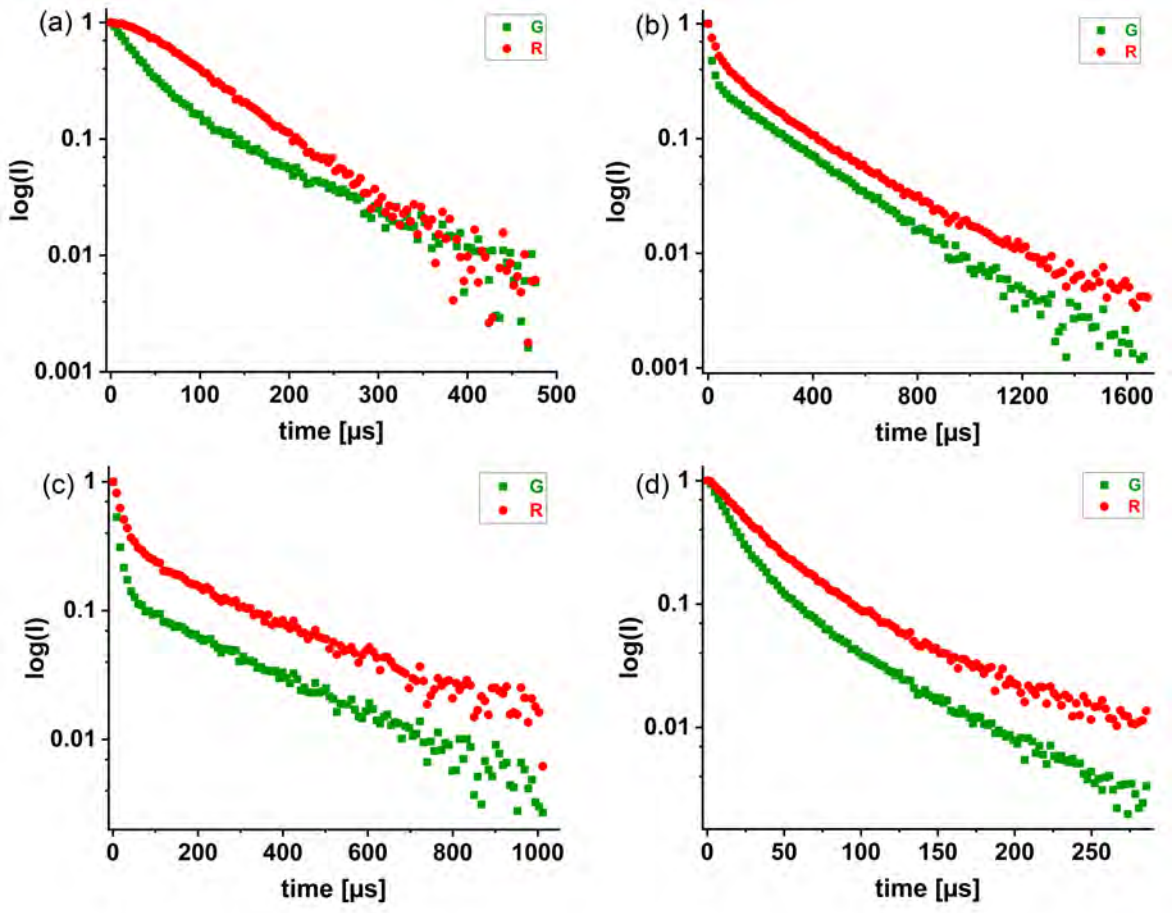

Figure A.4: Normalized UCL decay kinetics of the G_T and R emissions of Er^{3+} for (a) $NaSc:Gd_0$ (b) $NaSc:Gd_{7.5}$ (c) $NaSc:Gd_{15}$ (d) $NaSc:Gd_{30}$.

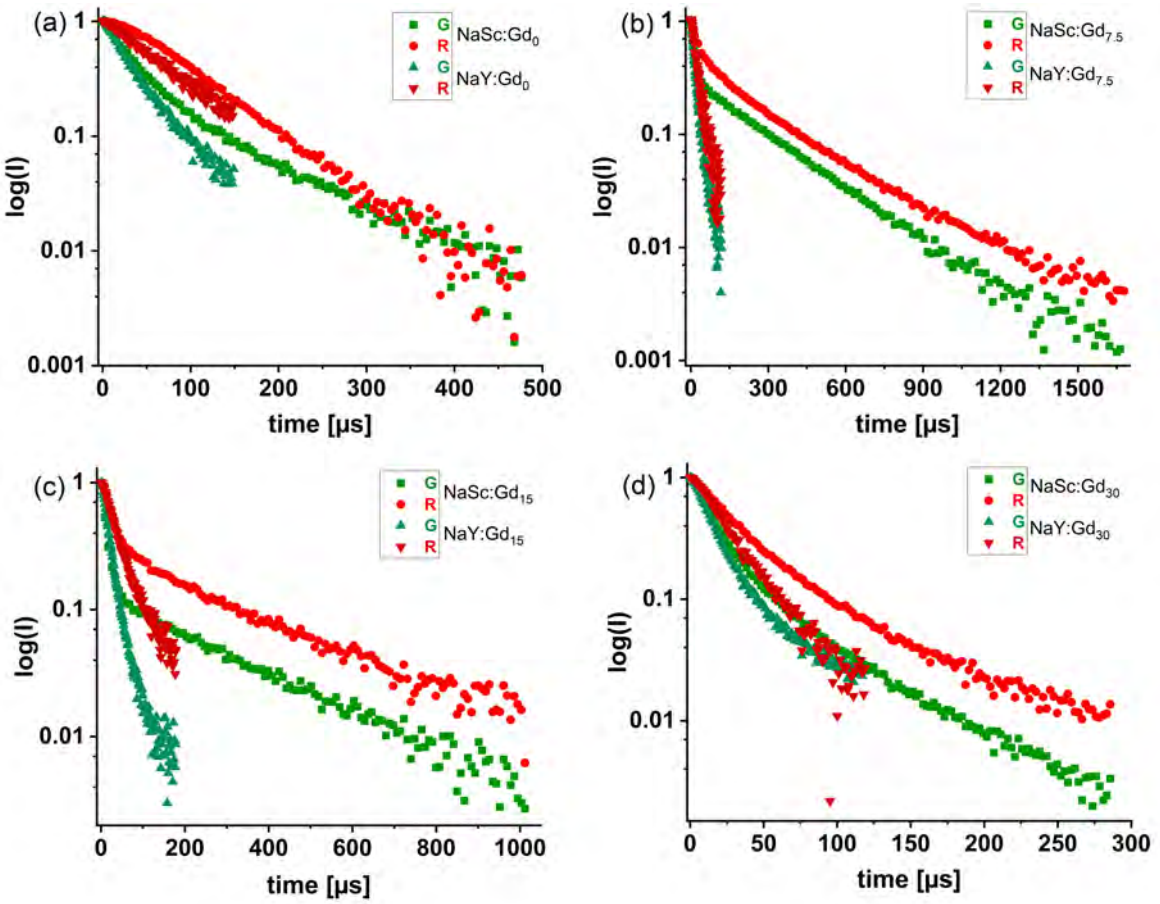

Figure A.5: Normalized UCL decay kinetics of the G_T and R emissions of Er^{3+} for (a) NaY:Gd_0 and NaSc:Gd_0 (b) NaY:$Gd_{7.5}$ and NaSc:$Gd_{7.5}$ (c) NaY:Gd_{15} and NaSc:Gd_{15} (d) NaY:Gd_{30} and NaSc:Gd_{30}.

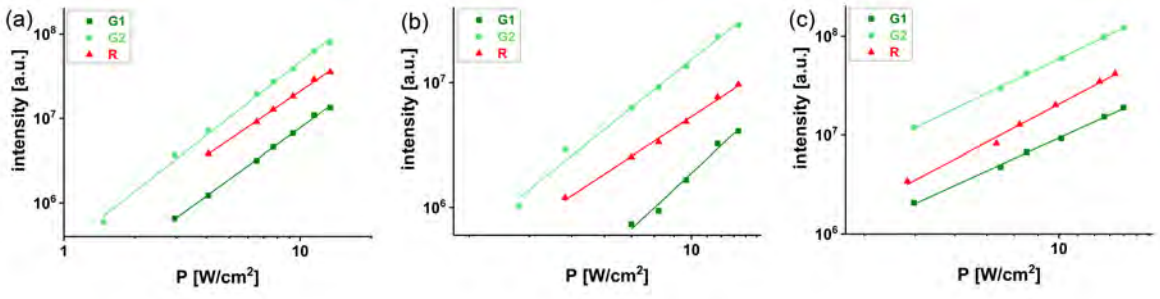

Figure A.6: The double logarithmic plots of G1, G2 and R emission intensities of Er^{3+} versus pump power density for the samples (a) NaY:Gd_0 (b) NaY:$Gd_{7.5}$ (c) NaY:Gd_{15}.

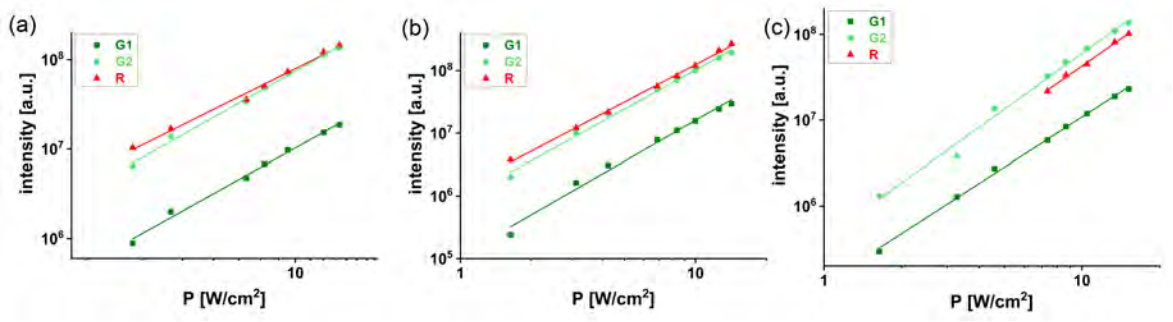

Figure A.7: The double logarithmic plots of G1, G2 and R emission intensities of Er^{3+} versus pump power density for the samples (a) NaSc:Gd_0 (b) NaSc:$Gd_{7.5}$ (c) NaSc:Gd_{15}.

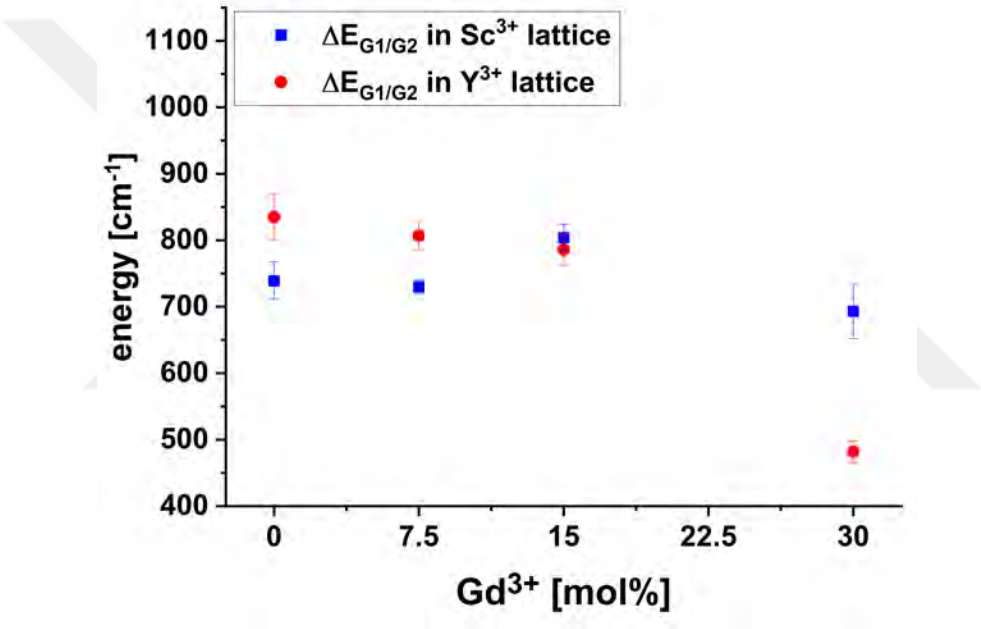

Figure A.8: The energy gap between $^2H_{11/2}$ and $^4S_{3/2}$ states of Er^{3+}.

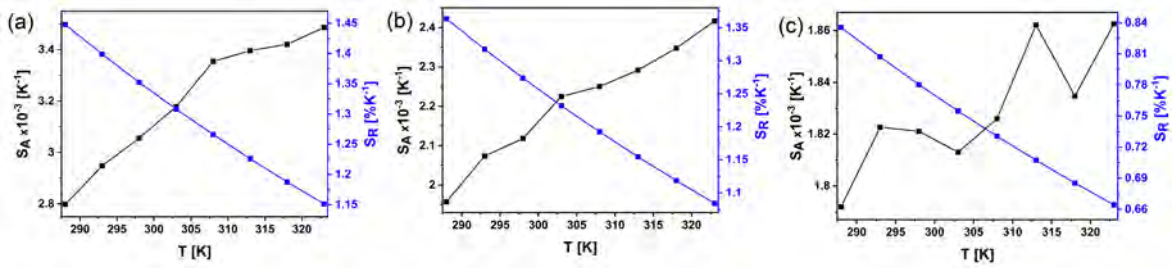

Figure A.9: Absolute and relative sensitivity of the samples NaY:$Gd_{0,15,30}$ for the temperature range of 288 K- 323 K based on the G1/G2 intensity ratio.

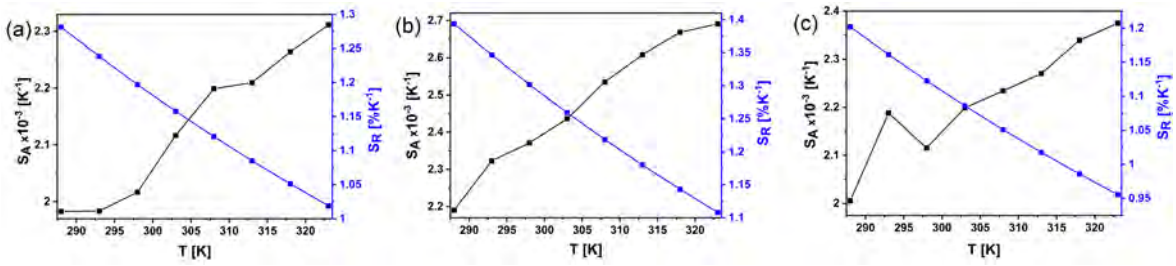

Figure A.10: Absolute and relative sensitivity of the samples NaSc:$Gd_{0,15,30}$ for the temperature range of 288 K- 323 K based on the G1/G2 intensity ratio.

Table A.2: Luminescence decay parameters of Eu^{3+} for UCNPs under pulsed wave excitation of about 578.5 nm at 4 K.

mol% Gd^{3+} (Y^{3+})	λ_{em} [nm]	Y^{3+} host lattice τ_1[µs]	τ_2[µs]	Sc^{3+} host lattice τ_1[µs]	τ_2[µs]
0	593 nm 614 nm	417±19	3604±84	302±12	1750±55
7.5		497±12	2172±35	264±6	1650±26
15		263±16	2339±59	310±15	2294±64
30		647±15	3038±40	669±21	4001±74

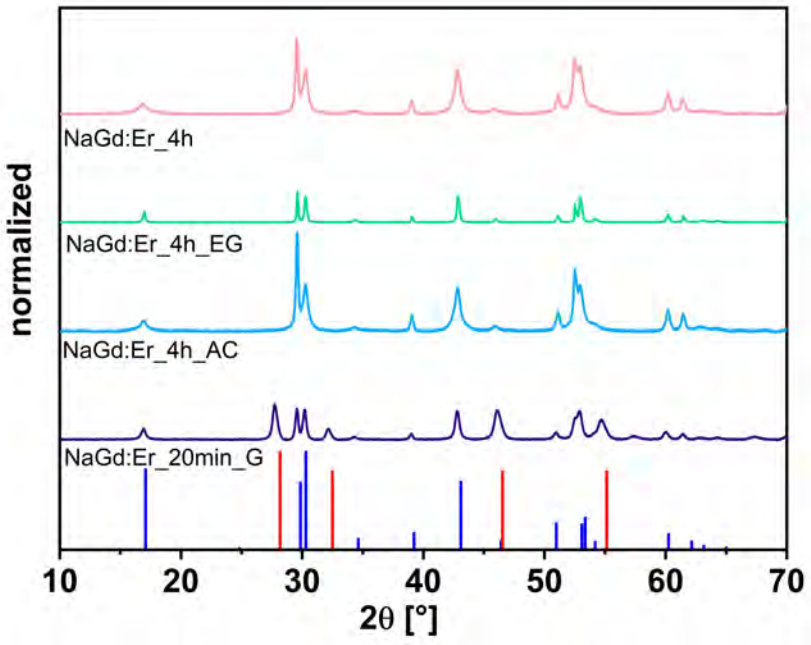

Figure A.11: (c) NaGd:Er_4h, NaGd:Er_4h_EG, NaGd:Er_4h_AC, NaGd:Er_20min_G_1/3V (red columns belong to the standard XRD patterns of the cubic phase $NaGdF_4$ (drawn based on Chen´s paper (087)) and blue columns to the hexagonal phase $NaGdF_4$ (ICSD card 424381)).

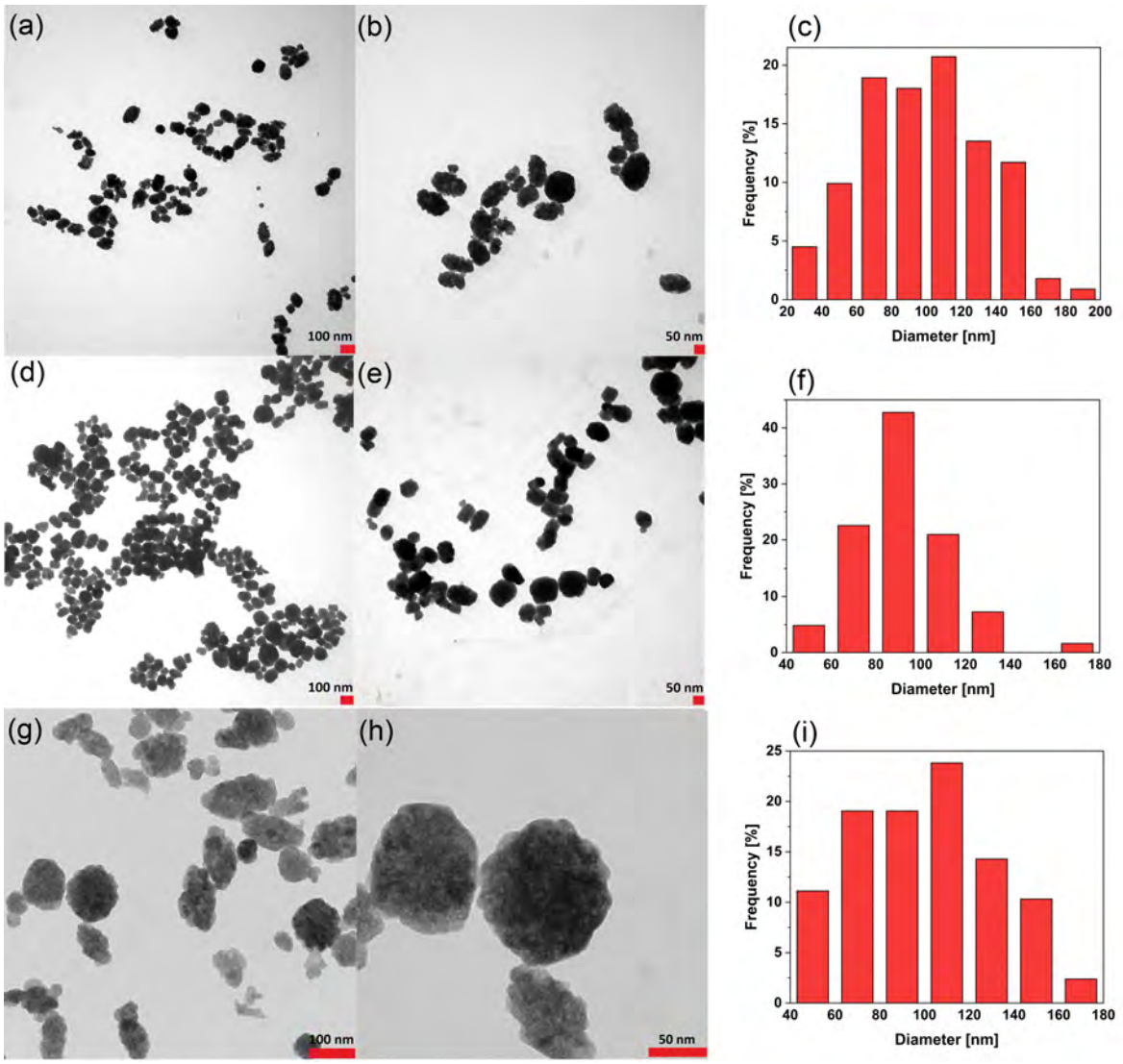

Figure A.12: (a,b) SEM1 images of NaGd:Er_1h UCNPs with a scale bar = 100 and 50 nm, respectively (c) Particle size distribution histogram of NaGd:Er_1h according to SEM1 (d,e) SEM1 images of NaGd:Er_2h UCNPs with a scale bar = 100 and 50 nm, respectively (f) Particle size distribution histogram of NaGd:Er_2h according to SEM1 (g,h) SEM1 images of NaGd:Er_3h UCNPs with a scale bar = 100 and 50 nm, respectively (i) Particle size distribution histogram of NaGd:Er_3h according to SEM1.

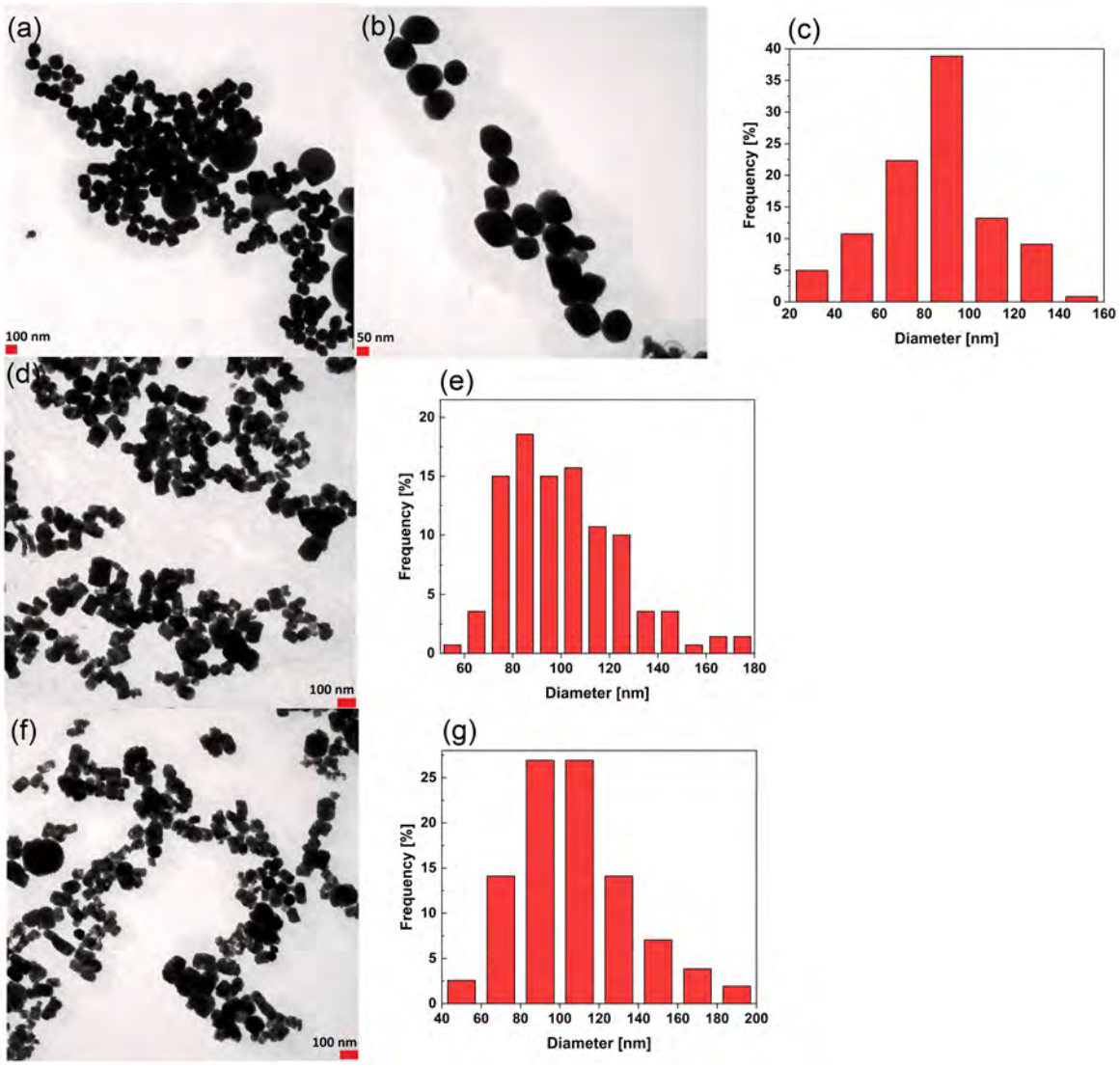

Figure A.13: (a,b) SEM1 images of NaGd:Er_4h UCNPs with a scale bar = 100 and 50 nm, respectively (c) Particle size distribution histogram of NaGd:Er_4h according to SEM1 (d) SEM1 image of NaGd:Er_4h_(1:4:3) UCNPs with a scale bar = 100 nm (e) Particle size distribution histogram of NaGd:Er_4h_(1:4:3) according to SEM1, (f) SEM1 image of NaGd:Er_4h_(1.5:3:3) UCNPs with a scale bar = 100 nm (g) Particle size distribution histogram of NaGd:Er_4h_(1.5:3:3) according to SEM1.

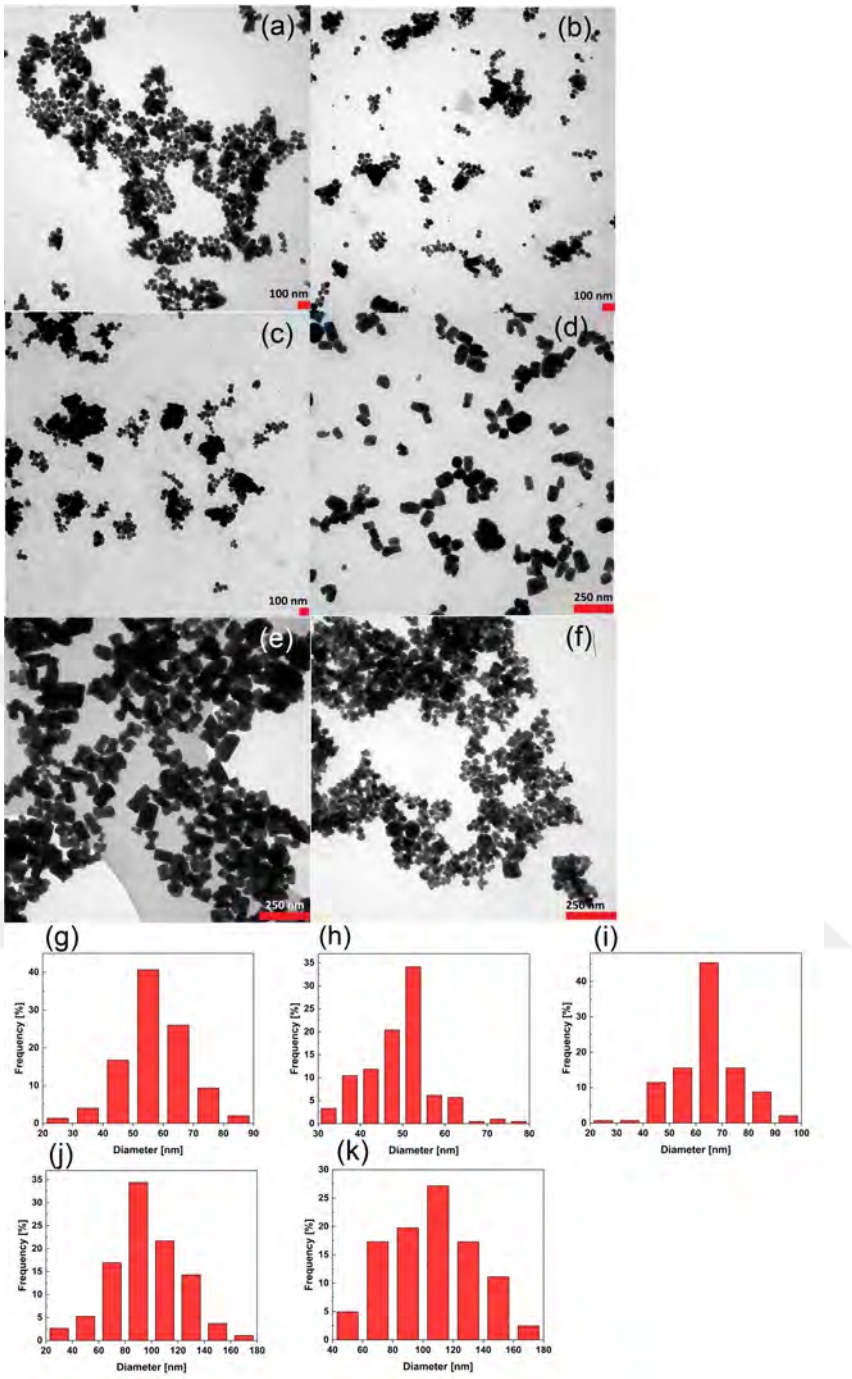

Figure A.14: SEM1 images of (a) NaGd:Er_20min_EG UCNPs with a scale bar = 100 nm (b) NaGd:Er_1h_EG UCNPs with a scale bar = 100 nm (c) NaGd:Er_2h_EG UCNPs with a scale bar = 100 nm (d) NaGd:Er_4h_EG_1000rpm UCNPs with a scale bar = 250 nm (e) NaGd:Er_4h_EG_200°C UCNPs with a scale bar = 250 nm (f) NaGd:Er_20min_EG_1/3V UCNPs with a scale bar = 250 nm, Particle size distribution histogram of (g) NaGd:Er_20min_EG (h) NaGd:Er_1h_EG (i) NaGd:Er_2h_EG (j) NaGd:Er_4h_EG_1000rpm (k) NaGd:Er_4h_EG_200°C according to SEM1.

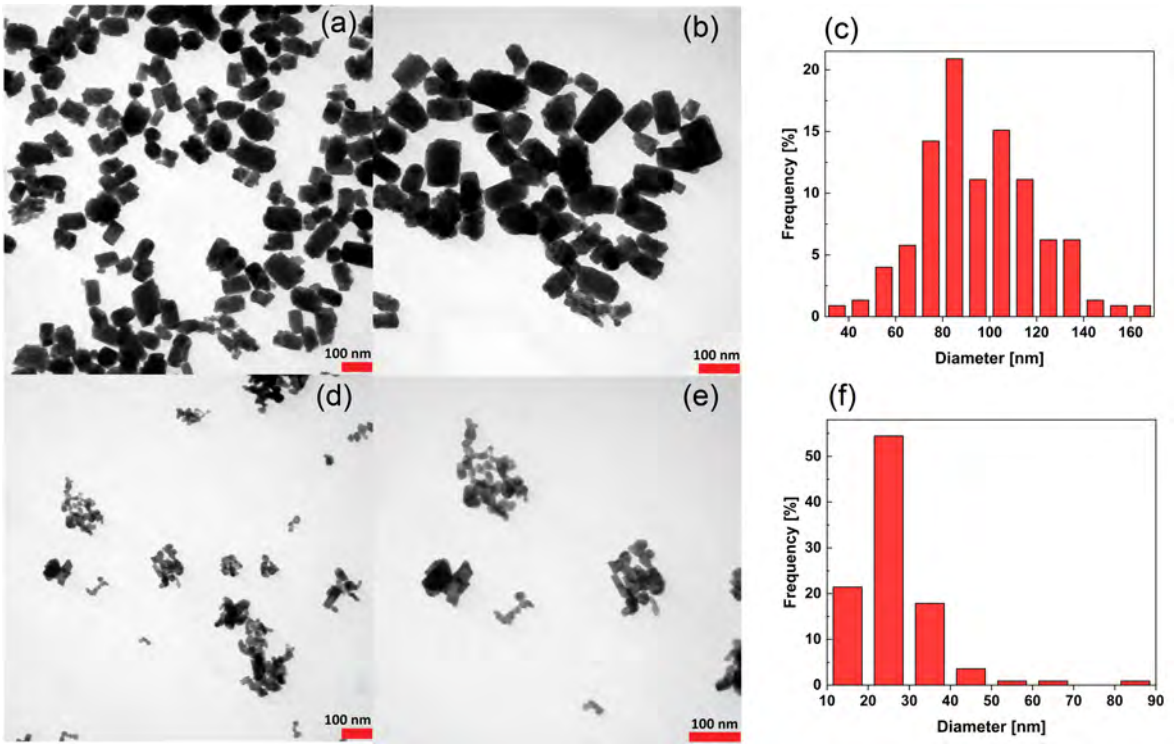

Figure A.15: (a,b) SEM1 images of NaGd:Er_4h_AC UCNPs with a scale bar = 100 and 100 nm (c) Particle size distribution histogram of NaGd:Er_4h_AC according to SEM1 (d,e) SEM1 images of NaGd:Er_20min_G_1/3V UCNPs with a scale bar = 100 and 100 nm (f) Particle size distribution histogram of NaGd:Er_20min_G_1/3V according to SEM1.

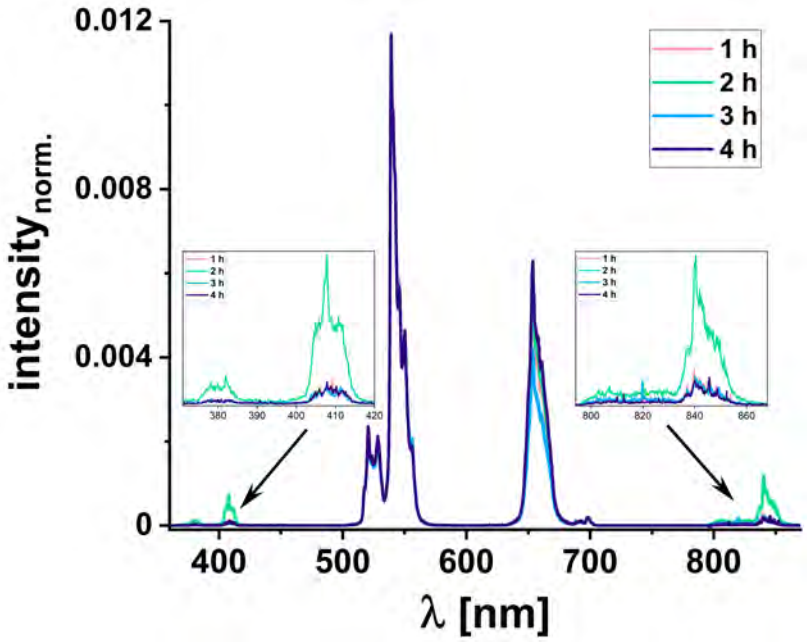

Figure A.16: Normalized UCL spectra of UCNPs (a)NaGd:Er_1h, NaGd:Er_2h, NaGd:Er_3h, NaGd:Er_4h. All measurements carried out under 976 nm pulsed excitation in Milli-Q water.

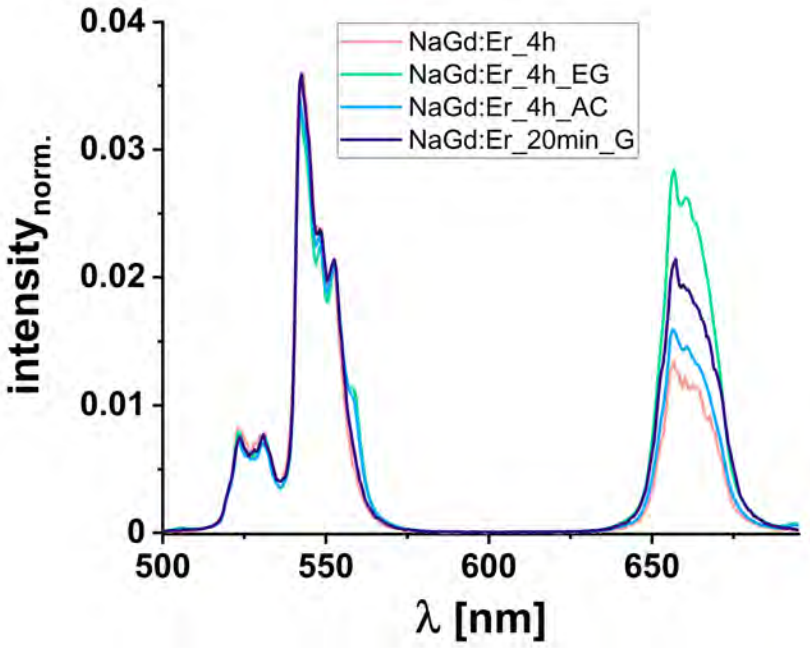

Figure A.17: Normalized UCL spectra of UCNPs NaGd:Er_4h, NaGd:Er_4h_EG, NaGd:Er_4h_AC, NaGd:Er_20min_G_1/3V. All measurements carried out under 976 nm pulsed excitation in Milli-Q water.

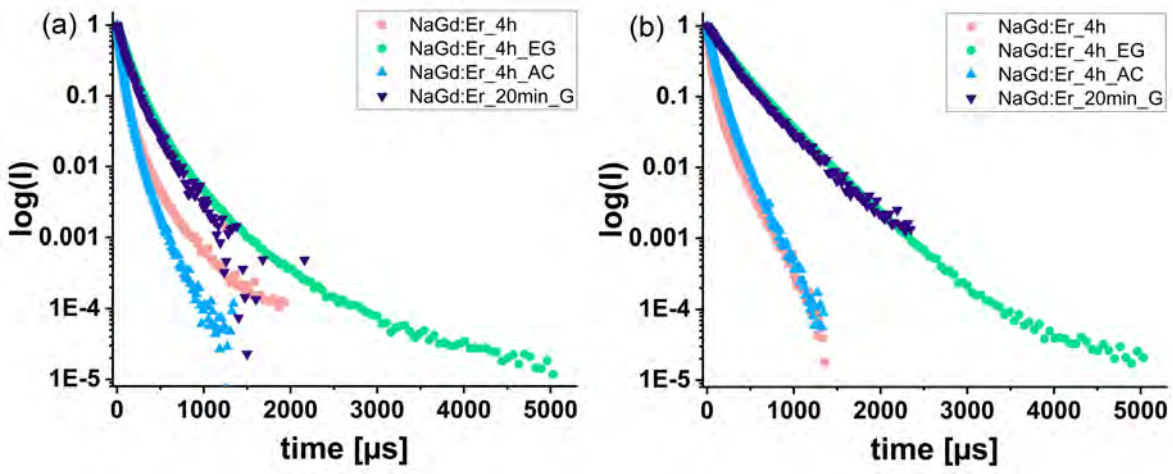

Figure A.18: Normalized UCL decay kinetics of (b) the G_T (c) the R emissions of Er^{3+} for samples NaGd:Er_4h, NaGd:Er_4h_EG, NaGd:Er_4h_AC, NaGd:Er_20min_G_1/3V. All measurements carried out under 976 nm pulsed excitation in Milli-Q water.

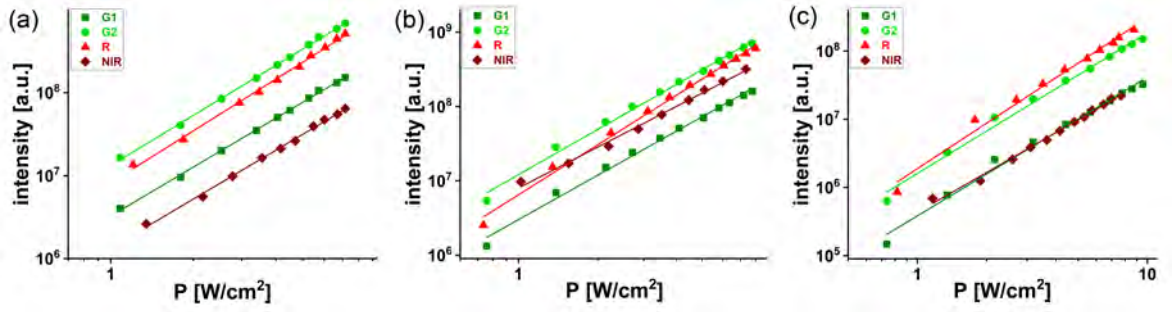

Figure A.19: The double logarithmic plots of G1, G2, R and one NIRE emission intensities of Er^{3+} versus pump power density for the samples (a) NaGd:Er_1h (b) NaGd:Er_2h (c) NaGd:Er_3h.

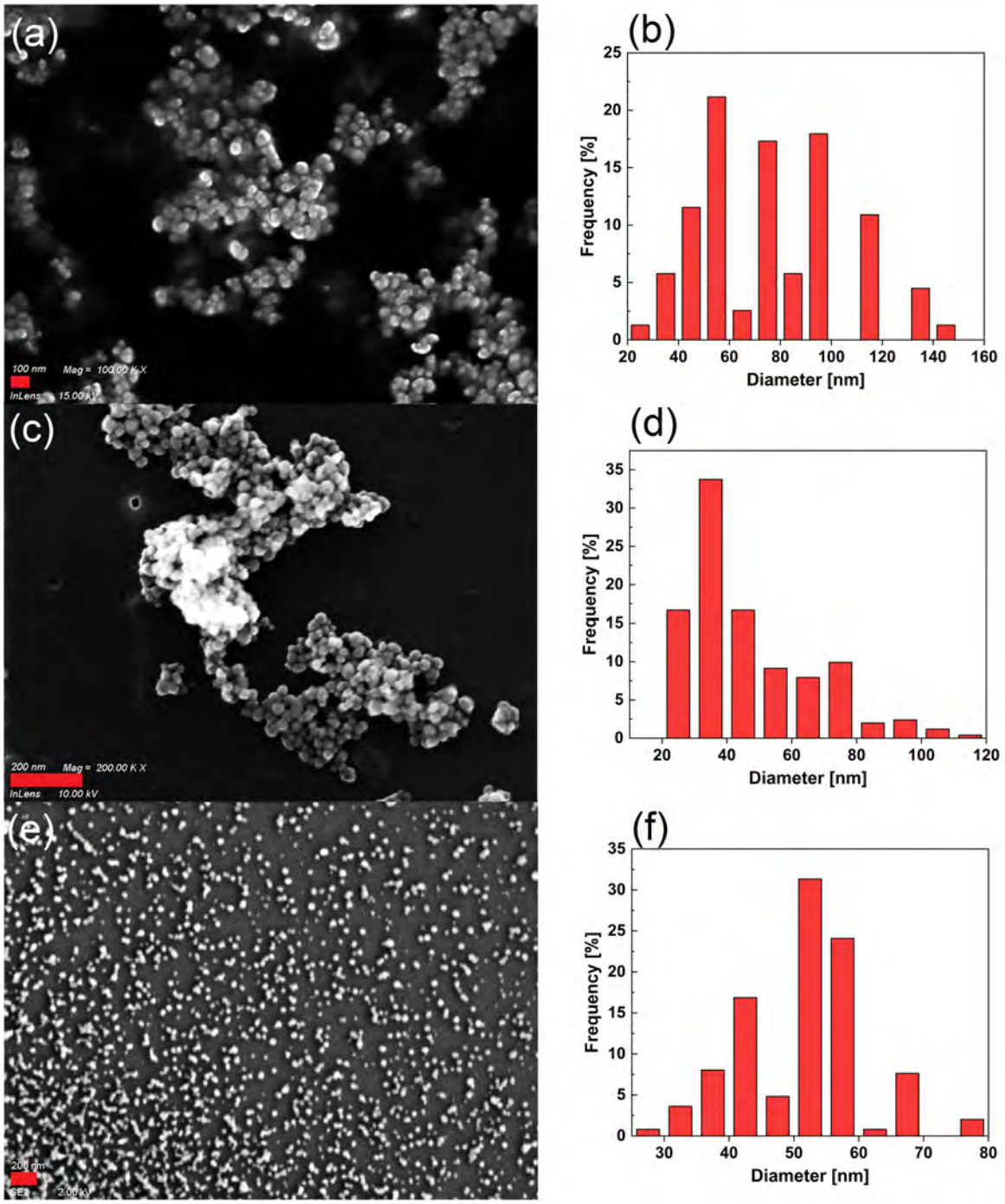

Figure A.20: (a) SEM1 images of A@NaY:Gd_0 UCNPs with a scale bar = 100 nm (b) Particle size distribution histogram of A@NaY:Gd_0 according to SEM2 (c) SEM2 images of A@NaY:$Gd_{7.5}$ UCNPs with a scale bar = 200 nm (d) Particle size distribution histogram of A@NaY:$Gd_{7.5}$ according to SEM2 (e) SEM2 images of A@NaY:Gd_{15} UCNPs with a scale bar = 200 nm (f) Particle size distribution histogram of A@NaY:Gd_{15} according to SEM2.

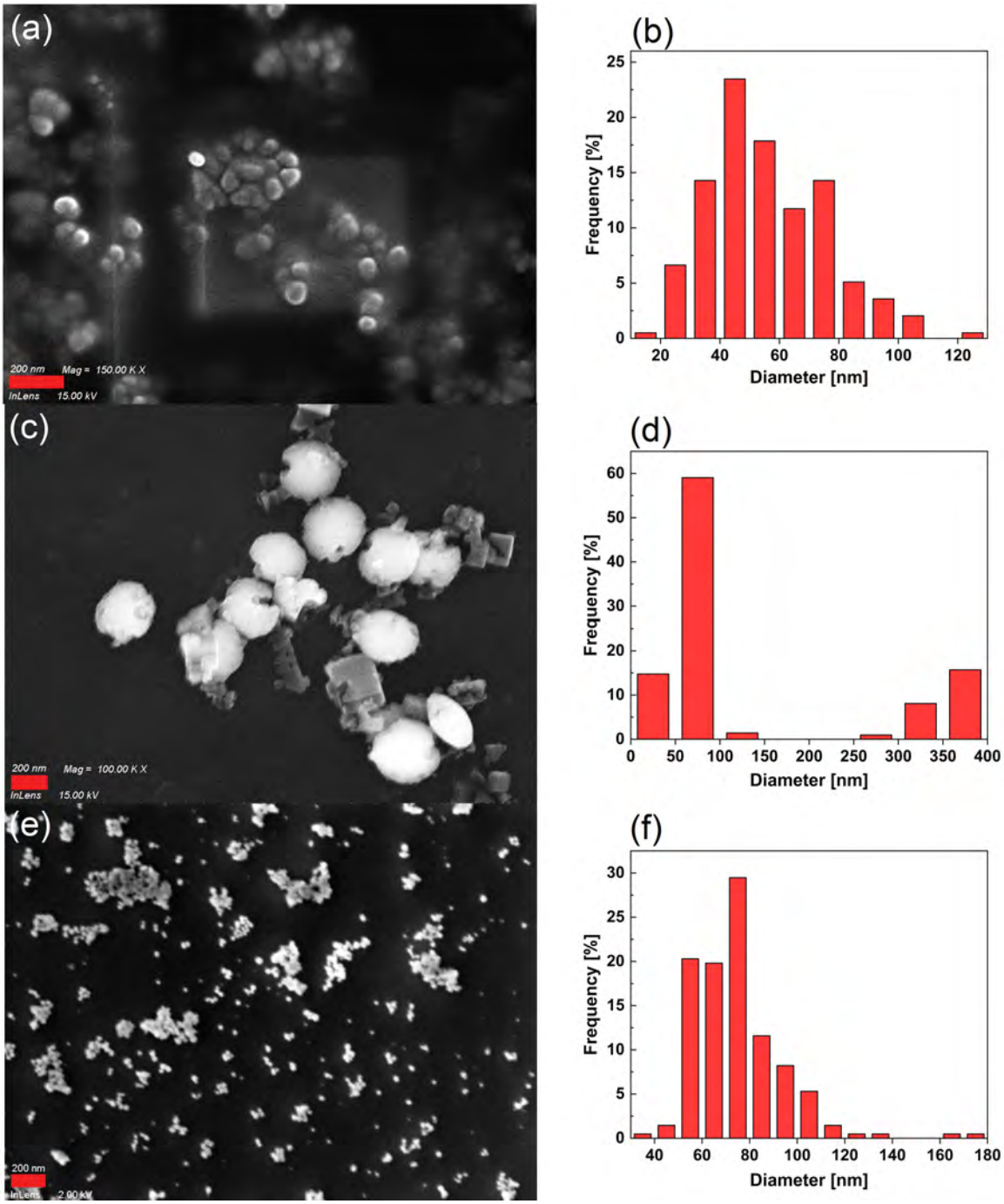

Figure A.21: (a) SEM2 images of A@NaSc:Gd_0 UCNPs with a scale bar = 200 nm (b) Particle size distribution histogram of A@NaSc:Gd_0 according to SEM2 (c) SEM2 images of A@NaSc:$Gd_{7.5}$ UCNPs with a scale bar = 200 nm (d) Particle size distribution histogram of A@NaSc:$Gd_{7.5}$ according to SEM2 (e) SEM2 images of A@NaSc:Gd_{15} UCNPs with a scale bar = 200 nm (f) Particle size distribution histogram of A@NaSc:Gd_{15} according to SEM2.

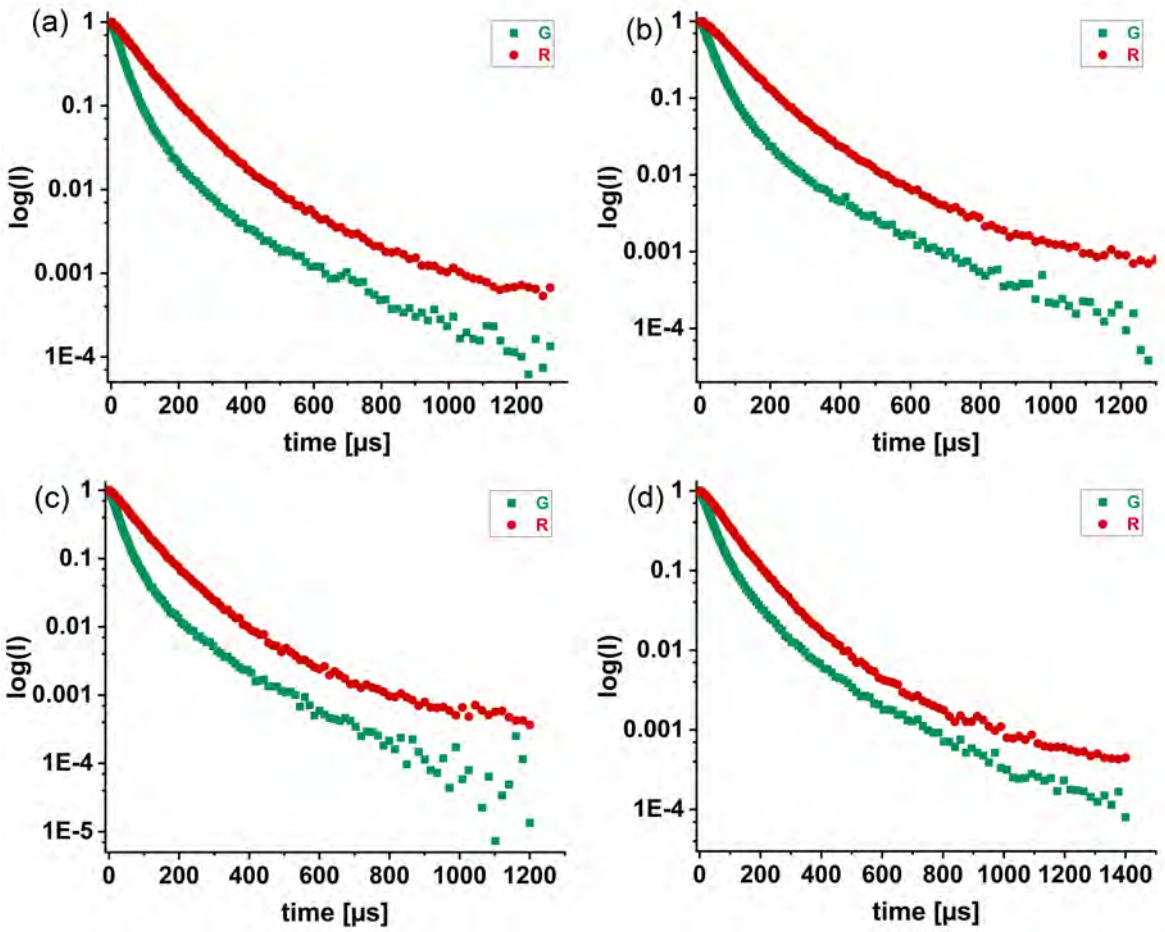

Figure A.22: Normalized UCL decay kinetics of the G_T and R emissions of Er^{3+} for (a) A@NaY:Gd_0 (b) A@NaY:$Gd_{7.5}$ (c) A@NaY:Gd_{15} (d) A@NaY:Gd_{30}. All measurements carried out in Milli-Q water with experimental parameters: λ_{ex} = 976 nm, exposure time = 0.017 secs, delay time after the laser pulse = 500 ns, gate width = 500 μs, number of accumulations = 1000 (steady state) and 100-200 (time resolved).

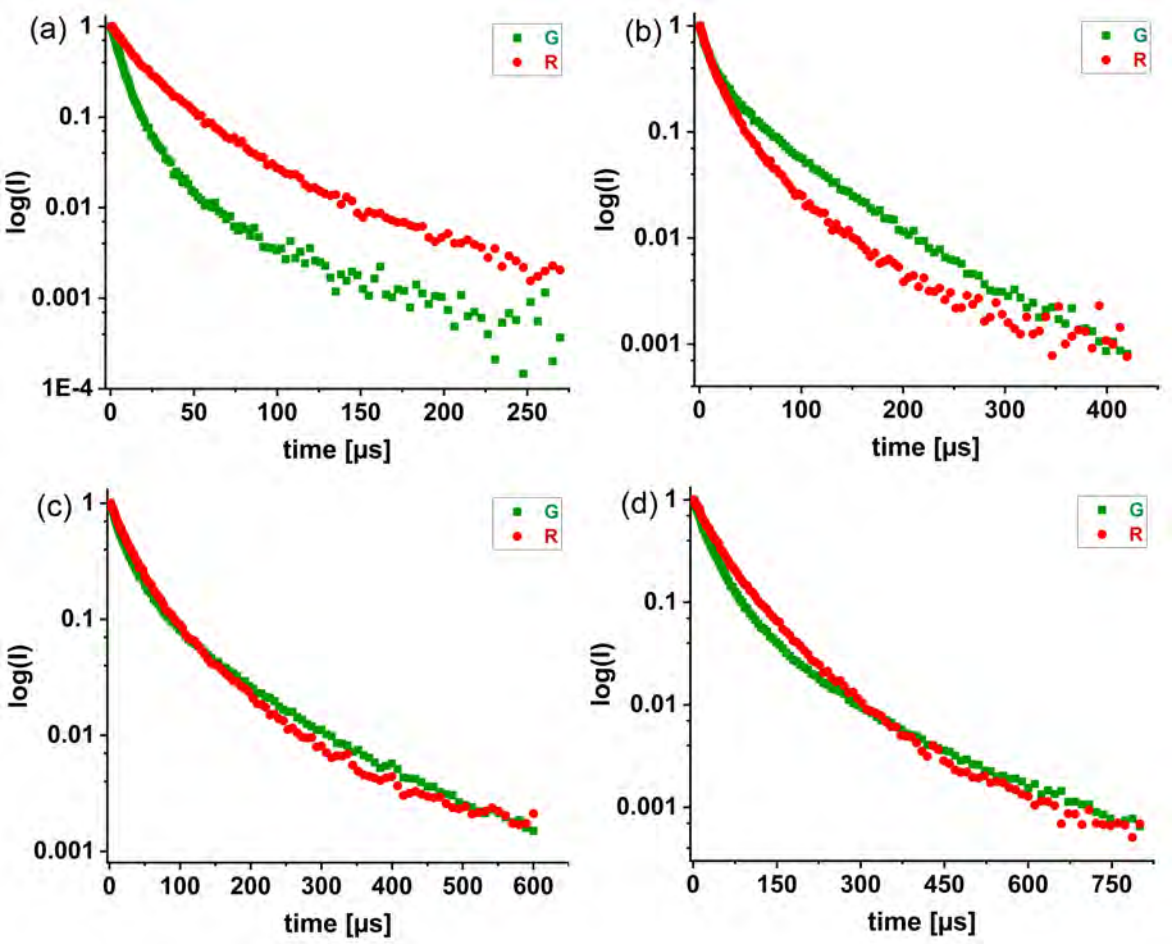

Figure A.23: Normalized UCL decay kinetics of the G_T and R emissions of Er^{3+} for (a) A@NaSc:Gd_0 (b) A@NaSc:$Gd_{7.5}$ (c) A@NaSc:Gd_{15} (d) A@NaSc:Gd_{30}. All measurements carried out in Milli-Q water with experimental parameters: λ_{ex} = 976 nm, exposure time = 0.017 secs, delay time after the laser pulse = 500 ns, gate width = 500 μs, number of accumulations = 1000 (steady state) and 100-200 (time resolved).

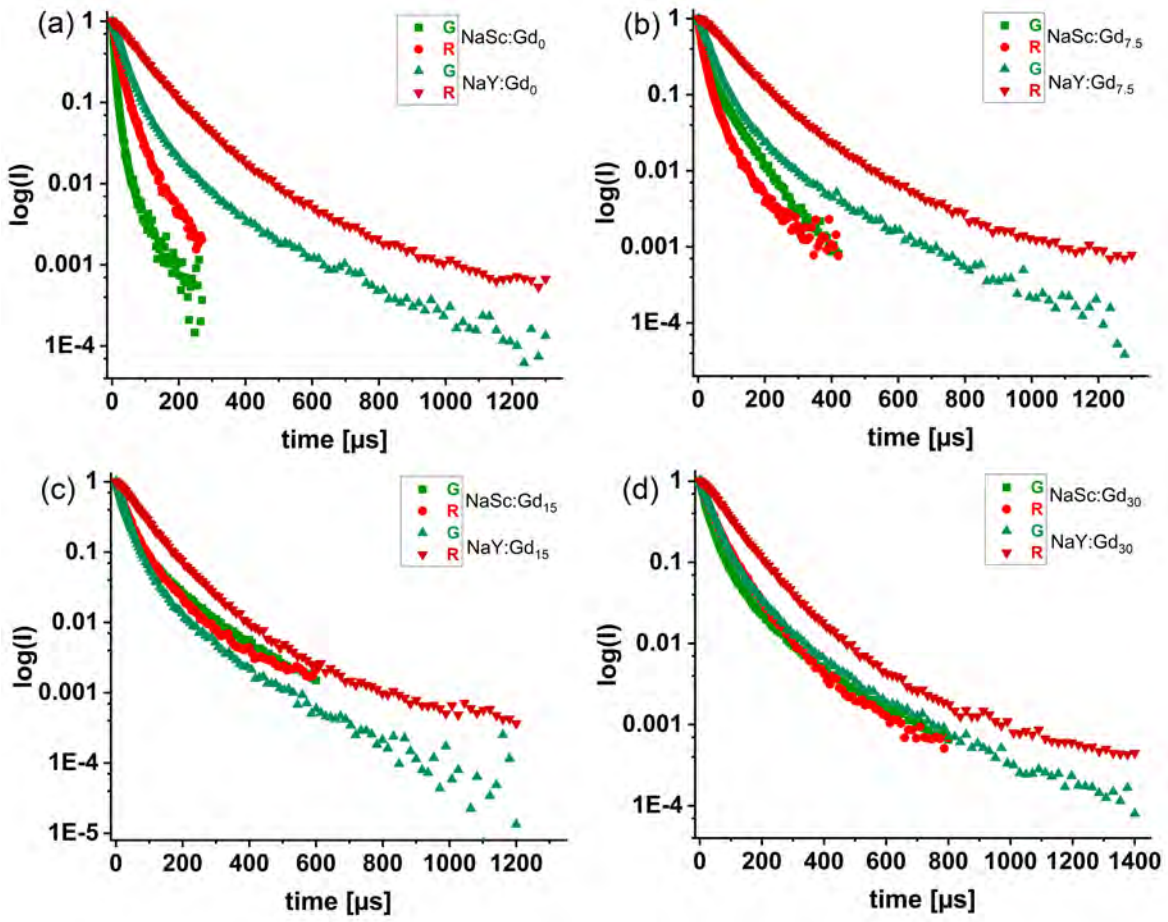

Figure A.24: Normalized UCL decay kinetics of the G_T and R emissions of Er^{3+} for (a) A@NaY:Gd_0 and A@NaSc:Gd_0 (b) A@NaY:$Gd_{7.5}$ and A@NaSc:$Gd_{7.5}$ (c) A@NaY:Gd_{15} and A@NaSc:Gd_{15} (d) A@NaY:Gd_{30} and A@NaSc:Gd_{30}. All measurements carried out in Milli-Q water with experimental parameters: λ_{ex} = 976 nm, exposure time = 0.017 secs, delay time after the laser pulse = 500 ns, gate width = 500 μs, number of accumulations = 1000 (steady state) and 100-200 (time resolved).

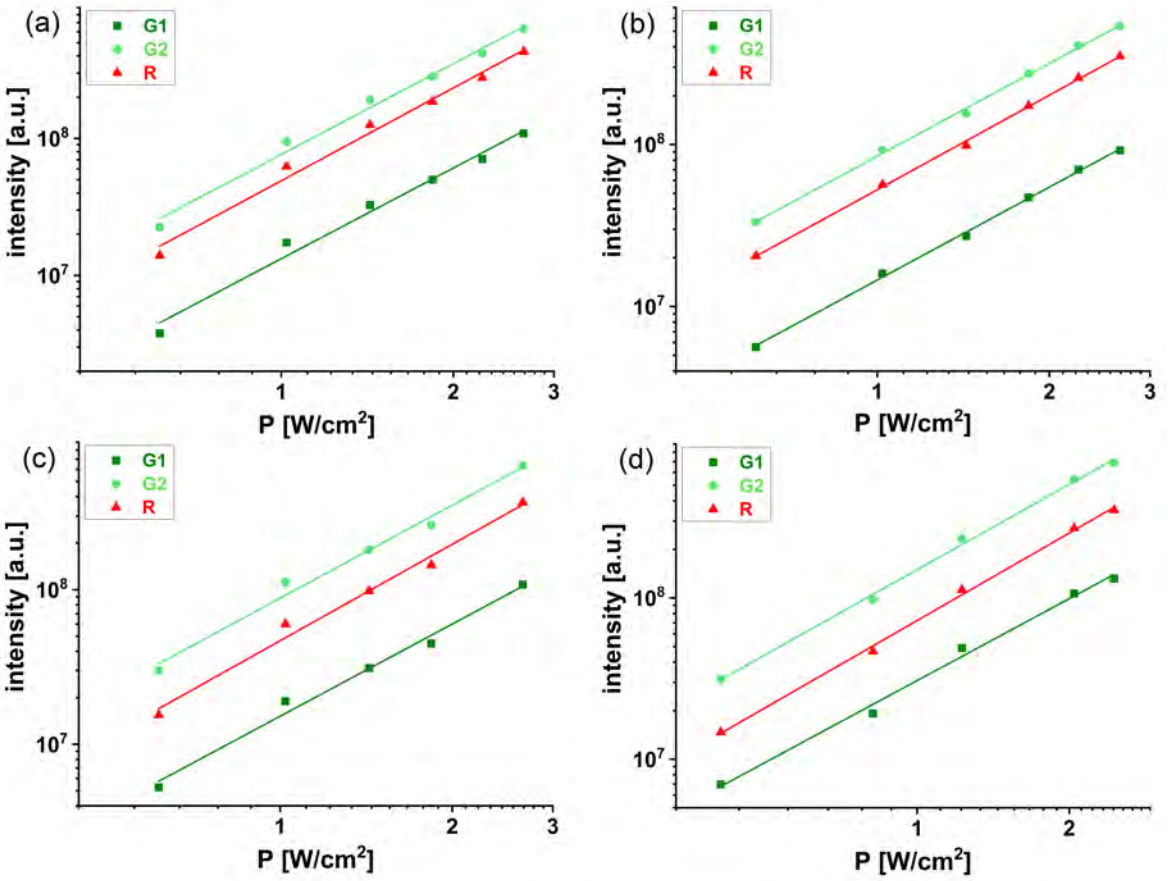

Figure A.25: The double logarithmic plots of G1, G2 and R emission intensities of Er^{3+} versus pump power density for the samples (a) A@NaY:Gd_0 (b) A@NaY:$Gd_{7.5}$ (c) A@NaY:Gd_{15} (d) A@NaSc:Gd_0.

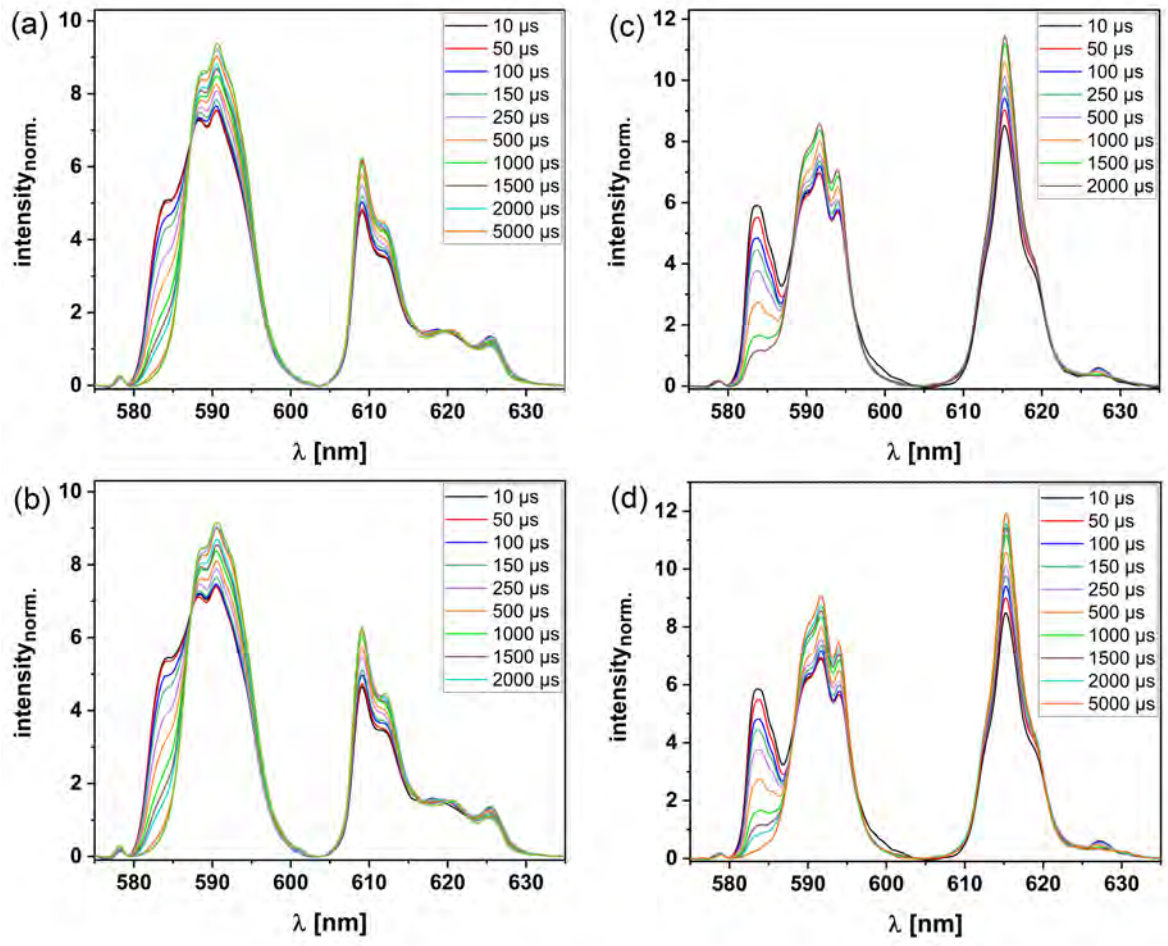

Figure A.26: TRANES of (a) NaY:Gd_{15} (b) NaY:Gd_{30} (c) NaSc:Gd_{15} (d) NaSc:Gd_{30}. All measurements carried out in Milli-Q water with experimental parameters: λ_{ex} = 464.1 nm, exposure time = 0.05 secs, delay time after the laser pulse = 500 ns, number of accumulations = 200 – 2000.

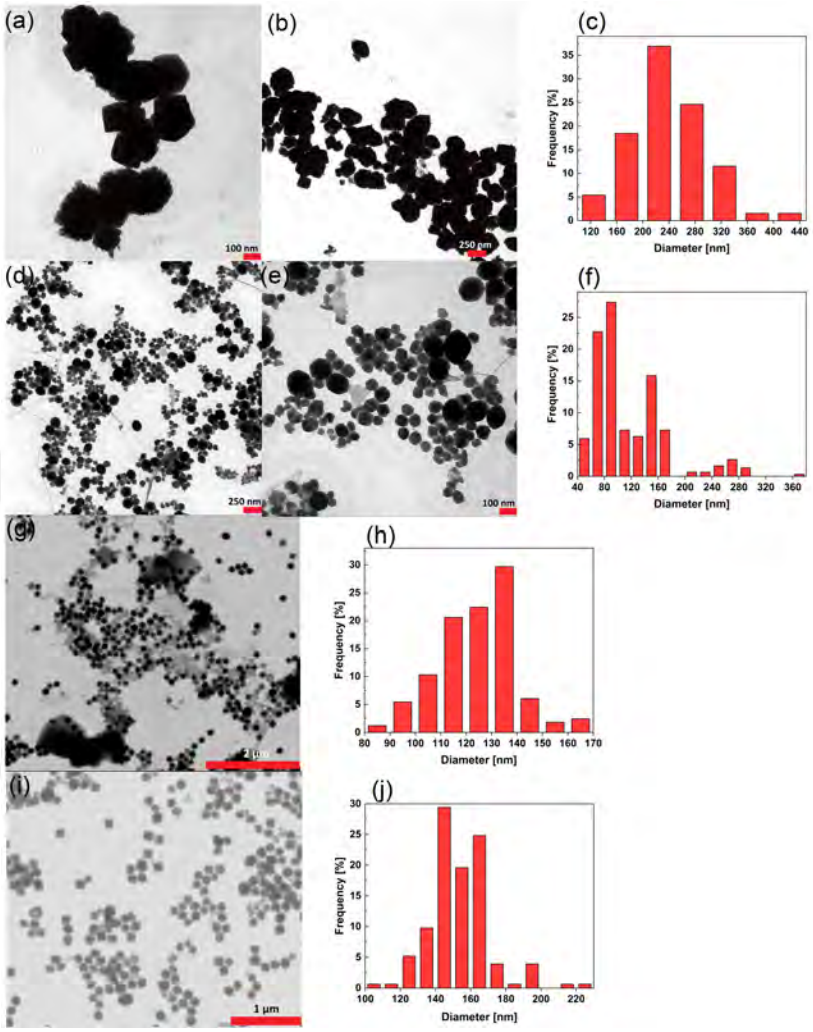

Figure A.27: (a,b) TEM2 images of PEI800$_5$_200°C UCNPs with a scale bar = 250 and 100 nm, respectively (c) Particle size distribution histogram of PEI800$_5$_200°C according to TEM2 (d,e) TEM2 images of PEI25000$_5$_200°C UCNPs with a scale bar = 250 and 100 nm, respectively (f) Particle size distribution histogram of PEI25000$_5$_200°C according to TEM2 fine and large together (g) SEM1 image of PEI25000$_{10}$_250°C with a scale bar = 2 μm, (h) Particle size distribution histogram of PEI25000$_{10}$_250°C according to SEM1 (i) SEM1 image of PEI25000$_{10}$_300°C with a scale bar = 1 μm, (j) Particle size distribution histogram of PEI25000$_{10}$_300°C according to SEM1.

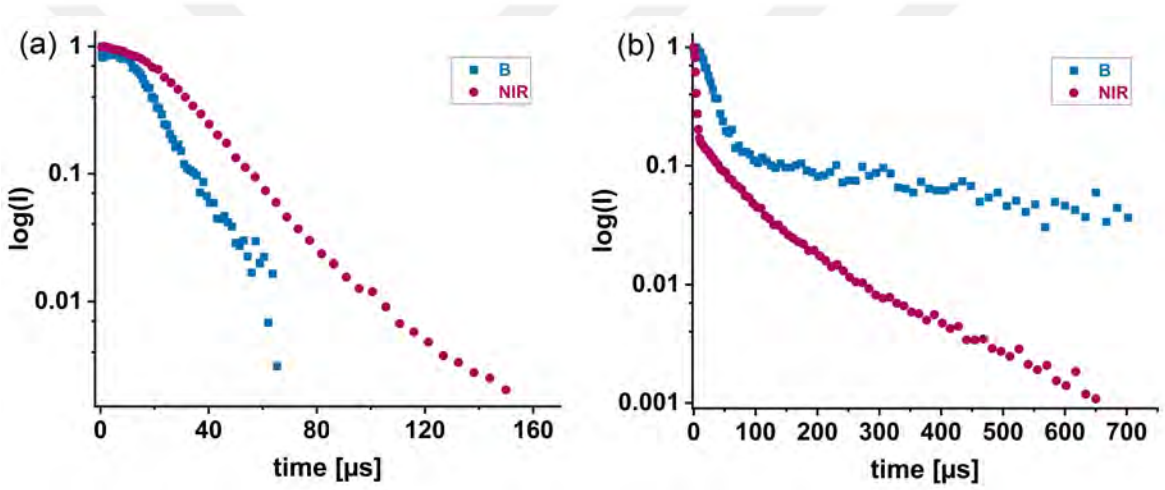

Figure A.28: (a)PEI800$_5$_200°C, (b) PEI25000$_{10}$_250°C UCNPs.

Abbrevations:

6AA — 6- aminohexanoic acid
AcOH — acetic acid
AC — amino cellulose
AEP — aminoethyl dihydrogen phosphate
AREF4 — rare-earth fluoride UC nanoparticles
CSU — cooperative sensitization upconversion
B1 — $^1D_2 \rightarrow {}^3F_4$ transition of Tm^{3+}
B2 — $^1G_4 \rightarrow {}^3H_6$ transition of Tm^{3+}
B — total emission band of $^1D_2 \rightarrow {}^3F_4$ and $^1G_4 \rightarrow {}^3H_6$ transitions of Tm^{3+}
CCD — charge coupled device
CT — computed tomography
DLS — dynamic light scattering
E1 — intermediate electronic state
E2 — higher electronic state
ED — electric dipole
EDTA — ethylenediaminetetraacetic acid
EEMS — excitation-emission-matrix spectra
EG — ethylene glycol
EMU — energy migration upconversion
ESA — excited states absorption
EtOH — ethanol
ETU — energy transfer upconversion
G1 — $^2H_{11/2} \rightarrow {}^4I_{15/2}$ transition of Er^{3+}
G2 — $^4S_{3/2} \rightarrow {}^4I_{15/2}$ transition of Er^{3+}
G_T - total emission band of $^2H_{11/2} \rightarrow {}^4I_{15/2}$ and $^4S_{3/2} \rightarrow {}^4I_{15/2}$ transitions of Er^{3+}
GS — ground state
GSA — ground state absorption
IR — infrared
MD — magnetic dipole
MRI — magnetic resonance imaging
M_W — average molecular weight
NIR — Near infrared
NIR_E — $^3H_4 \rightarrow {}^3H_6$ transition of Tm^{3+}
OA — oleic acid
ODE — 1 - octadecene
OM — oleylamine
OPO — optical parametric oscillator
QD — quantum dots
PA — photon avalanche
PAA — poly(acrylic acid)
PAH — poly(allylamine hydrochloride)
PARAFAC — parallel factor analysis
PEG — poly(ethyleneglycol)

PEG-b-PLA — poly((ethylene glycol)-block-lactic acid
PEI — polyethyleneimine
PL — photoluminescence
PMA — N-dodecyl-polyisobutylene-alt-maleamic acid
PMAO — poly(maleic anhydride-alt-1-octadecene
PSS — poly(styrene sulfonate)
PVP — polyvynilpyrrolidon
R — $^4F_{9/2} \rightarrow {}^4I_{15/2}$ transition of Er^{3+}
SEM — scanning electron microscopy
SBR — signal-to-background ratio
TCL — thermally coupled energy levels
TEM — transmission electron microscopy
TLS — total luminescence spectra
TRANES — Time resolved area normalised emission spectra
UC — upconversion
UCL — upconversion luminescence
UV — ultraviolet
XRD — X-Ray diffraction
wt% — weight percentage

Publications and communications

Publications:

P.U. Bastian, S. Nacak, V. Roddatis, and M.U. Kumke. Tracking the motion of lanathanide ions within core-shell-shell $NaYF_4$ Nanocrystals via Resonance Energy Transfer. *The Journal of Physical Chemistry C* 2020, 124 (20), 11229-11238

Oral presentations:

P. Bastian, S. Nacak, and M. Kumke. Multiplexed targeting of cells and tissue - novel surface-modulated upconversion nanoparticles for biosensing and -imaging. *JCF - Frühjahrsymposium*, Mainz, Germany, 2017
P. Bastian, S. Nacak, and M.U. Kumke. Multiplexed targeting of cells and tissue - novel surface-modulated upconversion nanoparticles for biosensing and -imaging. *DBS EBS Biosensor symposium 2017*, Potsdam, Germany, 2017
D.T. Klier, S. Nacak, S. McGee, A. Lopez and M.U. Kumke. Upconversion nanoparticles (UCNP) as versatile probe in life science application. Workshop in field of action: *Biomaterials and photonics*, Potsdam, Germany, 2016.
D.T. Klier, S. Nacak, S. McGee and M.U. Kumke. Potential of Upconversion nanoparticles (UCNP) in life-science/bioanalytics. Workshop in field of action: *Biomedical optics and ophthalmic optics*, Potsdam, Germany, 2015. D.T. Klier, S. Nacak and M.U. Kumke. Upconversion NaSc/YF_4:Yb:Er nanoparticles co-doped with Gd^{3+} and Nd^{3+} for thermometry on nanoscale. *Optics in the Life Sciences Congress*, Vancouver, Kanada, 2015.

Poster presentations:

S. Nacak, and M.U. Kumke.Comparison of $NaScF_4$:Yb^{3+}, Er^{3+} vs. $NaYF_4$:Yb^{3+}, Er^{3+} upconversion nanoparticles co-doped with Eu^{3+}. *The 2ndConference and Spring School on Properties, Design, and Applications of Upconversion Nanomaterials*, UPCON 2018, Valencia, Spain, 2018
P. Bastian, S. Nacak, L. Yu, M. Kumke, and R. Haag. Multiplexed targeting of cells and tissue - novel surface-modulated upconversion nanoparticles for biosensing. *GDCh-Wissenschaftsforum Chemie 2017*, Berlin, Germany, 2018
S. Nacak,P. Bastian, and M. Kumke. Multiplexed targeting of cells and tissue - novel surface-modulated upconversion nanoparticles for biosensing and -imaging. *116th Bunsentagung*, Kaiserslautern, Germany, 2017

D.T. Klier, S. Nacak, M.U. Kumke. Upconversion NaSc/YF_4 :Yb:Er nanoparticles co-doped with Gd^{3+} and Nd^{3+} for thermometry on nanoscales. *29. Tag der Chemie*, Berlin, Germany, 2015. D.T. Klier, S. Nacak, M.U. Kumke. Upconversion NaSc/YF_4 :Yb:Er nanoparticles co-doped with Gd^{3+} and Nd^{3+} for thermometry on nanoscales. *Anakon*, Graz, Austria, 2015.

Scholarships:

PHD scholarship from Ministry of National Education, Republic of Turkey, 2015-2021.

Bibliography

[1] R. Kumar, M. Nyk, T. Y. Ohulchanskyy, C. A. Flask, and P. N. Prasad, *Advanced Functional Materials*, 2009, **19**(6), 853–859.

[2] O. S. Wolfbeis, *Chemical Society Reviews*, 2015, **44**(14), 4743–4768.

[3] N. Bedard, M. Pierce, A. El-Naggar, S. Anandasabapathy, A. Gillenwater, and R. Richards-Kortum, *Technology in cancer research & treatment*, 2010, **9**(2), 211–217.

[4] X. Zhu, J. Zhang, J. Liu, and Y. Zhang, *Advanced Science*, 2019, **6**(22), 1901358.

[5] B. Valeur and M. Berberan-Santos, Molecular fluorescence: Principles and applications 2nd edn (weinhein wiley, 2012.

[6] D. K. Chatterjee, M. K. Gnanasammandhan, and Y. Zhang, *Small*, 2010, **6**(24), 2781–2795.

[7] G. Chen, H. Qiu, P. N. Prasad, and X. Chen, *Chemical reviews*, 2014, **114**(10), 5161–5214.

[8] A.-H. Li and G. Chen, *Journal of Physics D: Applied Physics*, 2019, **53**(4), 043001.

[9] U. Resch-Genger and H. H. Gorris, *Analytical and bioanalytical chemistry*, 2017, **409**(25), 5855–5874.

[10] M. V. DaCosta, S. Doughan, Y. Han, and U. J. Krull, *Analytica chimica acta*, 2014, **832**, 1–33.

[11] N. Bloembergen, *Physical Review Letters*, 1959, **2**(3), 84.

[12] F. Auzel and D. Pecile, *journal of Luminescence*, 1973, **8**(1), 32–43.

[13] A. Nadort, J. Zhao, and E. M. Goldys, *Nanoscale*, 2016, **8**(27), 13099–13130.

[14] R. L. Sutherland, *Handbook of nonlinear optics*, CRC press, 2003.

[15] F. Auzel, *Chemical reviews*, 2004, **104**(1), 139–174.

[16] J.-C. G. Bünzli, *Accounts of chemical research*, 2006, **39**(1), 53–61.

[17] Y. Huang *Upconverting nanoparticles for integration in bioimaging and therapeutic applications.* PhD thesis, Université du Québec, Institut national de la recherche scientifique, 2017.

[18] J.-C. G. Bünzli and S. V. Eliseeva in *Lanthanide Luminescence;* Springer, 2010; pp. 1–45.

[19] U. Rocha, C. Jacinto da Silva, W. Ferreira Silva, I. Guedes, A. Benayas, L. Martinez Maestro, M. Acosta Elias, E. Bovero, F. C. van Veggel, J. A. Garcia Sole, et al., *Acs Nano*, 2013, **7**(2), 1188–1199.

[20] *Dissertation.*

[21] C.-H. Huang, *Rare earth coordination chemistry: fundamentals and applications*, John Wiley & Sons, 2011.

[22] W. Ahmed, M. J. Jackson, and M. J. Jackson, *Emerging nanotechnologies for manufacturing*, William Andrew, 2009.

[23] F. Wang, D. Banerjee, Y. Liu, X. Chen, and X. Liu, *Analyst*, 2010, **135**(8), 1839–1854.

[24] S. V. Eliseeva and J.-C. G. Bünzli, *New Journal of Chemistry*, 2011, **35**(6), 1165–1176.

[25] C. Chen, C. Li, and Z. Shi, *Advanced Science*, 2016, **3**(10), 1600029.

[26] H. Dong, L.-D. Sun, and C.-H. Yan, *Nanoscale*, 2013, **5**(13), 5703–5714.

[27] F.-M. Matysik, *Advances in Chemical Bioanalysis*, Springer, 2014.

[28] C. Duan, L. Liang, L. Li, R. Zhang, and Z. P. Xu, *Journal of Materials Chemistry B*, 2018, **6**(2), 192–209.

[29] M. Joubert, S. Guy, and B. Jacquier, *Physical Review B*, 1993, **48**(14), 10031.

[30] M. S. Meijer, P. A. Rojas-Gutierrez, D. Busko, I. A. Howard, F. Frenzel, C. Würth, U. Resch-Genger, B. S. Richards, A. Turshatov, J. A. Capobianco, et al., *Physical Chemistry Chemical Physics*, 2018, **20**(35), 22556–22562.

[31] M. Haase and H. Schäfer, *Angewandte Chemie International Edition*, 2011, **50**(26), 5808–5829.

[32] P. Singh, N. Jain, A. K. Tiwari, S. Shukla, V. Baranwal, J. Singh, and A. C. Pandey, *Journal of Luminescence*, 2021, **233**, 117737.

[33] E. A. Grebenik, A. B. Kostyuk, and S. M. Deyev, *Russian Chemical Reviews*, 2016, **85**(12), 1277.

[34] S. Wen, J. Zhou, K. Zheng, A. Bednarkiewicz, X. Liu, and D. Jin, *Nature communications*, 2018, **9**(1), 1–12.

[35] J. Zhou, Z. Liu, and F. Li, *Chemical Society Reviews*, 2012, **41**(3), 1323–1349.

[36] V. K. LaMer and R. H. Dinegar, *Journal of the American Chemical Society*, 1950, **72**(11), 4847–4854.

[37] H.-X. Mai, Y.-W. Zhang, L.-D. Sun, and C.-H. Yan, *The Journal of Physical Chemistry C*, 2007, **111**(37), 13730–13739.

[38] F. Wang and X. Liu, *Journal of the American Chemical Society*, 2008, **130**(17), 5642–5643.

[39] Z. Li and Y. Zhang, *Angewandte Chemie*, 2006, **118**(46), 7896–7899.

[40] J.-H. Zeng, J. Su, Z.-H. Li, R.-X. Yan, and Y.-D. Li, *Advanced Materials*, 2005, **17**(17), 2119–2123.

[41] F. Zhang, Y. Wan, T. Yu, F. Zhang, Y. Shi, S. Xie, Y. Li, L. Xu, B. Tu, and D. Zhao, *Angewandte Chemie*, 2007, **119**(42), 8122–8125.

[42] C. Song, S. Zhang, Q. Zhou, L. Shi, L. Du, D. Zhi, Y. Zhao, Y. Zhen, and D. Zhao, *RSC advances*, 2017, **7**(43), 26633–26639.

[43] N. Panov, R. Marin, and E. Hemmer, *Inorganic chemistry*, 2018, **57**(23), 14920–14929.

[44] M. A. Gomes, A. S. Lima, K. I. Eguiluz, and G. R. Salazar-Banda, *Journal of Materials Science*, 2016, **51**(10), 4709–4727.

[45] X. Liu, J. Zhao, Y. Sun, K. Song, Y. Yu, C. Du, X. Kong, and H. Zhang, *Chemical Communications*, 2009, pp. 6628–6630.

[46] S. Fan, S. Wang, W. Xu, M. Li, H. Sun, and L. Hu, *Journal of Materials Science*, 2017, **52**(2), 869–877.

[47] Y. Liu, D. Tu, H. Zhu, E. Ma, and X. Chen, *Nanoscale*, 2013, **5**(4), 1369–1384.

[48] W. Fang and Y. Wei, *Journal of Innovative Optical Health Sciences*, 2016, **9**(04), 1630006.

[49] A. Escudero, A. I. Becerro, C. Carrillo-Carrión, N. O. Núñez, M. V. Zyuzin, M. Laguna, D. González-Mancebo, M. Ocaña, and W. J. Parak, *Nanophotonics*, 2017, **6**(5), 881–921.

[50] A. Escudero, C. Carrillo-Carrión, M. V. Zyuzin, and W. J. Parak, *Topics in Current Chemistry*, 2016, **374**(4), 48.

[51] R. Naccache, F. Vetrone, V. Mahalingam, L. A. Cuccia, and J. A. Capobianco, *Chemistry of Materials*, 2009, **21**(4), 717–723.

[52] J.-C. Boyer, M.-P. Manseau, J. I. Murray, and F. C. Van Veggel, *Langmuir*, 2010, **26**(2), 1157–1164.

[53] K. Song, X. Kong, X. Liu, Y. Zhang, Q. Zeng, L. Tu, Z. Shi, and H. Zhang, *Chemical Communications*, 2012, **48**(8), 1156–1158.

[54] D. Tu, L. Liu, Q. Ju, Y. Liu, H. Zhu, R. Li, and X. Chen, *Angewandte Chemie International Edition*, 2011, **50**(28), 6306–6310.

[55] M. Liras, M. González-Béjar, E. Peinado, L. Francés-Soriano, J. Pérez-Prieto, I. Quijada-Garrido, and O. García, *Chemistry of Materials*, 2014, **26**(13), 4014–4022.

[56] Z. Chen, H. Chen, H. Hu, M. Yu, F. Li, Q. Zhang, Z. Zhou, T. Yi, and C. Huang, *Journal of the American Chemical Society*, 2008, **130**(10), 3023–3029.

[57] L. Wang, R. Yan, Z. Huo, L. Wang, J. Zeng, J. Bao, X. Wang, Q. Peng, and Y. Li, *Angewandte Chemie International Edition*, 2005, **44**(37), 6054–6057.

[58] A. Generalova, V. Rocheva, A. Nechaev, D. Khochenkov, N. Sholina, V. Semchishen, V. Zubov, A. Koroleva, B. Chichkov, and E. Khaydukov, *RSC advances*, 2016, **6**(36), 30089–30097.

[59] S. J. Budijono, J. Shan, N. Yao, Y. Miura, T. Hoye, R. H. Austin, Y. Ju, and R. K. Prud'homme, *Chemistry of Materials*, 2010, **22**(2), 311–318.

[60] B. Wu, L. Zhao, Y. Wang, H. Dong, and H. Yu, *RSC Advances*, 2019, **9**(72), 42228–42235.

[61] O. Dukhno, F. Przybilla, V. Muhr, M. Buchner, T. Hirsch, and Y. Mély, *Nanoscale*, 2018, **10**(34), 15904–15910.

[62] L. Graña-Suárez, W. Verboom, S. Sarkar, V. Mahalingam, and J. Huskens, *ChemistrySelect*, 2016, **1**(13), 4068–4074.

[63] G.-M. Han, H.-X. Jiang, Y.-F. Huo, and D.-M. Kong, *Journal of Materials Chemistry B*, 2016, **4**(19), 3351–3357.

[64] K. L. Reddy, N. Prabhakar, R. Arppe, J. M. Rosenholm, and V. Krishnan, *Journal of Materials Science*, 2017, **52**(10), 5738–5750.

[65] M. Wang, C.-C. Mi, J.-L. Liu, X.-L. Wu, Y.-X. Zhang, W. Hou, F. Li, and S.-K. Xu, *Journal of Alloys and Compounds*, 2009, **485**(1-2), L24–L27.

[66] J. Senthilselvan, S. Thomas, L. Anbharasi, D. Sarkar, V. N. Adusumalli, S. A. Kumar, S. Yamini, M. Gunaseelan, J. Manonmani, and V. Mahalingam, *Journal of Materials Science: Materials in Electronics*, 2019, **30**(23), 20376–20392.

[67] A. Bagheri, H. Arandiyan, C. Boyer, and M. Lim, *Advanced Science*, 2016, **3**(7), 1500437.

[68] N. Beckmann, *Brazilian journal of physics*, 2006, **36**(1A), 16–22.

[69] K. Binnemans, *Coordination Chemistry Reviews*, 2015, **295**, 1–45.

[70] M. H. Werts, *Science progress*, 2005, **88**(2), 101–131.

[71] M. K. Mahata, H. C. Hofsäss, and U. Vetter, *Luminescence—An Outlook on the Phenomena and Their Applications; InTech: Rijeka, Croatia*, 2016, pp. 109–131.

[72] E. J. Nassar, K. J. Ciuffi, P. S. Calefi, L. Avila, L. C. Bandeira, A. Cestari, E. H. de Faria, A. L. Marçal, and M. Matos III, *Europium III: Different Emission Spectra in Different Matrices, the Same Element*, Nova Science Publishers, 2010.

[73] P.-A. Primus, T. Ritschel, P. Y. Siguenza, M. A. Cauqui, J. C. Hernandez-Garrido, and M. U. Kumke, *The Journal of Physical Chemistry C*, 2014, **118**(40), 23349–23360.

[74] S. Chemura, T. Haubitz, P. A. Primus, M. Underberg, T. Hülser, and M. U. Kumke, *The journal of physical chemistry. A*, 2020, **124**(24), 4972–4983.

[75] M. González-Béjar, L. Francés-Soriano, and J. Pérez-Prieto, *Frontiers in bioengineering and biotechnology*, 2016, **4**, 47.

[76] D. T. Klier and M. U. Kumke, *Rsc Advances*, 2015, **5**(82), 67149–67156.

[77] F. Wang, D. K. Chatterjee, Z. Li, Y. Zhang, X. Fan, and M. Wang, *Nanotechnology*, 2006, **17**(23), 5786.

[78] A. López de Guereñu, P. Bastian, P. Wessig, L. John, and M. U. Kumke, *Biosensors*, 2019, **9**(1), 9.

[79] D. T. Klier and M. U. Kumke, *The Journal of Physical Chemistry C*, 2015, **119**(6), 3363–3373.

[80] D. T. Klier and M. U. Kumke, *Journal of Materials Chemistry C*, 2015, **3**(42), 11228–11238.

[81] L. M. Jin, X. Chen, C. K. Siu, F. Wang, and S. F. Yu, *ACS nano*, 2017, **11**(1), 843–849.

[82] B. Marmodée, J. S. de Klerk, F. Ariese, C. Gooijer, and M. U. Kumke, *Analytica chimica acta*, 2009, **652**(1-2), 285–294.

[83] P. U. Bastian, S. Nacak, V. Roddatis, and M. U. Kumke, *The Journal of Physical Chemistry C*, 2020, **124**(20), 11229–11238.

[84] P. Lei, R. An, C. Li, J. Feng, and H. Zhang, *CrystEngComm*, 2020, **22**(20), 3432–3438.

[85] S. Radunz, A. Schavkan, S. Wahl, C. Wurth, H. R. Tschiche, M. Krumrey, and U. Resch-Genger, *The Journal of Physical Chemistry C*, 2018, **122**(50), 28958–28967.

[86] J. Cao, L. Yuan, S. Hu, J. Tang, X. Zhou, and J. Yang, *CrystEngComm*, 2016, **18**(31), 5940–5951.

[87] M. W. Pin, E. J. Park, S. Choi, Y. I. Kim, C. H. Jeon, T. H. Ha, and Y. H. Kim, *Scientific reports*, 2018, **8**(1), 1–10.

[88] F. Wang, Y. Han, C. S. Lim, Y. Lu, J. Wang, J. Xu, H. Chen, C. Zhang, M. Hong, and X. Liu, *nature*, 2010, **463**(7284), 1061–1065.

[89] J. A. Damasco, G. Chen, W. Shao, H. Ågren, H. Huang, W. Song, J. F. Lovell, and P. N. Prasad, *ACS applied materials & interfaces*, 2014, **6**(16), 13884–13893.

[90] H. Qin, D. Wu, J. Sathian, X. Xie, M. Ryan, and F. Xie, *Scientific reports*, 2018, **8**(1), 1–8.

[91] M. Liu, Z. Shi, X. Wang, Y. Zhang, X. Mo, R. Jiang, Z. Liu, L. Fan, C.-g. Ma, and F. Shi, *Nanoscale*, 2018, **10**(43), 20279–20288.

[92] X. Li, X. Liu, D. M. Chevrier, X. Qin, X. Xie, S. Song, H. Zhang, P. Zhang, and X. Liu, *Angewandte Chemie International Edition*, 2015, **54**(45), 13312–13317.

[93] C. Zhao, X. Kong, X. Liu, L. Tu, F. Wu, Y. Zhang, K. Liu, Q. Zeng, and H. Zhang, *Nanoscale*, 2013, **5**(17), 8084–8089.

[94] J. Bai, P. Duan, X. Wang, G. Han, M. Wang, and G. Diao, *RSC Advances*, 2020, **10**(32), 18868–18874.

[95] J. Zhao, Y. Hu, S. wei Lin, U. Resch-Genger, R. Zhang, J. Wen, X. Kong, A. Qin, and J. Ou, *Journal of Materials Chemistry B*, 2020, **8**(30), 6481–6489.

[96] W.-B. Pei, B. Chen, L. Wang, J. Wu, X. Teng, R. Lau, L. Huang, and W. Huang, *Nanoscale*, 2015, **7**(9), 4048–4054.

[97] X. Teng, Y. Zhu, W. Wei, S. Wang, J. Huang, R. Naccache, W. Hu, A. I. Y. Tok, Y. Han, Q. Zhang, et al., *Journal of the American Chemical Society*, 2012, **134**(20), 8340–8343.

[98] Y. Ai, D. Tu, W. Zheng, Y. Liu, J. Kong, P. Hu, Z. Chen, M. Huang, and X. Chen, *Nanoscale*, 2013, **5**(14), 6430–6438.

[99] S. Wilhelm, M. Kaiser, C. Würth, J. Heiland, C. Carrillo-Carrion, V. Muhr, O. S. Wolfbeis, W. J. Parak, U. Resch-Genger, and T. Hirsch, *Nanoscale*, 2015, **7**(4), 1403–1410.

[100] D. Manzani, J. F. da Silveira Petruci, K. Nigoghossian, A. A. Cardoso, and S. J. Ribeiro, *Scientific reports*, 2017, **7**, 41596.

[101] O. A. Savchuk, J. J. Carvajal, Y. Cesteros, P. Salagre, H. D. Nguyen, A. Rodenas, J. Massons, M. Aguiló, and F. Díaz, *Frontiers in chemistry*, 2019, **7**, 88.

[102] F. Li, J. Li, L. Chen, Y. Huang, Y. Peng, Y. Luo, L. Zhang, and J. Mu, *Nanoscale research letters*, 2018, **13**(1), 1–9.

[103] E. Zhurova, B. Maksimov, S. Hull, S. Wilson, B. Sobolev, and V. Simonov, *Crystallography Reports*, 1997, **42**(2), 238–242.

[104] A. Grzechnik, P. Bouvier, M. Mezouar, M. Mathews, A. Tyagi, and J. Köhler, *Journal of Solid State Chemistry*, 2002, **165**(1), 159–164.

[105] P. Dahlke and D. Babel, *Zeitschrift für anorganische und allgemeine Chemie*, 1994, **620**(10), 1686–1691.

[106] A. Sedlmeier and H. H. Gorris, *Chemical Society Reviews*, 2015, **44**(6), 1526–1560.

[107] C. F. Gainer and M. Romanowski, *Journal of Innovative Optical Health Sciences*, 2014, **7**(02), 1330007.

[108] *Dissertation*.

[109] J. Kong, X. Shang, W. Zheng, X. Chen, D. Tu, M. Wang, J. Song, and J. Qu, *The Journal of Physical Chemistry Letters*, 2020, **11**(9), 3672–3680.

[110] A. Li, D. Xu, Y. Zhang, H. Lin, S. Yang, Z. Chen, and Y. Shao, *Journal of the American Ceramic Society*, 2016, **99**(5), 1657–1663.

[111] J. Suyver, A. Aebischer, S. García-Revilla, P. Gerner, and H. Güdel, *Physical Review B*, 2005, **71**(12), 125123.

[112] M. Kraft, C. Würth, V. Muhr, T. Hirsch, and U. Resch-Genger, *Nano Research*, 2018, **11**(12), 6360–6374.

[113] D. Xu, C. Liu, J. Yan, S. Yang, and Y. Zhang, *The Journal of Physical Chemistry C*, 2015, **119**(12), 6852–6860.

[114] P. Du and J. S. Yu, *Microchimica Acta*, 2018, **185**(4), 1–8.

[115] K. Lu, Y. Yi, L. Xu, X. Sun, L. Liu, and H. Li, *Nanomaterials*, 2020, **10**(1), 24.

[116] Q. Qiang and Y. Wang, *Frontiers in chemistry*, 2019, **7**, 425.

[117] H. Dong, L.-D. Sun, and C.-H. Yan, *Chemical Society Reviews*, 2015, **44**(6), 1608–1634.

[118] T. C. Eliana Cavaleiro and Luis, *NanoTBTech*, 2019.

[119] Y. B. Band, *Light and matter: electromagnetism, optics, spectroscopy and lasers*, Vol. 1, John Wiley & Sons, 2006.

[120] R. Bajaj, M. Gupta, R. Nagarajan, A. Rao, and G. V. Prakash, *Dalton Transactions*, 2020, **49**(29), 10058–10068.

[121] R. Reisfeld*, E. Zigansky, and M. Gaft, *Molecular Physics*, 2004, **102**(11-12), 1319–1330.

[122] P.-A. Primus, A. Menski, M. P. Yeste, M. A. Cauqui, and M. U. Kumke, *The Journal of Physical Chemistry C*, 2015, **119**(19), 10682–10692.

[123] H. Chang, J. Xie, B. Zhao, B. Liu, S. Xu, N. Ren, X. Xie, L. Huang, and W. Huang, *Nanomaterials*, 2015, **5**(1), 1–25.

[124] D. Wang, L. Ren, X. Zhou, X.-z. Wang, J. Zhou, Y. Han, and N. Kang, *Nanotechnology*, 2012, **23**(22), 225705.

[125] Y. Wang, R. Cai, and Z. Liu, *CrystEngComm*, 2011, **13**(6), 1772–1774.

[126] Y. Sun, Y. Chen, L. Tian, Y. Yu, X. Kong, J. Zhao, and H. Zhang, *Nanotechnology*, 2007, **18**(27), 275609.

[127] P. Ptacek, H. Schäfer, K. Kömpe, and M. Haase, *Advanced Functional Materials*, 2007, **17**(18), 3843–3848.

[128] H. Chen, P. Zhang, H. Cui, W. Qin, and D. Zhao, *Nanoscale research letters*, 2017, **12**(1), 1–9.

[129] M. H. Hussain, N. F. A. Bakar, A. N. Mustapa, K.-F. Low, N. H. Othman, and F. Adam, *Nanoscale research letters*, 2020, **15**(1), 1–10.

[130] Q. Chen, Y. Ge, H. Granbohm, and S.-P. Hannula, *Nanomaterials*, 2018, **8**(6), 362.

[131] G. Tessitore, A.-V. Mudring, and K. W. Krämer, *RSC advances*, 2019, **9**(60), 34784–34792.

[132] M. Runowski, N. Stopikowska, D. Szeremeta, S. Goderski, M. Skwierczynska, and S. Lis, *ACS applied materials & interfaces*, 2019, **11**(14), 13389–13396.

[133] F. Wang, J. Wang, and X. Liu, *Angewandte Chemie International Edition*, 2010, **49**(41), 7456–7460.

[134] J. Chen, C. Guo, M. Wang, L. Huang, L. Wang, C. Mi, J. Li, X. Fang, C. Mao, and S. Xu, *Journal of materials chemistry*, 2011, **21**(8), 2632–2638.

[135] H.-T. Wong, H. L. W. Chan, and J. Hao, *Optics express*, 2010, **18**(6), 6123–6130.

[136] H.-T. Wong, F. Vetrone, R. Naccache, H. L. W. Chan, J. Hao, and J. A. Capobianco, *Journal of Materials Chemistry*, 2011, **21**(41), 16589–16596.

[137] R. Arppe, I. Hyppänen, N. Perälä, R. Peltomaa, M. Kaiser, C. Würth, S. Christ, U. Resch-Genger, M. Schäferling, and T. Soukka, *Nanoscale*, 2015, **7**(27), 11746–11757.

[138] L. Wang, W. Qin, Z. Liu, D. Zhao, G. Qin, W. Di, and C. He, *Optics express*, 2012, **20**(7), 7602–7607.

[139] M. Tou, Y. Mei, S. Bai, Z. Luo, Y. Zhang, and Z. Li, *Nanoscale*, 2016, **8**(1), 553–562.

[140] B. Purohit, Y. Guyot, D. Amans, M.-F. Joubert, B. Mahler, S. Mishra, S. Daniele, C. Dujardin, and G. Ledoux, *ACS photonics*, 2019, **6**(12), 3126–3131.

[141] H. Söderlund, M. Mousavi, H. Liu, and S. Andersson-Engels, *Journal of biomedical optics*, 2015, **20**(8), 086008.

[142] N. Rakov and G. S. Maciel, *Journal of Materials Chemistry C*, 2016, **4**(23), 5442–5447.

[143] S. Yu, L. Fu, Y. Zhou, and H. Su, *Photochemical & Photobiological Sciences*, 2011, **10**(4), 548–553.